CORTICAL MICROCIRCUITRY SUPPORTING ATTENTIONAL SELECTION, AND ITS EXTRACRANIAL CONSEQUENCES

By

JACOB ALAN WESTERBERG

Dissertation

Submitted to the Faculty of the

Graduate School of Vanderbilt University

in partial fulfillment of the requirements

for the degree of

DOCTOR OF PHILOSOPHY

in

PSYCHOLOGY

August 31st, 2022

Nashville, Tennessee

Approved:

Alexander Maier, Ph.D.

André M. Bastos, Ph.D.

John H. Reynolds, Ph.D.

Jeffrey D. Schall, Ph.D.

Geoffrey F. Woodman, Ph.D.

To my wife, sister, grandparents, and mother.
Thank you for inspiring me to achieve.

ACKNOWLEDGMENTS

I would like to thank my dissertation committee — Dr. André M. Bastos, Dr. Alexander Maier, Dr. John H. Reynolds, Dr. Jeffrey D. Schall, and Dr. Geoffrey F. Woodman — for providing helpful feedback and invaluable support that contributed to the studies presented in this dissertation.

The study presented in Chapter Two was published in *The Proceedings of the National Academy of Sciences* in 2021 (vol. 180) (Westerberg et al., 2021). Co-authors on this manuscript include Elizabeth A. Sigworth, Dr. Jeffrey D. Schall, and Dr. Alexander Maier. I thank I. Haniff, M. Feurtado, M. Maddox, S. Motorny, D. Richardson, L. Toy, B. Williams, and R. Williams for technical advice and assistance. I would like to thank S. Errington, Dr. K. Lowe, and Dr. P. Martin for useful conversations regarding the work. The work in Chapter Two was supported by research grants from the National Eye Institute [grant numbers: P30EY008126, R01EY008890, R01EY019882, R01EY027402] and the NIH Office of the Director [grant number: S10OD021771]. I was supported by fellowships from the National Eye Institute [grant numbers: F31EY031293, T32EY007135] when this work was done.

The study presented in Chapter Three is available on *bioRxiv* (Westerberg et al., 2022a). Co-authors on this manuscript include Dr. Jeffrey D. Schall, Dr. Geoffrey F. Woodman, and Dr. Alexander Maier. I thank I. Haniff, M. Feurtado, M. Maddox, S. Motorny, D. Richardson, L. Toy, B. Williams, and R. Williams for technical advice and assistance. I would like to thank Dr. G. Logan, Dr. T. Palmeri, Dr. G. Bahg, Dr. S. Lilburn, and Dr. J. Theeuwes for useful conversations regarding the work. The work in Chapter Three was supported by research grants from the National Eye Institute [grant numbers: P30EY008126, R01EY008890, R01EY019882, R01EY027402] and the NIH Office of the Director [grant number: S10OD021771]. I was supported by fellowships from the National Eye Institute [grant numbers: F31EY031293, T32EY007135] when this work was done.

The study presented in Chapter Four has been published in *eLife* in 2022 (vol. 11) (Westerberg et al., 2022b). The work was carried out by me, Michelle S. Schall, Dr. Alexander Maier, Dr. Geoffrey F. Woodman, and Dr. Jeffrey D. Schall. I thank I. Haniff, M. Feurtado, M. Maddox, S. Motorny, D. Richardson, L. Toy, B. Williams, and R. Williams for technical advice and assistance. I would like to thank Dr. B. Purcell and K. Weigand for collecting data. I would like to thank S. Errington, B. Herrera, Dr. K. Lowe, Dr. T. Reppert, Dr. J. Riera, Dr. A. Sajad, and E. Sigworth for useful conversations regarding the work. The work in Chapter Four was supported by research grants from the National Eye Institute [grant numbers: P30EY008126, R01EY008890, R01EY019882, R01EY027402] and the NIH Office of the Director [grant number: S10OD021771]. I was supported by fellowships from the National Eye Institute [grant numbers: F31EY031293, T32EY007135] when this work was done.

The study presented in Chapter Five is under review at *NeuroImage* and a version of the manuscript is available on *bioRxiv* (Herrera et al., 2022). In addition to myself, authors for Chapter Five include Beatriz Herrera (co-first author), Michelle S. Schall, Dr. Alexander Maier, Dr. Geoffrey F. Woodman, Dr. Jeffrey D. Schall, and Dr. Jorge J. Riera. I thank I. Haniff, M. Feurtado, M. Maddox, S. Motorny, D. Richardson, L. Toy, B. Williams, and R. Williams for technical advice and assistance. I would like to thank S. Errington, Dr. K. Lowe, and Dr. A. Sajad for useful conversations regarding the work. The work in Chapter Five was supported by research grants from the National Eye Institute [grant numbers: P30EY008126, R01EY008890, R01EY019882, R01EY027402], the NIH Office of the Director [grant number: S10OD021771], and the Natural Sciences and Engineering Research Council of Canada [grant number: RGPIN-2022-04592]. I was supported by fellowships from the National Eye Institute [grant numbers: F31EY031293, T32EY007135] when this work was done.

TABLE OF CONTENTS

LIST OF TABLES

LIST OF FIGURES

CHAPTER 1

Introduction

"I define nothing. Not beauty, not patriotism. I take each thing as it is, without prior rules about what it should be."

- Bob Dylan

1.1 What Are We Looking For?

In a world with an ever-growing enormity of useful and engaging information, and likewise increasing distractions, we are constantly guiding our attention to explore our environment. By directing our attention to specific people, places, and things, we can more carefully gather information and engage meaningfully with the world around us. While the usefulness of this attentional selection as a core cognitive function is not in doubt, an understanding of how our brains realize this mechanism is by no means complete. This dissertation serves to build on our understanding of attentional selection in the brain by investigating how certain neural circuits engage in attentional selection of useful visual information. Along the way, we can determine how these circuits produce signals across a range of spatial scales, from populations of neurons to electric fields outside the brain, yielding important discoveries towards linking attention research across species and techniques.

1.2 Visual Search and Attentional Selection

To reiterate, our environment is filled with information, some is useful to our goals, and some of it is not. To focus on useful information we deploy selective attention. From the psychological perspective, selective attention is the process through which we scrutinize items in our environment (Pashler, 1998). In deploying selective attention, we effectively prioritize the processing of specific stimuli, perhaps at the expense of processing others. A number of well-controlled behavioral tasks have been developed throughout the history of psychological research to investigate selective attention, one of which is known as visual search. Visual search is a simple task where the subject is required to identify the presence or exact location of a target object in a visual display. In the broadest sense, visual search is the process by which we explore our environment to gather information regarding the present stimuli. The "Where's Waldo?" series of children's books and "I Spy With My Little Eye" game exemplify the visual search task and its behavioral requirements. Visual search is an especially effective attention task in investigating how items are *selected* for directed attention, a process known as attentional selection. Experimental work on selective attention

began in the mid-twentieth century (Cherry, 1953; Broadbent, 1958) as did research on visual search (Ellis, 1947; Carpenter, 1948; Mackworth, 1948). Since these earliest studies, decades of research has produced thousands of works on visual search, attentional selection, and their intersection. As such, these research programs taken a variety of directions, pursuing differing aspects of visual search and attentional selection. For instance, you can imagine versions of visual search that are more or less difficult. Searching for Waldo when there are dozens of other individuals wearing red-and-white striped clothing is substantially more difficult than when every other person is wearing solid green and Waldo is the lone red-striped individual. For the purposes of this dissertation, we will focus on the latter, a form of visual search known as 'pop-out'. With pop-out we are afforded a window into the attentional selection process in a simple task which has a substantial history to contextualize findings.

1.3 Pop-out, Clearly

Pop-out visual search, perhaps the simplest form of visual search, is characterized by identification of a conspicuous target. That is, pop-out refers to search conditions where an object is noticeably different in one feature dimension relative to the objects surrounding it, as for example is a red berry among green leaves. With the simplicity comes a notable behavioral observation. In the early 1950's, the first study was performed investigating the speed at which items in visual search displays are selected through careful manipulation of the features making up the objects participants searched through (Eriksen, 1952). It was found that targets distinguished by single features (i.e., pop-outs) were identified faster than conjunctions of features. Conjunctions of features refers to items that are comprised of more than one notable feature such as a red square or green circle. From here, indexing attentional selection in time through behavioral response times (RTs) in visual search has become a staple of psychological research and, as will be discussed in detail later on, have become immensely powerful in relating selection times measured in the brain to the psychological measures of attentional selection.

Another seminal moment in pop-out search investigation was when direct comparisons were made between pop-out search response times and conjunction search response times as a function of the number of items in the search array (Treisman and Gelade, 1980). It was noted that while increasing the number of items in conjunction search linearly increased response time, response times in pop-out search were relatively invariant. Ultimately this supported the idea that a single feature dimension could be processed in parallel, no matter the number of items in the display. Therefore, in the case of single-feature pop-out, it might therefore be that the process of attentional selection is unfolding without the need for multiple shifts of directed spatial selective attention that would be necessary for scrutinizing items made up of several useful features. One key takeaway is that this suggests that the timing of attentional selection in pop-out

search can perhaps be indexed more reliably due to this relative invariance. Another takeaway was given the seemingly 'parallel' nature of single-feature pop-out processing and the rapid RTs that were associated with these searches, pop-out could be resolved at a relatively low-level. In fact, modeling work puts forward that these simple feature contrasts can be resolved in a purely feedforward network (Itti and Koch, 2000). In other words, pop-out visual search could be resolved even in the earliest stages of sensory processing. To summarize, pop-out search is unique in that the task itself is rather simple visual search, but the processing required to resolve it has the potential to be either high- or low-level (Chun et al., 2011).

From these highlights of the otherwise extensive literature that is pop-out research, we gain key insights moving forward. With our ultimate goal of understanding circuits supporting attentional selection across measurement scales, pop-out (1) allows us to evoke attentional selection in (2) a relatively simple (and reliably trainable) task which (3) utilizes individual features and (4) has the potential of being accomplished through anything from early sensory processing to higher-level cognitive control. To contextualize, these points have allowed previous investigations, and the work to be presented here, into attentional selection in nonhuman primates with the ability to manipulate search conditions (e.g., individual features) in ways useful for pursuits into understanding the requisite underlying neural activity.

1.4 A Primer on Neuronal Attentional Selection in Visual Search

Following extensive behavioral studies, and once the technology had become sufficiently sophisticated, neuroscientific investigations into attention ensued. Early studies focused on attentional modulation of sensory responses with directed cuing (Moran and Desimone, 1985). In other words, how do responses of neurons representing items in space change as a function of whether or not the subject has been informed to attend to the part of space where that item exists. In short, these early studies discovered that neurons representing items in the part of space being attended to responded more vigorously than those outside the area of attention. With this seminal finding demonstrating neural correlates of attention, soon after the neuronal mechanisms of attentional selection in visual search, as well as other tasks, became a heavily pursued topic of investigation.

Neural correlates of visual search performance have been identified across the brain. Visual, temporal, parietal, frontal, thalamic, and midbrain areas have all been shown to modulate their activity as a function of behavioral requirements in searching visual displays (see (Schall, 2015; Saalmann and Kastner, 2011; Carrasco, 2011; Moore and Zirnsak, 2017; Reynolds and Heeger, 2009; Krauzlis et al., 2013; Colby and Goldberg, 1999) for reviews). As our primary objective in this dissertation is obtain a greater understanding of visual information processing and selection rather than, say, motor planning (Schall, 2015) or performance monitoring (Schall et al., 2002)), we can narrow our focus to certain findings.

Visual cortical areas have been a focus of intense investigation in the realm of resolving the attentional selection component of visual search. At a 30,000 foot view, this is because visual search arrays are comprised of multiple alternatives that can be represented in retinotopic visual space with the sensible spatial and featural representations that exist in visual cortex (Kaas, 1997). With respect to specific areas in visual cortex, one area is especially pertinent to the overall aims of the dissertation and have also been the primary focus of visual search research: area V4.

V4 is classified as a mid-level area in the ventral visual pathway (Felleman and Van Essen, 1991). Originally termed the V4 complex and thought to contain multiple representations of the visual field (Zeki, 1969), it was later determined that V4 proper is only a subset of the originally described area with a single visual field representation. V4 itself appears to be modular in organization featuring side-by-side topographical representations for color and form among other visual features (Yoshioka et al., 1992; Deyoe and Vanessen, 1988; Deyoe et al., 1994; Felleman et al., 1997; Xiao et al., 1999; Tootell et al., 2004).

In the time since these anatomical descriptions, V4 has been investigated with respect to visual search. One pair of studies investigated the selection of features and behaviorally relevant stimuli in V4 during visual search. Monkeys identified a target stimulus composed of two features (shape and color) in conjunction. The target stimulus was defined by one of the features cued prior to trial onset. For example, if the objective of the trial was to identify the white stimulus among black stimuli, the monkey would identify the white circle or square among black circles and squares. This work demonstrated that the individual V4 neurons had feature selectivity and primarily reflected that selectivity rather than the behavioral relevance of that stimulus in their receptive field during task performance (Ogawa and Komatsu, 2004). However, at the population level, behavioral relevance of stimuli could be inferred. While V4 does primarily represent feature selectivity initially, closer in time to when the response is made to the target stimulus, the activity of those same V4 neurons more closely represents the behavioral relevance of the stimulus in their receptive field (Ogawa and Komatsu, 2006). Together these findings suggest that V4 initially represents features at the individual neuron level and behavioral relevance at the population level. Ultimately, in taken with consideration to other works on visual search in V4 (Bichot et al., 2005; Zhou and Desimone, 2011), we have an exemplar area that seemingly maps the visual and behavioral information pertinent to the resolution of visual search.

1.5 The Emergence of Laminar Physiology in Attention Research

While an enormous literature on the neural mechanisms of attention has been produced in the last several decades, like the investigations described in the previous section, it has in some ways been limited by technology. With respect to neurophysiological recordings, one limiting factor has been the design and

complexity of electrodes used to measure the neural activity. Relatively recent advances in recording electrode technologies have opened up a new avenue for attention research: laminar physiology of attention through linear multielectrode arrays (LMAs). LMAs are a line of equally spaced recording contacts that can each independently measure neural activity. This linear design is useful in measuring cortical columns, in particular. These cortical columns, a mesoscopic unit of cortical structure and where the bulk of attention research has been conducted, is a layered structure. That is, if you view the anatomy of a slice of cortex under a microscope, you will immediately notice distinct bands with varying types and densities of neurons.

With some exceptions (e.g., agranualar cortex (Shepherd, 2009)), granular laminar structure is largely preserved across a wide range of functionally distinct brain areas. This has led to an influential model of cortical function: the canonical cortical microcircuit (CCM) (Douglas et al., 1989; Douglas and Martin, 1991). The CCM puts forward the layered structure of cortex as a fundamental unit of cortical computation with a prescribed pattern of activation. Crucially, these patterns of activation arise from putative patterns of connectivity between cortical layers as well as external connections. In having this guiding framework, one can begin to speculate on the origins of and direction of flow throughout the brain for certain neural computations given observed patterns of neural activation. Among researchers of other neuroscience disciplines, this has provided attention researchers a hypothesis-generating mechanism for research at the mesoscopic circuit level with well-defined predictions for top-down vs. bottom-up contributions to attention given the expected laminar patterns of the CCM.

With this in mind, does attention influence processing precisely within cortical columns and how is attentional selection computed across cortical layers? Some evidence already exists for cortical layers playing an important role in attention with differential effects of attention across layers in visual cortex (Nandy et al., 2017; van Kerkoerle et al., 2017; Ferro et al., 2021; Cox et al., 2019a; Mehta et al., 2000b). However, given the recent rise of laminar recordings, we do not know exactly the role of this structure in attentional selection during visual search. Laminar insights could be particularly interesting for pop-out search. As mentioned earlier, the mechanism giving rise to the attentional selection of pop-out stimuli could stem from a bottom-up or top-down mechanism given its relative simplicity with respect to types of visual search, and its cognitive demands (Chun et al., 2011). The putative connectivity patterns of the CCM afford a window into these top-down vs. bottom-up contributions for attentional selection of pop-out stimuli.

While the laminar scope of investigation for attention research promises crucial insight into how attentional selection comes about in neural circuits, it seemingly has a curious side-effect making it an exciting prospect for translational neuroscience: Cortical columns can generate EEG, one of the most commonly used measures in human neuroscience.

1.6 The Consequences of Laminar Patterns of Activation - EEG Generation

Of course, neuroscientific research has not been limited to intracranial investigations. Beyond just attention research, human neuroscience has flourished through the use of noninvasive methods. One ubiquitous method is electroencephalography (EEG), a noninvasive electrophysiological measure which benefits from its high temporal resolution but suffers from its comparatively poor spatial resolution. That is, while invasive neurophysiological measures such as single-unit extracellular recordings are very finely spatially localized (to the level of individual neurons), noninvasive EEG is considered a 'global' signal. Because EEG is measured some distance from its intracranial generators, and the signal must propagate through several intermediaries (such as the skull), the signal is effectively filtered and integrated such that it reflects the activity of multiple brain areas. Even so, numerous indices of sensory, perceptual, cognitive, and motor processes have been identified in the global EEG signal. And while the spatial localization of EEG signals leaves something to be desired, understanding something about where specific signals are generated is by no means futile. while most EEG indices are observed across multiple recording positions across the scalp, the relative magnitude of these indices can vary sensibly. As a result, hypotheses have been formulated as to which brain areas generate which EEG indices and what patterns of neural activity are necessary to yield a signal that can be measured outside the skull. This has been an especially trendy topic as knowing where an EEG signal is generated exactly has the potential to better inform which neural processes these signals index and moreover bridge noninvasive and invasive programs of research.

One popular method for investigating the putative neural generators for EEG signal has become inverse source modeling (Grech et al., 2008; Michel et al., 2004). This procedure utilizes the spatial distribution of EEG voltage over the scalp to predict the intracranial source of the signal. However, the method has a major shortcoming. The inverse method, from a mathematical perspective, is indefinite. That is, there are multiple configurations of neural activity that can give rise to the same distribution of EEG which this method cannot distinguish between to determine the empirical generator. Unfortunately, this means that definite determination of the neural generators of specific EEG components has eluded the field. To obtain a definite answer and reveal these neural sources requires directly recording the generator, something that cannot be accomplished through noninvasive methods alone. Nonetheless, this has not prevented theorists and biophysicists to speculate as to what patterns of neural activity would give to EEG signals.

The cortical column seems to be a fundamental unit for the generation of EEG signals (Nunez et al., 2006). The structure and orientation of the neurons within cortical columns is such that they can feasibly generate electric fields that would be measurable outside the brain. Crucially, cortical columns are heterogeneous structures with distinct layers and densities of cell bodies and dendritic arbors along said

layers. In fact, studies in the rat have already demonstrated that the biophysical geometry and activation of cortical columns can produce EEG potentials (Riera et al., 2012). However, these studies have been primarily conducted through computational modeling with the empirical measurement of cortical columns generating EEG signals being relatively limited. Moreover, to date there have been no direct demonstrations of laminar activity within cortical columns of primates leading to the generation of EEG signals. However, there have been other ways researchers have thus far begun to better understand EEG signals and their biological substrates even if direct measurement has thus far eluded us.

1.7 The Relationship Between Intra- and Extracranial Signals in Primate Electrophysiology

Parallels have been drawn between patterns of neural activity and the EEG, often in comparing EEG and single-unit spiking (Snyder and Smith, 2015; Sandhaeger et al., 2019; Sajad et al., 2019) or EEG and LFP (Ng et al., 2013; Musall et al., 2014; Sandhaeger et al., 2019). These studies have demonstrated that like-signals can be observed across measurement scales. While finding neurons that seemingly indicate the same psychological process as an EEG signal is a step towards functional localization of EEG components, there is a crucial gap between the two presenting a interpretive pitfall. As mentioned in the previous section, it is thought the the patterns of activity across cortical columns generates EEG. And while cortical columns are comprised of distinct layers of neurons and the activation of neurons is what generates EEG, it is not their action potentials that yield it. That is to say, while many parallels have been drawn between EEG activity and single-unit neuronal spiking, this spiking is one step removed from the putative generator activity. Instead of spiking, it is predominantly the synaptic activations of neurons across the cortical column that produces local current fluctuations and the ultimate production of electric fields comprising EEG (Nunez et al., 2006). What this means is that while these previous studies have no doubt provided crucial insight into functional localization of processes indexed by EEG components, they are perhaps not directly measuring the exact activity giving rise to the EEG. Therefore, there is a gap in primate physiology beyond just relating patterns of laminar activity to EEG: We must also empirically measure the putative generating activity within those columns. And while this would ideally be performed for each and every EEG index of sensation, perception, cognition, and action, we can start by investigating the one pertinent to this dissertation, attentional selection and the EEG's 'N2pc' index of it.

1.8 Understanding Attentional Selection with the N2pc

While significant progress in attention research has been achieved through intracranial neurophysiology, it is by no means the only method being used. For instance, a substantial fraction of neuroscientific research into attention is done with human participants through use of noninvasive methods. One method proven as

effective as it is popular is through EEG. In human research, EEG is commonly performed by placing electrodes on the scalp and recording electrical potentials from the brain propagating through the skull. Originally developed in animals (Caton, 1875), EEG was popularized in the early twentieth century as a way to reliably measure brain activity in human participants (Berger, 1929). In combination with its more invasive sister-method, electocorticography (ECoG), the field of human electrophysiology research has blossomed in recent decades. Crucially, many insights have been gained in attention research through these methods.

While several EEG indices of attention have been identified, one in particular seems especially relevant to attentional selection. The N2pc is a event-related potential (ERP) of the EEG signal which indicates where spatial selective attention is deployed (Luck and Hillyard, 1994; Eimer, 1996). Physically, the N2pc manifests as a difference in polarization of the N2 component of the event-related potential of the EEG when visual selective attention is covertly directed contra- or ipsilateral relative to the position of the recording electrode. It is also important to note that the N2pc is primarily observed over the posterior half of the brain. For example, you would observe an N2pc over the back of your head as the difference between hemispheres if you were to maintain gaze at the center of this page and covertly read the word in the top-left corner. The N2pc was originally described in the early 1990's, and hundreds of studies have since been performed using the N2pc as a primary indicator of attention. The N2pc has even shown to be modulated in clinical cases of attentional disruptions such as in schizophrenia (Luck et al., 2006; Verleger et al., 2013; Fuggetta et al., 2015) and attention deficit/hyperactivity disorder (Wang et al., 2016, 2017; Shushakova et al., 2018; Rodriguez-Martinez et al., 2021). And while these works have yielded significant findings into how attentional processing is instantiated, there is a substantial gap in knowledge associated with the N2pc: What neural activity gives rise to this signal?

In evaluating the parallels between neural activity and the N2pc specifically, a couple of crucial observations have been made. First, the N2pc seemingly mimics neural activity present in the frontal cortex. That is, the frontal eye fields (FEF) and the N2pc indicate the same patterns of attentional selection (Cohen et al., 2009; Purcell et al., 2013). FEF is a prefrontal cortical area found bilaterally along the bank of the arcuate sulcus. Defined as a portion of Brodmann area 8 (Brodmann, 1909) and first described in the 19th century by David Ferrier, it was characterized by its ability to evoke saccadic eye movements when the area was electrically stimulated (Ferrier and Burdon-Sanderson, 1875). In the years since, FEF has served as a target for visual attention research (Schall, 2015). As attentional selection unfolds in visual search, spiking activity in FEF indicates first, followed in time by LFP in FEF, and lastly the N2pc. This temporal sequence seemingly indicates a putative role for frontal cortex in computationally generating the selection signal that ultimately leads to the N2pc. However, the biophysical geometry of FEF makes it an unlikely neural source

for the N2pc. Second, a magnetoencephalographic (MEG) investigation into the N2pc found putative biophysical generators in posterior cortex. Specifically, dipole sources in posterior parietal and extrastriate visual cortex (Hopf et al., 2000). Given these findings, we can begin to formulate more concrete hypotheses about which brain areas performing attentional selection might be at the heart of N2pc generation. In combination, an area like V4, which is functionally connected to FEF, is attentionally modulated, and exists in the posterior part of the brain, could serve as a plausible source.

1.9 Linking Attentional Selection, Cortical Columns, and the N2pc

Thus far we have introduced three key topics in neuroscience research: attention, laminar cortical circuitry, and EEG. We focused on highlighting their overlap. For instance, cortical columns in certain brain areas are implicated in attentional modulation. Cortical columns putatively generate EEG signals. Indices of attentional selection manifest in the EEG. And while there are these clear connections between the topics, a comprehensive description of the intersection of the three has not been demonstrated empirically. By linking the psychological process of attentional selection to its neural substrates within cortical columns and exploring the patterns of activation given rise, we can perhaps understand what the N2pc is. Ultimately, better understanding the neural generation of the N2pc provides interpretive value. With an understanding of how the N2pc is generated, researchers can more readily speculate as to the underlying neural processes when measuring the EEG signal alone. Therefore, linking cognitive processing in cortical circuits to the biophysical generation of EEG has the potential to provide key insight for the field of human neuroscience and yield a greater understanding of the function of cortical circuits in attentional selection along the way.

1.10 What to Expect

In the following five chapters we elaborate four studies designed to further our understanding of attentional selection across spatial scales. Specifically, this dissertation seeks to accomplish two primary aims. For one, we sought to characterize the changes present in visual cortical columns (specifically area V4) associated with attentional selection of pop-out stimuli. And two, we sought to determine whether the hypothesized changes in the same visual cortical columns lead to the generation of the EEG signal known as N2pc. Together, resolving these aims significantly advances our understanding of the circuits producing attentional selection and reveal what can be understood from attention-associated EEG from a neurobiological level. In chapter two, you will read on our initial search for whether attentional modulations of sensory processing are present along the layers of visual cortex during visual search. If V4 is generating the N2pc index of attention, we expect to observe attention-induced changes in cortical columnar processing. We found layer-specific changes in sensory processing associated with the attentional selection of targets in visual

search. In chapter three, we describe the temporal evolution of attentional selection along the layers of visual cortex during visual search. If V4 is generating the N2pc, selection signals should be present at or before the time we would expect the N2pc. We found the timing of attentional selection in visual cortex preceded the usual timing of the N2pc. In chapter four, we sought to describe the parallels and putative relationship between activity generated across visual cortical columns and the overlying N2pc. If V4 is generating the N2pc, we expect simultaneous signaling of attentional selection in the cortical columnar activity and the EEG which should covary on a trial-by-trial basis. We found layer-specific relationships between attentional selection in visual cortex and the N2pc. In chapter five, we go beyond simple comparisons of intra- and extracranial signals and demonstrate that V4 can biophysically generate the N2pc. If V4 is generating the N2pc, we should see patterns of simulated EEG resembling the N2pc from forward modeled activity of visual cortical columns. We demonstrate that the synaptic currents across cortical layers in visual cortex are capable of regenerating the canonical N2pc distribution. In the final chapter, we will integrate the findings of these studies and discuss what their implications are towards our ultimate goal of understanding attentional selection across multiple scales.

CHAPTER 2

Impact of Attention on Sensory Columnar Processing

Westerberg, J. A., Sigworth, E. A., Schall, J. D., and Maier, A. (2021) Pop-out search instigates beta-gated feature selectivity enhancement across V4 layers. *Proceedings of the National Academy of Sciences* 118(50):e2103702118.

"Whatever she might become she would never be static."

- Sinclair Lewis

2.1 Summary

Visual search is a work-horse for investigating how attention interacts with processing of sensory information. Attentional selection has been linked to altered cortical sensory responses and feature preferences (i.e., tuning). However, attentional modulation of feature selectivity during visual search is largely unexplored. Here we map the spatiotemporal profile of feature selectivity during a singleton search task. Monkeys performed search where a single pop-out feature determined the target of attention. We recorded laminar neural responses from mid-level visual area V4. We first identified "feature columns" which showed preference for individual colors. In the unattended condition with no target in the receptive field, V4 feature columns were significantly more selective in the superficial relative to the middle and deep layers. Attending a stimulus increased feature selectivity in all layers but not equally. Feature selectivity increased most in the deep layers, leading to higher selectivity in the extragranular layers as compared to the middle layer. This attention-induced enhancement was rhythmically gated in phase with the beta-band local field potential. Beta power dominated both extragranular laminar compartments, but current source density analysis pointed to an origin in superficial layers, specifically. While beta-band power was present regardless of attentional state, feature selectivity was only gated by beta in the attended condition with the target in the receptive field. Neither the beta oscillation nor its gating of feature selectivity varied with microsaccade production. Importantly, beta modulation of neural activity predicted response times, suggesting a direct link between attentional gating and behavioral output. Together, these findings suggest beta-range synaptic activation in V4's superficial layers rhythmically gates attentional enhancement of feature tuning in a way that affects the speed of attentional selection.

2.2 Introduction

Throughout cortex, sensory information is organized into maps. This phenomenon is readily observable in visual cortex where maps organize information in both the radial (e.g., within cortical columns) and tangential (e.g., across a cortical area) dimensions (Hubel et al., 1977; Hubel and Wiesel, 1968; Kaas, 1991; Hubel and Wiesel, 1962). Importantly, sensory information attributed to these maps is malleable. For example, selective attention is linked to profound changes in neural activity organizing sensory information in both space and time (Cohen and Maunsell, 2011; Cohen et al., 2009; Desimone and Duncan, 1995; Ferro et al., 2021; Fries et al., 2001, 2008; Kastner and Ungerleider, 2000; Martínez-Trujillo and Treue, 2002; McAdams and Maunsell, 1999, 2000; Ni and Maunsell, 2017, 2019; Pooresmaeili et al., 2010; Poort et al., 2012; Recanzone and Wurtz, 2000; Reynolds et al., 1999, 2000; Reynolds and Desimone, 2003; Reynolds and Chelazzi, 2004; Reynolds and Heeger, 2009; Roelfsema et al., 2007, 1998; Rotermund et al., 2009; Sani et al., 2017; Stănişor et al., 2013; Thiele et al., 2009; Treue and Martínez Trujillo, 1999; Vinck et al., 2013; Wegener et al., 2004; Williford and Maunsell, 2006).

In visual cortex, cortical columnar microcircuits comprise many neurons that respond to the same location of visual space and similar stimulus features. For example, primary visual cortex (V1) features "orientation columns" consisting of neurons sharing response preference for the same stimulus orientation (Hubel and Wiesel, 1974; Vanduffel et al., 2002) and "ocular dominance columns" consisting of neurons that preferentially respond to the same eye (LeVay et al., 1975). Similar columnar organization for feature selectivity has been described across many other visual cortical areas including area V2 (Tootell and Hamilton, 1989; Tootell and Nasr, 2017; Vanduffel et al., 2002), area V3 (Adams and Zeki, 2001), middle temporal area (area MT) (Albrecht et al., 1984; DeAngelis and Newsome, 1999; Liu and Newsome, 2003), and inferotemporal cortex (Fujita et al., 1992; Tanaka, 1996, 2003). Mid-level visual cortical area V4, a well-studied area with respect to attentional modulation, follows suit with columnar organization of visual responses and feature preferences (Conway and Tsao, 2009; Kobatake and Tanaka, 1994; Kotake et al., 2009; Schein et al., 1982; Tootell et al., 2004; Yoshioka et al., 1996; Zeki, 1973, 1980). Yet, we do not know the extent to which attention impacts feature preferences along columns. While canonical microcircuit models of cortex predicts laminar differences for attentional modulation (e.g., feedback-recipient extragranular layers modulating before granular layers (Douglas et al., 1989; Douglas and Martin, 1991; Bastos et al., 2012)), how this modulation interacts with columnar feature selectivity is largely unknown.

We sought to determine the spatiotemporal profile of feature preferences within the V4 laminar microcircuit during attentional selection. To address this question, we performed neurophysiological recordings along V4 layers in monkeys performing an attention-demanding pop-out search task. We

identified feature columns demonstrating homogeneous feature preference along cortical depth. When the search array item presented in the column's receptive field was unattended, the upper cortical layers were most selective. However, when attended, feature selectivity in the deep layers enhanced the most, resulting in overall strongest feature selectivity in both extragranular compartments. We further found that the enhancement of feature selectivity associated with attention was rhythmically gated in the beta-range. While beta activity was measurable across both unattended and attended conditions, rhythmic gating of feature selectivity was only present with attention. Moreover, beta power modulating the neural response was predictive of response time, suggesting a link between attentional gating and behavior. Synaptic currents revealed the beta rhythm originates in superficial cortical layers, which is compatible with top-down influence.

2.3 Results

2.3.1 Behavioral Performance

Both monkeys performed a pop-out visual search task necessitating attentional selection of, followed by an accurate eye movement to, an oddball stimulus to receive a juice reward (Figure 2.1A). Both monkeys performed the task well above chance (accuracy: monkey Ca, 88%; He, 81%) with response times (RT) consistent with previous reports of monkeys performing this task (Figure 2.1B-C; median RT: monkey Ca, 243 ms; He, 224 ms) (see previous reports for comparable behavioral data from a different cohort of macaques (Purcell et al., 2012; Westerberg et al., 2020b)).

2.3.2 Laminar Recordings in V4

To evaluate the laminar profile of feature selectivity in primate area V4, we recorded neural activity throughout the layers of cortex in 2 macaque monkeys using a linear electrode array with 100 m spacing between recording contacts (Plexon S-Probe). Prior to any surgical procedures, monkeys underwent a magnetic resonance (MR) scan to identify the location of V4 (Figure 2.1D). Following implantation of a recording chamber, monkeys underwent a second MR scan with a gadolinium-filled recording grid to identify chamber locations where an electrode could be introduced orthogonally into the prelunate gyrus (Figure 2.1E). On each recording, we positioned and oriented the linear electrode array to span all V4 layers (Figure 2.1G). At the end of the experiment, penetration locations were verified anatomically (Figure 2.1F).

Monkeys performed a fixation task during which we flashed randomized, monochromatic stimuli uniform in brightness to perform reverse-correlation-based receptive field (RF) mapping (Cox et al., 2019b; Dougherty et al., 2019; Westerberg et al., 2019). Overlapping RFs through vertically (radially) aligned recording sites were used to confirm the perpendicular orientation of the probe (Figure 2.1H) (Cox et al.,

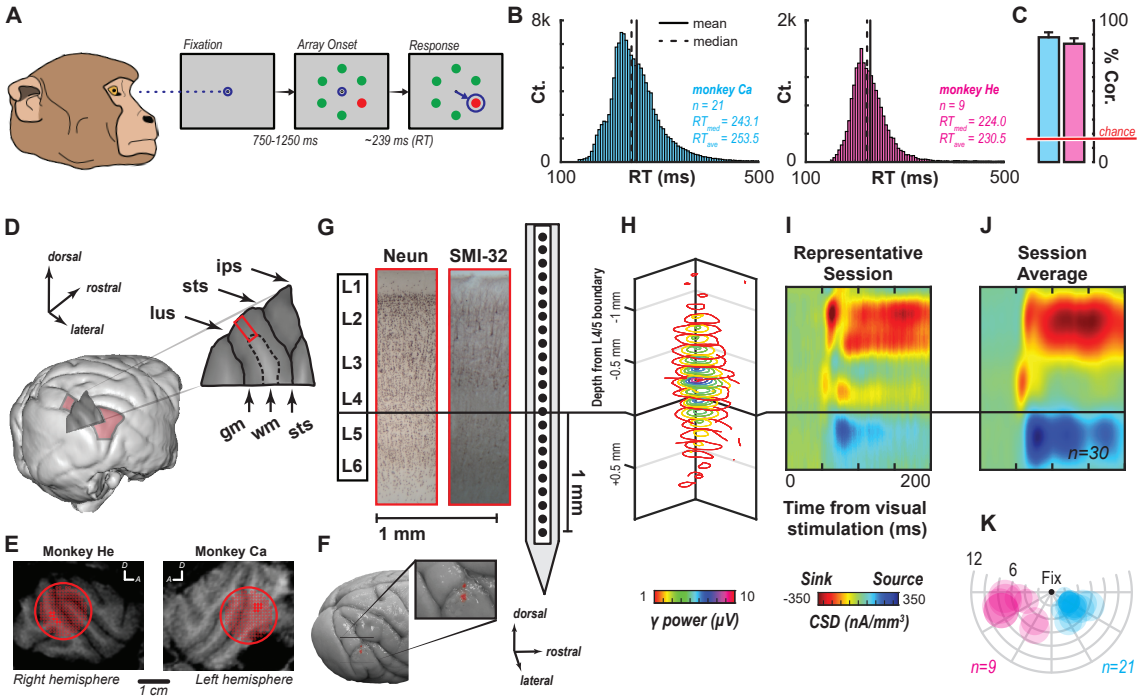

Figure 2.1: Task design and laminar recording technique

A. Monkeys fixated a dot. Following a variable delay, an array was presented. Monkeys were tasked to saccade to the oddball to receive a reward. B. Response times across all sessions for both monkeys (left, cyan: monkey Ca; right, magenta: He). C. Behavioral performance for both monkeys across all sessions (cyan: monkey Ca; magenta: He). D. Occipital view of a 3D render of a macaque brain. Area V4 is highlighted in red. The cortical structure is revealed by the section through the prelunate gyrus. This slice is magnified at the right, with labels indicating structural landmarks (lus, lunate sulcus; sts, superior temporal sulcus; ips, intraparietal sulcus; gm, gray matter; wm, white matter). The red box indicates a portion of V4 where linear electrode arrays can be introduced orthogonally to record across the layers of a cortical column. E. MR scans for monkey He (left) and monkey Ca (right). The section was taken orthogonal to the 19 mm diameter recording chamber (red outline) oriented 55° off vertical axis, 23 mm from the midline. The superior temporal sulcus can be seen running through the center of each chamber. A grid of possible penetration locations is overlaid with solid red dots indicating locations sampled in this study on the prelunate gyrus, ventroposterior to the superior temporal sulcus. F. Ex vivo image of the posterior half of the brain of monkey He with expanded view of the area between lus and sts. Red marks are diiodine deposited by the final two recordings in monkey He. G. Histological stains, depicting the laminar structure of V4. Labels are indicated at the far left. Neun stain (left center) highlights the distribution of neuronal cell bodies. SMI-32 (right center) highlights pyramidal cells. Cartoon probe shows laminar positioning. H. Receptive fields (RF) across recording sites of a single array penetration, indicating perpendicular penetration. I. CSD for the same session as H. Current sinks are indicated in red and sources in blue. The initial sink following visual stimulation was used as a functional marker to determine the L4/5 boundary. The black horizontal line indicates granular input sink. Data are smoothed along depth and across time for visualization. J. Mean CSD profile following alignment of the 30 sessions (21, monkey Ca; 9, He). Formatting identical to I. K. RF locations across sessions and monkeys (cyan, monkey Ca; magenta, He). RF centers determined online, and diameters estimated from previous reports.

2019b; Nandy et al., 2017). The distribution of RFs across cortex was consistent with the previously established representation of visual space on the prelunate gyrus (Figure 2.1K) (Gattass et al., 1988). To compare columns across sessions, we aligned individual recording sites relative to the granular input sink of

the current source density (CSD) following visual stimulation, which identifies the boundary between the granular (L4) and infragranular layers (L5/6) of cortex (Figure 2.1I) (Maier et al., 2010; Nandy et al., 2017; Schroeder et al., 1998; Westerberg et al., 2019). 10 electrode contacts including and above the L4/5 boundary and 5 sites below were included for analysis. Relative to the population-based (grand average) evoked CSD profile (Fig. 1.1J), the topmost 5 sites corresponded to the supragranular sink, the middle 5 to the granular sink, and the deepest 5 to the infragranular source.

2.3.3 V4 Feature Columns

As a first step, we identified feature columns in V4. Columnar organization for color tuning has previously been reported for V4 (Conway and Tsao, 2009; Kotake et al., 2009; Tootell et al., 2004; Zeki, 1973, 1980). During performance of the visual search task, small, isoluminant red or green stimuli were presented within the population RF of the column (Westerberg et al., 2020a). We estimated neural activity by evaluating high gamma power (70-150 Hz) at each recording site as it reliably reflects feature selectivity in visual cortex (Ray and Maunsell, 2010), and can be reliably measured at laminar V4 recording sites, unlike single- or multi-unit activity. To eliminate volume conducted signals, we recalculated the locally-generated gamma power from the columnar CSD (Kajikawa and Schroeder, 2011; Nicholson and Llinas, 1971). Initially, and for the results reported in this section, these analyses were restricted to the 'unattended' condition. This condition was defined as the presence of a distractor stimulus within the receptive field of the cortical column regardless of the position of the target in the array (5 out of 6 array configurations where target is outside of the RF) and the trial was performed correctly.

To quantify the selectivity of each recording site for stimulus color, we computed the ratio of the red vs. green responses with values bounded between -1 (100% green preference) and 1 (100% red preference). Hereafter we will refer to this as the feature selectivity index (FSI). We then calculated the mean FSI along cortical depth to compute a columnar feature selectivity index (CFSI). The CFSI quantifies the degree of feature preference across the entire column. Qualitatively, we found a high degree of consistency of columnar feature selectivity, with some columns strongly preferring red or green and other columns not distinguishing red from green Figure 2.2A. To quantify this observation, we performed Wilcoxon signed rank tests on the magnitudes of FSI along depth, where columns were deemed feature selective if $p < 0.05$. We found significant feature selectivity in 19 of 30 columns (63.3%) across both monkeys (monkey Ca, 12 of 21; He, 7 of 9).

Note that the CFSI alone does not indicate how consistent feature selectivity is within a column. To evaluate the columnar consistency of feature selectivity, we performed Bartlett's tests for the FSI variance of each column relative to the null distributions derived from 15 random samples of all measured FSIs,

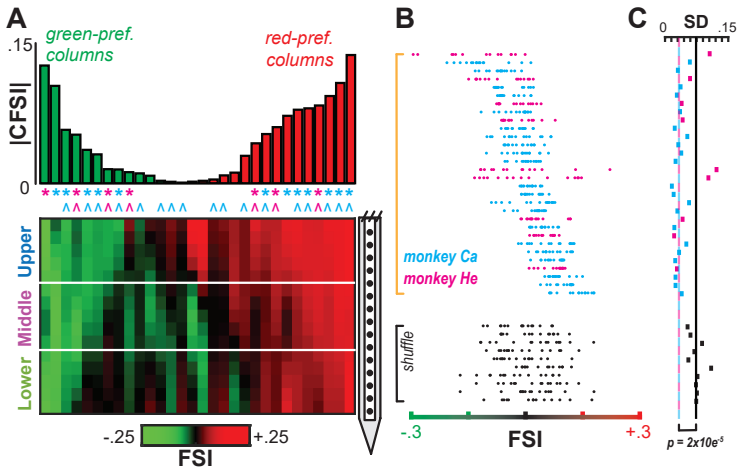

Figure 2.2: Identifying feature columns in V4
A. Feature selectivity index (FSI) for each recording site (bottom). Each plotted column corresponds to one cortical column. Data are sorted from the most green- to most red-preferring columns. Hue indicates the preferred color of each recording site and saturation indicates the magnitude of the preference. Horizontal lines indicate laminar boundaries. Average FSI along each column (CFSI) indicated in bar chart (top). Each bar corresponds to the column underneath. Significant selectivity along depth indicated by an asterisk between plots. Significant consistency of color preference, or lack of color preference, is denoted by a carrot between the bar and color plots. Color of asterisks and carrots indicates monkey from which the column was recorded (cyan, monkey Ca; magenta, He). B. Dot plot of FSI for each recording site (top). Black data are 10 of 1000 shuffle distributions generated where FSI were picked at random from all columns (shuffle control). C. Scatter plot of the standard deviation along depth for each cortical column as well as for a randomly chosen sample of 10 of the 1000 shuffle control null distributions. Color of bar indicates data source (cyan, monkey Ca; magenta, He; black, shuffle). Vertical lines indicate the median standard deviations for the data and for the shuffle. The p value of a statistically significant result of a signed rank test is indicated at the bottom.

bootstrapped 1000 times. The median value was taken to determine significance with $p < 0.05$. Feature selectivity was more consistent across columns than would be predicted by the null distribution in 23 of 30 columns (76.7%) across both monkeys (monkey Ca, 17 of 21; He, 6 of 9). Only 4 of 30 columns exhibited no or inconsistent selectivity across depth through these measures. We further quantified the degree of similarity within a column relative to the variance across columns by computing intraclass correlation coefficients (ICC) (Shrout and Fleiss, 1979; McGraw and Wong, 1996). ICC reveals how consistent individual columns are in feature selectivity relative to the overall sample of V4 columns. Values towards 1 indicate a high degree of consistency within a column, and values towards 0 indicate little to no consistency. Across the sample, we found consistency within columns to be significantly greater than chance ($\rho = 0.773, F(29,406) = 52.19, p << 0.001$) in both monkeys (monkey Ca, $\rho = 0.848, F(20,280) = 84.96, p << 0.001$; He, $\rho = 0.550, F(8,112) = 19.27, p << 0.001$) (Figure 2.2B). For comparison, we generated shuffle control distributions of FSI values and computed the ICC. This control yielded the expected lack of consistency ($\rho = 0.003, F(999,13986) = 1.08, p = 0.37$). These results

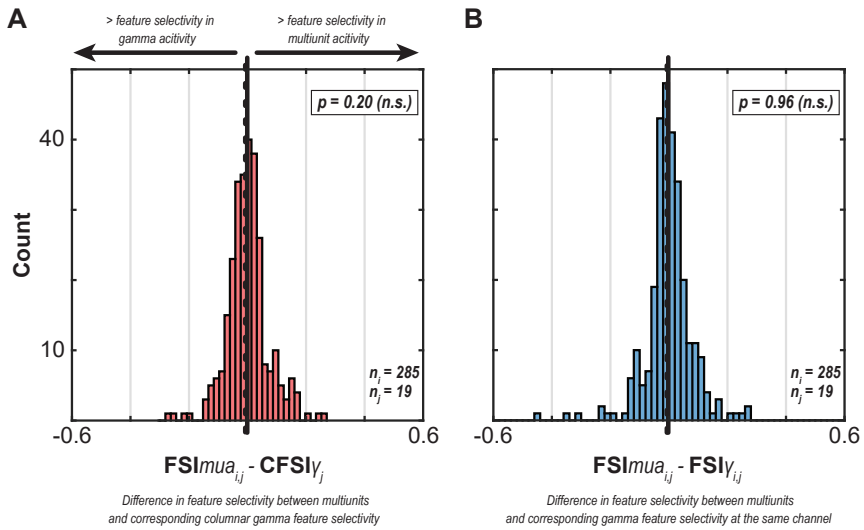

Figure 2.3: Consistency between gamma and MUA feature selectivity indices
Feature selectivity measured with multiunit samples does not differ from feature selectivity measured with high gamma. A. Histogram of differences between feature selectivity of multiunits ($n = 285$) and the corresponding column's high gamma feature selectivity ($n = 19$). Multiunits were sampled in cortical columns that exhibited feature selectivity in the unattended condition with a distractor in the receptive field. Columnar feature selectivity index for the high gamma was then subtracted from the feature selectivity index found for the multiunits found in each column. Prior to subtraction, FSI was made relative to the preferred color (as defined by the CFSI of the high gamma) to examine both red and green columns together. Values right of zero indicate greater selectivity in the multiunit activity and left indicate greater selectivity in the high gamma (at the column level). Result of Wilcoxon signed rank shown in upper righthand corner. B. Identical to panel A except instead of computing difference between a multiunit FSI and its corresponding column high gamma FSI, the difference between the multiunit FSI is taken against the high gamma FSI at the recording site where the multiunit was isolated. Again, no significant differences were observed as indicated by the Wilcoxon signed rank test show in the upper right hand corner of the panel.

suggest that most V4 columns are homogeneous in their feature selectivity. Lastly, we assessed the distribution of standard deviations of FSI across columns relative to that of the null distributions Figure 2.2C. We performed a Wilcoxon signed rank test on these distributions. The result showed a significant difference ($Z = -4.02, p = 5.79e^{-5}$), providing further evidence for the homogeneity of columnar feature selectivity in V4.

We compared the feature selectivity of recorded multiunits ($n = 285$) along cortical columns to the columnar feature selectivity of each multiunit's corresponding column. We found no significant differences between the multiunit feature selectivity and their corresponding columns (Wilcoxon signed rank, $Z = 1.21, p = 0.22$) (Figure 2.3), bolstering confidence that the locally generated gamma is a useful measure of columnar feature selectivity.

To further bolster our confidence in the columnar organization for feature selectivity, we turned to Bayesian modeling. Using a Bayesian framework, we directly evaluated and compared the likelihood of

Model Identifier	Model Statement	Parameter Priors	LOO-ELPD [SE]	DIFF	Bayes Factor
COLUMN X DEPTH X ATTENTION	$FSI_{i,j,k} \sim N(\mu + d_i \cdot c_j + d_i \cdot a_k + d_i + c_j + a_k + e_{i,j,k}, \sigma^2_{i,j,k})$	$\mu, d_i, c_j, a_k \sim N(0, \sigma)$ $\sigma \sim Half-t(3,0,1)$	*Reference*		
COLUMN X DEPTH	$FSI_{i,j,k} \sim N(\mu + d_i \cdot c_j + d_i + c_j + e_{i,j,k}, \sigma^2_{i,j,k})$	$\mu, d_i, c_j \sim N(0, \sigma)$ $\sigma \sim Half-t(3,0,1)$	$-186.9[12.9]*$		$7.20e^6$
COLUMN	$FSI_{i,j,k} \sim N(\mu + c_j + e_{i,j,k}, \sigma^2_{i,j,k})$	$\mu, c_j \sim N(0, \sigma)$ $\sigma \sim Half-t(3,0,1)$	$-185.8[13.0]*$		0.0001
DEPTH	$FSI_{i,j,k} \sim N(\mu + d_i + e_{i,j,k}, \sigma^2_{i,j,k})$	$\mu, d_i \sim N(0, \sigma)$ $\sigma \sim Half-t(3,0,1)$	$-371.3[26.5]*$		$1.01e^{69}$
NULL	$FSI_{i,j,k} \sim N(\mu + e_{i,j,k}, \sigma^2_{i,j,k})$	$\mu \sim N(0, \sigma)$ $\sigma \sim Half-t(3,0,1)$	$-370.5[26.5]*$		0.0019

Table 2.1: Bayesian multilevel models for spatial organization of feature selectivity in V4 and the influence of attention condition

COLUMN x DEPTH x ATTENTION models feature selectivity as a function of cortical column, depth of recording site, and attention condition with a trio of interactions. *COLUMN x DEPTH* models selectivity as a function of cortical column and depth of recording site with an interaction between the two. *COLUMN* and *DEPTH* only account for either cortical column or depth of recording site, respectively. NULL represents a model which assumes there is no spatial organization for feature selectivity and attention. Leave-One-Out cross-validation Expected Log Predicted Density (LOO-ELPD) is a measure of the predictive ability of the model, with larger values indicating higher predictive accuracy. LOO-ELPD difference values and the associated standard error are shown with respect to the best performing model. Bayes Factor describes support for one model over the another model, with larger values (¿1) indicating greater support for the model above and smaller values (¡1) indicating support for the model below. c_j is the random effect due to column, d_i is the depth of the recording site, a_k is a binary coded attention condition, μ is the mean response, $e_{i,j,k}$ is random error, and $FSI_{i,j,k}$ is the feature selectivity index for cortical column j at depth i and attention condition k; $\sigma^2_{i,j,k}$ is the variance in feature selectivity index and is assumed fixed. $*$ denotes a significant difference.

several models of the organization of feature representation. Each column contributed 15x2 data points – 1 per recording site for each attention condition (which will be elaborated on in a later section). Model comparisons were based on samples of the posterior distribution from each model. The results are summarized in Table 2.1. Briefly, we find that the models utilizing columnar information are more accurate in predicting the observed feature selectivity. We quantified relative model performance using the so-called leave-one-out cross-validation expected log predictive density difference (LOO-ELPD DIFF). This measure was computed between increasingly more complex models (i.e., the intercept only model to the model incorporating all independent variables). The models without a column parameter (e.g., NULL and DEPTH) had the lowest values and therefore performed worse than models including a column parameter. It should be noted that depth alone does not improve accuracy as seen in the LOO-ELPD DIFF between NULL and DEPTH, indicating a lack of trends in feature selectivity within individual layers across columns. In other words, there was no observed tendency for any given layer to have a bias. These model comparisons confirm the results found through our other frequentist methods.

2.3.4 Laminar Variation in Strength of Feature Selectivity and its Modulation with Attention

We next investigated whether changes in feature selectivity were observable with directed attention. To do so, we plotted the FSI for each recording site for both the unattended and attended conditions (Figure 2.4A). The unattended condition inclusion criteria remained the same and the attended condition was restricted to trials where the search target stimulus was present in the column's RF and the trial was performed correctly. We noticed several qualitative changes between the unattended and attended conditions (Figure 2.4A). Many columns showed enhanced feature selectivity with attention ($n = 14$, 47%). We performed Wilcoxon signed rank tests on the difference between the FSI between conditions across recording sites within each column ($p < 0.05$). This analysis confirmed that attending the stimulus in the RF mostly leads to enhancement of feature selectivity (Figure 2.4B). This enhancement was so pronounced that some non-selective columns became significantly selective ($n = 6$; 20%) when attention was deployed. However, some columns did not appear to change in selectivity ($n = 13$, 43%). Fewer showed suppressed selectivity ($n = 2$, 6%) or loss of selectivity ($n = 1$, 3%). Given their small sample size, we disregard these outliers from further consideration and focus on the population of columns that were enhanced with attention.

Next, we sought to investigate laminar differences for feature selectivity and whether the enhancement associated with attention follows a distinct laminar profile. We combined recording sites within their respective laminar compartments and measured feature selectivity. Specifically, we subtracted the nCFSI from the nFSI at each recording site to compute the deviation of individual V4 laminar compartments from the columnar mean (Figure 2.4C). We performed pairwise Wilcoxon signed rank tests of the magnitude of

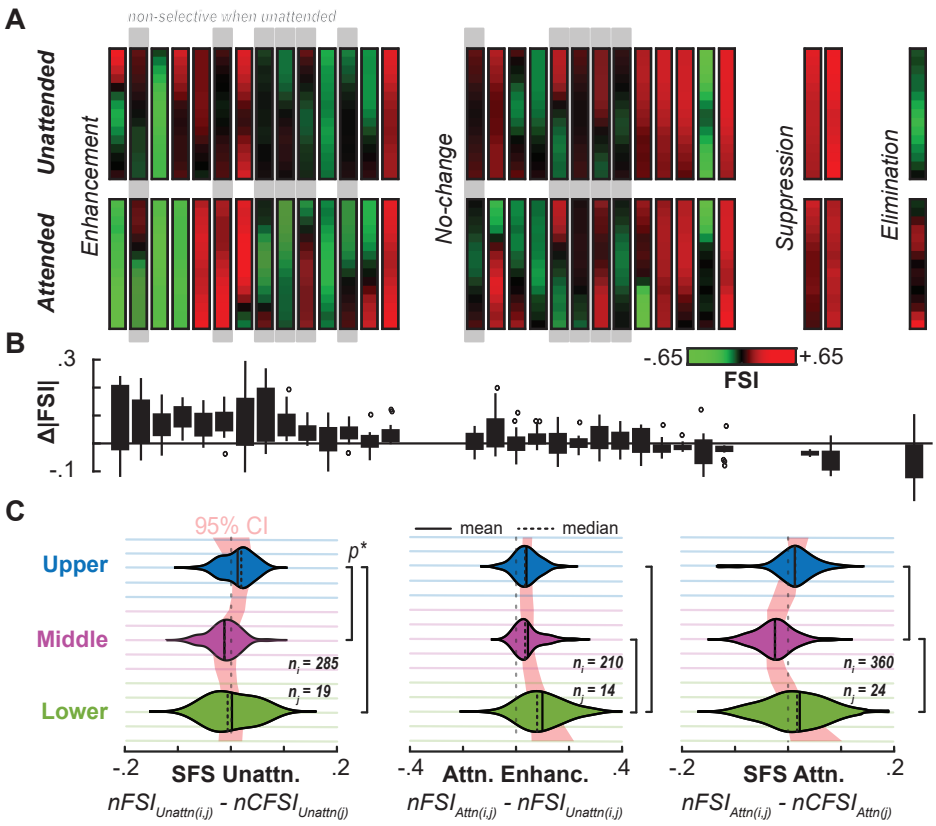

Figure 2.4: Color columns and their modulation of selectivity with attention
A. Comparing selectivity differences between unattended (top) and attended (bottom) conditions for each column. Each vertical color plot represents a column with the intensity of red or green denoting the strength in feature selectivity for that color. Columns are grouped by the change associated with attention: enhancement, no change, suppression, and elimination of feature selectivity from left to right. Columns highlighted with the gray bars were columns originally measured to have no significant feature selectivity. B. Box and whisker plot for the change in FSI for each recording site in each column corresponding to A directly above. C. Laminar profiles of strength of feature selectivity. Strength of feature selectivity is taken as the difference in feature selectivity relative to the column mean with higher values indicating stronger feature selectivity relative to the column and negative values indicating weaker feature selectivity than the column average. Recording sites were divvied into their corresponding laminar compartment. Normalized feature selectivity for each of laminar compartment shown as a violin plot for the unattended condition (left, $n = 19$), attended (right, $n = 24$), and the enhancement from unattended to attended (middle, $n = 14$). Normalization was performed such that values ranged for each recording site from -1 to 1 for non-preferred to preferred feature such that red- and green-preferring columns could be analyzed together. Solid vertical line and dashed vertical line in each distribution denote the mean and median, respectively. Red cloud behind distributions shows 95% confidence interval cloud for strength or change in strength along depth (rather than the agglomerated compartments). Brackets to the right of each plot denote significant differences between the distributions measured by Wilcoxon signed rank test ($p < 0.05$).

FSIs between the laminar compartments. We found differences between layers (upper and middle: $Z = 4.55, p = 5.2e^{-6}$; upper and lower: $Z = 5.19, p = 2.1e^{-7}$; middle and lower: $Z = 0.94, p = 0.34$), with upper layers exhibiting stronger feature selectivity than middle and lower layers. We used the same method to investigate the laminar profile in the attention condition (Figure 2.4C). In the attended condition, both

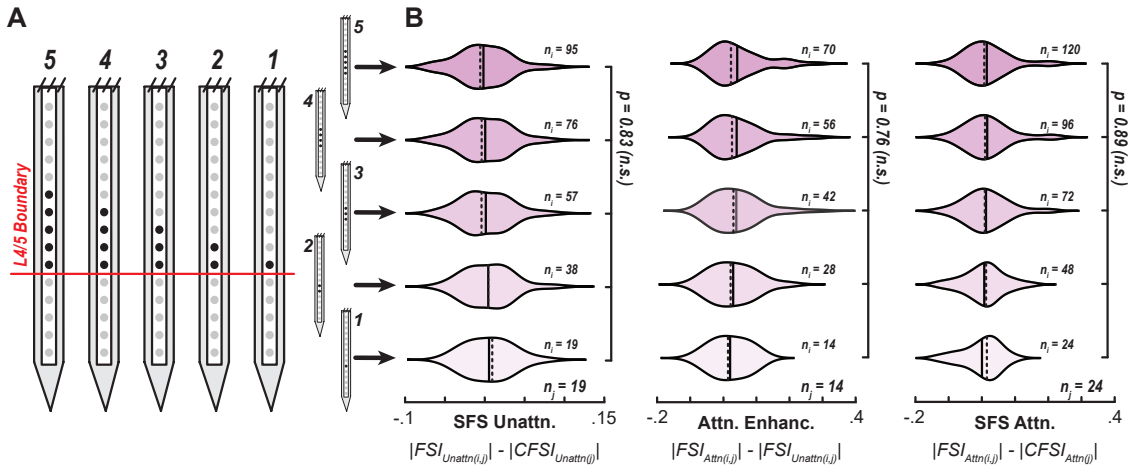

Figure 2.5: Testing different estimates of granular layer size
Testing different middle layer channel counts to account for uncertainty about thickness of layer 4. A. Cartoon depicting number and positions of channels included in this analysis determining whether size of middle layer compartment affects results with respect to attentional modulation of feature selectivity. The number of channels used decreased from 5 (the configuration used throughout main text) to 1 by eliminating successive more superficial channels as indicated by the highlighted channels. This was done relative to the L4/5 boundary where we have a well-defined physiological indicator consistent with anatomy. B. Strength of feature selectivity (SFS) is taken as the difference in feature selectivity relative to the column mean with higher values indicating stronger feature selectivity relative to the column and negative values indicating weaker feature selectivity than the column average. Feature selectivities for each middle layer compartment size are shown as a violin plot for the unattended condition (left, $n = 19$), attended (right, $n = 24$), and the enhancement from unattended to attended (middle, $n = 14$). Solid vertical line and dashed vertical line in each distribution denote the mean and median, respectively. Brackets to the right of each plot denote the result of an ANOVA. No significant differences were observed using differing numbers of channels for the middle layer.

extragranular compartments were significantly more feature selective than the middle layers (upper and middle: $Z = 2.67, p = 0.007$; upper and lower: $Z = -0.96, p = 0.34$; middle and lower: $Z = -3.70, p = 2.1e^{-4}$). Accordingly, we observed the largest attentional modulation of feature selectivity in the lower layers with the smallest in the middle and upper layers (upper and middle: $Z = -0.93, p = 0.35$; upper and lower: $Z = -3.80, p = 1.4e^{-4}$; middle and lower: $Z = --2.92, p = 0.0035$). Nonetheless, attentional enhancement of feature selectivity was significant in all laminar compartments as measured through Wilcoxon signed rank tests on the differences between conditions for columns with feature selectivity (upper: $Z = 2.24, p = 0.02$; middle: $Z = 2.15, p = 0.03$; lower: $Z = 4.06, p = 4.9e^{-5}$).

As we do not have a reliable physiological indicator of the boundary between the middle and upper layers (like we do for middle and lower layers), one possibility might be that the 0.4-0.5 mm used for middle layer specification is not representative of the granular layer, specifically. V4's granular layer has been estimated to be less extensive (Hof and Morrison, 1995) and effects limited to the granular layer might be masked, accordingly. To control for this possibility we measured the feature selectivity, and the impacts of

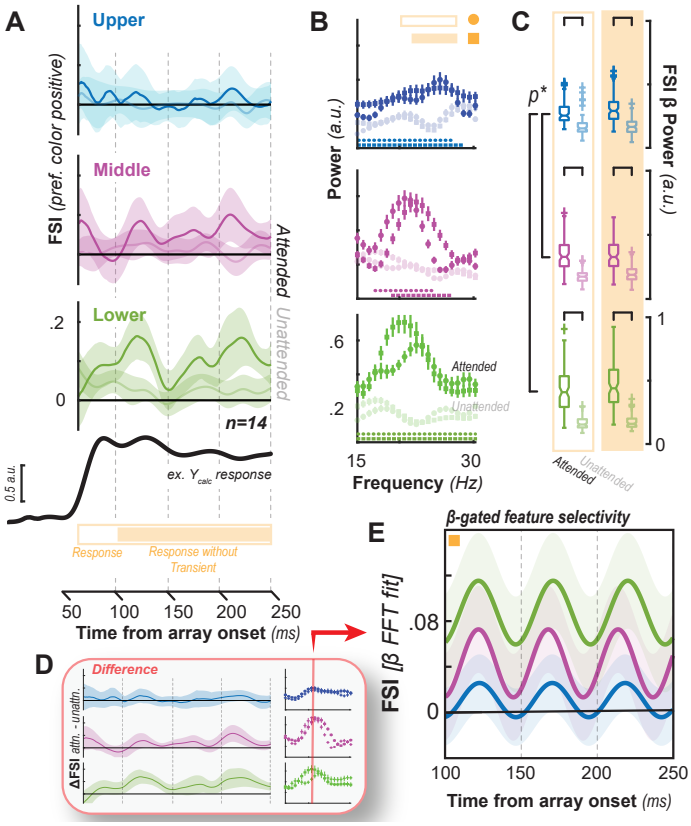

Figure 2.6: Rhythmic feature selectivity across cortical layers
A. Temporal profile of high gamma feature selectivity across sessions found to have significant enhancement of feature selectivity with attention (left, $n = 14$). Traces are shown from time since stimulus array onset. Upper, middle, and lower layer compartments shown in blue, magenta, and green, respectively. Attended condition shown as opaque lines, unattended as translucent. 95% confidence intervals shown as clouds around lines. Black trace shows example locally-generated high gamma power response for reference relative in time to the FSI traces. Orange bar at the bottom indicates response time periods including transient (60-250 ms) and excluding transient (100-250 ms) for subsequent analysis. B. Normalized power from Fourier transform (FFT) of the temporal profiles of FSI in the beta-frequency band for the attended (opaque) and unattended (translucent) conditions. Circles denote FFT on data including transient and square, data excluding transient. Dotted lines at bottom of each plot denote significant difference between attended and unattended conditions for the respective data sets ($p < 0.05$). C. Summary differences between conditions and layers for the beta FSI power (15-30 Hz) taken as the average for respective conditions in B. Data in orange outline are including transient, data in orange fill are excluding transient. Brackets denoting p¡0.05 in Wilcoxon signed rank test indicating differences between attention conditions and differences between relative power in beta-oscillating feature selectivity between layers. D. Difference in temporal profiles of feature selectivity between attention conditions and corresponding FFT in beta range indicating oscillation exists in attention condition and not unattended. E. Fourier fit of temporal profile of feature selectivity for the response excluding transient at the frequency with peak power across the laminar compartments taken from the difference measures in D. Clouds denote 90% prediction intervals of the model fits.

attention, on increasingly conservative estimates (5 sites down to 1). This showed that the results described above are consistent between middle layer sizes (Figure 2.5) and granular layer-specific effects are unlikely to be masked.

Lastly, we considered Bayesian modeling again (Table 2.1). Notably, addition of the attention condition, and the associated interactions, improves model performance as the complete model including the ATTENTION parameter has the highest LOO-ELPD. In Table 2.1 this is seen in the LOO-ELPD difference where all other models relative to the ATTENTION-sensitive model are negative (i.e., lower values). However, there are factors other than maximal model performance to consider in evaluating likelihood – model parsimony. To address model parsimony, the standard error (SE) of the LOO-ELPD difference between the complete model (COLUMN x DEPTH x ATTENTION) and all other models exceeds 5 – indicating all terms in the model are useful. Exceeding 5 times the standard error is a conservative threshold for evaluating the difference between models through this method (Bengio and Grandvalet, 2004).

2.3.5 Rhythmic Modulation of Feature Selectivity with Attention

We next sought to determine whether there was temporal variability in feature selectivity. To do so, we computed the FSI as a function of time from the peak of the transient visual response, taken as the peak of the population response averaged across recording sites and columns, to 250 ms following the stimulus array onset. We limited this analysis to the sessions found to show significant enhancement of feature selectivity with attention. We clipped the calculation at the peak of the visual transient response as the lack of activity prior to the response results in highly variable FSI (presumably because the measure is based on a ratio). We further divvied the data into the individual laminar compartments. We noticed that there appears to be rhythmicity of selectivity along all layers - but only in the attention condition. Note that this is an oscillation in feature selectivity, not just neural activity which, if significant, would suggest feature preferences oscillate in time. Qualitatively, a beta-range (15-30 Hz) rhythm seems to only appear in the attention condition (Figure 2.6A). This corresponds well to a beta oscillation apparent within the locally-generated high gamma signal. Quantitatively, a Fourier transform (FFT) of the temporal profile of feature selectivity in the beta range showed a significant boost in the attended condition relative to the unattended condition (Figure 2.6B). This was observed in both a subset of the data including the transient response as well as a subset excluding the transient, suggesting that this boost is not solely an artifact of the transient peak. In comparing differences between the attention conditions and layers across the beta range we find that the beta boost linked to attention is present along all layers, albeit stronger in the middle and lower layers than the upper layers (Wilcoxon signed rank, $p < 0.05$). All differences are depicted in Figure 2.6C. Interestingly, the beta rhythm survives a difference computation (Figure 2.6D) - meaning the same rhythmicity is not present, or at least mostly attenuated, in the unattended condition. Performing a Fourier fit on the temporal profiles of enhancement in feature selectivity at a beta frequency suggests the enhancement contains a beta oscillatory component as these model fits better explain the enhancement than a model without a timevarying

component (R^2: Fourier fit, upper=0.33, middle=0.45, lower=0.38; intercept-only fit, upper=$-1.1e^{-13}$, middle=$4.9e^{-13}$, lower=$-5.3e^{-15}$). Importantly, the rhythmic modulation of feature selectivity did not depend on microsaccades (Figure 2.7), suggesting this is not simply a result of motor-related activity.

2.3.6 Laminar Origins for the Synaptic Currents Generating the Beta Rhythm

As a next step, we sought to determine if there are changes in synaptic activity that might relate to the generation of the beta oscillation. To do so, we identified troughs in the non-recalculated beta oscillation (to avoid circular analysis) on a trial-by-trial level and extracted the time-locked CSD, as an estimate of synaptic activation, for both the attended and unattended condition (Figure 2.8). We found a significant current sink in middle and upper layers, time-locked to beta troughs in both conditions. Specifically, we computed t-tests over time, where significance was defined as 10 consecutive ms of $p < 0.05$. Electrode contacts within each laminar compartment were averaged for computing statistics. In computing the difference between the resultant spatiotemporal profiles of CSD, we found that the superficial current sink was significantly stronger in the attention condition using the same criteria. Moreover, this significant difference largely preceded the beta trough, perhaps indicative of a causal relationship. Thus, beta-driven activation seems to be linked to synaptic interactions in the upper layers of V4.

2.3.7 Beta Coupling

We sought to better characterize the rhythmic activity during this task. We first plotted the gamma power responses along depth, averaged across sessions for both the attended and unattended conditions (Figure 2.9B). We next confirmed that these gamma responses were significantly modulated by attention by performing a t-test across time, where significance was defined as $p < 0.05$ for 10 consecutive ms. We noticed a beta-range rhythm along all layers in both conditions. To confirm this observation, we filtered the gamma power in the beta frequency band (15-30 Hz) and plotted the result (Figure 2.9B). This transformation yields beta modulation of gamma power, hereafter referred to as gamma-beta. We noticed that there was no significant difference between the gamma-beta in the attended and unattended condition (conditions detailed in Figure 2.9A). Hence, although beta rhythmicity of feature selectivity is exclusive to the attention condition, beta modulation of the gamma response occured with or without attention.

We then measured coupling between gamma power along V4 layers and beta. These analyses were limited to low-frequency oscillations during the sustained response (100-250 ms following array onset) to eliminate confounds related the transient response. First, we observed beta power along layers for both attention conditions (Figure 2.9C). We then performed a Wilcoxon signed rank test between each of the possible combinations of pairs of laminar compartments to determine if there was a significant difference in

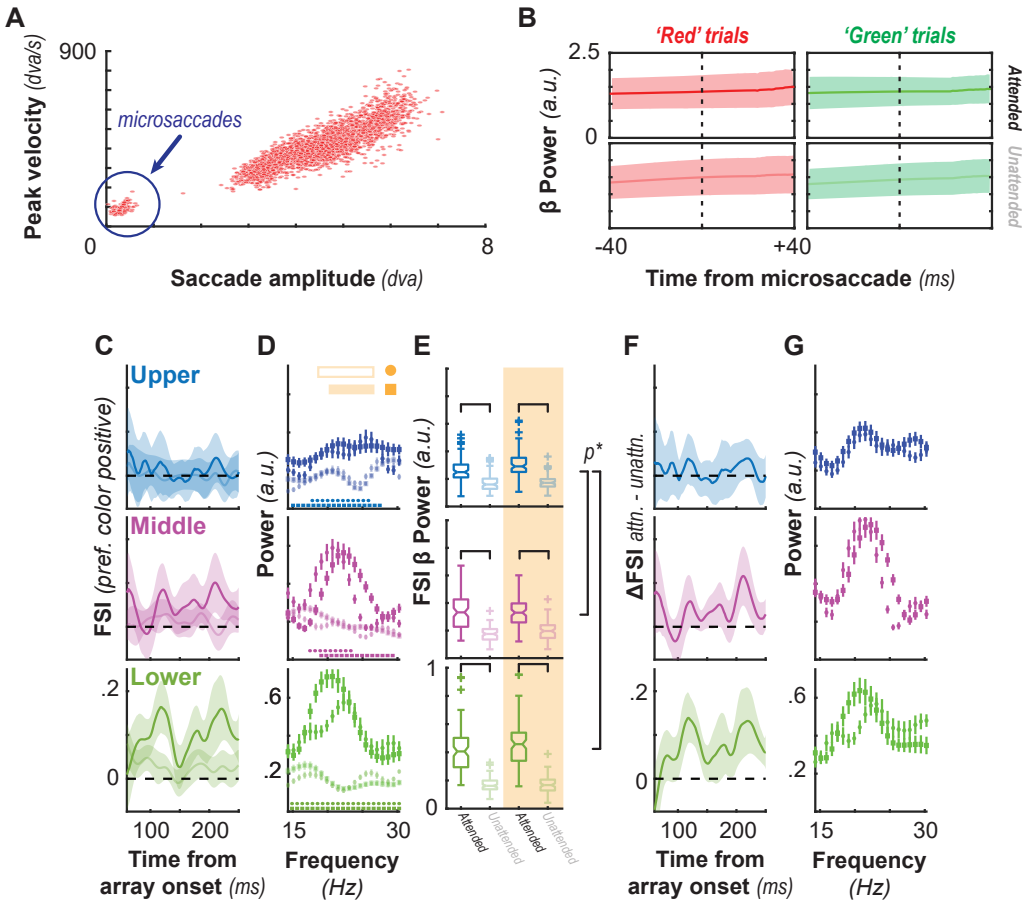

Figure 2.7: Microsaccades cannot explain gated selectivity

A. Example main sequence from correctly performed trials in a single session by monkey Ca. Detected microsaccades circled in blue. Note, microsaccades greater than 0.5 dva are not included in this analysis because they resulted in aborted trials. B. Beta power triggered to the time of microsaccades across both monkeys and all sessions where attention significantly enhanced feature selectivity ($n = 14$). Microsaccades included in this analysis must have occurred 100-250 ms following array onset and on a correctly performed trial. Trials were sorted by attention condition and stimulus color to ensure no differences existed between those trial types. C. Temporal profile of high gamma feature selectivity across sessions found to have significant enhancement of feature selectivity with attention (left, $n = 14$). Upper, middle, and lower layer compartments shown in blue, magenta, and green, respectively. Attended condition shown as opaque lines, unattended as translucent. 95% confidence intervals shown as clouds around lines. D. Orange bars at the top indicate response timeperiods including transient (circle marker, 60-250 ms) and excluding transient (square marker, 100-250 ms) for subsequent analysis. Normalized power from Fourier transform (FFT) of the temporal profiles of FSI in the beta-frequency band for the attended (opaque) and unattended (translucent) conditions. Circles denote FFT on data including transient and square, data excluding transient. Dotted lines at bottom of each plot denote significant difference between attended and unattended conditions for the respective datasets ($p < 0.05$). E. Summary differences between conditions and layers for the beta FSI power (15-30 Hz) taken as the average for respective conditions in D. Data in orange outline are including transient, data in orange fill are excluding transient. Brackets denote $p < 0.05$ in Wilcoxon signed rank test indicating differences between conditions and differences between relative power in selectivity between layers. F. Difference in temporal profiles of feature selectivity between attention conditions. G. FFT in the beta range corresponding to F indicating oscillation exists in attention condition and not unattended.

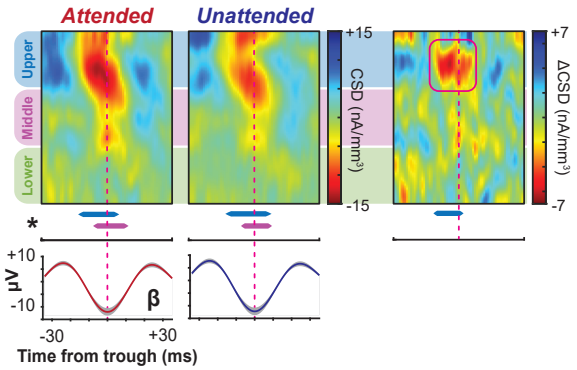

Figure 2.8: Laminar profile of beta-locked CSD across attention conditions
Synaptic activation measured as CSD for the attended and unattended conditions locked to beta for each respective condition averaged across sessions ($n = 30$). Beta rhythm shown here is taken as the average across recording channels along the cortical column with 95% CI. Current sink is observable in the upper and middle layers of cortex coupled to beta. Difference between attended and unattended conditions shown at right. Greater activation in the upper layers is observable in the attention condition highlighted with a outline. Significant synaptic activation and difference between conditions shown below each color plot. Blue line represents upper layer CSD and magenta, middle layer CSD. Abscissa uniform throughout each plot.

beta ($p < 0.05$). We found that beta power was stronger in the extragranular compartments than the granular and strongest in the lower layers, coinciding with the strongest beta modulation of feature selectivity. At the same time, we determined whether there was a significant difference in beta power along the layers between conditions (Wilcoxon signed rank; $p < 0.05$). This analysis revealed a significant difference between attention conditions across all layers. We then computed the coupling between gamma and beta within the upper layers of cortex – where the beta-generating CSD was found (Figure 2.9D). We found that gamma power along all layers was coupled to the upper layer beta oscillation to a significant degree. However, there was no observable difference in the spatiotemporal profiles between attention conditions. In other words, attention does not seem to modulate beta-frequency coupling of V4 neuronal responses, which eliminates a simple, response timing-related explanation for attentional gating of feature selectivity. To ensure this finding was beta-specific, we also measured the spatiotemporal profile of power in other low-frequency bands – specifically, alpha (8-15 Hz) and high theta (7-8 Hz) – as well as their coupling with the gamma activity (Figure 2.10). We found the profiles of power were not identical across frequency bands nor were the coupling profiles similar. This suggests that our findings are specific to the beta band and not due to generalized broadband low-frequency coupling.

2.3.8 Gamma-Beta Strength Predicts Behavior

Low-frequency oscillations have been linked to performance during attention tasks (Landau and Fries, 2012; Saalmann et al., 2012; Fiebelkorn et al., 2013, 2018, 2019; Helfrich et al., 2018; Kienitz et al., 2018; Ferro

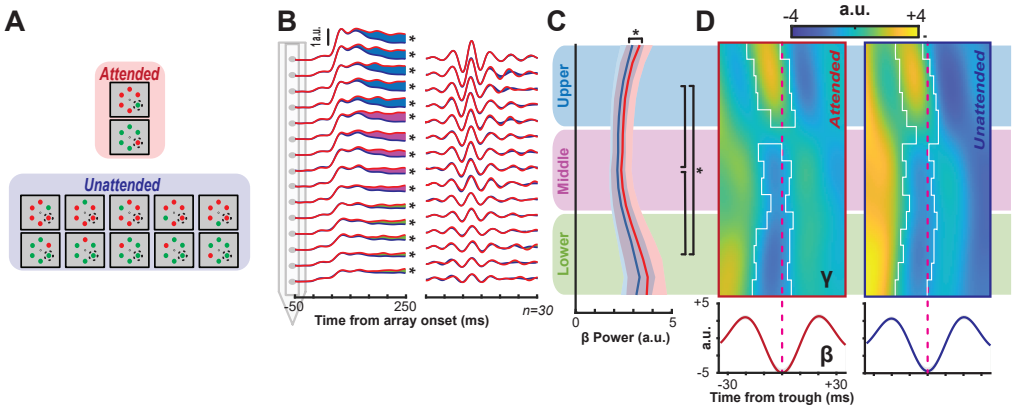

Figure 2.9: Laminar profile of gamma and beta activity
A. Search array configurations and their respective attention condition assignment. B. Temporal profile of gamma power shown across recording sites averaged across cortical columns (left, $n = 30$) from time since stimulus array onset. Upper, middle, and lower compartments shown as the top 5, middle 5, and bottom 5 traces, respectively. Attended condition shown as red lines, unattended in blue. Significant difference between attended and unattended conditions observed across all recording sites denoted by an asterisk next to each pair of traces measured through t-test through time where $p < 0.05$ for more than 10 ms. Gamma power responses filtered in the beta band (15-30 Hz) shown at right, referred to hereafter as gamma-beta. Beta rhythm observable across both conditions along all recording sites with no measurable significant differences between traces through the same method. C. Strength of beta power (not gamma-beta) along recording sites for attended (red) and unattended (blue) conditions taken as the average 100-250 ms following array onset. Significant difference denoted at right between attended and unattended conditions through a Wilcoxon signed rank test ($p < 0.05$). Brackets show significant differences in beta power strength between laminar compartments regardless of attention condition. D. Gamma power across recording sites (top) coupled to the upper layers beta oscillation (mean and 95% confidence interval cloud) for the attended (left) and unattended (right) conditions taken as the average across sessions ($n = 30$). Significant coupling shown as outline through t-test along recording sites and samples relative to beta trough with a Bonferroni correction applied. Significant coupling between gamma power and beta oscillation observed in both attention conditions around the time of the beta trough along all layers.

et al., 2021). We thus investigated whether low frequencies, specifically those measureable in the locally generated gamma response, were linked to the animals' behavioral output. Given the coupling between gamma and beta (Figure 2.9), we suspected beta as the most promising candidate for a relationship with behavior. To see if this was the case, we extended our investigation to other low frequencies (theta and alpha). For this analysis, we used the power estimate from the FFT of high gamma as predictors, and RT (i.e., initiation time of saccade to target) to measure behavioral outcome. Only correct trials were considered and trials in the unattended condition were subsampled to match the attended condition. To evaluate these potential relationships, we turned to a form of multiple linear regression.

We used a proportional odds logistic regression (POLR) model to assess the relationship between low frequency power in the gamma response and behavioral outcome. This structure allowed us to vincentize the response time data, and corresponding neural data, into quartiles (i.e., the fastest 25%, the faster 25%, the slower 25%, and the slowest 25% of trials), and treat it as an ordered factor outcome. In this structure, each

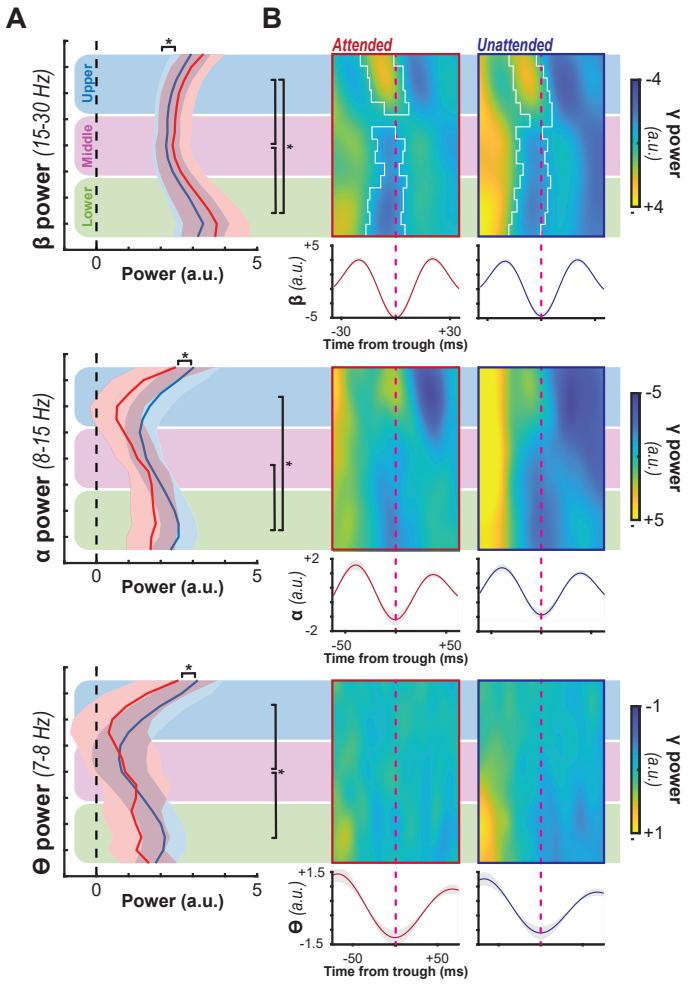

Figure 2.10: Spatiotemporal profile of low-frequency power and coupling with gamma activity
A. Power in the beta (top), alpha (middle), and high theta (bottom) low-frequency bands (abscissa) for each depth (ordinate) averaged across sessions ($n = 30$) for the attended (red) and unattended (blue) conditions. Solid lines denote means and translucent clouds are the 95% confidence intervals. Brackets above each subplot indicate significant difference between attention conditions through a Wilcoxon signed rank test ($p < 0.05$). Brackets to the right of each subplot indicate significant differences between laminar compartments through a Wilcoxon signed rank test ($p < 0.05$). B. Gamma power across recording sites coupled to the upper layers beta (top), alpha (middle), and high theta (bottom) oscillations for the attended (left) and unattended (right) conditions taken as the average across sessions ($n = 30$). Significant coupling shown as outline through t-test along recording sites and samples relative to beta trough with a Bonferroni correction applied.

recording site contributed 4 data points (1 for each vincentized bin) for each evaluated condition. Results of this approach are summarized in Table 2.2. The model was fit with the 3 (theta, alpha, beta) low-frequency power measures as independent variables, each interacted with attention condition and tested under frequentist and Bayesian frameworks. A negative coefficient indicates that stronger magnitude of that frequency modulating the locally generated gamma response is associated with faster response times and vice versa. We found that both beta power and alpha power were significantly predictive of response time in

		Frequentist			*Bayesian*	
Model Term	**Value [SE]**	**t**	**p**	**95% Confidence Interval**	**Median**	**95% Credible Interval**
$\gamma-\theta$:Unattend	-81.8 [97.1]	-0.84	0.40	-272.1, 108.4	-82.9	-599.9, 431.3
$\gamma-\alpha$:Unattend	-8.8 [77.6]	-0.11	0.91	-160.9, 143.9	-64.2	-642.2, 520.6
$\gamma-\beta$:Unattend	40.5 [59.3]	0.68	0.49	-75.7, 156.7	70.9	-323.1, 467.5
$\gamma-\theta$:Attend	-29.9 [92.5]	-0.31	0.75	-210.3, 152.4	78.6	-548.9, 702.1
$\gamma-\alpha$:Attend	326.9 [73.1]	4.47	**$7.7e^{-4}$**	183.7, 470.3	284.6	-357.1, 930.8
$\gamma-\beta$:Attend	-342.9 [40.49]	-8.47	**$2.4e^{-17}$**	-422.3, -263.6	-330.1	**-605.4, -65.1**

Table 2.2: Strength of oscillatory activity modulating locally-generated high gamma predicts behavioral responses when attended

Results of multiple linear regression in the form of proportional odds logistic regression (POLR). Both the frequentist and Bayesian forms of the POLR were tested. Model was designed to fit vincentized response time (RT) using 3 coefficients: power in theta (θ), alpha (α), and beta (β) derived from a Fourier transform (FFT) of the locally-generated gamma power (γ). These were interacted with attention condition. Data from both monkeys ($n = 2$) across all sessions ($n = 30$) were included. Each recording site ($n = 450$) contributed 24 data points (4 vincentized bins x 3 modulating frequencies x 2 attention conditions). Significant coefficients displayed in red (frequentist form, p column; Bayesian form, 95% Credible Interval column), with direction of relationship between coefficient and outcome indicated as negative or positive numbers in the value column.

the attended condition. As beta power increased, response time decreased. As alpha power increased, response time increased. In the unattended case, none of the low frequency powers were associated with RT. As we have found laminar dependencies in previous analyses, we also tested models including depth as an interaction term with each of the low-frequency oscillatory independent variables, however they did not improve model performance (likelihood ratio tests of ordinal regression models: $LR(20) = 22.82, p = 0.30$), which is why we report the more parsimonious model here. Of most import to this study, these findings demonstrate the beta rhythm modulating the neural response is associated with behavior, but only with attention – paralleling our finding regarding the beta-gated feature selectivity.

2.4 Discussion

Sensory responses in visual cortical microcircuits are modified with attention (Desimone and Duncan, 1995; McAdams and Maunsell, 1999, 2000; Treue and Martínez Trujillo, 1999; Kastner and Ungerleider, 2000; Recanzone and Wurtz, 2000; Reynolds et al., 1999, 2000; Martínez-Trujillo and Treue, 2002; Martinez-Trujillo and Treue, 2004; Reynolds and Desimone, 2003; Reynolds and Chelazzi, 2004; Williford and Maunsell, 2006; Reynolds and Heeger, 2009; Nandy et al., 2017; Ni and Maunsell, 2017, 2019; Sani et al., 2017). We sought to understand how feature selectivity is modified in an attention task. To do so, we focused on the columnar microcircuit of V4. We found that enhancement of feature selectivity occurred across the layers of cortex, albeit with variable magnitude. Interestingly, this enhancement was coupled to several cycles of a beta oscillation in the local field potential. Notably, the coupling of feature selectivity to

beta oscillations in the neural response was not present in the unattended condition. In other words, feature selectivity only oscillated in synchrony with the beta rhythm when attention was deployed, reminiscent of prior reports where attention-related behavior was linked to low-frequency oscillations in neural activity (Fries et al., 2001; Womelsdorf et al., 2007; Lakatos et al., 2008; Gregoriou et al., 2012; Landau and Fries, 2012; Fiebelkorn et al., 2013, 2019; Zalta et al., 2020). Our findings are the first to demonstrate mechanistically that low frequency rhythms in attentional performance are not just linked to response magnitude, but also to periodic changes in feature selectivity (tuning) in visual cortex.

As an initial step in our study, we identified columnar cortical representations for feature selectivity in area V4. Previous work testing for the existence of color columns yielded conflicting results (Zeki, 1973, 1980; Schein et al., 1982; Yoshioka et al., 1996), however the more recent studies ubiquitously support their existence (Tootell et al., 2004; Kotake et al., 2009; Conway and Tsao, 2009). Our findings confirm these recent conclusions. It is perhaps worth noting the value in our approach to this question. That is, none of the previous studies recorded neurons simultaneously along the layers of V4 as orthogonal penetrations of V4 are notoriously difficult. Thus, virtually all prior findings relied on indirect assessments of columnar functional architecture. Using MR-guided linear array recordings, we were able to measure simultaneous activity along V4 columns and thus confirm the existence of color columns. Moreover, our results shed some light on discrepancies in previous results. Specifically, we found that different columns prefer different colors, and that they do so at different relative strengths. This finding reconciles both previous functional imaging studies (Conway et al., 2007; Wade et al., 2008; Tanigawa et al., 2010), as well as prior neurophysiological studies on color selectivity in V4 (Zeki, 1973, 1980; Schein et al., 1982; Schein and Desimone, 1990; Roe et al., 2012; Liebe et al., 2011; Bushnell and Pasupathy, 2012). The variability we found at the laminar level might explain the conflicting results regarding the magnitude of selectivity across studies using differing methodological approaches. That is, we found that despite the existence of color columns, the strength of selectivity for a specific color along depth is not uniform. Instead, V4's upper layers generally show stronger selectivity than the lower layers – but only in the unattended condition. This is consistent with previous findings along a different feature dimension - namely, orientation tuning (Pettine et al., 2019) – perhaps suggesting a common attribute of feature processing in the absence of attention. Taken together, our results demonstrate that despite the existence of color columns, V4 color selectivity varies considerably in both the tangential and the radial dimension.

One important limitation of the current study when considering precision in these color representations is that we were limited to testing only two colors out of the entire gamut available to trichromats. Moreover, our determination of isoluminance was based on a human ideal observer rather than psychophysical testing of each animal. Many of our conclusions thus are based 1) on the assumption that there were little to no

luminance differences between our stimuli that could explain our results in the absence of hue selectivity and 2) that the evidence for red and green color columns can be extended to other parts of the color spectrum as well. We believe that assumption 1) can be justified by the fact that the absorption spectra of macaque and human L and M cones differ negligibly ((Nunn et al., 1984), but see (Dobkins et al., 2000)) and that direct psychophysical evaluation suggests that humans and macaques perceive colors similarly (Gagin et al., 2014). Importantly, evidence that we gathered from indirect measures suggested that luminance varied negligibly. Both response time (Tanaka et al., 2013) and neural response latencies (Geisler et al., 2007) vary with luminance of stimuli. In our dataset, we find no variability in these measures between the red and green stimuli (Table 2.3). Furthermore, previous work has found no support for a functional organization for luminance in V4 (Tootell et al., 2004) making our interpretation that the columnar organization we observe is due to color-selectivity rather than luminance, the more parsimonious conclusion. Nonetheless, it is important to note that it cannot entirely be ruled out that at least some of the results we obtained are due to differences in luminance rather than hue. Similarly, while assumption 2) remains largely a conjecture, it rests on our direct findings for colors red and green as well as the array of previous studies providing indirect evidence for V4 color columns across a wider area of the gamut (Zeki, 1973, 1980; Conway and Tsao, 2009; Kotake et al., 2009). Further investigation is necessary to determine whether the laminar differences we found extend to different colors. Furthermore, given the representation and tuning for color varies across the cortical sheet (Bohon et al., 2016) and the limited portion of V4 where orthogonal laminar recordings can easily be achieved, additional variability might exist beyond what we observed here. While more general questions regarding the nuances of the laminar organization of color selectivity remain, the finding that V4 columns act as functional microcircuits for the processing of different color stimuli is consistent with the principles of a canonical cortical microcircuit (Douglas et al., 1989; Douglas and Martin, 1991; Bastos et al., 2012).

Perhaps our most surprising result was not just that the attention enhanced feature selectivity fluctuated in a beta-rhythm, but also that the beta-rhythm was present in our neural activity regardless of attention condition. This result might suggest that the beta-rhythm observed in our data is not necessarily generated through a cognitive process, but is rather more associated with sensory or perceptual processing. Support for this conclusion can be found in other work. Notably, direct modification of low-frequency neural oscillations in V4 through optogenetics impairs perception (Nandy et al., 2019). However, other work suggests that these low-frequency oscillations are top-down in origin and regulate the enhancement of bottom-up responses (Richter et al., 2017) and are not dependent on early visual cortical areas (Schmiedt et al., 2014). Other studies more generally suggest a top-down role for beta activity with respect to attention (Lopes da Silva et al., 1970; Bekisz and Wróbel, 2003; Buschman and Miller, 2007; Bosman et al., 2012; Grothe et al.,

	Dataset	*n*	*Mean Diff. (ms)*	*SD (ms)*	*95% CI (ms)*	*Median Diff. (ms)*	*Signed Rank*	*z*	*p*
Behavioral RT Difference (Red-Green Target Trials)	Complete	30	0.30	5.21	-1.56, 2.17	-0.77	242	0.20	0.85
	Monkey Ca	21	0.43	4.17	-2.22, 1.35	-0.98	123.5	0.28	0.78
	Monkey He	9	0.58	5.94	-3.30, 4.46	1.02	23	0.06	0.95
Neural Response Latency Difference (Red-Green in RF)	Complete	445	-0.28	10.33	-1.24, 0.68	0	45057	0.69	0.49
	Monkey Ca	310	0.17	9.90	-0.93, 1.28	-1	22067	0.06	0.95
	Monkey He	135	-1.26	11.21	-3.15, 0.62	0	4106	1.07	0.28

Table 2.3: Comparisons of behavioral RT and neural response latency between red and green stimuli show no evidence for differing luminance between stimuli

Measurements and statistics of the differences in response time (RT) for red vs. green target trials (top) and the differences in neural response latency for red vs. green stimuli in the column's receptive field (RF) (bottom). Results reported for the complete dataset as well as each monkey individually. Behavioral RT taken as the initiation time of the saccadic response. Neural response latency taken as the time at which the multiunit spiking activity exceeded 30% of its maximum response. Mean difference, standard deviation (SD), 95% confidence interval (CI), and median difference. Statistical differences, or a lack thereof, reported using a Wilcoxon signed rank test yielding a signed rank statistic, z value, and p value.

2012), subjective visual detection (Wilke et al., 2006; Maier et al., 2008), working memory (Tallon-Baudry et al., 2005; Salazar et al., 2012), and other phenomena involving feedback (Bao et al., 2010). As our data is limited to V4, we cannot directly test for a source for the beta oscillations. It is noteworthy, however, that the beta rhythm in both attention conditions has associated current sinks in both the granular, feedforward input layer and in the superficial layers of cortex. Perhaps more insight can be gained from exploring the putative functional architecture that would be supporting these findings as well as the instantiating mechanism.

One consideration is the array of afferent and efferent connections of V4. Area V4 seemingly assumes an important position in the visual cortical hierarchy with respect to attentional selection and modulation when considering its anatomical connections. It shows attentional modulation across various tasks and has connections to both earlier and later visual cortical areas as well as connections to frontal attentional control structures (Schall et al., 1995; Roe et al., 2012; Ungerleider et al., 2008; Pouget et al., 2009). Moreover, these frontal structures have a demonstrable impact on sensory processing in V4 (Moore and Armstrong, 2003). For example, inactivation of frontal eye field (FEF) at sites corresponding retinotopically to recorded V4 neurons reveals that FEF contributes to the presaccadic specification of visual target features (Noudoost et al., 2014). Also of note, inactivation of ventral prearcuate areas (VPA) in frontal cortex, eliminates effects of feature attention in V4 (Bichot et al., 2019).

Assuming the beta-oscillation we describe has a prefrontal origin, the target of frontal feedback connections to V4 would likely be the extragranular layers (Douglas et al., 1989; Douglas and Martin, 1991; Anderson et al., 2011; Bastos et al., 2012), which coincides with where we observe the difference in beta-generating CSD. However, it is worth noting that the deep layers of V4 have previously been shown to be most associated with behavioral outcome (Pettine et al., 2019) whereas the behavior-associated synaptic

activity in our study was located to the upper layers of V4. This apparent discrepancy could be reconciled by upper-layer synaptic activity perhaps driving apical dendrites from deep-layer visual cortical neurons (Mountcastle, 1997). Regardless, the extragranular nature of this signal might suggest that top-down connections play a role in our findings.

Models of visual attentional selection promote an important role for area V4 interacting with other visual cortical and frontal areas (Hamker, 2005). With these connections and interactions in mind, the connections between frontal areas like FEF or VPA and V4 are one likely source for the mechanism manifesting the frequency-gating we observe in sensory processing and seem a good candidate for further investigation. Specifically, frontal attentional control structures might excite V4 in a beta-rhythmic fashion and with laminar specificity such that targets of attention are enhanced only with that rhythm. That is, frontal structures could regulate the bottom-up neural response such that the recipients of V4 output are more sensitive to behaviorally-relevant information. However, recent work also provides causal evidence of a role of posterior parietal cortex in pop-out modulation and the saccadic selection of salient stimuli (Chen et al., 2020). Given the interconnectivity of V4 and parietal areas (Ungerleider et al., 2008) coupled with these findings, posterior parietal cortex becomes another possible source for the results reported here.

Recent reports have demonstrated a link between spiking activity and low-frequency oscillations that is predictive of behavioral outcome in fronto-parietal attention networks (Fiebelkorn and Kastner, 2021). Given the similarity with our findings, it seems a link could be hypothesized between this network and the sensory processing stage we document here. However, it is important to note that their findings were restricted to visuomovement neurons in FEF. In another attention task visual neurons in FEF, but not movement or visuomovement neurons, showed enhanced gamma frequency synchronization with activity in V4 (Gregoriou et al., 2012). Yet, it may also be that the populations of functional cell types in FEF are more nuanced than previously thought, so alternative labeling of these populations might reveal a link through functional mappings (Lowe and Schall, 2018). While speculative, this hypothesis can be tested empirically to determine whether there is a direct link between the behavior-associated beta found in the oculomotor system and that found at the sensory processing stage documented here.

In considering possible instantiating mechanism neural pathways, it is also useful to consider the nature and conditions of the attention allocation. Specifically, do these findings arise from an endogenous, goal-directed process or from and exogenous, stimulus-driven mechanism. Pop-out singleton stimuli are known to capture attention (Theeuwes, 1993; Folk et al., 1992; Luck et al., 2021; Cosman et al., 2018). The exogenous factors of the task used in this study are known to modulate V4 activity when endogenous factors are controlled for (Burrows and Moore, 2009), but endogenous saccadic preparation can also modulate V4 activity (Steinmetz and Moore, 2014). Thus, the findings of this paper could result through exogenous or

endogenous means.

Speculatively, an exogenous mechanism seems most plausible. This rests on three independent observations: 1) The animals' task was efficient pop-out search, which is thought to involve exogenous, stimulus-driven attention. 2) The V4 response to the array of visual stimuli comprises a beta-component regardless of attention condition, suggesting that attention-related feedback is not necessary for beta-range rhythmicity to emerge in V4. 3) The beta-modulated feature selectivity arises within the initial transient response, before feedback can evolve. To bolster support for point #3, enhancement of feature selectivity should be significant before feedback activity (about 100 ms following array onset (Mehta et al., 2000a,b), see Fig. S6). Sensory cortex may be sufficient to select the attentional target in this task without frontal or parietal help. Models of exogenous selection can locate salient items solely through local lateral inhibition (e.g., (Itti and Koch, 2000; Soltani and Koch, 2010)). Taken together, these factors are consistent with the conjecture that the beta-gated enhancement with attention arises through a bottom-up process. It is noteworthy that slow, rhythmic fluctuations of V4 responses coupled to attention have previously been shown to emerge through competitive interactions between neighboring neurons (Kienitz et al., 2018). However, as noted, the dissociation of exogenous and endogenous attentional components in this task is indirect, so further work is required to disentangle them.

2.5 Methods

2.5.1 Surgical Procedures and MRI

Monkeys were implanted with a custom head post and MR-compatible recording chamber (Crist Instruments) concurrent with a craniotomy over V4. Chamber placement was confirmed with structural MRI (Fig. 1). Recording sites were also confirmed postmortem in one monkey using DiI injections (Westerberg et al., 2020a) (He). A third monkey (Z, *Macaca mulatta*, 12.0 kg), exclusively contributing MR scans for 3D renders, also underwent similar surgical procedures. Tranquilization was performed under aseptic conditions with the animals under $N_20/0_2$, isoflurane (1–5%) anesthesia mixture. Vital signs were monitored continuously. Expired PCO_2 was maintained at about 4%. Postoperative antibiotics and analgesics were administered. Further elaboration of surgical methods is documented elsewhere (Westerberg et al., 2020a,b). MR images for chamber localization and guiding linear electrode penetrations perpendicular to the cortical surface were taken from anesthetized animals placed inside a 3T MRI scanner (Philips). Vital signs were monitored continuously. T1-weighted 3D MPRAGE scans were acquired with a 32-channel head coil equipped for SENSE imaging. Images were acquired using a 0.5 mm isotropic voxel resolution with the following parameters: repetition time 5 s, echo time 2.5 ms, and flip angle 7°. 2D and 3D renders were performed offline using the multi-image analysis GUI, "Mango" (Research Imaging Institute, UTHSCSA).

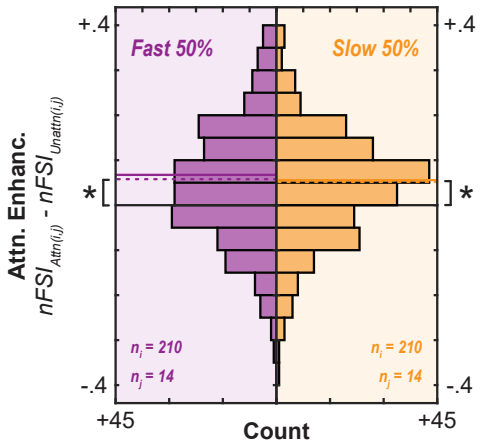

Figure 2.11: Feature selectivity is enhanced early in response regardless of behavioral response timing Correctly performed trials were median split such that they were divvied into the 'fast 50%' of trials (purple) and the 'slow 50%' of trials (orange). Feature selectivity was computed for each recording site for both the fast and slow trials independently. Data contributing to the feature selectivity computation were restricted to the time 60 ms following array onset to 100 ms following array onset as to only capture the transient feedforward visual response. The 14 columns which showed significant enhancement of feature selectivity with attention, totaling 210 recordings sites, were included in the comparison. Normalized feature selectivity was used to accommodate data from both red- and green-preferring columns. Significant enhancement of feature selectivity with attention was found for both fast ($Z = 6.82$, $p = 9.4e^{12}$) and slow ($Z = 6.02$, $p = 1.7^{e9}$) trials through a Wilcoxon signed rank test during this early response epoch - as indicated by the asterisk next to each histogram. No significant difference was found between the fast and slow trials ($Z = 1.64$, $p = 0.10$).

2.5.2 V4 Localization

Recordings took place on the convexity of the prelunate gyrus in approximately the dorso-lateral, rostral aspect of the V4 complex, where receptive fields are located at 2–10 dva eccentricity in the lower contralateral visual hemifield (Gattass et al., 1988). Laminar recordings must take place at a location where the array can be positioned orthogonal to the cortical surface, which limits potential locations. Recording sites were confirmed through staining the recording site locations by dipping the electrode arrays in DiI on the final recordings in monkey He (Fig. 1). Recording locations are highlighted in Fig. 1 on MR scans for each monkey.

2.5.3 Stimuli and Task

Monkeys viewed arrays of stimuli presented on a CRT monitor with 60 Hz refresh rate, at 57 cm distance. Stimulus presentations and task timing were achieved using TEMPO (Reflective Computing). Visual presentations were monitored with a photodiode positioned on the CRT monitor so that electrophysiological signals could be reliably aligned offline. Due to study constraints, we were limited to red (CIE coordinates: $x = 0.648$, $y = 0.331$) and green circles (CIE coordinates: $x = 0.321$, $y = 0.598$), rendered isoluminant to a

human observer at 2.8 cd/m^2 on a uniform gray background. As the stimuli were rather limited and determination of isoluminance was based on a human ideal observer rather than individual measurements for each of the monkeys included in the study, we define our test features as the red and green stimulus. Because we are limited to two colors and cannot account for potential differences in perceived luminance between the macaques, we qualify our two stimuli as distinct 'features' as the intersection of color and luminance information. Nonetheless, we report the information regarding the colors used in this study for the ideal human observer. Cone excitation was computed from the CIE coordinates and luminance (Cole and Hine, 1992):

$$\begin{aligned}
\varepsilon_L &= Y \cdot \left[0.15514 \cdot \frac{x}{y} + 0.54312 - 0.03286 \cdot \frac{(1-x-y)}{y} \right] \\
\varepsilon_M &= Y \cdot \left[-0.15514 \cdot \frac{x}{y} + 0.45684 - 0.03286 \cdot \frac{(1-x-y)}{y} \right] \\
\varepsilon_S &= Y \cdot \left[0.00801 \cdot \frac{(1-x-y)}{y} \right]
\end{aligned}$$

where the following cone excitations were measured for red stimulus: $\varepsilon_L = 2.37$, $\varepsilon_M = 0.43$, $\varepsilon_S = 0.0014$; green stimulus: $\varepsilon_L = 1.74$, $\varepsilon_M = 1.06$, $\varepsilon_S = 0.0030$; and the background: $\varepsilon_L = 1.86$, $\varepsilon_M = 0.94$, $\varepsilon_S = 0.023$. Cone contrasts were then computed by:

$$\begin{aligned}
C_L &= \frac{(\varepsilon_{L,Stimulus} - \varepsilon_{L,Background})}{\varepsilon_{L,Background}} \\
C_M &= \frac{(\varepsilon_{M,Stimulus} - \varepsilon_{M,Background})}{\varepsilon_{M,Background}} \\
C_S &= \frac{(\varepsilon_{S,Stimulus} - \varepsilon_{S,Background})}{\varepsilon_{S,Background}}
\end{aligned}$$

where cone contrasts for red stimulus were found to be: $C_L = 0.27$, $C_M = -0.54$, $C_S = -0.94$; and the green stimulus: $C_L = -0.06$, $C_M = 0.13$, $C_S = -0.87$.

Trials were initiated when monkeys fixated within 0.5 degree of visual angle (dva) a small, white fixation dot (diameter=0.3 dva). The time between fixation acquisition and array presentation varied between 750–1250 ms, taken from a function designed to produce a nonaging foreperiod as to eliminate any potential effect of stimulus expectation (Nickerson and Burnham, 1969; Näätänen, 1970, 1971). Taking fixation period times from a nonaging foreperiod function results in sets of trials with a non-uniform probability of a given foreperiod duration with a bias towards shorter foreperiods with a reduction in probability as duration increases within the range. Following the fixation period, the stimulus array

consisting of 6 items was presented. Stimuli were scaled with eccentricity at 0.3 dva per 1 dva eccentricity so that they were smaller than the estimated V4 receptive field size (0.84 dva per 1 dva eccentricity (Freeman and Simoncelli, 2011)). The polar angle positioning of the items relative to fixation varied from session to session so that one item of the stimulus array was positioned at the center of the receptive field. Items were spaced such that only one item was in the V4 column receptive field, with uniform spacing in polar angle and equal eccentricity. Monkeys engaged in a task while viewing the stimulus array. One item in the array was a different feature (red or green) from the others. The oddball item could be in any one of the six positions of the stimulus array. Position of the oddball on each trial was randomly chosen with equal probability for any of the positions (16.6%). Monkeys earned fluid reward for shifting gaze directly to the oddball item within 1000 ms of array presentation and maintaining fixation within a 2–5 dva window around the oddball for 500 ms. Additionally, eye movements were monitored continuously at 1 kHz using an infrared corneal reflection system (SR Research). If the monkey failed to look at the oddball, no reward was given and a 1-5 s timeout ensued.

2.5.4 Neurophysiological Procedure

Laminar V4 neurophysiology data were acquired at 24.4 kHz resolution using a 128-channel PZ5 Neurodigitizer and RZ2 Bioamp processor (Tucker-Davis). Raw signals were filtered online and output between 0.1 Hz and 12 kHz. Data were collected from 2 monkeys (left hemisphere, monkey Ca; right hemisphere, He) across 70 recording sessions (31, monkey Ca; 39, He) using 32 channel linear microelectrode arrays with 0.1 mm interelectrode spacing (Plexon). Each recording session, electrode arrays were introduced into the prelunate gyrus through the intact dura mater using a custom micromanipulator (Narishige). Electrode arrays were positioned so they spanned all layers of V4 and had a subset of electrodes positioned outside of cortex. 30 (21, monkey Ca; 9, He) of 70 sessions were included in the final analysis. The remaining 40 sessions were found to either not have a discernable CSD profile for laminar alignment or not be orthogonal to the cortical surface and were thus removed from analysis as to only include electrode penetrations where we had a high degree of confidence that they were positioned precisely.

2.5.5 Receptive Field Mapping

To determine the orientation and eccentricity of the visual receptive field, monkeys performed a receptive field mapping task prior to the main (feature search) item task. Monkeys fixated for 400–7000 ms while a series of 1 – 7 stimuli were presented that spanned the visual field contralateral to the recording chamber. Stimuli were five high-contrast concentric white and black circles that scaled in size with eccentricity (0.3 dva per 1 dva eccentricity). In all recording sessions, stimuli could appear in any location spanning the

lower visual quadrant contralateral to the recording chamber placement in 5° angular increments relative to fixation and in eccentricities ranging from 2 dva to 10 dva in 1 dva increments. Each stimulus was presented for 200–500 ms with an interstimulus interval of 200–500 ms. If the monkey maintained fixation for the duration of the stimulus presentation sequence, they received a juice reward. During this receptive field mapping task, multiunit activity, gamma power, and evoked local field potentials (LFPs, 1–100 Hz) were measured across all recording sites (Cox et al., 2019b, 2013; Dougherty et al., 2019; Westerberg et al., 2019). Online, we measured the response across visual space for each recording site. Recordings proceeded to the feature search task if there was qualitative homogeneity of receptive fields along depth (Fig. 1) similar to those described previously (Nandy et al., 2017). The receptive field center was chosen to be the stimulus location that evoked the largest response along the depth of recording sites. Following receptive field identification, the stimulus array in the feature search task was then oriented so that its eccentricity coincided with the location of the receptive field (eccentricity: 3–10 dva) and a single array item was placed at the center of the receptive field (size: 0.9–3 dva).

2.5.6 CSD and Laminar Alignment

Positions of the individual recording sites relative to the layers of V4 were determined using current source density (CSD) analysis. CSD reflects local synaptic currents resulting from excitatory and inhibitory postsynaptic potentials (Mitzdorf, 1985). CSD was computed from the raw neurophysiological signal by taking the second spatial derivative along the electrode contacts (Nicholson and Freeman, 1975; Schroeder et al., 1998; Maier et al., 2010; Westerberg et al., 2019). CSD activation following presentation of a visual stimulus reliably produces a specific pattern of activation which can be observed in primate visual cortex (Schroeder et al., 1998; Maier et al., 2010), including V4 (Givre et al., 1994; Bollimunta et al., 2008; Nandy et al., 2017). Specifically, current sinks following visual stimulation first appear in the granular input layers of cortex, and then ascend and descend to the extragranular compartments. To compute the CSD from the LFP, we used the previously described procedure (Nicholson and Freeman, 1975):

$$CSD_{t,d} = -\sigma \left(\frac{x_{t,d-z} + x_{t,d+z} - 2x_{t,d}}{z^2} \right)$$

where the CSD at timepoint t and at cortical depth d is the sum of voltages x at electrodes immediately above and below (z is the interelectrode distance) minus 2 times the voltage at d divided by the interelectrode-distance-squared. That yields the voltage local to d. To transform the voltage to current, we multiplied that by $-\sigma$, where σ is a previously reported estimate of the conductivity of cortex (Logothetis et al., 2007). For each recording session, we computed the CSD and identified the initial granular input sink

following visual stimulation. Sessions were aligned using the bottom of the initial feedforward input sink as a functional marker. We defined the size of individual laminar compartments uniformly relative to space. Throughout, 'middle' refers to the estimate of the granular input layer 4 (0.5 mm space above the CSD functional marker), 'upper' refers to the estimate of supragranular layers 2 and 3 (0.5 mm space above the L4 compartment), and 'lower' refers to the estimate of infragranular layers 5 and 6 (0.5 mm space below the L4 compartment). CSD was then also used to recalculate the gamma activity as our measure of the localized neural activity.

2.5.7 Locally Generated Gamma Recalculation

LFP measured from an electrode contains far field, volume-conducted signals which challenge the interpretability of results concerning localized function. To understand local circuit interactions, such as columnar organization of feature preferences, additional steps can be taken to account for the volume-conducted signals. The configuration of microelectrodes in the linear array provides the opportunity to recalculate the low-frequency LFP signal without volume-conducted components. Specifically, we calculated the locally generated component of the LFP from the measured laminar CSD (LFP_{calc}) using a previously described model (Nicholson and Llinas, 1971; Kajikawa and Schroeder, 2011):

$$LFP_{calc}(d_i,t) = A\sum_j \frac{CSD_{d_j,t}}{\sqrt{h^2+|d_j-d_i|^2}}$$

where LFP_{calc} at depth i (d_i) for each timepoint t is taken as the sum of CSD at depths j (d_j) for each timepoint divided by the Euclidean distance to account for the attenuating impact of local currents on distant field potentials. The factor value of A acts is only as a scaling factor. Because we cannot accurately estimate the magnitude of the one-dimensional CSD-derived waveform, we eliminate this parameter from the calculation. This omission is consistent with previous reports (Kajikawa and Schroeder, 2011) but limits the interpretability of locally generated LFP_{calc} signals as the absolute magnitude of the response is only an estimation. However, relative magnitude differences can readily be observed between conditions with this method. Also, for our purposes, we set h to 0 as we assume that our observed CSD and the recalculated LFP are colocalized.

From the recalculated LFP, gamma power was extracted using previously reported filtering methods (Maier et al., 2010). Briefly, the recalculated LFP signal at each recording site was band-pass filtered for the desired frequency band (gamma, 70–150 Hz). This signal was also filtered for high theta (7-8 Hz), alpha (8-15 Hz), and beta (15-30 Hz) where necessary, but did not go through the subsequent power conversion. For the gamma, the signal was then full-wave rectified and low-pass filtered at half the frequency of the cut

off of the original high-pass filter to obtain power. 4th order Butterworth filters were used for both steps. Gamma power was used for both the online receptive field mapping and for offline analysis of neural activity along cortical depth. Gamma responses were baseline corrected at the trial level by subtracting the average activation in the 300 ms preceding search array presentation from the response at all timepoints. This baseline correction procedure was performed prior to any further analysis of the data. Data were clipped 10 ms prior to the saccade at the trial level to eliminate any potential influence of eye movements.

2.5.8 Feature Selectivity Index

Feature (red vs. green) selectivity was derived from the gamma power observed along recording sites. Responses were taken when a red stimulus was presented to the receptive field (RF) of the cortical column and when a green stimulus was present in the receptive field. Only trials where the stimulus was unattended (e.g., not the array oddball/saccade target) were included in the initial analysis of feature selectivity. For later analyses where comparisons of attended and unattended conditions were made, trials where the oddball feature stimulus was in the RF or outside the RF were used, respectively. The responses were taken as the average activation 50–150 ms following array presentation. An index was computed from these responses, referred to hereafter as the feature selectivity index (FSI). Feature selectivity index for recording site i from cortical column j and attention condition k ($FSI_{i,j,k}$) was defined as the difference between the mean response x for the recording site on trials where the stimulus was red ($x_{red,i,j,k}$) and when the stimulus was green ($x_{green,i,j,k}$) divided by the sum of those two responses:

$$FSI_{i,j,k} = \frac{x_{red,i,j,k} - x_{green,i,j,k}}{x_{red,i,j,k} + x_{green,i,j,k}}, \quad where\ i = 1,\ldots,15,\ j = 1,\ldots,30,\ k = 1,2$$

this provided a value bounded between -1 and 1 where larger magnitude indices indicate a greater degree of selectivity for either green (towards -1) or red (towards 1). A columnar feature selectivity index (CFSI) was taken as the average of FSI across the column.

For certain computations, feature preference is unimportant because the interpretation of the result depends on the presence not the quality of the preference. In those circumstances, we normalized FSI ($nFSI_{i,j,k}$) and CFSI ($nCFSI_{j,k}$) to change the sign of each feature selectivity index so that +1 indicates selectivity towards the preferred color of the column and -1, the non-preferred color of the column. Being based on a specific feature preference, this adjusted index was only useful for columns selective for a color feature.

2.5.9 Feature Selectivity Index Statistics

To evaluate whether columns showed significant feature selectivity and whether they were consistent along depth at the single session level, we generated null distributions for which to compare the experimental data to. We did so by taking the FSI measured for all recording sites ($n = 15$) across all columns ($n = 30$), totaling 450 indices, and randomly selected 15 values, 1000 times. In this way, we ended up with a large number of distributions that comprised measured data, but that did not retain the effect of the individuality of a column. That is, these null distributions represent columns where the variability within and across columns is identical. That way any difference observed when comparing to these bootstrap columns is a result of the effect of the column. To evaluate whether individual columns showed significant feature selectivity for either red or green stimuli, we employed Wilcoxon signed rank tests. The Wilcoxon signed rank test does not make any assumption of homogeneity of variance like standard t-tests or ANOVAs, which is relevant given our second test. We performed this test 1000 times for each column, comparing each observed column to the bootstrap columns. We took the median p-value resulting from those repeated tests to determine whether a column had significant feature selectivity. To evaluate whether individual columns were consistent in their FSI's along depth, we employed Bartlett's test. We used the same procedure as the Wilcoxon signed rank tests to evaluate significant consistency along depth for each session ($p < 0.05$).

2.5.10 Intraclass Correlation Coefficient

To assess the consistency of feature selectivity along a cortical column relative to the variability that might exist across columns, we computed an intraclass correlation coefficient (ICC) (Shrout and Fleiss, 1979) of type ICC(C,1) (McGraw and Wong, 1996). Under this type of ICC, we are interested in the degree of consistency among measurements made under the fixed levels of recording site locations (e.g. their individual positions along cortical depth). We used a 2-way mixed effects model without an interaction:

$$FSI_{i,j,k} = \mu + c_{j,k} + d_{i,j,k} + e_{i,j,k}, \quad where\ i = 1,\ldots,15,\ j = 1,\ldots,30,\ k = 1,2$$

where $FSI_{i,j,k}$ is the FSI for column j at depth/recording site i and attention condition k, μ is the population mean for all observations and is constant. $c_{j,k}$ is the cortical column effect which is random, independent, and normally distributed with mean 0 and variance σ_c^2. $d_{i,j,k}$ is the effect of the recording site depth, which is fixed so that $\sum d_{i,j,k} = 0$ and has variance $\theta_d^2 = \sum d_{i,j,k}^2/(m-1)$ where m is the number of recording sites for each column, 15. $e_{i,j,k}$ are the residual effects which are random, independent, and normally distributed with mean 0 and variance σ_e^2. All effects are pairwise independent. For ICC(C,1) the true value of ρ is defined as:

$$\rho = \frac{\sigma_c^2}{\sigma_c^2 + \sigma_e^2}$$

where ρ is bounded between 0 and 1. 0 indicates a lack of consistency within the cortical column relative to the variability that exists across columns and 1 indicates the recording sites along depth are highly consistent relative to the variability across columns. We estimate ρ with $\hat{\rho}$ as:

$$\hat{\rho} = \frac{MS_C - MS_E}{MS_C + (m-1)MS_E}$$

where MS_C is the mean square for cortical columns and MS_E is the mean square error. We computed $\hat{\rho}$ for both monkeys individually as well as for the data spanning both monkeys. We also computed $\hat{\rho}$ for a shuffle control where null distributions for feature selectivity along depth were taken at random from all experimental data 1000 times. In computing $\hat{\rho}$ from this distribution, we gain a sense of the consistency in feature selectivity along depth if there was no specificity to column.

2.5.11 Layer Comparisons

While we observed consistency in feature preference along depth within a cortical column, we sought to investigate whether laminar differences exist with respect to the strength of selectivity. We did so by computing an index for each recording site that indicated whether the selectivity at that recording site was greater or less than the mean FSI for the cortical column in which it was recorded from. Hereafter we refer to this index as the strength of feature selectivity (SFS) where the strength of feature selectivity for recording site i in cortical column j ($SFS_{i,j,k}$) is taken as the difference between the unsigned FSI for recording site ($nFSI_{i,j,k}$) and the mean unsigned feature selectivity index for the cortical column which contains it ($nCFSI_{j,k}$):

$$SFS_{i,j,k} = nFSI_{i,j,k} - nCFSI_{j,k}, \quad where\ i = 1,\ldots,15,\ j = 1,\ldots,30,\ k = 1,2$$

Pairwise Wilcoxon signed rank tests were performed between each of the laminar compartments where all recording sites located within a laminar compartment contributed ($n = 75$ per compartment). This was done to evaluate whether there was a significant shift in SFS with depth. The same test methodology was used to evaluate the relative enhancement.

2.5.12 Bayesian Modeling

To further determine the likelihood of a columnar structure to feature representations in V4, we modeled feature selectivity as a function of attention, column, and/or depth of recording site by generating five

models and performing direct model comparisons using a Bayesian multilevel framework. Specifically, four Bayesian mixed effects models as well as a null Bayesian model were computed for comparisons. All Bayesian modeling was performed in R using the brms and performance packages and evaluated with the loo package. Model statements, prior distributions, and resultant statistics are reported in Table 2.1. All models began with a non-informative prior distribution. For model evaluation, 5000 samples were taken from the posterior distribution from each of 4 independent chains using STAN's Hamiltonian Monte Carlo algorithm via the RStan interface. For model comparison, we computed the leave-one-out cross-validation expected log predictive density (LOO-ELPD) and Bayes factor for each experimental model relative to another.

2.5.13 Fourier Transform of Feature Selectivity Index and Gamma Response

To estimate the temporal profile of feature selectivity, a feature selectivity index (FSI) for each recording site was computed at each timepoint. The timeseries of FSI was then subjected to a Fourier transform (FFT) to estimate the power of the oscillation. The FFT was performed on two epochs, one including the transient visual response (60-250 ms following search array onset) and the other omitting the transient visual response (100-250 ms following search array onset) to control for contamination in the Fourier space by the transient response. Where shown (e.g., Fig. 3), 95% confidence intervals were estimated by subsampling 80% of the data, 1000 times.

FFT was also used to estimate the power of certain frequencies (7-30 Hz) found in the high gamma response. Where applicable (e.g., Table 2.2 Fig. S5), the power datapoints used for modeling were taken as the average power in that frequency band (θ, 7-8 Hz; α, 8-15 Hz; β, 15-30 Hz). Only the response excluding the transient (100-250 ms following search array onset) were included for these analyses.

2.5.14 Microsaccade Detection

Variation in the production of microsaccades is one potential explanation for the observations. To address this possibility, we traced microsaccades using a openly available toolbox utilizing unsupervised clustering (Otero-Millan et al., 2014). Using this method we identified trials in which a microsaccade occurred between search array onset and saccadic response time as well as the times in which they occurred.

2.5.15 Proportional Odds Logistic Regression Modeling

To model the relationship between low frequencies (θ, 7-8 Hz; α, 8-15 Hz; β, 15-30 Hz) embedded in the locally generated high gamma response and behavioral response time (RT), we fit a proportional odds logistic regression (POLR), also referred to as an ordered logit model. Under this model framework, we group the outcome (RT) into four ordered categories based on their quartiles, namely 'fastest', 'faster',

'slower', and 'slowest', yielding 4 vincentized response time bins (RT_{vin}) For convenience, we refer to these quartiles as 1, 2, 3, and 4 respectively, forming the V outcome categories. The POLR model uses the log odds of the ordinal outcome RT_{vin} being less than or equal to a particular category $v = 1, \ldots, V-1$ as the outcome, which can be simplified to the logit as:

$$log\left(\frac{P(RT_{vin} \leq v)}{P(RT_{vin} > v)}\right) = logit(P(RT_{vin} \leq v))$$

The full model parameterization in this case is then:

$$logit(P(RT_{vin} \leq v)) = \omega_v + \phi_1\theta + \phi_2\alpha + \phi_3\beta + \phi_4\theta A + \phi_5\alpha A + \phi_6\beta A$$

where ω_v is the intercept estimate specific to category v, and $\phi_1, \ldots, \phi_6$ are the coefficient estimates used to describe each category comparison. A is an indicator variable for the attention condition. This model structure makes the assumption that the data meets the proportional odds assumption. More specifically, suppose that we define the proportions of the data that fall into each of these categories as v_1, v_2, v_3, and v_4 respectively. The proportional odds assumption says that the log odds of being in these categories are:

$$\begin{aligned}
logit(P(RT_{vin} \leq 1)) &= log\left(\frac{v_1}{v_2 + v_3 + v_4}\right) \\
logit(P(RT_{vin} \leq 2)) &= log\left(\frac{v_1 + v_2}{v_3 + v_4}\right) \\
logit(P(RT_{vin} \leq 3)) &= log\left(\frac{v_1 + v_2 + v_3}{v_4}\right)
\end{aligned}$$

To meet the proportional odds assumption, the difference between each row of the above array needs to be the same number (Mccullagh, 1980). Since we assigned the outcome based on the quartiles of the observed data, we know that $v_1 = v_2 = v_3 = v_4 = 0.25$. Thus, the difference between rows 1 and 2 is $log(1) - log(0.25/0.75) = 0.477$, and the difference between rows 2 and 3 is $log(3) - log(1) = 0.477$. Thus, the assumption holds in this case. To further confirm that this assumption holds, we used Brant's test (Brant, 1990), which fits a generalized ordered logistic regression that allows different regression coefficients $\phi_{1,v}, \ldots, \phi_{6,v}$ to be estimated for each group comparison. It then tests the joint hypothesis that $\phi_{1,v} = \phi_1, \ldots, \phi_{6,v} = \phi_6$ for $v = 1, 2, 3$. In both the attended and unattended model cases these tests were non-significant, further demonstrating that the proportional odds assumption is met by these data.

The regression coefficients $\phi_1, \ldots, \phi_6$ represent the change in the log odds of the outcome RT_{vin} being

less than or equal to a particular category v for every one unit increase in the corresponding covariate. By exponentiating these coefficients, we get the multiplicative proportional odds ratios, which have a similar interpretation to the odds ratios produced by a binary logistic regression.

We fit the POLR model both under a frequentist framework, with coefficients estimated using maximum likelihood, and, for the sake of consistency with other models in the manuscript, under a Bayesian framework with coefficients estimated using MCMC sampling and non-informative priors. From the frequentist model, mean and 95% confidence intervals for parameters are reported, and from the Bayesian model we report medians and 95% credible intervals.

2.5.16 Cross-frequency Coupling and Beta-Locked CSD

We computed the coupling between our low-frequency (beta) and our high-frequency responses (gamma power). To do so we first detected troughs in each of the band-limited beta signals (Dougherty et al., 2017). We triggered the time-varying gamma response from all recording contacts of the laminar probe to the time of beta troughs. More specifically, we averaged the gamma power response 100 ms preceding to 100 ms following the lowest point of the trough, the duration of more than one full beta frequency cycle. Only beta troughs during the time of the visual response leading up to the time of behavioral response, on a trial-by-trial basis, were included in this analysis. This procedure resulted in multiple beta-locked gamma response events for each trial and recording site. We averaged the trough-locked gamma response within each recording site and each trial. To account for possible differences in the magnitude of the gamma response between the layers of V4 (as exists in other visual cortical areas, (Maier et al., 2010)), we calculated the difference between the average beta-locked gamma response and the average gamma response amplitude across the epoch for each recording site (e.g., depth) in each of the recorded cortical columns. Significance of coupling was determined by computing a t-score for each time point for each recording site. To calculate this t-score, we compared our results against a randomly shuffled control, obtained by shuffling procedure where we paired the beta signal from one trial with the gamma power response from a different, randomly selected trial, and did so for all trials and sessions in the data set. All statistics for cross-frequency coupling analyses were Bonferroni-corrected for multiple comparisons. We also extracted CSD around the time of the beta troughs in the same window as the coupling analysis.

2.5.17 Multiunit Activity

Spiking activity at the level of population multiunits was used for control analyses as it reliably reflects neural population dynamics (Trautmann et al., 2019). Detection of multiunit activity was done through previously described means (Legatt et al., 1980). This method has proved useful across brain areas and

research groups (Logothetis et al., 2001; Self et al., 2013; Shapcott et al., 2016; Tovar et al., 2020; Westerberg et al., 2020a; Xing et al., 2012). Briefly, broadband neural activation was filtered between 0.3-3 kHz – the range were spiking activity predominates. The signal was then full-wave rectified and refiltered at half the original high-pass filter (0.15 kHz) thereby estimating the power of the multiunit activity. For filtering steps, we used a 4th-order Butterworth filter.

CHAPTER 3

Attentional Selection in Sensory Cortical Columns

Westerberg, J. A., Schall, J. D., Woodman, G. F., and Maier, A. (2022) Feedforward attentional selection in sensory cortex. *bioRxiv*, 2022.06.06.495037.

"An artist is someone who can hold two opposing viewpoints and still remain fully functional."

-F. Scott Fitzgerald

3.1 Summary

Salient objects stand out (pop-out) from their surroundings, grabbing our attention. Whether this phenomenon is a consequence of bottom-up sensory processing or predicated on top-down influence is debated. We show that the neural computation of attentional pop-out is embedded in the earliest cortical sensory response, seemingly devoid of feedback from higher-level areas. We measured synaptic and spiking activity across cortical columns in mid-level area V4 of monkeys searching for an attention-grabbing stimulus. Indexed by reaction times and behavioral accuracy, attention was captured at variable times. This moment of attentional capture occurred within the earliest feedforward response, both in terms of timing and spatial location. Moreover, the magnitude of the earliest sensory response predicted reaction times. Crucially, errant attentional selection and consequent behavior was associated with errant selection in sensory cortex. Together, these findings demonstrate a dominant role for feedforward activation of sensory cortex for dictating attentional priority and subsequent behavior.

3.2 Introduction

We constantly filter through our complex environment to extract information pertinent to our goals. In this effort, some objects seem to grab our attention when they differ from their surroundings. However, the mechanisms supporting this attentional prioritization through salience-based capture ("pop-out") remain elusive (Folk et al., 1992; Theeuwes, 1993; Luck et al., 2021). The behavioral and phenomenal consequences associated with pop-out are frequently described as "exogenous attention" or "stimulus-driven attention" (Chun et al., 2011), suggesting that feedforward sensory processes take a preeminent role. However, this has never been demonstrated directly. As a consequence, attentional prioritization through salience-based capture has been conflictingly theorized to arrive automatically and feedforward (Theeuwes, 1993) or via cognitive mediation (Folk et al., 1992). An intermediate hypothesis proposes that an automatic

priority signal is generated in response to attention-grabbing objects which is biased to promote behaviorally useful objects (Luck et al., 2021).

We tested the predictions of these competing theoretical views by recording across the layers of primate area V4 while macaque monkeys searched for oddball targets in arrays of objects. Area V4 is ideal for testing predictions of the competing accounts of attentional capture as it receives from, and projects to, both earlier visual cortical areas and higher-order cortex implicated in cognitive control (Roe et al., 2012; Ungerleider et al., 2008) while showing robust attentional modulation (Luck et al., 1997b) during visual search (Bichot et al., 2005; Ogawa and Komatsu, 2004). We found that the neural computations underlying attentional capture occur within the earliest synaptic and spiking activation within the feedforward-recipient layers of V4 that comprise the initial spatio-temporal volley of sensory responses. This finding is incompatible with hypotheses involving extensive feedback from higher areas. Instead, these data suggest that "exogenous" or "stimulus-driven" attentional priority largely arises from bottom-up processes in early sensory cortex.

3.3 Results

3.3.1 Mechanistic Predictions

The feedforward account of attentional capture posits that attention-grabbing objects automatically engender capture (Luck et al., 2021; Theeuwes, 1993). For this account to hold, feedforward sensory activation elicited by these objects should predict behavioral measures of attentional capture, such as reaction time. This finding would suggest the priority (Fecteau and Munoz, 2006) of attention-grabbing objects is computed rapidly and in sensory cortex. Priority indexes the utility (as opposed to a sensory feature) of a stimulus. In pop-out, salience and priority are tightly coupled, yet these two attributes are experimentally distinguishable since a non-salient stimulus can sometimes be (erroneously) chosen as having the highest utility. However, feedforward sensory activation has not yet been shown to be tightly coupled to behavioral accuracy and reaction time in attention-demanding search tasks.

In contrast, the feedback account of attentional capture puts forward that stimulus features are prioritized more or less independently of the magnitude of sensory activation. In the extreme case, this view predicts modulation of cortical activity in the absence of visual stimulation. The latter phenomenon might manifest, for example, as persistent changes to ongoing activity, or during intertrial periods (Luck et al., 1997b; Supèr et al., 2003; van der Togt et al., 2006). Top-down attentional modulations of neural activity can manifest when spatial selective attention is deployed (Armstrong and Moore, 2007; Bosman et al., 2012; Desimone and Duncan, 1995; Fries et al., 2008, 2001; Gregoriou et al., 2012; Martínez-Trujillo and Treue, 2002; Martinez-Trujillo and Treue, 2004; McAdams and Maunsell, 2000, 1999; Moore and Armstrong,

2003; Moran and Desimone, 1985; Nandy et al., 2017; Ni and Maunsell, 2019; Reynolds et al., 2000, 1999; Reynolds and Chelazzi, 2004; Reynolds and Desimone, 2003; Roelfsema et al., 1998; Treue and Martínez Trujillo, 1999; van Kerkoerle et al., 2017; Westerberg et al., 2021), but whether this feedback-driven mechanism of attentional modulation is also instantiated for pop-out selection is an open question. Finally, on the intermediate account we expect both mechanisms to emerge.

We first tested predictions of the feedforward hypothesis. If attentional capture were computed in a feedforward fashion, we expect two key pieces of evidence in V4 presented with an attention-capturing oddball (Figure 3.1A-B). For one, oddball signals should propagate through cortical pathways in a pattern specific to feedforward processing (Douglas et al., 1989; Douglas and Martin, 1991; Maier, 2013; Mitzdorf, 1985; Schroeder et al., 1998; van Kerkoerle et al., 2014). Second, the stimulus-driven response to the oddball (that is, the initial volley of activity preceding attentional feedback (Roelfsema et al., 2007)) should predict behavior. Both these tests require a neural measure of attentional capture. Here we do so by quantifying a time-resolved attentional capture (oddball selection) metric via population reliability analysis (Figure 3.1C-E). We also identified when the oddball most effectively captured attention by sorting trials by reaction time (Figure 3.1F).

3.3.2 Temporal Evidence for Feedforward Selection

We first evaluated temporal evidence via population reliability analysis. Population reliability analysis has previously been employed to derive selection times in a decision-making task (Bichot et al., 2001). Based on neurophysiological data, this analysis provides quantitative insights into both when a selection process is completed as well as the neural population size that is required for this selection to occur reliably. Briefly, population reliability analysis assumes there is a neural population representing each of the selectable objects or surfaces in a task. At each millisecond in time, we summed the activity of a randomly chosen population of multiunits to determine which item produced the largest population response. As we did not simultaneously record all 6 stimulated regions of V4, we instead employed sampling simulations. That is, we subsampled responses across trials representative of the varying stimulation conditions (i.e., oddball vs. distractor inside receptive field). The stimulus yielding the largest response in this sample is taken as the selected item. This process is then repeated, each time taking randomly selected trial-level multiunit responses to the stimulus array to determine the frequency with which the oddball is selected. Crucially, this analysis can be performed over time to determine when population-level selection for the oddball stimulus is significant relative to chance. This analysis also affords the ability to vary the number of multiunits included in the population to determine the requisite population size to detect population-level selection. We defined the oddball selection frequency computed by this analysis as our attentional capture metric. Values

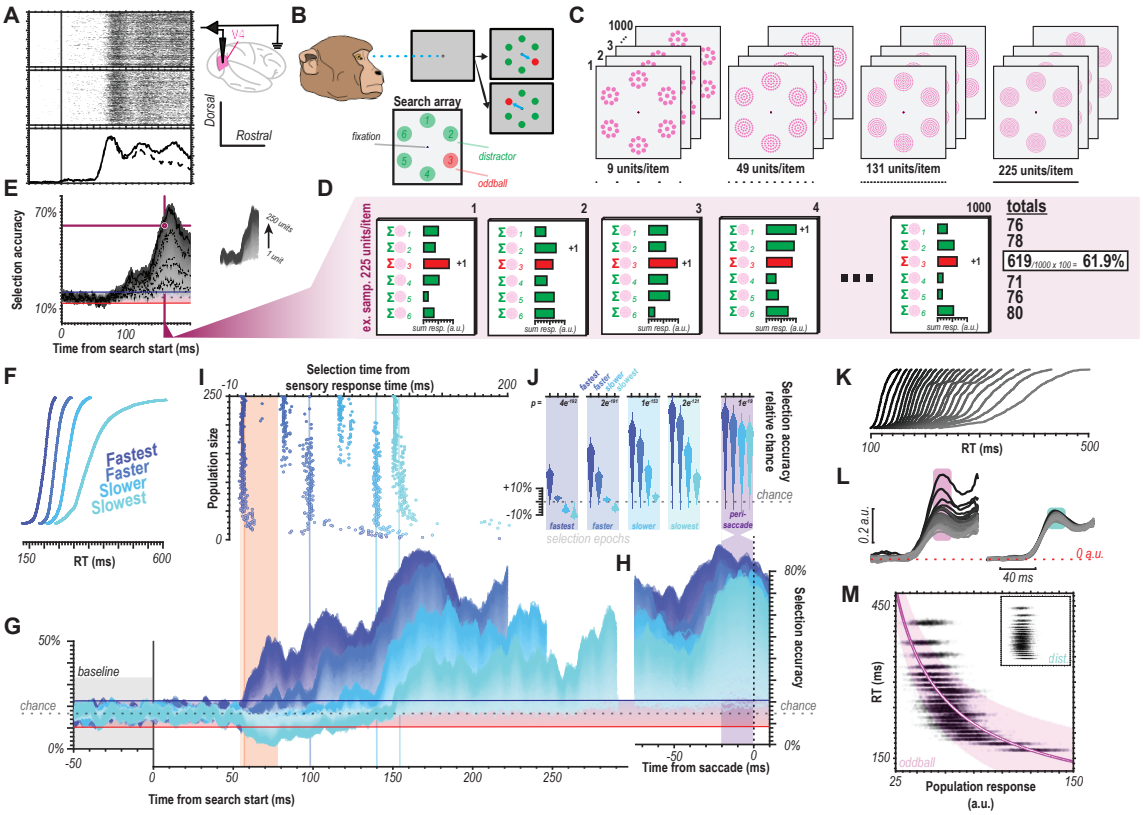

Figure 3.1: Temporal evidence for feedforward attentional selection
(Continued on the following page.)

exceeding chance threshold indicate reliable, statistically significant attentional selection of the oddball stimulus (see Methods and Figure legends for details on the statistical hypothesis tests).

To illustrate this analysis, consider an example calculation. First, we determined the frequency with which the oddball is accurately selected 130 ms after presentation of the array for a population size of 225 multiunits (Figure 3.1D-E). We assumed each of the 6 items is represented by the activity of 225 multiunits. We randomly selected 225 trial-level multiunit responses for each type of relevant stimulus. We summed those 225 multiunit responses for each item. The item with the largest summed response was tallied. We then repeated this process 1000 times using random (Monte Carlo) sampling. Of those 1000 samples, we counted the tallies for the oddball stimulus to find the frequency with which the oddball evoked the largest summed response (61.9% of the time, Figure 3.1D). That provided 1 data point on the ordinate in the selection time plots (e.g., Figure 3.1E). All other points were calculated by changing the time window (abscissa) and/or the number of multiunits (trace).

We found that oddball detection varied in concert with reaction time (Figure 3.1G-H). Moreover, significant detectable differences in population activation to oddball vs. distractor stimuli can already be

Figure 3.1: A. Rasters show 1000 randomly chosen V4 multiunit responses to an oddball or distractor stimulus, respectively. Traces at bottom show convolution of responses to oddball (solid) vs. distractor (dashed) stimuli. B. Monkeys performed 6-object oddball search. C. Visualization of population reliability analysis, with magenta circles representing multiunits comprising the response to each stimulus. D. The summed response of each of the 6 samples was computed and their maximum was defined as selection of the associated stimulus. Each sample is a random set of responses for the stimulus type (i.e., oddball or distractor). This was repeated 1000 times for each population size for each ms in time to compute an oddball selection metric (percent of time oddball had the largest response). E. Oddball selection in pop-out search for population sizes 1-250 considering all correct trials ($n = 1320282$). Values above chance window indicate oddball selection. Chance window is the variability in selection in the absence of visual stimulation computed as the 99% CI during the baseline (100 ms prestimulus). 4 dashed lines traces correspond to the 4 population sizes show in C. Crossing point of magenta lines indicate time and population size exemplified in D. F. CDF of RT organized in quartiles. G. Oddball detection for each RT quartile shown in F. Data clipped 10 ms prior to each respective median RT. Orange highlights duration of the initial transient of sensory response. Population sizes 1-250 for each bin are lightest to darkest traces. H. Oddball selection across time for each of the 4 quartiles, aligned on gaze shift to the oddball. Population sizes 1-250 for each bin represented as the lightest to darkest traces. Chance is identical to G. I. Time when each population for each bin first exceeded chance threshold in G. Color indicates each RT quartile. Orange indicates the transient of sensory response. J. 20 ms average oddball selection for each RT quartile immediately following the time where population 250 exceeded the chance window as well as the window immediately preceding RT (far right). Background indicates each selection epochs' corresponding quartile. Violin plots are relative to chance (16.67%). Upper righthand corner indicates result of ANOVA between quartiles. K. CDFs for RTs divided into 24 bins. L. Responses to oddball (left) vs. distractor (right) corresponding to 24-bin RTs. Darkest traces are fastest trials, lightest are slowest. M. Bayesian modeling with population 250. RT as a function of feedforward response (mean 58-78 ms postdisplay) to oddball, 1000 trials per bin. Inset is distractor responses on identical scale. Magenta line shows result of power function fit. White data in magenta line are median estimates for simulated trials. Cloud is 89% CI of median estimates.

observed in the earliest (50-60 ms following visual stimulation) sensory responses (Figure 3.1I). Crucially, we observed significant differences in the attentional capture metric across four successive epochs (bins) of the feedforward response (Figure 3.1J). This observation indicates that while the initial response to the oddball may not always evoke the largest population response, it entails sufficient information to predict the associated reaction time.

Next, we more finely investigated the exact relationship between population responses and reaction time (Figure 3.1K-L). No systematic differences in distractor responses were observed with reaction time; however, oddball response covaried nonlinearly with reaction time (Figure 3.1L-M). We performed Bayesian modeling to determine whether the relationship was significant, with reaction time as the dependent variable and feedforward population spiking response as the independent variable (Figure 3.1M). This analysis revealed significant predictive value in the independent variable's (i.e., feedforward oddball response) coefficient estimates (r: $M = -0.73$, $89\%CI = [-0.71, -0.74]$; $\beta : M = 4.90$, $89\%CI = [4.68, 5.15]$), explaining a large fraction of the variance ($R^2 = 0.62$).

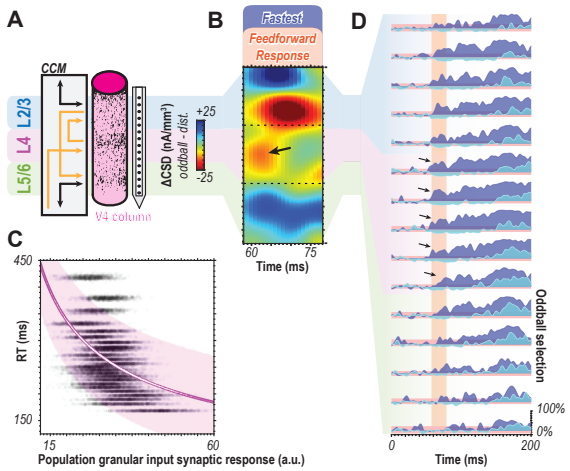

Figure 3.2: Spatial evidence for feedforward attentional selection across the canonical cortical microcircuit A. Cartoon illustrating the key laminar compartments (upper-L2/3, middle-L4, and deep-L5/6) with canonical microcircuit connectivity. Since earlier stages of sensory processing primarily project to L4 while feedback terminals innervate the layers above and below, feedforward computations should be indicated by differences in initial middle layer activation. B. Laminar current source density (CSD, indicating synaptic activation) difference between oddball and distractor for the fastest, attention-capturing trials. Window shows 50 ms at the time of feedforward activation of the cortical column. Arrow indicates difference present in L4 where the oddball evoked a greater response. C. Bayesian modeling of 24-bin data with population size 250 using synaptic currents in L4. Reaction time (RT) as a function of granular CSD magnitude (mean 58-78 ms post-display) to oddball, 1000 trials for each bin. Magenta line is the result of a power function fit. White data within magenta line are median estimates for simulated trials. Magenta cloud shows 89% credible interval of median estimates for fit. Slope indicates a negative relationship between L4 CSD magnitude to oddball stimulus and behavioral RT. D. Oddball detection by cortical depth for fastest and slowest bins relative to visual display for population size 250 using multiunit responses. Samples were localized to each depth (n=15). Arrows denote significant oddball detection in the feedforward response in the middle layer. Orange highlights initial 20 ms window of feedforward visual response.

3.3.3 Spatial Evidence for Feedforward Selection

We next evaluated spatial evidence. The canonical columnar microcircuit puts forward layer-specific activations for feedforward vs. feedback computations (Bastos et al., 2012; Douglas et al., 1989; Douglas and Martin, 1991). These patterns are robustly observed in sensory cortex (Ferro et al., 2021; Mitzdorf, 1985; Nandy et al., 2017; Pettine et al., 2019; Schroeder et al., 1998; van Kerkoerle et al., 2014, 2017; Westerberg et al., 2022b, 2021) (Figure 3.2A). Differences in granular layer (L4) synaptic activation as a function of oddball vs. distractor stimulation thus would indicate feedforward oddball signaling. Analyzing the fastest reaction time trials, we indeed observed a significant difference in synaptic activity L4 as a function of oddball vs. distractor presentations to the column's population receptive field (Figure 3.2B). This result indicates differences at the level of feedforward input into V4. We quantified this relationship using the modeling techniques used for spiking data, listed above (Figure 3.2C). We again found a significant relationship between L4 feedforward synaptic activation to the attention-grabbing oddball and reaction time

($r : M = -0.56, 89\%CI = [-0.54, -0.57]$; $\beta : M = 1.70, 89\%CI = [1.64, 1.77]$; $R^2 = 0.26$).

In further evaluating the laminar profile of oddball detection, we observed greater than chance detection during the initial response in the granular input layers for the fastest response trials (Figure 3.2D). Both findings indicate feedforward computation of attentional capture in sensory cortex. In other words, the oddball stimulus gets emphasized over other stimuli during the initial volley of synaptic activation following stimulus onset. The underlying computation thus happens either at this moment and location, prior to that, or both. If the oddball detection occurred at a previous (upstream) location of visual processing, it thus must have been derived without feedback from area V4 or other downstream areas. Also note that the initial activation of V4 input layers precedes full sensory activation of earlier areas, such as V1 and V2 (Schmolesky et al., 1998), as well as the onset of distinguishable feedback responses in these areas (van Kerkoerle et al., 2014). This context further suggests that pop-out oddball detection occurs within the first wave of stimulus-evoked spikes (VanRullen and Thorpe, 2002) rather than during reverberant processing. Summarizing these findings, we find both temporal and spatial evidence for feedforward generation of a priority signal for attentional capture.

3.3.4 Errant Selection Precedes Errant Behavior

An interesting secondary question is whether attentional capture in the feedforward response is entirely a factor of salience or if the information is truly relayed as a priority signal (Fecteau and Munoz, 2006). While priority signals have been described for frontal (Thompson et al., 2005a), parietal (Ipata et al., 2009), and temporal (Stemmann and Freiwald, 2019) cortex, there has been no strong neurophysiological evidence for sensory cortical priority signals. We thus decided to test for the presence of priority signals in sensory cortex. While incorrect behavioral responses are a small minority in pop-out search, the monkeys performed sufficient trials to yield a representative sample of error trials. We thus can determine whether the population signal in V4 reflects the salience of the stimulus (which is constant between correct and error trials) or priority (which differs between correct and error trials). Crucially, examined this process during the feedforward response period.

Two alternative hypotheses emerge from this line of reasoning. If the feedforward response reflects salience, we expect robust attentional capture for the oddball, even when a distractor was (erroneously) selected as the target. If the feedforward response computes priority, however, we expect the population response to reflect the incorrect target selection (Heitz et al., 2010; Thompson et al., 2005b). We performed population reliability analysis to distinguish between these two possibilities.

In line with the hypothesis that the feedforward sensory response represents a priority signal, V4 population responses selected (misidentified) the distractor, errantly capturing attention (Figure 3.3A).

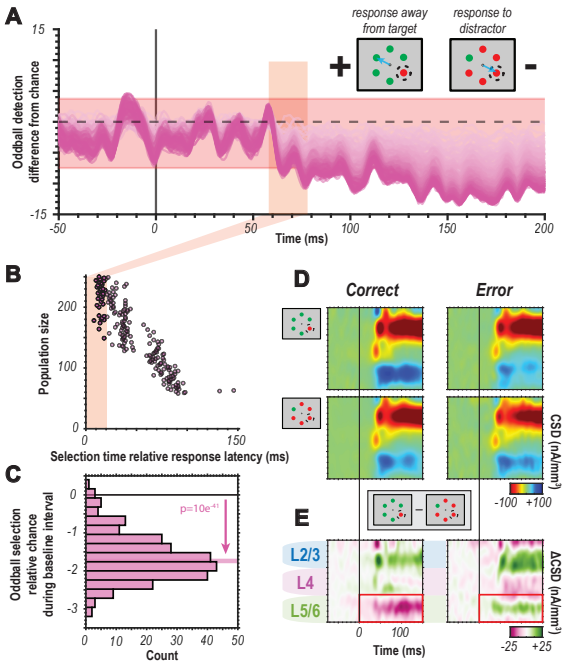

Figure 3.3: Errant selection precedes errant behavior
A. Oddball selection for population size 1-250 (light to dark magenta) on incorrectly performed trials. Negative selection accuracy values indicate selection for the distractor. Feedforward visual response time window indicated in orange. Cartoon visualization of error types in upper righthand corner. B. Selection times for prioritized distractor for each population size. Feedforward response time window highlighted in orange. C. Histogram of oddball selection during baseline period (50 ms prestimulus window). Small, but reliable bias in selection for misprioritized distractor observable before visual display (result of two sample t test indicated in plot). D. Comparison of synaptic activity for correct (left) vs. incorrect (right) trials across sessions for stimulus captured (top) vs. distractor (bottom) conditions. E. Difference in synaptic activity between captured stimulus and distractor conditions for correct (left) vs. incorrect (right) trials. Red arrows indicate notable difference in granular input sink and red box denotes observed difference in deep-layer synaptic source.

Moreover, this selection was present in the initial response (Figure 3.3B).

Somewhat unexpectedly, we also found a small but significant selection bias during the pre-display (fixation) period (Figure 3.3C). This observation suggests errant capture could be partially explained by modulated ongoing activity. In further pursuing this question, we observed that errant capture was predominantly related to changes in synaptic activity in the deep layers of cortex (Figure 3.3D-E). Deep layers in V4 have been linked to behavioral output, and the difference found here is in line with that association (Pettine et al., 2019).

3.3.5 Prestimulus Modulation of Pertinent Feature Selective Columns

After noting the relationship between baseline activity and behavior in error trials (Figure 3.3), we hypothesized that coordinated modulation of baseline activity (Figure 3.4A-B) could bias capture. Previous

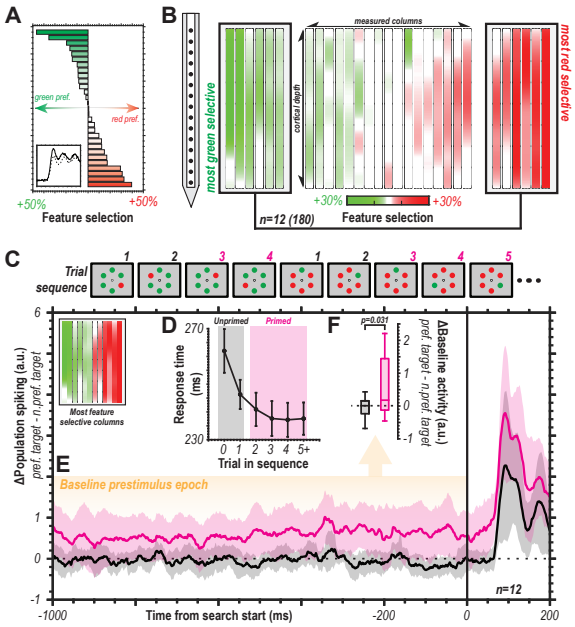

Figure 3.4: Selection history modulates ongoing activity

A. Columnar feature selectivity organized from most green-preferring to most red-preferring columns (n=29). Bar size indicates degree of feature selectivity across each column's multiunit spiking activity. Inset displays representative average red vs. green response for a red-preferring column (solid line, red response; dashed line, green response). Selectivity metric represents application of population reliability analysis at the individual multiunit level for selection of red vs. green. B. Feature selectivity along depth for each column. Six most red- and green-preferring columns highlighted for further analysis. C. Example trial sequence where target feature (red among green or vice versa) repeated before switching. This induced priming of target feature where primed (magenta) can be compared to unprimed responses (gray). D. Reaction time (medians with 95% confidence intervals) decreases with repeated search for a feature (n=29 sessions). E. Mean difference in baseline population spiking between preferred feature oddball and non-preferred feature oddball for unprimed (black) and primed (magenta) trials for feature columns (inset top-left) (n=12 columns, n=180 multiunits). Clouds are 95% confidence intervals. F. Boxplot of differences in baseline spiking for preferred feature target vs. non-preferred feature target for unprimed vs. primed trials. Central mark indicates median, and the bottom and top edges indicate the 25th and 75th percentiles. Whiskers are +/-2.7 SD. Statistic is two-sided t test.

work has implicated altered baseline activity in perceptual sensitivity to visual objects (Luck et al., 1997b; Supèr et al., 2003; van der Togt et al., 2006; van Vugt et al., 2018). We thus structured the task to induce feature priming. Specifically, we employed "priming of pop-out" to promote attentional capture of a specific feature, such as the red or green color (Figure 3.4C). Searching for the same feature (e.g., red oddball among green distractors) repeatedly results in faster reaction times (Maljkovic and Nakayama, 1994). Swapping the target feature reinitiates priming for the new feature. This effect translates across species (Westerberg and Schall, 2021) and is also observed here (Figure 3.4D). Neural correlates of attentional priming exist in frontal (Bichot and Schall, 2002) and visual cortex (Westerberg et al., 2020a); however, these findings do not explain how feature representations are promoted for capture. This latter type of attentional priming can be

thought to reflect changes in the attentional prioritization of salient features.

We tested this by first identifying color-selective feature columns in V4. Topographic organization for color exists across V4 (Conway and Tsao, 2009; Tanigawa et al., 2010; Westerberg et al., 2021) and can be observed at the cortical columnar level (Figure 3.4A-B). We measured the difference in baseline activity for the preferred vs. non-preferred feature before and after establishing behavioral relevance via priming (Figure 3.4E). We found that baseline activity was significantly higher in columns selective for a color when the color was behaviorally relevant (Figure 3.4F). Note that this difference in firing persists in the absence of visual stimulation, thereby supporting the proposition of feedback modification in the case of task repetitions (priming).

3.3.6 Feedforward Selection Does Not Require Priming

With the understanding that feature-selective cortical columns can be modulated to promote their responses for attentional selection, we sought to determine whether feedforward selection was only present under priming conditions. To test this, we reduced the data to trials immediately following a switch in the priming sequences (e.g., the trial when the task switched from red among green to green among red). In these trials, the search target is not primed (and may in fact be negatively primed). We then repeated the Bayesian modeling of reaction time as predicted by oddball multiunit responses for these unprimed trials. The procedure was identical to that described in Figure 3.1. We found significant predictive value in the independent variable's coefficient estimates ($r : M = -0.45$, $89\%CI = [-0.43, -0.48]$; $\beta : M = 1.73$, $89\%CI = [1.64, 1.86]$) explaining a sizeable fraction of the variance ($R^2 = 0.18$). This finding indicates that even when feedback is putatively promoting the feature representations associated with the distractors, the predictive relationship between oddball feedforward responses and reaction times is preserved. Thus, even though presentation of an oddball array leads to modulating feedback following task completion, this feedback cannot sufficiently explain the feedforward selection we observed. In other words, feedforward attentional selection during pop-out is not predicated on prior feedback.

3.4 Discussion

We found that the magnitude of neuronal population responses in sensory cortex to an attention-grabbing stimulus is predictive of reaction time and accuracy during attentional capture. Crucially, this relationship emerged in the earliest parts of the stimulus-driven response propagating feedforward. Moreover, oddball detection was observed in the initial current sink that marks the synaptic activity propagating through the granular input layer of sensory cortex. Remarkably, feature columns were tonically modulated by repeated task demands, adjusting ongoing activity to promote attentional capture for consistently pertinent features.

In line with this notion, errantly biased activation during the pre-stimulus epoch was associated with errant behavior. These findings demonstrate an unexpectedly dominant role for sensory cortex in dictating attentional priority. From a theoretical perspective, these observations resolve a long-standing debate on attentional capture (Folk et al., 1992; Theeuwes, 1993; Luck et al., 2021). Specifically, we find that a priority signal is automatically generated in a feedforward fashion. That signal is then used for tonic modulation via feedback to promote the detection of similar objects in subsequent searches. In other words, our attention is automatically captured by salient features. The speed of our behavior in response to these objects is dictated by the variability in their engendered sensory response. However, behavioral goals and historical context can influence which features we are more sensitive to, effectively promoting repeated attentional capture for objects comprised of those features.

In evaluating population codes for the representation of sensory information, it becomes important to consider the size of a neural population that allows for certain computations to be performed (Averbeck et al., 2006). For example, in behavioral tasks, an observation requiring an inordinately large population of neurons, could be inconsequential if that information cannot be relayed downstream for the execution of behavior. In our study, gaze must be redirected for our behavioral measure (reaction time) to occur. This process likely engages areas like the frontal eye fields (FEF) (Schall, 2004, 2015), which receive sensory information from V4 (Anderson et al., 2011; Gregoriou et al., 2012; Ninomiya et al., 2012; Schall et al., 1995; Stanton et al., 1995; Ungerleider et al., 2008; Zhou and Desimone, 2011). Therefore, the population representation of the oddball stimulus must be relayed effectively from populations of V4 to FEF neurons through biologically plausible pathways. With this in mind, it is worth noting that reliable oddball detection at the population level can be observed in sets of 20 or fewer multiunits during the feedforward period (Figure 3.1).

It is also interesting to consider population size as a source for the variability of reaction time that is not explained by the modeling. The different percentages of time the oddball is selected between traces suggest that the exact population size does impact the magnitude of detectability, at least in this population reliability metric. Therefore, it could be hypothesized that some variability observed in the behavioral response as a function of behavioral capture might be due to the size of the population propagating the signal.

While we have found that modification of the priority signal exists tonically, is there an antecedent? That is, what instigates the persistent change in activity found in the behaviorally relevant feature columns? One hypothesis is that the initial presentation of the attention-grabbing oddball leaves sensory cortex in an altered state, more sensitive to the established pertinent feature (Westerberg and Schall, 2021). Adaptation in sensory cortex can have potent effects (Albrecht et al., 1984; Carandini, 2000; Clifford et al., 2007; Dragoi et al., 2000; Kohn, 2007; Kohn and Movshon, 2004), and is implicated in changing response characteristics

at the level of cortical columns (Hansen and Dragoi, 2011; Westerberg et al., 2019). An alternative view might be that the frontal cortex regulates feature-based attentional modulation in the visual cortex; a candidate area (VPA) has been identified that could serve as a source (Bichot et al., 2015, 2019). Either hypothesis does not change the interpretation that the sensory cortex automatically computes attentional capture; however, resolving between them would provide insight into the minimum required neural circuitry to modify the priority signal.

3.5 Methods

3.5.1 Animal Care

In this study (Westerberg et al., 2022a), two male macaque monkeys (Macaca radiata; monkey Ca, He) participated in this study. All procedures were in accordance with the National Institutes of Health Guidelines and the Association for Assessment and Accreditation of Laboratory Animal Care International's Guide for the Care and Use of Laboratory Animals, and approved by the Vanderbilt Institutional Animal Care and Use Committee in accordance with United States Department of Agriculture and United States Public Health Service policies. Animals were pair-housed. Animals were on a 12-hour light-dark cycle and all experimental procedures were conducted in the daytime. Each monkey received nutrient-rich, primate-specific food pellets twice a day. Fresh produce and other forms of environmental enrichment were given at least five times a week.

3.5.2 Surgery

All surgical procedures were performed under aseptic conditions. Anesthesia was conducted with animals under N_2O/O_2, isoflurane (1-5%) anesthesia mixture. Vital signs were monitored continuously. Expired PCO_2 was maintained at 4%. Postoperative antibiotics and analgesics were administered while animals remained under close observation by veterinarians and staff. Monkeys were implanted with a custom-design head post and MR-compatible recording chamber using ceramic screws and biocompatible acrylic. A craniotomy over V4 was opened concurrent with the recording chamber.

3.5.3 Magnetic Resonance Imaging

MR images for chamber localization and guiding of linear electrode penetrations perpendicular to the cortical surface were taken from anesthetized animals placed inside a 3T MRI scanner (Philips). T1-weighted 3-dimensional MPRAGE scans were acquired with a 32-channel head coil equipped for SENSE imaging. Images were acquired using a 0.5 mm isotropic voxel resolution with the following parameters: repetition time 5 s, echo time 2.5 ms, and flip angle 7°.

3.5.4 Identification of V4

Recordings took place on the convexity of the prelunate gyrus in approximately the dorsolateral, rostral aspect of the V4 complex, where receptive fields are located at about 2–10 degrees of visual angle (dva) eccentricity in the lower contralateral visual hemifield (Gattass et al., 1988). Laminar recordings took place at locations where the array could be positioned orthogonal to the cortical surface, as verified by MRI and neurophysiological criteria (i.e., overlapping receptive fields). Recording sites were also confirmed via histological staining by dipping the electrode arrays in diiodine prior to the final recordings in monkey He (Westerberg et al., 2020a).

3.5.5 Task Design: Pop-out Search

Monkeys viewed arrays of stimuli presented on a CRT monitor with 60 Hz refresh rate, at 57 cm distance. Stimulus presentations and task timing was controlled using TEMPO (Reflective Computing). Visual presentations were monitored with a photodiode positioned on the CRT monitor so that electrophysiological signals could be reliably aligned offline. Red (CIE coordinates: $x = 0.648$, $y = 0.331$) and green circles (CIE coordinates: $x = 0.321$, $y = 0.598$) were used as stimuli, rendered isoluminant to a human observer at 2.8 cd/m^2 on a uniform gray background. As we are limited to two colors and cannot account for potential differences in perceived brightness between macaques, we qualify our two stimuli as distinct 'features' at the intersection of color and luminance information. Nonetheless, we report the colors used in this study for the ideal human observer. Cone excitation was computed from the CIE coordinates and luminance (Cole and Hine, 1992). The following cone excitations were measured for red: $\varepsilon_L = 2.37$, $\varepsilon_M = 0.43$, $\varepsilon_S = 0.0014$; green: $\varepsilon_L = 1.74$, $\varepsilon_M = 1.06$, $\varepsilon_S = 0.0030$; and the background: $\varepsilon_L = 1.86$, $\varepsilon_M = 0.94$, $\varepsilon_S = 0.023$. Cone contrasts for red stimulus were found to be: $C_L = 0.27$, $C_M = -0.54$, $C_S = -0.94$; and the green stimulus: $C_L = -0.06$, $C_M = 0.13$, $C_S = -0.87$.

Trials were initiated when monkeys fixated within 0.5 dva of a small, white fixation dot (diameter of 0.3 dva). The time between fixation acquisition and array presentation varied between 750–1250 ms, taken from a nonaging foreperiod function to eliminate any potential effect of stimulus expectation (Näätänen, 1970, 1971; Nickerson and Burnham, 1969). Following the fixation period, the stimulus array consisting of 6 items was presented. Stimuli were scaled with eccentricity at 0.3 dva per 1 dva eccentricity so that they were smaller than the estimated V4 receptive field size (0.84 dva per 1 dva eccentricity (Freeman and Simoncelli, 2011)). The polar angle positioning of the items relative to fixation varied from session to session so that one item of the stimulus array was positioned at the center of the population receptive field under study. Items were spaced such that only one item was in the V4 receptive field, with uniform spacing in polar angle and equal eccentricity.

Monkeys engaged in a search task while viewing the stimulus array. One item in the array was a different feature (red or green, respectively) from the others. Position of the oddball on each trial was randomly chosen with equal probability for any of the positions (16.6%). Monkeys earned fluid reward for shifting gaze directly to the oddball item within 1000 ms of array presentation and maintaining fixation within a 2–5 dva window around the oddball for 500 ms. Eye movements were monitored continuously at 1 kHz using an infrared corneal reflection system (SR Research). If the monkey failed to look at the oddball, no reward was given, and a 1-5 s timeout ensued. Trials were organized into blocks such that the animal searched for the same target feature for 5-15 repetitions. Target feature remained the same, but target location varied randomly. Completing the block resulted in the target and distractor features swapping.

3.5.6 Neurophysiology

Laminar extracellular voltages were acquired at 24.4 kHz resolution using a 128-channel PZ5 Neurodigitizer and RZ2 Bioamp processor (Tucker-Davis). Raw signals were output between 0.1 Hz and 12 kHz. Data were collected from 2 monkeys (left hemisphere, monkey Ca; right hemisphere, He) across 70 recording sessions ($n = 31$, monkey Ca; $n = 39$, He) using 32 channel linear microelectrode arrays with 0.1 mm interelectrode spacing (Plexon). Each recording session, electrode arrays were introduced into the prelunate gyrus through the intact dura mater using a custom micromanipulator (Narishige). Electrode arrays were positioned so they spanned all layers of V4 and had a subset of electrodes positioned outside of cortex. 29 ($n = 20$, monkey Ca; $n = 9$, He) of 70 sessions were included in the final analysis. The remaining 41 sessions were found to either not have a discernable CSD profile for laminar alignment, not be orthogonal to the cortical surface, or not have enough priming blocks for the feedback mechanism analysis and were thus removed from analysis.

3.5.7 Receptive Field Mapping

To determine the orientation and eccentricity of the visual receptive fields, monkeys performed a receptive field mapping task prior to the main task. Monkeys fixated for 400–7000 ms while a series of 1–7 stimuli were presented that spanned the visual field contralateral to the recording chamber. Stimuli were 5 high-contrast concentric white and black circles that scaled in size with eccentricity (0.3 dva per 1 dva eccentricity). In all recording sessions, stimuli could appear in a random location. These random locations spanned the lower visual quadrant contralateral to the recording chamber. Location spacing was in 5° angular increments relative to fixation and in eccentricities ranging from 2 dva to 10 dva in 1 dva increments. Each stimulus was presented for 200–500 ms with an interstimulus interval of 200–500 ms. If the animal maintained fixation for the duration of the stimulus presentation sequence, they received a juice

reward. During this receptive field mapping task, multiunit activity, gamma power (30-90 Hz), and evoked local field potentials (LFPs, 1–100 Hz) were measured across all recording sites. Online, we measured the response across visual space for each recording site. Recordings proceeded to the feature search task if there was qualitative homogeneity of receptive fields along depth. Receptive field overlap for these data have been reported previously (Westerberg et al., 2021). The receptive field center was chosen to be the stimulus location that evoked the largest response along the depth of recording sites. Following receptive field identification, the stimulus array in the feature search task was then oriented so that its eccentricity coincided with the location of the receptive field (eccentricity: 3–10 dva) and a single array item was placed at the center of the receptive field (size: 0.9–3 dva).

3.5.8 Identification of Cortical Laminae

Positions of the individual recording sites relative to the layers of V4 were determined using current source density (CSD) analysis. CSD reflects local synaptic currents (net depolarization) resulting from excitatory and inhibitory postsynaptic potentials (Mitzdorf, 1985). CSD was computed from the raw neurophysiological signal by taking the second spatial derivative along the electrode contacts (Maier et al., 2010, 2011; Nicholson and Freeman, 1975; Schroeder et al., 1998; Westerberg et al., 2019). CSD activation following presentation of a visual stimulus reliably produces a specific pattern of activation which can be observed in primate visual cortex (Maier et al., 2010; Schroeder et al., 1998), including V4 (Bollimunta et al., 2008; Givre et al., 1994; Nandy et al., 2017; Westerberg et al., 2022b, 2021). Specifically, current sinks following visual stimulation first appear in the granular input layers of cortex, and then ascend and descend to the extragranular compartments. To compute the CSD from the LFP, we used previously described procedure (Nicholson and Freeman, 1975):

$$CSD_{t,d} = -\sigma \left(\frac{x_{t,d-z} + x_{t,d+z} - 2x_{t,d}}{z^2} \right)$$

where the CSD at timepoint t and at cortical depth d is the sum of voltages x at electrodes immediately above and below (z is the interelectrode distance) minus 2 times the voltage at d divided by the interelectrode-distance-squared. That computation yields the voltage local to d. To transform the voltage to current, we multiplied that by $-\sigma$, where σ is a previously reported estimate of the conductivity of cortex (Logothetis et al., 2007). For each recording session, we computed the CSD and identified the initial granular layer (L4) input sink following visual stimulation. Sessions were aligned using the bottom of the initial feedforward input sink as a functional marker. We defined the size of individual laminar compartments uniformly relative to space. Throughout, ‘middle’ refers to the estimate of the granular input

layer 4 (0.5 mm space above the CSD initial sink functional marker), 'upper' refers to the estimate of supragranular layers 2 and 3 (0.5 mm space above the L4 compartment), and 'lower' refers to the estimate of infragranular layers 5 and 6 (0.5 mm space below the L4 compartment).

3.5.9 Population Spiking

Spiking activity at the level of multiunits was used for control analyses as it reliably reflects neural population dynamics (Trautmann et al., 2019). Detection of multiunit activity was achieved through previously described means (Legatt et al., 1980). This method has proved useful across brain areas and research groups (Logothetis et al., 2001; Teeuwen et al., 2021; Tovar et al., 2020; Westerberg et al., 2020a; Supèr and Roelfsema, 2005; Shapcott et al., 2016; Self et al., 2013). Briefly, broadband neural activation was filtered between 0.5-5 kHz, the predominate range of spiking activity. The signal was then full-wave rectified and filtered again at half the original high-pass filter (0.25 kHz) thereby estimating the power of the multiunit activity. For filtering, we used a 4th-order Butterworth filter. Spiking responses were baseline corrected by subtracting the average activity in the 100 ms window preceding visual display onset at the trial level. This baseline correction was not performed for the feedback analysis.

3.5.10 Feedforward Sensory Response Window

Determining the implications of the feedforward response to attentional capture required accurate identification of the timing of said feedforward response. Here, the window of the feedforward response is defined as the 20 ms following the time at which the mean population spiking response first reaches 50% of its maximum response. This definition yielded a response latency of 58 ms (mean=58, 95% confidence interval=[57, 59]) with the window being defined as 58-78 ms following visual display onset.

3.5.11 Sorting Responses by Reaction Time

Several analyses were conditioned on sorting trials by behavioral reaction time. Through this procedure, trials were rank ordered by reaction time from fastest to slowest on a session-by-session basis. For example, if session n contained 2000 trials, each trial was ranked from 1 to 2000 by reaction time, and then normalized as a percentile. This ranking was completed individually for each session so that individual sessions could be sampled equally for each binned condition. Two binning procedures were performed, one coarse (4 bins) and one fine (25 bins). For the fine-binning-conditioned analyses, the slowest bin (slowest 2% of trials) was omitted from analysis as outliers in otherwise efficient, pop-out search.

3.5.12 Population Reliability Analysis

Population reliability analysis was used to establish whether and when populations of V4 neurons selected an attention-grabbing oddball (Bichot et al., 2001). Crucially, this analysis estimates when selection occurs in time as well as how many neural units are required for this selection to occur reliably. This analysis is performed by simulating trials using data from the entire population of multiunit responses across all sessions. Each simulated trial is defined as an event where a behavioral response must be made to a stimulus with multiple alternatives present. For this computation, each alternative is represented by the response of a distinct neural population with a predetermined size. We varied the population size between 1 and 250. In this study, the search task contains six alternatives, thus we estimated a population response for each of the six stimuli. The population response is defined as the sum of responses of each of the sampled responses – where each response is an empirically measured trial-level multiunit response to the stimulus germane to the alternative's response that is being estimated. Therefore, we chose five distinct, randomly sampled population responses to distractor 'alternatives' and one to an oddball 'alternative'. For each point in time within each simulated trial, we measured which alternative provoked the highest response magnitude. This selection metric represents our estimated priority signal. By simulating more and more trials (n=1000 for each computation in this study), we computed the percent of time each alternative is selected at each timepoint during a simulated trial. Here, we were specifically interested in the percent of time the oddball was selected by this measure. We defined this percentage as the selection accuracy in identifying the behaviorally relevant oddball. For six objects, chance (selection invariability between population responses) was calculated to be 16.67%. We computed empirical selection bounds to estimate when the selection accuracy exceeded chance by measuring the variability in selection accuracy for all 1–250-unit populations during the baseline, prestimulus display, epoch and setting the thresholds to the 99% confidence interval.

3.5.13 Bayesian Modeling

Bayesian modeling was performed using Stan through the RStan interface. Sampling was done using Markov chain Monte Carlo (MCMC) methods with the following parameters: chains, 4; warmup samples, 2000; total samples, 5000; thinning, 2. A power function fit was assessed. The outcome RT_i (reaction time on simulated trial i) can be modeled as:

$$RT_i|\alpha,\beta,r,SPK_i \sim N(\phi_i,\sigma_e)$$

where:

$$\phi_i = \beta * SPK_i^r + \alpha$$

Reaction time (RT) for simulated trial i is modeled as the population multiunit spiking activity (SPK) for simulated trial i with coefficient β. r is the exponent for the power function fit. Population spiking activity was defined as the sum of activity across the population. In supplementary analyses we also explored the same relationship to reaction time, but with the magnitude of the granular input sink taken as the average of 5 recording channels immediately above the L4/5 boundary for each trial. We set minimally informative priors for the power function fit as: $\alpha \sim LogNormal(0, 0.5)$, $\beta \sim LogNormal(1, 0.5)$, $r \sim Gamma(1, 3)$, $\sigma_e \sim Gamma(0.5, 5)$.

From this modeling, we computed median estimates for each simulated trial as well as the associated 89% credible intervals. We also computed reaction time estimates for the range of population spiking responses observed using the median estimate of each coefficient. In evaluating the posterior distributions, we were interested in the median (M) estimates for the coefficients β and r as they reflect the predictive utility of the independent variable (population spiking response). In particular, non-zero β and r different than 1 indicate significant utility provided the 89% credible intervals (89% CI) for those estimates do not include their respective non-predictive values.

3.5.14 Feature Selectivity

Feature (red vs. green) selectivity was derived from population spiking observed along recording sites. Responses were taken when a red stimulus was presented to the receptive field of the cortical column and when a green stimulus was present in the receptive field. We employed a two-alternative version of the population reliability analysis to estimate the selectivity of each multiunit for red vs. green. For each multiunit we took 100 red and 100 green stimulus presentations (effectively population size 100) 1000 times (bootstrapped simulated trials) for the reliability analysis. Specifically, we took the average response 60-160 ms following visual display. This yielded a selection accuracy metric for red vs. green where deviation from 50% chance indicated preference for one color or the other. Presence of feature selective columns in this dataset was confirmed in previous reports (Westerberg et al., 2022b, 2021).

CHAPTER 4

Relating Attention Signals Across Measurement Scales

Westerberg, J. A., Schall, M. S., Maier, A., Woodman, G. F., and Schall, J. D. (2022). Laminar microcircuitry of visual cortex producing attention-associated electric fields. *eLife* 11:e72139.

"I like Hollywood. I just like Minneapolis a little bit better."

- Prince

4.1 Summary

Cognitive operations are widely studied by measuring electric fields through EEG and ECoG. However, despite their widespread use, the neural circuitry giving rise to these signals remains unknown because the functional architecture of cortical columns producing attention-associated electric fields has not been explored. Here we detail the laminar cortical circuitry underlying an attention-associated electric field measured over posterior regions of the brain in humans and monkeys. First, we identified visual cortical area V4 as one plausible contributor to this attention-associated electric field through inverse modeling of cranial EEG in macaque monkeys performing a visual attention task. Next, we performed laminar neurophysiological recordings on the prelunate gyrus and identified the electric-field-producing dipoles as synaptic activity in distinct cortical layers of area V4. Specifically, activation in the extragranular layers of cortex resulted in the generation of the attention-associated dipole. Feature selectivity of a given cortical column determined the overall contribution to this electric field. Columns selective for the attended feature contributed more to the electric field than columns selective for a different feature. Lastly, the laminar profile of synaptic activity generated by V4 was sufficient to produce an attention-associated signal measurable outside of the column. These findings suggest that the top-down recipient cortical layers produce an attention-associated electric field that can be measured extracortically with the relative contribution of each column depending upon the underlying functional architecture.

4.2 Introduction

Research into extracortical electric fields provides fundamental insights into the mechanisms of human perception, cognition, and intention. For instance, event-related potential (ERP) components like the N2pc (Luck and Hillyard, 1994; Eimer, 1996; Woodman and Luck, 1999) and Pd (Hickey et al., 2009) reliably index selective attention in humans and monkeys, alike. However, the interpretation of these extracortical

measures of attention is severely limited by uncertainty about the exact neural processes that generate these signals (Nunez et al., 2006). Understanding what brain processes an electric field indicates requires knowing how it is generated (e.g., (Cohen, 2017)). One avenue to localize neural generators of electric fields is through inverse source localization (Michel et al., 2004; Grech et al., 2008). However, the results are indefinite and cannot offer conclusive answers. Moreover, these methods do not allow for the probing of the underlying neural circuitry. For example, most EEG signals are hypothesized to be generated by interlaminar interactions in cortical columns (Nunez et al., 2006). Columnar microcircuits are ubiquitous across the brain (Douglas et al., 1989; Douglas and Martin, 1991), having a well-defined anatomical structure (Mountcastle, 1997; Kaas, 2012) and consistent physiological activation pattern ((Bastos et al., 2012) but see (Godlove et al., 2014)). The canonical cortical microcircuit offers a framework in which to interpret columnar dynamics in sensory or cognitive tasks, yet the relationship between this functional architecture and electric fields related to cognition commonly measured in humans is unexplored.

Electric fields measured at the surface of the brain (ECoG) and scalp (EEG) are theorized to be generated by dipoles in cortex. However, measuring current dipoles requires sampling electrical potentials across all the layers of the cerebral cortex. Such laminar neurophysiological measurements are rare and unsystematic in humans. Work in rodents has uncovered intriguing insights into cortical laminar microcircuits underlying evoked EEG signals, but all of these were limited to sensory responses (Jellema et al., 2004; Næss et al., 2021; Bruyns-Haylett et al., 2017). Fortunately, macaque monkeys produce homologues of the attention-associated EEG signals (N2pc: (Woodman et al., 2007; Cohen et al., 2009; Purcell et al., 2013); Pd: (Cosman et al., 2018)). Laminar neurophysiological measurements (Schroeder et al., 1998; Maier et al., 2010; Buffalo et al., 2011; Hansen and Dragoi, 2011; Self et al., 2013; Godlove et al., 2014; Engel et al., 2016; Klein et al., 2016; Hembrook-Short et al., 2017; Nandy et al., 2017; Trautmann et al., 2019; Westerberg et al., 2019; Tovar et al., 2020; Ferro et al., 2021) and EEG (Woodman et al., 2007; Sandhaeger et al., 2019; Schmid et al., 2006) are well established in macaques. However, despite many studies linking intra- and extracortical signals (Schroeder et al., 1992; Whittingstall and Logothetis, 2009; Musall et al., 2014; Snyder and Smith, 2015), to date, little is known about the laminar origins of ERPs in primates.

Here we show that visual cortex generates dipoles through layer-specific transsynaptic currents that give rise to electric fields that track the deployment of selective attention. These dipoles were generated by the extragranular compartments of cortex, indicating these cognitive operations likely arise from top-down interactions. Moreover, functional architecture – in the form of feature columns – was associated with the relative contribution of individual, local cortical columns to the global electric field. These results are the first to our knowledge to describe laminar specificity in synaptic activations contributing to the generation of

electric fields associated with cognitive processing.

4.3 Results

4.3.1 Attention Task

To investigate extracortical manifestations of attention-associated electric fields, we trained macaque monkeys to perform a visual search task (Figure 4.1A). Three macaque monkeys (designated Ca, He, and Z) performed visual search for an oddball color target (red or green), presented within an array of 5 or 7 uniform distractors (green or red) (N sessions for each monkey: Ca 21, He 9, Z 18). A fourth monkey (P) performed visual search for an oddball shape (T or L) presented within an array of up to 7 uniform distractors (L or T) (N sessions: monkey P, 22). Each animal performed well above chance [chance level for monkeys Ca, He: 16.6%; P, Z: 12.5%] (behavioral accuracy in color search: Ca 88%, He 81%, Z 85%, shape search monkey P 66%). We sampled cortical neural signals during the color pop-out search to be certain of which item received the benefit of attention in the array. We used the more difficult search data to determine the generality of our findings. Two different recording types were used, necessitating four monkeys total.

4.3.2 Inverse Modeling of Attention-associated Extracortical Electric Fields Points to Visual Cortex

Once animals could perform visual search, we implanted an array of electrodes approximating the human 10-20 system in monkeys P and Z (Figure 4.1A). Using these electrodes, we observed extracortical electric dynamics in both monkeys. An index of attention known as the N2pc manifests during visual search. The N2pc electric field indexes attention allocation in this task. The magnitude of the N2pc was largest over occipital sites (Figure 4.1B, Figure 4.2A), consistent with previous reports in humans and macaques (Luck and Hillyard, 1994; Eimer, 1996; Woodman and Luck, 1999; Hopf et al., 2000; Woodman et al., 2007; Cohen et al., 2009; Purcell et al., 2013). We used sLORETA inverse modeling for source localization. Previous source estimates for the N2pc identified the human homologue of V4 (Luck and Hillyard, 1990, 1994; Hopf et al., 2000). These findings are consistent with numerous reports that areas in mid-level visual cortex in monkeys produce robust attention signals (Moran and Desimone, 1985; Luck et al., 1997a; McAdams and Maunsell, 1999; Reynolds et al., 1999; Fries et al., 2001; Roe et al., 2012) across cortical layers (Engel et al., 2016; Nandy et al., 2017). Consistent with these earlier studies, the inverse model showed that current sources include V4 on the prelunate gyrus (Figure 4.1C, Figure 4.1B). However, the modeled current sources also included other cortical regions, as is common for inverse solutions. Notably, the inverse solution identifies V1 to be about as strong as V4 in contributing to the N2pc, which is unlikely given current knowledge on attentional modulation for each area (Motter, 1993; Luck et al., 1997a; Kastner et al., 1999; Buffalo et al., 2010). Given the primary feature used in the search task was color, we

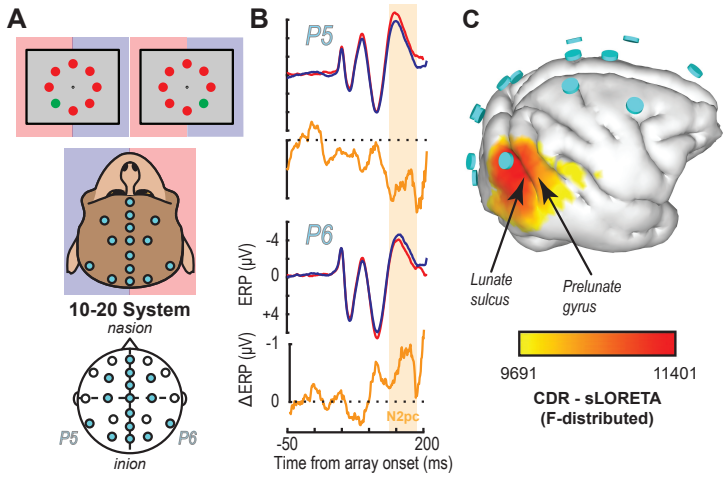

Figure 4.1: EEG traces and inverse source localization for the N2pc index of attention in monkeys A. EEG was recorded from electrodes arranged according to the 10–20 system in monkeys performing visual search by shifting gaze to a colored oddball stimulus (monitor diagrams show two example arrays). Blue and red shading highlights mapping between visual hemifield and cerebral hemisphere. B. Trial-averaged P5 and P6 EEG traces from monkey Z following presentation of search arrays with the target in either the right (blue) or left (red) visual hemifield as well as the difference (orange). The voltage difference between the target in the left versus right hemifields reveals the N2pc 150 ms after array presentation. The N2pc was significant (dependent samples t test between polarizations averaged between 125 and 250 ms after array presentation ($t(35) = 2.42$, $p = 0.02$)). C. Inverse solution of current distribution consistent with difference in voltage distribution during the N2pc (113–182 ms) when the target was in the left hemifield versus right hemifield using sLORETA. Current density is displayed over the three-dimensional (3D) boundary element model derived from a magnetic resonance scan of monkey Z. Data was clipped below the 85% maximum value for display purposes. Cyan disks indicate EEG electrode positions. Current density is concentrated beneath electrode P6 caudal to the lunate sulcus and in area V4 on the prelunate gyrus. Results are reproduced for a second monkey in Figure 4.2

investigated the laminar profile of attention-associated electric field generation in V4 where color is better represented (Roe et al., 2012).

4.3.3 V4's Laminar Microcircuit Produces Dipoles That Predict the Attention-associated Electric Field

Guided by magnetic resonance imaging, linear multielectrode arrays (LMAs) were inserted into area V4 of monkeys Ca and He. LMAs were placed perpendicular to the cortical surface, spanning supragranular (L2/3), granular (L4), and infragranular (L5/6) cortical layers (Figure 4.3). We confirmed that attentional modulation of spiking activity could be observed during pop-out search performance consistent with previous reports (Westerberg et al., 2020a). Moreover, the laminar profile of attentional modulation matched that of attentional modulation in a different task with spiking activity in the middle layers being the most highly enhanced with attention (Figure 4.4) (Nandy et al., 2017). Critically, while attentional modulation is present in the laminar data prior to the emergence of extracortical attention-associated fields such as the

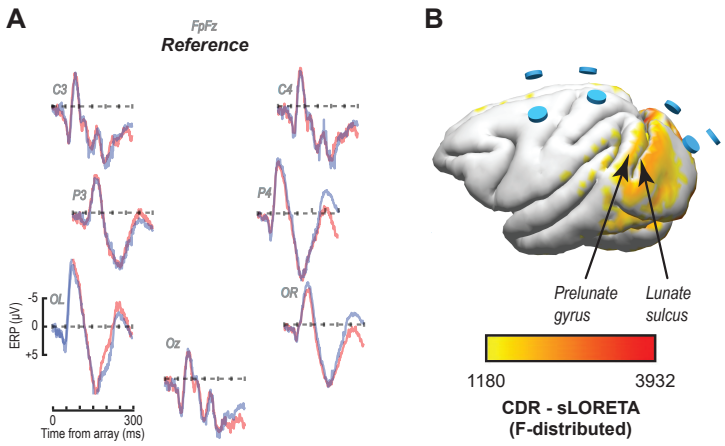

Figure 4.2: N2pc distribution of monkey P (10–20 EEG recordings)
A. EEG traces for right (blue) and left (red) visual hemifield target presentations. Organization of traces reflects electrode positions. Scale is consistent across traces and is indicated by OL. N2pc was found to be significant through an ANOVA measured as the interaction between posterior electrode sites, the target position in the array, and the set size sites (sites OR and OL, $F(2,42) = 8.39$, $p < 0.001$). B. Inverse solution using sLORETA for N2pc (difference function mean 190–300 ms following array onset) during a right visual hemifield target presentation displayed over the three-dimensional (3D) render of MR scan for monkey P. Data clipped below 30% maximum value. Cyan cylinders indicate EEG electrode positions.

N2pc, that cross-laminar modulation persists through this interval.

Simultaneous with LMA recording, an extracortical electric signal was recorded immediately above V4 – critically the recording took place outside of the cortical column itself. Current source density (CSD) was derived from the local field potentials (LFPs) sampled across V4 layers. To relate the extracortical signal (Figure 4.5A) to synaptic currents estimated as CSD (Figure 4.5B-D), we employed information theory to capture multivariate factors and nonlinearities between signals (Shannon, 1948; Cover and Thomas, 2012). Importantly, information theory analyses are model independent (Timme and Lapish, 2018). Information theory thus is superior to standard linear models since these models cannot capture all potential relationships between signals. The relationship between the extracortical signal and CSD were assessed in four distinct steps, as illustrated by a representative session (Figure 4.5E-F, Figure 4.6). We use the interval of the N2pc to determine whether laminar circuitry in V4 can contribute to the attention-associated electric fields. This interval occurred before the median response times for each monkey contributing laminar V4 data ([median ± standard deviation]: monkey Ca 227±49 ms, He 225±44 ms).

First, we employed Monte Carlo simulations of the mutual information analysis to verify that the extracortical signal exhibited significantly enhanced information about target position during the time window of the N2pc. Second, we measured target information across the layers of V4 during the N2pc interval. This analysis revealed enhanced information in L2/3 and L5/6 but not in L4. Third, we computed

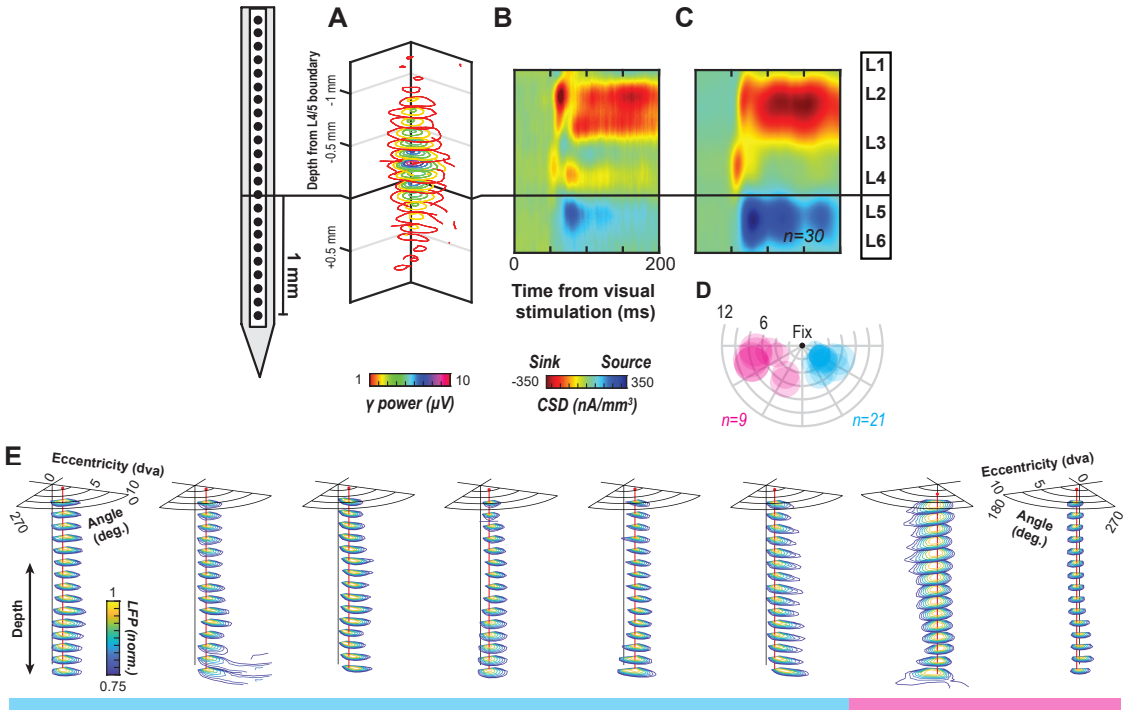

Figure 4.3: Laminar alignment and receptive field mapping

A. Representative receptive fields (RFs) measured with gamma power across recording sites of a single array penetration. RFs across recording sites (z axis) are well aligned, indicating perpendicular penetration. Electrode positioned at left for reference. B. Current source density (CSD) profile for the same session as C. The initial sink following visual stimulation was used as a functional marker to determine the layer 4/5 boundary. Current sinks are indicated in red and sources in blue. The black horizontal line indicates the bottom of the granular input sink. Data are smoothed along depth and across time for visualization purposes. C. Mean CSD profile following alignment of the 30 sessions (monkey Ca 21; He 9). Formatting identical to B. D. Columns' RF locations across sessions and monkeys (cyan, monkey Ca; magenta, He). RF centers determined online, and diameters estimated from previous reports (see V4 RF mapping and electrode orthogonality for details). Concentric circles indicate eccentricities in degrees of visual angle (dva). Radial lines indicate angular positions relative to central fixation (black dot at top center). E. Additional RF alignments using the magnitude of local field potential (LFP) response along depth, rather than gamma power as in A, for electrodes found to be in cortex. Leftmost six are examples from monkey Ca (indicated with cyan bar at bottom) and rightmost two are from monkey He (indicated with magenta bar at bottom). Magnitude of LFP response was found for each recording site and normalized from smallest to largest response across visual space leading to the 0–1 normalization. Contours show the location of the largest LFP response along depth. Red vertical line through three-dimensional plot, and red point shown at the top of each plot, indicates the RF measured along depth with black vertical line indicating central fixation. Note the angle for monkey Ca indicates RF's between 270 degrees (lower visual field vertical meridian) and 0 degrees (right-hand visual field horizontal meridian) and for monkey He indicates RF's between 180 degrees (left-hand visual field horizontal meridian) and 270 degrees – both consistent with the contralateral positioning of recording chambers for each monkey (monkey Ca left V4, He right V4).

the mutual information between the extracortical signal and CSD during the N2pc window, irrespective of target position. This analysis showed a significant relationship between the extracortical signal and the CSD in L2/3 and L5/6 but not in L4. Fourth, we measured the transmitted information about target location from

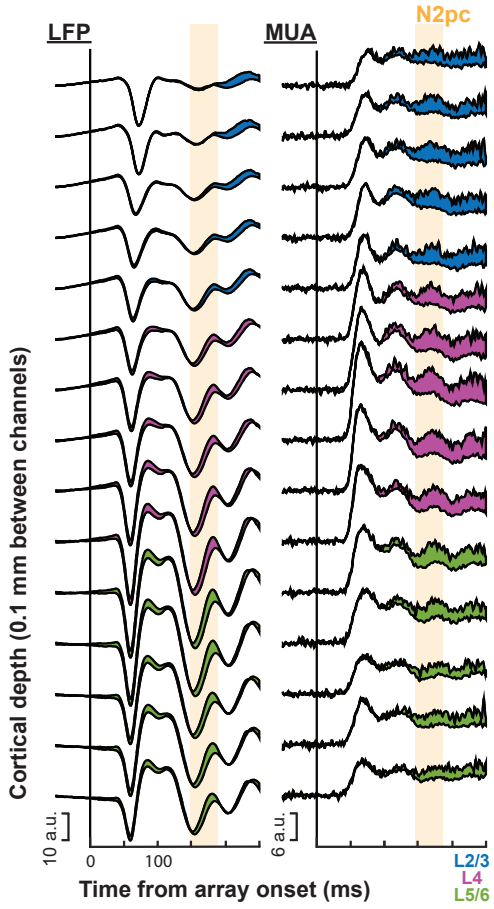

Figure 4.4: Laminar profile LFP and MUA attentional selection during visual search
Responses were averaged across sessions ($n = 30$) at each of the depths ($n = 15$) relative to the L4/5 boundary (magenta to green). Difference between target (attended) and distractor (unattended) responses represented by the fill color corresponding to the recording channels' laminar compartment. Top line of each trace combination is the attended condition, bottom trace is the unattended condition. Significant differences in magnitude of attention effect, averaged 150–190 ms after search array onset, across laminar compartment were detected through an ANOVA for both LFP ($F(2,442) = 22.43$, $p = 5.2e^{-10}$) and MUA ($F(2,442) = 3.87$, $p = 0.022$). Note the effect of attention in the MUA was largest in the middle layers ($M_{L2/3} = 2.68$, $M_{L4} = 3.50$, $M_{L5/6} = 2.38$), consistent with previous reports (Nandy et al., 2017). Time of the N2pc as measured throughout the main text (150–190 ms following array onset) indicated with orange.

CSD to extracortical signal during the N2pc interval (Timme and Lapish, 2018). This analysis demonstrated significant information transmission to the extracortical signal from L2/3 and L5/6, but not L4.

Averaged across sessions, we observed that the electric field during the N2pc interval (Figure 4.7A) was associated with a consistent CSD pattern (Figure 4.7B). This relationship was observed in each monkey (Figure 4.8A-B). Presentation of the search array in any configuration elicited an early current sink in L4, followed by a prolonged sink in L2/3 that was associated with a briefer source in L5/6.

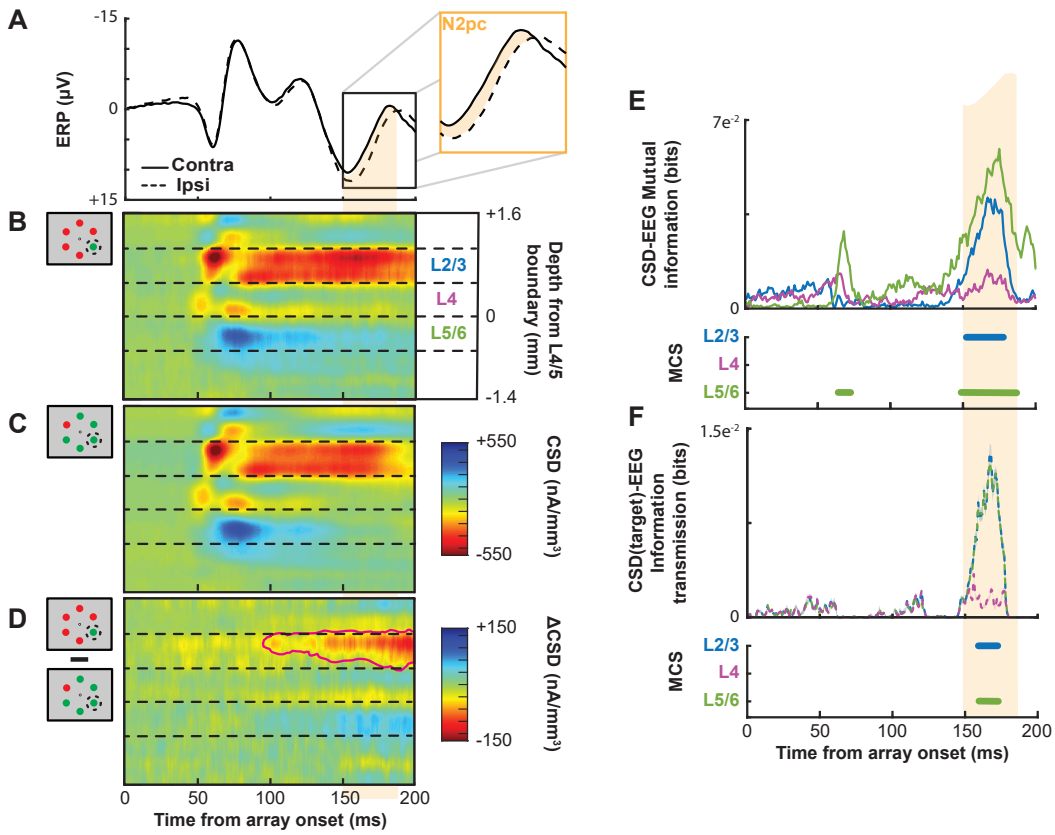

Figure 4.5: Extracortical attention-associated signal and V4 synaptic currents during representative session A. Extracortical event-related potential (ERP) voltages after search array presentation, averaged over all trials when the target was presented contra- (solid) or ipsilateral (dashed) to the electrode. Inset magnifies the N2pc interval defined as the difference in potentials 150–190 ms after the array appeared (orange highlight). B. Simultaneous current source density (CSD) when the target appeared in the population receptive field of the column. Dashed lines indicate boundaries between supragranular (L2/3), granular (L4), and infragranular (L5/6) layers. CSD values were interpolated and smoothed along depth for display only. Current sinks have hotter hues, and current sources, cooler. The earliest sink arises in putative L4, likely from rapid feedforward transmission, followed by intense, prolonged sinks in L2/3 accompanied by weaker source in L5/6. C. CSD evoked by distractor in the receptive field has similar pattern. D. Subtraction of CSD responses to target versus distractor in receptive field. The only statistically significant differences (determined through a t test across time-depth with $p < 0.05$, outlined by magenta line) were due to a current sink in L2/3 that arose gradually 100 ms after array presentation. This relative sink was associated with a weak relative source in L5/6. E. Simultaneous mutual information between CSD and the extracortical signal for L2/3 (blue), L4 (purple), and L5/6 (green). Times with significant mutual information were computed through Monte Carlo shuffle simulations (MCS). N2pc interval is highlighted. Intervals with significant mutual information persisting for at least 10 ms are indicated by horizontal bars. No mutual information with EEG was observed in L4. F. Information transmission about target position from V4 CSD to the extracortical signal. Conventions as in E.

We next computed information transmission about target location from the CSD to the extracortical signal for each session (Figure 4.7C). All cortical layers provided significant information transmission in ¿75% of sessions during the N2pc window (150-190 ms following array onset). However, the magnitude of

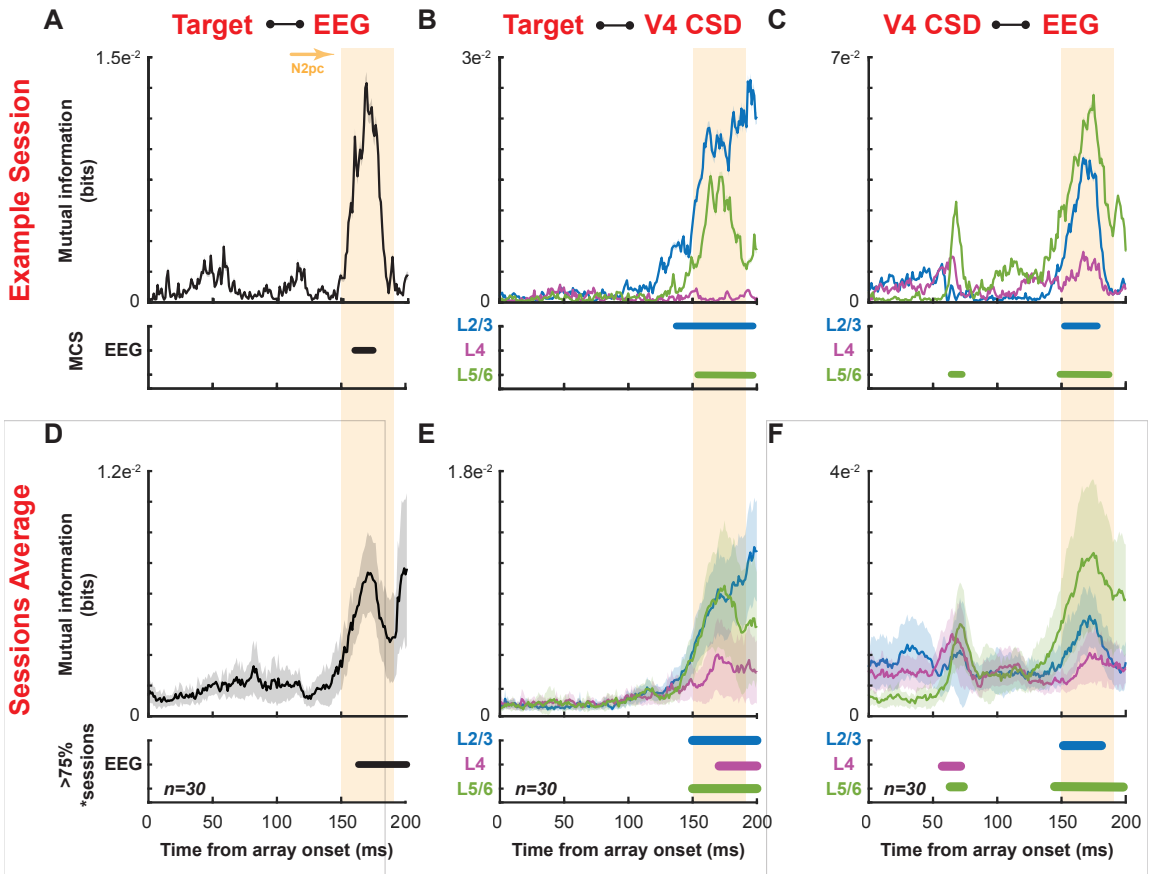

Figure 4.6: Mutual information measures for the extracortical signal, V4 current source density (CSD), and target position

A. Mutual information between target position (binarily coded contra- or ipsi-presentation) and the extracortical signal along time (top) aligned on array onset with 95% confidence interval (CI) cloud estimated from subsampling 75% of the data 100 times and recomputing. Significance established through Monte Carlo simulations is indicated below. Only intervals where significance ¿10 ms were included. Orange region indicates N2pc. B. Mutual information between target position (binarily coded inside or opposite column receptive field [RF]) and each laminar compartment (L2/3 [blue], L4 [purple], and L5/6 [green]). Panel organization identical to A. C. Mutual information between the extracortical signal and each laminar compartment. Panel organization identical to A. D–F. Population averages ($n = 30$) mutual information measures. Same organization as representative session, A–C respectively. Clouds around averages denote 95% CI across sessions. Statistical measures for population averages reflect interval's where 75% sessions were found to be significant through Monte Carlo simulations for ¿10 ms.

transmitted target information was significantly greater in L2/3 and L5/6 relative to L4 (L2/3-L4: $t(29) = 2.15$, $p = 0.040$; L5/6-L4: $t(29) = 2.20$, $p = 0.036$). The magnitude of information transmission was not significantly different between L2/3 and L5/6 ($t(29) = 0.21$, $p = 0.84$). Across sessions, the three other information theoretic analyses were consistent with the example session (Figure 4.6). Moreover, significant information transmission during the N2pc was observed in each monkey (Figure 4.8C).

To verify the results, we applied the information theoretic analysis over a longer interval (Figure 4.9).

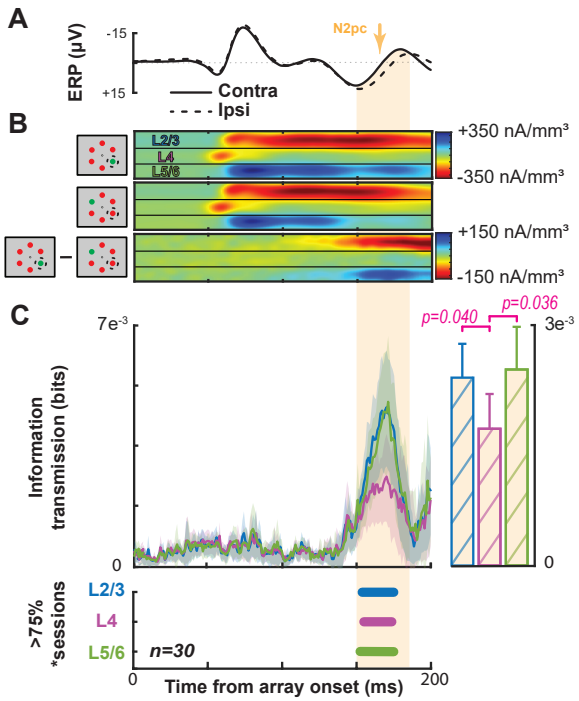

Figure 4.7: Grand average demonstrating the link between V4 CSD and the extracortical attention-associated electric field

Conventions as in Figure 4.5. A. Average event-related potential (ERP) across all sessions and animals with the target contra- (solid) or ipsilateral (dashed). The N2pc interval is indicated by orange shading. B. Average V4 CSD with the target in (top) or out of the receptive field (RF) (center) with the difference between the two at the bottom. C. Grand average information transmission about target position from V4 layers to the extracortical signal as a function of time (left). Average +2 SEM of information transmission during the N2pc window (right). Panel below shows that information transmission from L2/3 and in L5/6 was significantly greater than that from L4 (t test $p < 0.05$). Timepoints with significant information transmission were assessed through Monte Carlo simulations during ¿75% of sessions. Intervals with significance persisting for at least 10 ms are indicated by horizontal bars, color coded for each laminar compartment (bottom).

Importantly, we found no signal differences or significant information transmission in the 100 ms pre-array baseline period as expected with baseline correction. We also evaluated the interval 200-250 ms following array presentation and found a polarization reversal in the extracortical signal likely corresponding to the Pd (Cosman et al., 2018). We observe persistent current differences in the extragranular CSD during this interval sufficient to contribute to the extracortical signal. However, we observed no statistically significant information theoretic relationship between the CSD and extracortical signal during this interval. The absence of a relationship could indicate no actual association or be a consequence of the reduced trial count due to the clipping of signals at saccade initiation. This uncertainty prevents further consideration of this interval in these data.

Lastly, we performed two additional analyses to determine whether the observed information theoretic

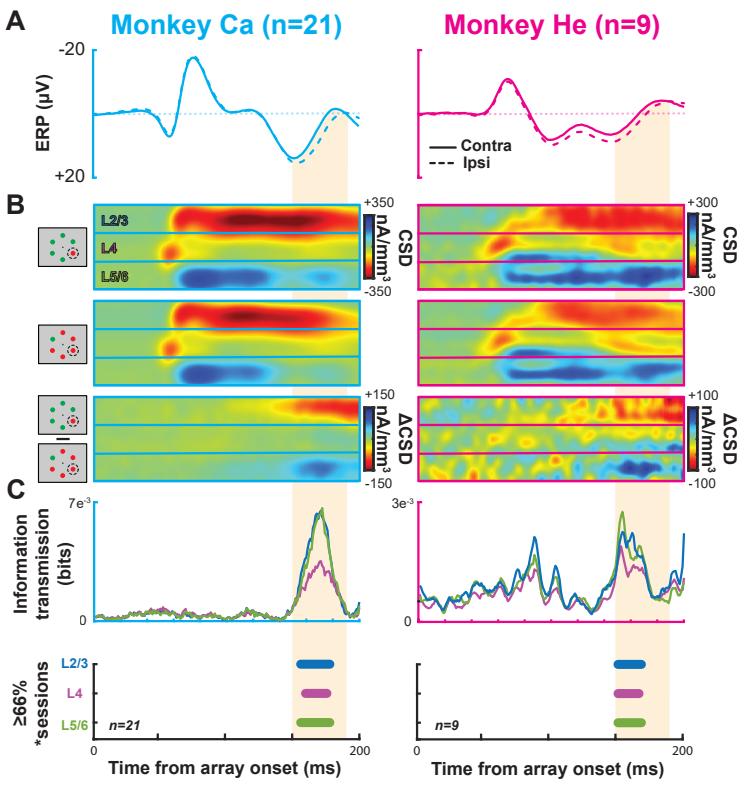

Figure 4.8: Individual monkey physiology and information transmission
Results for monkey Ca ($n = 21$) in left column and He ($n = 9$) in right column. A. Extracortical signal traces for target contralateral (solid line) and ipsilateral (dashed line) to recording site. Orange highlight represents the average time of N2pc used throughout the rest of the manuscript (150–190 ms). B. Current source density (CSD) profile for target in receptive field (RF) (top), outside RF (center), and the difference between the two (bottom). Horizontal boundaries indicate laminar compartments. C. Information transmission computed at each timepoint regarding target position from laminar CSD to the extracortical signal (top). Blue represents L2/3, purple represents L4, and green represents L5/6. Timepoints where 66% of recorded sessions showed significant information transmission for more than 10 consecutive milliseconds through Monte Carlo simulations for each laminar compartment are shown at the bottom.

relationship is confounded by spurious factors. First, we measured the contribution of V4 neuron selectivity for stimulus color. We computed information transmission separately for trials with a red stimulus and with a green stimulus in the receptive field. In the population average of the two calculations for each session we observed significant information transmission during the N2pc (Figure 4.10). Hence, the relationship between V4 activity and the EEG does not depend on color specificity. Second, we measured the contribution of microsaccades, which have been linked to attentional modulation in V4 (Lowet et al., 2018). We computed information transmission separately for trials without microsaccades (Figure 4.11). In the population average of the two calculations for each session we observed significant information transmission during the N2pc. Hence, microsaccade production was not responsible for the observed information theoretic associations between signals. The outcomes of these control analyses engender more

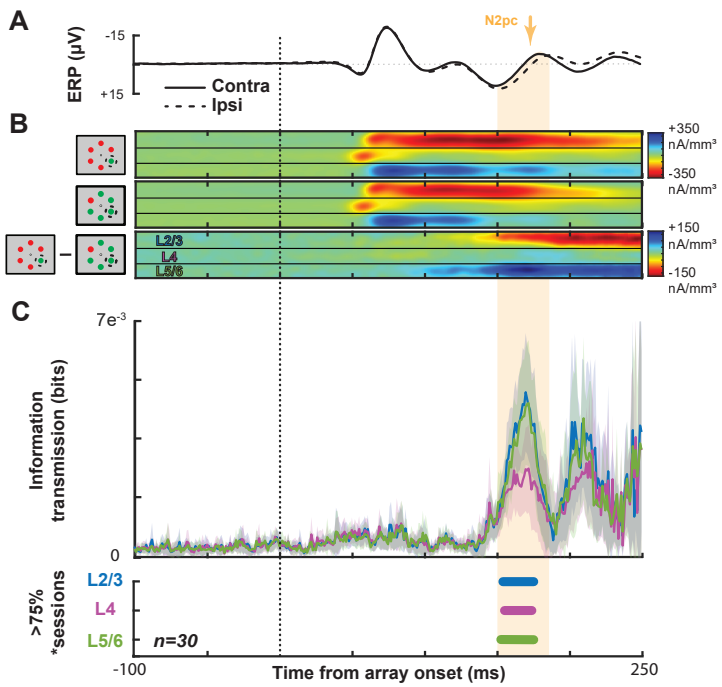

Figure 4.9: Grand average results with expanded interval
Conventions as in Figure 4.5. A. Average event-related potential (ERP) across all sessions and animals with the target contra- (solid) or ipsilateral (dashed). The N2pc interval is indicated by orange shading. B. Average V4 current source density (CSD) with the target in (top) or out of the receptive field (RF) (center) with the difference between the two at the bottom. C. Grand average information transmission about target position from V4 layers to the extracortical signal as a function of time (left). Average +2 SEM of information transmission during the N2pc window (right). Panel below shows that information transmission from L2/3 and in L5/6 was significantly greater than that from L4 (t test $p < 0.05$). Timepoints with significant information transmission were assessed through Monte Carlo simulations during ¿75% of sessions. Intervals with significance persisting for at least 10 ms are indicated by horizontal bars, color coded for each laminar compartment (bottom). Note that elevated information transmission persists into the 200–250 ms interval. Coupled with the sustained sink/source pattern observed along V4 layers and the inversion of the ERP polarization, this might indicate the coexistence of the N2pc and Pd during this interval with the polarization of the Pd masking the persistent N2pc in the ERP.

confidence that the current dipole in V4 generated by the L2/3 CSD sink and the L5/6 CSD source contributes to the N2pc measured in the extracortical electric field.

4.3.4 Columnar Feature Selectivity Influences Contribution to N2pc

Given the columnar organization of color tuning of V4 neurons (Figure 5A) (Roe et al., 2012; Zeki, 1973, 1980; Tootell et al., 2004; Conway and Tsao, 2009; Kotake et al., 2009), we investigated the association between the N2pc and the CSD in columns with different color preferences. To quantify color selectivity through depth, we computed the response ratio between red and green stimuli (Figure 4.12B) Responses were measured as power in the gamma range (30-150 Hz) because this signal reflects local circuit interactions (Ray and Maunsell, 2011) and feature selectivity in visual cortex (Berens et al., 2008) and is

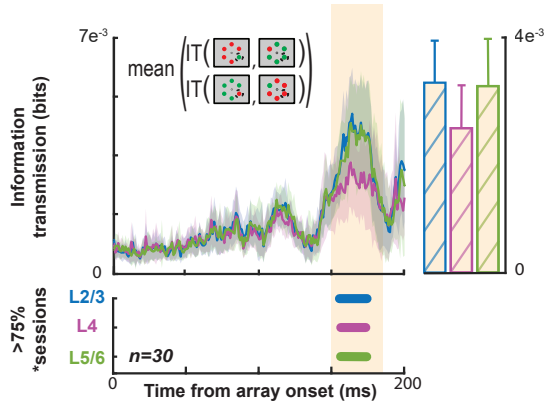

Figure 4.10: Information theoretic relationship between V4 CSD and extracortical signal persists when accounting for stimulus identity

Grand average information transmission about target position from V4 layers to the extracortical signal as a function of time (left). Information transmission was calculated twice for each recording session – once only taking into account only trials when the item in the receptive field (RF) was red (e.g., red target in RF and red distractor in RF trials) and once only taking into account trials when the item in the RF was green. The average of those two computations was taken for each session and the traces shown here are the average across sessions ($n = 30$). Average +2 SEM of information transmission during the N2pc window (right). Panel below shows that information transmission from L2/3 and in L5/6 was significantly greater than that from L4 (t test $p < 0.05$). Timepoints with significant information transmission were assessed through Monte Carlo simulations during ¿75% of sessions. Intervals with significance persisting for at least 10 ms are indicated by horizontal bars, color coded for each laminar compartment (bottom).

more reliably measured than spiking activity across all LMA contacts. This analysis collapses across differences in color tuning across layers, so although the interlaminar specificity of gamma activity is not fully understood, recent work indicates that laminar gamma power can reliably reflect feature selectivity in a spatially specific fashion (Westerberg et al., 2021).

To identify columns with significant selectivity for either red or green, we performed Wilcoxon sign rank tests between the distribution of ratios in each column against bootstrapped null distributions. Each bootstrapped null distribution contained 15 randomly selected ratios from the full dataset (450 experimental values) from which 1000 distributions were generated. The bootstrapped distributions represent the range of possible values observed across V4, but do not capture any difference in the homogeneity of feature selectivity within a column.

We found that more than half of V4 columns show selectivity for red or green stimuli (monkey Ca 12/21 [57.1%], He 5/9 [55.6%]). We computed the information transmission of target position for each color tuned column separately for trials when the preferred or the non-preferred color was in the column's population receptive field. Across sessions with different target and distractor colors, we observed no difference in the amplitude of the extracortical signal during the N2pc (paired sample $t(16) = 0.40$, $p = 0.69$) (Figure 4.12C) nor the laminar CSD (L2/3: $t(16) = -0.85$, $p = 0.41$; L4: $t(16) = 0.75$, $p = 0.46$;

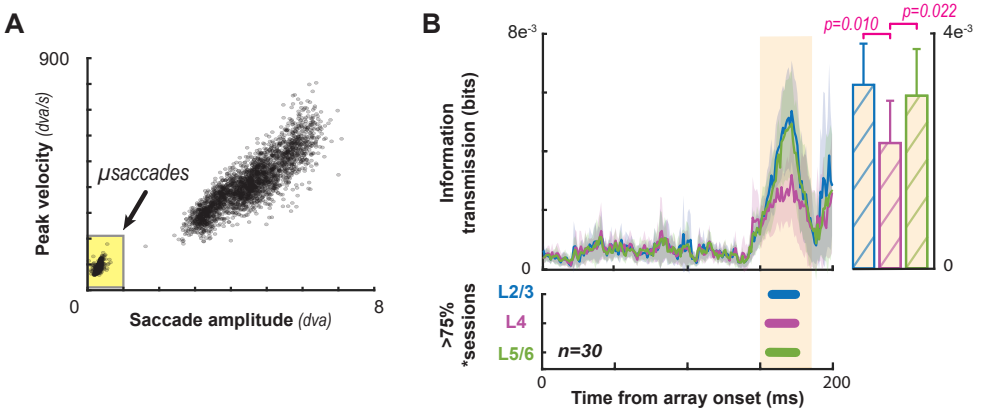

Figure 4.11: Microsaccades do not explain information theoretic relationship between V4 CSD and extracortical signal during the N2pc

A. Example saccade main sequence from one session in monkey Ca. Microsaccades detected during task performance highlighted in lower left. B. Grand average information transmission about target position from V4 layers to the extracortical signal as a function of time (left). Information transmission was calculated across all sessions ($n = 30$) from both monkeys. Only trials where no microsaccades were detected between array onset and saccade for behavioral choice were included in the information theoretic computation. Average +2 SEM of information transmission during the N2pc window (right). Panel below shows that information transmission from L2/3 and in L5/6 was significantly greater than that from L4 (t test $p < 0.05$). Timepoints with significant information transmission were assessed through Monte Carlo simulations during ¿75% of sessions. Intervals with significance persisting for at least 10 ms are indicated by horizontal bars, color coded for each laminar compartment (bottom).

L5/6: $t(16) = 0.36$, $p = 0.72$) (Figure 5D). However, information transmission during the N2pc was greater when a preferred rather than a nonpreferred color was in the RF (Figure 4.12G). This difference was significant in L2/3 and L5/6 but not in L4 (t test across time with at least 10 ms having $p < 0.05$) and is evident in single sessions (Figure 4.13).

We investigated whether the magnitude of information transmission varied with degree of color preference. In session-wise correlations of the difference in information transmission between preferred and nonpreferred colors at the time of peak information transmission (160-180 ms) as a function of CCSI, we found a significant relationship for L2/3 (Spearman's $R = 0.50$, $p = 0.005$) and L5/6 ($R = 0.51$, $p = 0.004$) but not L4 (Figure 4.12H).

We also tested whether feature selective columns, on average, transmitted more information than their non-feature-selective counterparts. We found that feature selective columns, in all laminar compartments, transmitted significantly more information (Figure 4.12I) (two-sample t test: L2/3, $p = 0.044$; L4, $p = 0.023$; L5/6, $p = 0.009$). As such, we wanted to determine if this was due to a lack of attentional modulation in the non-selective columns. This was not the case, we observed that non-selective columns were modulated with attention. Attentional modulation was observed in both the CSD in L2/3 and L5/6 (one-sample t test: L2/3: $t(64) = -6.01$, $p = 9.8e^{-8}$; L4: $t(64) = -0.18$, $p = 0.86$; L5/6: $t(64) = 5.24$,

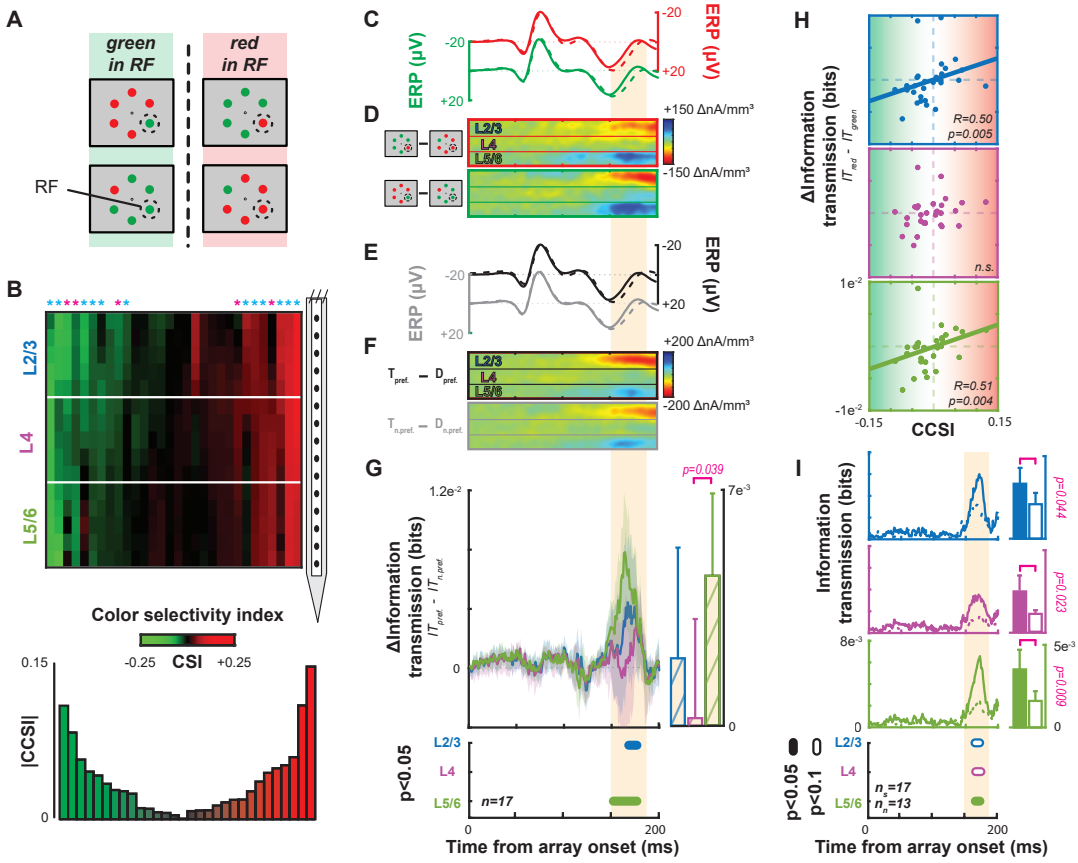

Figure 4.12: Contribution of columnar feature selectivity to the N2pc
Conventions as in Figure 4.5. A. Visual search array configurations used for color selectivity analyses. B. Laminar profiles of red/green color selectivity across all sessions. The hue of each point across cortical depth signifies the value of a color selectivity index (CSI), derived from local gamma power. CSI values ¡0 (¿0) indicate preference for green (red). CSI is smoothed across adjacent channels for display. Sessions are sorted from left to right based on a column color selectivity index (CCSI) that estimates each column's combined selectivity. A bar plot of session-wise CCSI is plotted below. Asterisks indicate columns with significant color-selectivity (Wilcoxon signed rank, $p < 0.05$). Asterisk color indicates monkey (Ca cyan; He magenta). C. Average event-related potentials (ERPs) for trials when a red (top) or green (bottom) target or distractor appeared in the receptive field (RF) of the 17 color selective columns. D. Difference in CSD when the target relative to distractor appeared in the columnar population RF when a red (top) or green (bottom) stimulus appeared in the RF ($n = 17$). E. Average ERP for trials when the preferred color (top) or non-preferred color (bottom) target or distractor appeared in the RF ($n = 17$). Conventions as in Figure 4. F. Difference in CSD when the target relative to distractor appeared in the RF with the preferred (top) or non-preferred (bottom) color. G. Average difference in information transmission between laminar CSD and N2pc when preferred relative to non-preferred stimulus color appeared in RF. Conventions as before. More information was transmitted when a stimulus of the preferred color appeared in the RF. H. Correlation between difference in information transmission across columns and CCSI for each session for L2/3 (blue, top), L4 (purple, center), and L5/6 (green, bottom). Spearman correlation reported in lower right of each plot with data from all 30 sessions. Color-specific information transmission scaled with magnitude of color selectivity. I. Information transmission for columns with (solid, $n = 17$) and without (dashed line, $n = 13$) feature selectivity for L2/3 (top), L4 (middle), and L5/6 (bottom). Intervals with significant differences are plotted below at two alpha levels for a t test (filled: 0.05; unfilled: 0.1). Bars plot average with upper 95% confidence interval of information transmission during the N2pc for columns with (left) and without (right) feature selectivity. Significant differences are indicated with a bracket and p value from a t test.

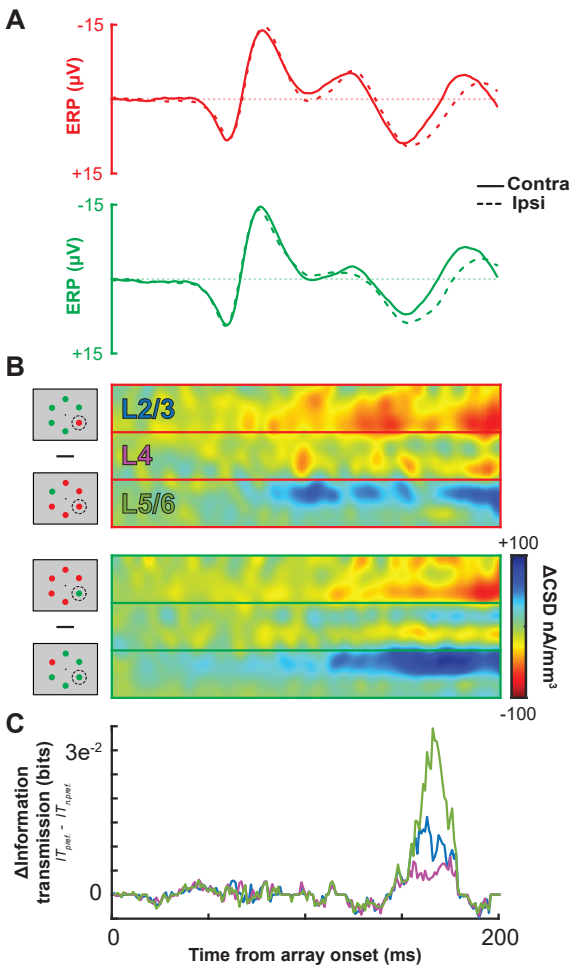

Figure 4.13: Contribution of columnar feature selectivity to the N2pc
A. Extracortical event-related potential averaged across correctly performed trials ($n = 2992$) for a single session with the target stimulus presented contralateral to the recording electrode (solid line; $n_{red} = 742$, $n_{green} = 766$) or ipsilateral to the recording electrode (dashed line; $n_{red} = 752$, $n_{green} = 732$) for trials where the target is red (top) or green (bottom). B. Average difference in current source density (CSD) profile for correctly performed trials between target present in receptive field (RF) and distractor present in RF for red item in RF trials (top) and green item in RF trials (bottom). C. Difference in information transmission between the preferred color and the non-preferred color for the same single session as in panels A and B.

$p = 1.9e^{-6}$) as well as across all layers in the population spiking activity (one-sample t test: L2/3: $t(64) = 8.00$, $p = 3.7e^{-11}$; L4: $t(64) = 9.66$, $p = 4.1e^{-14}$; L5/6: $t(64) = 7.58$, $p = 1.8e^{-10}$) during the N2pc interval (averaged 150-190 ms following array onset) (Figure 4.14).

Importantly, we tested whether the N2pc varied across sessions with or without color-selective columns sampled. We found no difference between N2pc polarization (150-190 ms after the array) between sessions with ($n = 17$) or without ($n = 13$) sampling of color selective columns (two sample t test: $t(28) = -0.75$, $p = 0.46$). This invariance is expected because extracortical EEG spatially integrates signals from multiple cortical columns.

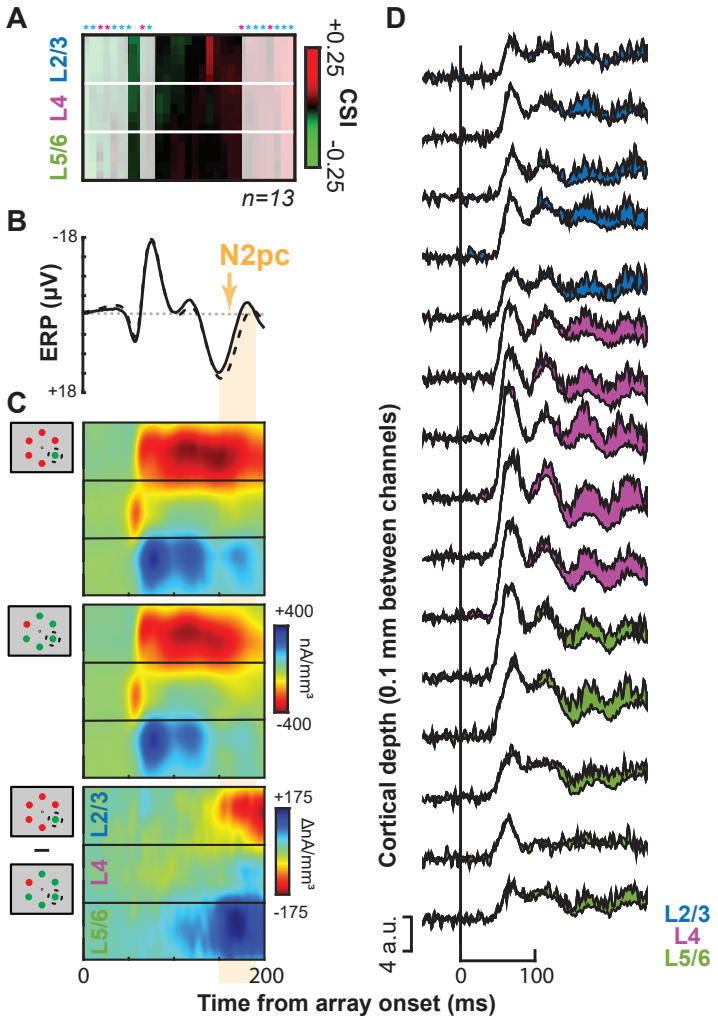

Figure 4.14: Attentional modulation is present in cortical columns not selective for an attentional target feature present in the pop-out search task

A. Cortical columns found to be non-selective for red or green were identified across both monkeys ($n = 2$) and selected for further analysis ($n = 13$). B. The N2pc was observable in the sessions where no significant feature selectivity was present. Contra- versus ipsilateral target presentations (relative to the recording electrode) were plotted in time relative to the search array onset. Intervals of N2pc as measured in the main text (150–190 ms following array onset) is highlighted in orange. C. Current source density (CSD) profiles for the target in receptive field (RF) (top), outside RF (middle), and the difference between the two (bottom) for the feature non-selective columns ($n = 13$). D. Multiunit spiking activity averaged across non-selective columns ($n = 13$). Recording channels shown for upper (blue), middle (magenta), and lower (green) laminar compartments. Top line of each trace is the response in the attended condition with the bottom line being the unattended condition. Fill reflects the difference between attention conditions.

4.3.5 Translaminar Currents in V4 Recapitulate the N2pc

CSD is computed by differentiating between local field potentials to eliminate volume-conducted signals that do not arise from local circuit activity. Using an inverse procedure (i.e., summing the CSD), it is possible to estimate the local field potential without contamination by volume conducted activity (Nicholson

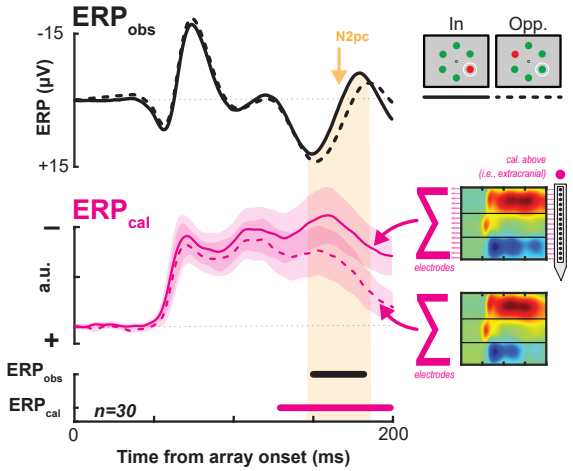

Figure 4.15: Comparing an estimated field potential generated from the CSD across the cortical columns to the observed ERP

Black lines indicate the empirically measured event-related potential (ERP_{obs}, top), averaged across sessions. The pink line indicates the estimated ERP calculated from the synaptic currents across V4 columns, averaged across sessions (ERP_{cal}, center). Synaptic currents at each electrode are measured and divided by the Euclidean distance of the electrode from the extracortical surface (see Methods; (Nicholson and Llinas, 1971; Kajikawa and Schroeder, 2011)). ERP for target present in the receptive field (RF) versus target opposite the RF is shown as solid and dashed lines, respectively (example array for each condition shown at top right). Clouds around ERP_{cal} lines indicate 95% confidence intervals across sessions for each condition. Note that despite differences in overall waveshape (which are likely due to the fact that V4 is not the only contributor to the attention-independent, visually evoked ERP), the timing of differences within signal types can be compared. The congruence in polarization of the difference in potentials is of similar note.

and Llinas, 1971; Kajikawa and Schroeder, 2011). We used this approach to compute an estimated extracortical event-related potential (ERP). Specifically, we computed the sum of currents produced by a cortical column to estimate the extracortical signal at a position directly above. The resultant potential (ERP_{cal}) distinguished the target from a distractor in the RF throughout the N2pc (Figure 4.15). In other words, the summed potential generated by currents along V4 columns differentiates between attention conditions simultaneous with the extracortically measured attention-associated signal. Note that the shape of the observed extracortical ERP (ERP_{obs}) differs from the estimated extracortical ERP_{cal}. This is expected because the ERP_{obs} reflects several more variables such as volume conducted contributions of nearby columns as well as the filtering and attenuating effects of the tissue and cranium above the gray matter (Nunez et al., 2006). Moreover, the ERP_{cal} does not reflect the potential contributions of other visual areas. Given these expected differences, it is remarkable how well the difference in ERP_{cal} predicts the timing of the attention-associated electric field.

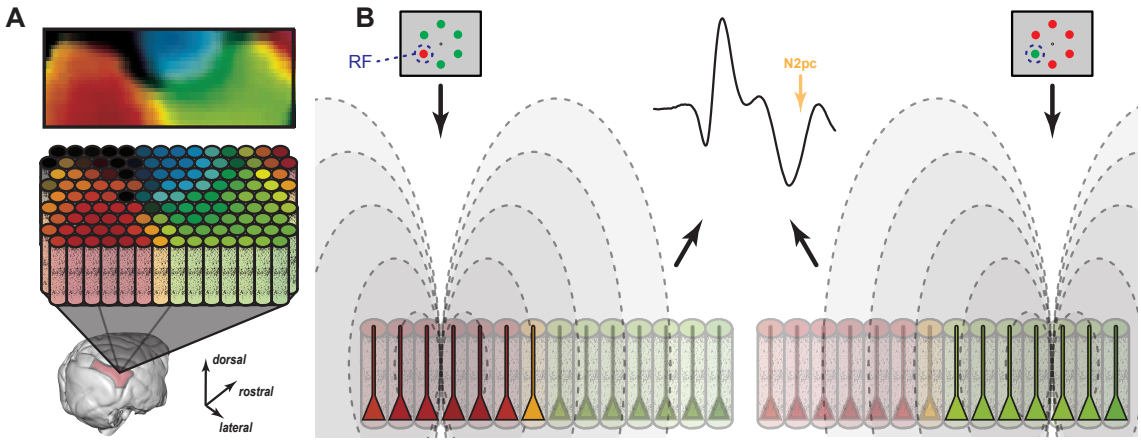

Figure 4.16: Feature mosaic hypothesis
A. A map of preferred color in area V4 derived from optical imaging (Tanigawa et al., 2010) with corresponding color columns in area V4. B. Relative contributions of color selective cortical columns to the N2pc when a red (left) or green (right) target appears in the receptive field (RF). Intensity of pyramidal neuron activity is indicated by saturation in the diagram. The mesoscopic columns produce electric fields (dashed lines) that sum to produce the equivalent event-related potential (ERP).

4.4 Discussion

Bioelectric potentials have practical and clinical applications when their generators are known. For example, the electrocardiogram is useful in medicine because the physiological process associated with each phase of polarization is understood. Likewise, the electroretinogram is useful because the cell layers associated with each polarization are understood. In contrast, human ERP components indexing cognitive operations will have limited and only fortuitous utility until their neural generators are known.

The ERP indices of attention such as the N2pc or Pd are commonly used to assess the deployment of attention in human participants, but can also be observed in macaque monkeys, enabling systematic concurrent EEG and intracranial neurophysiological recordings. Our objective was to identify the neural generator of the attention-associated electric fields that comprise ERPs like the N2pc. Using inverse modeling of cranial surface EEG and laminar resolved CSD in a cortical area, we demonstrate that translaminar synaptic currents in visual cortical area V4 contribute to the generation of attention-associated electric fields during visual search. The dipole resulting in this electric field stemmed from layer-specific interactions in extragranular (top-down recipient) cortical layers. Unexpectedly, we discovered that the contribution of a cortical column to the overlying electric field depended on whether the visual feature in the RF matched the selectivity of the column – an important consideration in the mechanism producing EEG potentials that may not be observable through the macroscopic EEG signal alone.

The attention-associated electric field measured in our task is most likely representative of the commonly measured N2pc component of the EEG ERP. Given our findings regarding the functional

architecture comprising attention-associated electric fields, it is conceivable that the N2pc arises from multiple, anatomically distinct cortical areas. That is, given the ubiquity of columnar architecture in sensory cortex and the specificity of visual feature representations to different cortical areas, electric dipoles formed across visual cortical layers could come about across multiple visual cortical areas with the relative contribution of each depending on the feature being attended to. This realization could help reconcile conflicting interpretations of the cognitive states and operations that are supposed to be indexed by the N2pc (Eimer, 1996; Kiss et al., 2008; Pagano and Mazza, 2012; Foster et al., 2020). It may also help account for variability in the N2pc as a function of attentional target presence in the lower versus upper visual hemifield (Luck et al., 1997b) given the positioning of retinotopic representations along the cortical surface (Gattass et al., 1988) – a potential focus for future study. Moreover, contributions from areas other than V4 are plausible because previous neurophysiological studies in macaques demonstrate attentional selection signals during visual search in the temporal (e.g., (Sato, 1988)), parietal (e.g., (Bisley and Mirpour, 2019)), and frontal (e.g., (Thompson et al., 2005b; Zhou and Desimone, 2011)) lobes. Of particular note, neuroimaging studies in humans indicate a contribution to the N2pc from posterior parietal cortex (Hopf et al., 2000). In the same vein, FEF neurons locate the target among distractors as early as, or even before, the N2pc arises (Cohen et al., 2009; Purcell et al., 2013). Given the interconnectivity of FEF and V4 (Schall et al., 1995; Ungerleider et al., 2008; Gregoriou et al., 2012; Ninomiya et al., 2012), the frontal lobe thus could be the functional origin of an attentional selection signal communicated to V4 and other posterior areas (Armstrong and Moore, 2007; Ekstrom et al., 2008; Gregoriou et al., 2009, 2012; Marshall et al., 2016; Popov et al., 2017), which in turn generate the N2pc (Westerberg and Schall, 2021).

Our discovery that dipoles established by synaptic currents in visual cortical columns underlie the generation of the attention-associated electric fields is consistent with the observation that ERP components such as the N2pc are largest over the occipital lobe in humans (Luck and Hillyard, 1990, 1994) and macaques (Woodman et al., 2007), which is also observed with MEG (Hopf et al., 2000). Our investigation to identify interlaminar interactions producing the N2pc has offered unexpected insights into the underlying neural circuitry. Visual cortical area V4 contains a functional map of hue along its surface (Tanigawa et al., 2010) with individual columns comprising the map preferring the same color (Zeki, 1973, 1980; Tootell et al., 2004; Conway and Tsao, 2009; Kotake et al., 2009; Westerberg et al., 2021). We replicated the finding of columns specified by color-feature selectivity and discovered that the contribution of a column to the global electric field was greater for the preferred feature. Specifically, columns that preferred green (or red) contributed more to the electric field when the item in the RF was green (or red) rather than red (or green). This circuitry likely supports the decoding of visual features like color from EEG (Sandhaeger et al., 2019; Sutterer et al., 2021). The biophysical implications of this unexpected finding are illustrated in Figure 4.16,

which portrays how an attention-associated electric field like the N2pc can arise from mosaics of different cortical columns. While all columns with the attended target in their RF contribute to the N2pc, columns with RF enclosing a target with preferred features establishes stronger dipoles than do columns representing other features or visual field locations. If target position or feature change, then other columns contribute the strongest dipoles.

However, these findings leave several unanswered questions. First, the details of the attentional mechanism enacted in the cortical microcircuit and in turn manifested in the EEG remain unknown. In this study, the task design required both spatial and feature-based attention. Existing models of attention put forward hypotheses for the findings reported here. For example, multiplicative gain would predict a larger increase in response for preferred vs. non-preferred stimuli when attended in the receptive field (e.g., (McAdams and Maunsell, 1999)). Alternatively, feature similarity gain would predict that regardless of what is in the receptive field, red-preferring columns would increase activity and green-preferring would decrease activity when attending red and vice versa (e.g., (Martinez-Trujillo and Treue, 2005)). Further work should be undertaken to disentangle the contributions of spatial and feature attention to this attention-associated field generation. Second, we do not know whether the spatial shifts in the voltage distribution entailed by the mosaic hypothesis can be resolved on the human scalp due to smearing of the signals as they propagate through the skull and scalp (Nunez et al., 2006). However, given decoding of features from EEG can be achieved (Sandhaeger et al., 2019; Sutterer et al., 2021), that would suggest some spatial information is preserved. Additionally, we do not know if this observation generalizes to other cortical areas or other ERP components. However, the discovery has this general implication: A given ERP can arise from qualitatively different neural circuit configurations. This implication entails specific limits on the nature of mechanistic inferences available from ERP measures.

Other aspects of the data deserve further consideration. First, our information theoretic analyses, while yielding clear results through rigorous means, produced values that were of noticeably smaller magnitude than what has been reported in previous studies (e.g., (Optican and Richmond, 1987; Reich et al., 2001; Timme and Lapish, 2018)). We are not concerned about this difference because no previous study has performed these measures on the relationship between intracortical synaptic currents and extracortical electric fields, so we have no strong prior about the magnitude of information theoretic results to expect. Also, the previous information theoretic analyses have been applied most commonly to measure relationships between pairs of single-units, but we are comparing mesoscopic currents with macroscopic EEG, which is likely comprised of the activity of many cortical columns beyond that being concurrently measured intracortically.

Second, the polarity of the N2pc measured concurrently with intracortical laminar activity was opposite

what has been previously described in macaque monkeys (Woodman et al., 2007). We believe this is an unfortunate consequence of differences in the referencing arrangements between the original and the present study. The previous work sampled EEG from an electrical lead embedded in the outer skull referenced to either linked-ears or a frontal, extracranial electrode. We sampled EEG from LMA contact(s) outside the skull referenced to a rod supporting the LMA, which extended into the brain. As such, imbalanced measurement of the electric fields across the putative generator could lead to the inverted ERP polarity. We should also acknowledge possible differences caused by the presence of the craniotomy over the lunate gyrus. This curiosity can be resolved by sampling EEG from the cranial surface before and after a craniotomy with the alternative referencing arrangements. Regardless of the explanation, though, our findings of a strong association between V4 laminar substrates and the N2pc does not depend on the EEG polarization.

As a final note, it is important to consider what comes next for this program of research. Two avenues seem promising. In this study we are limited in that we only observed relationships between otherwise unaltered signals. While causal manipulations to neural circuits in cognitive tasks come with their own limitations (e.g., you are no longer observing the normal functioning system and consequent behavior), much could be gleaned about relative contributions from direct stimulation or inactivation of the putative circuitry generating these electric fields. In a similar vein, a biophysical modeling approach will yield more information on the relationships of attention-associated signals across scales. That is, by now knowing something about the circuit and mechanism yielding these attention-associated electric fields, we are able to use biophysically plausible computational models to gain further insight through simulations. Both approaches seem well-suited to build on the findings detailed in this study. Ultimately the goal through these means and beyond should be to bridge the gap between what we know of the neurophysiology of attention at the microscopic scale to human attention-associated signals such as the N2pc.

4.5 Methods

4.5.1 Animal Care

Procedures were in accordance with National Institutes of Health Guidelines, Association for Assessment and Accreditation of Laboratory Animal Care Guide for the Care and Use of Laboratory Animals, and approved by the Vanderbilt Institutional Animal Care and Use Committee following United States Department of Agriculture and Public Health Services policies. Animals were socially housed. Animals were on a 12-hour light-dark cycle and all experimental procedures were conducted in the daytime. Each monkey received nutrient-rich, primate-specific food pellets twice a day. Fresh produce and other forms of environmental enrichment were given at least five times a week.

4.5.2 Surgical Procedures

Two male macaque monkeys (Macaca mulatta monkey Z, 12.5 kg; Macaca radiata monkey P, 9 kg) were implanted with head posts and skull-embedded EEG arrays using previously described techniques (Woodman et al., 2007). One monkey (monkey P) was implanted with a subconjunctive eye coil. Two male macaque monkeys (Macaca radiata; monkey Ca, 7.5 kg; He, 7.3 kg) were implanted with head posts and MR compatible recording chambers with craniotomy over V4. Anesthetic induction was performed with ketamine (10 mg/kg). Monkeys were then catheterized and intubated. Surgeries were conducted aseptically with animals under O2, isoflurane (1-5%) anesthesia. EKG, temperature, and respiration were monitored. Postoperative antibiotics and analgesics were administered. Further detail is documented elsewhere (Woodman et al., 2007; Westerberg et al., 2020b,a).

4.5.3 Magnetic Resonance Imaging

Anesthetized animals were placed in a 3 Tesla Magnetic Resonance Imaging (MRI) scanner. T1-weighted 3D MPRAGE scans were acquired with a 32-channel head coil equipped for SENSE imaging. Images were acquired using 0.5 mm isotropic voxel resolution with parameters: repetition 5 s, echo 2.5 ms, flip angle 7°.

4.5.4 Visual Search Tasks

Monkeys performed a color pop-out (monkeys Ca, He, and Z) or T/L (monkey P) search. Search arrays were presented on a CRT monitor at 60 Hz, at 57 cm distance. Stimulus generation and timing were done with TEMPO (Reflective Computing). Event times were assessed with a photodiode on the CRT. We used isoluminant red and green disks on a gray background (pop-out) or uniform gray T's and L's on a black background (T/L). Target feature varied within session for monkeys Ca, He, and Z. Monkey P identified the same target on any given session (T or L) but changed specific targets session to session. Trials were initiated by fixating within 1 (monkeys Ca and He) or 2 (monkeys P and Z) degrees of visual angle (dva) of a fixation dot. Time between fixation and array onset was at least 500 ms (monkey P: 500–1000 ms; Z: 500 ms; Ca and He: 750–1250 ms). For monkeys experiencing a range of fixation periods (monkeys Ca, He, P), a nonaging foreperiod function was used to determine the fixation period on a trial-by-trial basis. Arrays comprised of 6 (monkeys Ca and He) or 8 (monkeys P and Z) items. Monkeys P and Z experienced invariable array eccentricity (10 dva) and item size (monkey P: 1.3x1.3 dva; Z: 1x1 dva). 2 items were positioned on the vertical meridian, 2 on the horizontal, and the 4 remaining items equally spaced between. Monkeys Ca and He viewed items where size scaled with eccentricity at 0.3 dva per 1 dva eccentricity so that they were smaller than the average V4 receptive field (RF) (Freeman and Simoncelli, 2011). The angular position of items relative to fixation varied session to session so that 1 item was positioned at the

center of the RF. Items were equally spaced relative to each other and located at the same eccentricity. Each trial, 1 array item was different from the others. Monkeys saccaded to the oddball within 1 (monkeys Ca and He) or 2 seconds (monkeys P and Z) and maintained fixation within 2–5 dva of the target for more than 400 ms (monkeys Ca, He, and Z: 500 ms; monkey P: 400–800 ms). Note that monkeys Ca, P, and Z were trained to versions of their respective search tasks that included catch trials where no target was present and they were tasked to remain fixating. Monkey He did not experience catch trials. Juice reward was administered following successfully completion of the trial. The target item had an equal probability of being located at any of the 6 or 8 locations. Eye movements were monitored at 1 kHz or 250 Hz using a corneal reflection system (monkeys Ca, He, and Z) or a scleral search coil (monkey P), respectively. If the monkey failed to saccade to the target, they experienced a timeout (1–5 s).

4.5.5 10-20 EEG Recordings

Two monkeys with intact skulls (i.e., lacking craniotomies) were implanted with an array of electrodes approximating the human 10-20 system locations (monkey P: FpFz, C3, C4, P3, P4, OL, OR, Oz; monkey Z: FpFz, Fpz, F3, F4, FCz, Cz, C3, C4, Pz, P5, P6, POz, O1, O2, Oz) (Jasper, 1958). Referencing was done using either the FpFz electrode (monkey P) or through linked ears (Z). The impedance of the individual electrodes was confirmed to be between 2–5 kOhm at 30 Hz, resembling electrodes used for human EEG. EEG was recorded using a Multichannel Acquisition Processor (Plexon) at 1 kHz and filtered between 0.7–170 Hz. Data was aligned to array onset and baseline corrected by subtracting the average activity during the 50 ms preceding the array onset from all timepoints. Data was clipped 20 ms prior to saccade to eliminate eye movement artifacts.

4.5.6 Simultaneous Laminar V4 and Extracortical Recordings

The extracortical electric fields and laminar V4 neurophysiology were acquired at 24 kHz using a PZ5 and RZ2 (Tucker-Davis). Electric signals between 0.1 Hz and 12 kHz were observable with this system. V4 data was collected from 2 monkeys (monkey Ca: left hemisphere; He: right) across 30 sessions (monkey Ca: 21; monkey He: 9) using 32-channel linear electrode arrays with 0.1 mm interelectrode spacing (Plexon) introduced through the intact dura mater each session. Recordings were conducted with the electrode in a tube-grounded, reference-grounded configuration which grounds the stainless-steel support tube of the electrode and grounds the reference of the headstage. Arrays spanned layers of V4 with a subset of electrode contacts deliberately left outside of cortex. The extracortical electric field was derived from the most superficial electrode outside the brain (above the dura mater) using the same tube-grounded, referenced-grounded configuration and filtered between 1–100 Hz. CSD was computed from the raw signal

by first extracting the LFP (signal filtered between 1-100 Hz, identical to the extracortical signal) and then taking the second spatial derivative along electrodes (Nicholson and Freeman, 1975; Schroeder et al., 1998; Mehta et al., 2000a; Westerberg et al., 2019) and converting voltage to current (Logothetis et al., 2007). We computed the CSD by taking the second spatial derivative of the LFP:

$$CSD_{t,d} = -\sigma \left(\frac{x_{t,d-z} + x_{t,d+z} - 2x_{t,d}}{z^2} \right)$$

where x is the extracellular voltage at time t measured at an electrode contact at depth d and z is the inter-electrode distance and σ is conductivity. Both EEG and CSD were baseline corrected at the trial level by subtracting the average activation during the 300 ms preceding array onset from the response at all timepoints. Extracortical electric field potentials and CSD profiles were clipped 10 ms prior to saccade at the trial level to eliminate the influence of eye movements.

Population spiking was measured and analyzed to supplement primary LFP and CSD results. Multiunit activity was derived through well-documented means (Legatt et al., 1980) and has been demonstrated to be effective across multiple brain areas (Logothetis et al., 2001; Roelfsema et al., 2004; Self et al., 2013; Shapcott et al., 2016; Tovar et al., 2020; Westerberg et al., 2020a; Xing et al., 2009). The broadband neural signal was lowpass filtered at 3 kHz, highpass filtered at 300 Hz, full-wave rectified, and lastly, lowpass filtered at 150 Hz. This signal reliably reflect neural population dynamics (Trautmann et al., 2019). Additionally, multiunit activity in V4 has been shown to reliably reflect attentional modulation (Mehta et al., 2000a; Nandy et al., 2017).

4.5.7 Laminar Alignment

Orthogonal array penetrations were confirmed online through a reverse-correlation RF mapping procedure (Nandy et al., 2017; Cox et al., 2019a,b; Westerberg et al., 2019; Dougherty et al., 2019) (Figure 2 – figure supplement 1). RFs were found to represent portions of visual space consistent with previous reports of V4 (Gattass et al., 1988). Positions of recording sites relative to V4 layers were determined using CSD (Schroeder et al., 1998; Nandy et al., 2017). Current sinks following visual stimulation first appear in the granular input layers of cortex, then ascend to the supragranular compartment. Previously described observations of laminar V4 CSD include a sink in the infragranular layers following the ascent to the supragranular layers (Nandy et al., 2017), an observation we do not observe in our data. This is likely because we used task evoked CSD for alignment with stimulus presentation persisting throughout the measurement interval whereas the descending sink observation was found with very brief stimulus presentations. It is likely that the strength of the persistent supragranular sink is masking the previously

reported infragranular sink (Mitzdorf, 1985). We computed CSD and identified the granular input sink session-wise. Sessions were aligned by this input sink. 'L4' refers to granular input layer, 'L2/3' - supragranular layers, and 'L5/6' - infragranular layers. Each laminar compartment was assigned the same number of recording sites to alleviate biases during analysis.

4.5.8 Inverse Modeling

Inverse modeling of 10-20 EEG recordings was performed in CURRY 8 (Compumedics Neuroscan). 3D head reconstruction was created for each monkey (P and Z) using the boundary element method (Hämäläinen and Sarvas, 1989). This method takes into account individual monkey's surface morphologies to create models of cortex surface, inner and outer skull, and skin boundaries. This model was used in conjunction with EEG to compute a voltage distribution over the cortical surface. We calculated the current density with sLORETA, which calculates a minimum norm least squares that divides current by the size of its associated error bar, yielding F scores of activation. sLORETA produces blurred but accurate localizations of point sources (Pascual-Marqui, 2002). Other algorithms such as Minimum Norm and SWARM were modeled as well, with agreement between models sufficient not to change any conclusions.

4.5.9 Information Theory Analyses

Information theory (Shannon, 1948) analyses were chosen for several reasons. First, information theory analyses yield results in terms of 'bits' which can be used to directly compare effect sizes across measurement methods (e.g., CSD, Extracortical signal, and array composition [directed spatial attention]). Next, these analyses are inherently multivariate and able to capture linear and nonlinear relationships. Furthermore, information theory is model independent and does not necessitate a specific hypothetical structure in order to detect relationships between signals. This combination allows us to detect relationships between the extracortical signal and CSD signal that might not be linear and therefore would not be captured by linear models or correlation analyses. We chose to measure pairwise mutual information and information transmission to gauge the relationships between our three 'signals' (e.g., extracortical, CSD, and array composition [directed spatial attention]). Mutual information is the reduction in in uncertainty in one variable afforded by another known variable. That is, mutual information is greater when you know the state of one variable covaries with the state of the other variable. If the two variables do not correspond well, mutual information is low. Therefore, the reduction in uncertainty is formalized as 'information' which is relayed in bits. Mathematically, mutual information is captured by the following equation (Cover and Thomas, 2012; Beer and Williams, 2015):

$$I(X;Y) = H(X) - H(X|Y)$$

where $H(X)$ and $H(X|Y)$ are the entropy X and X given Y, respectively. Entropy for a signal (S) is computed by:

$$H(S) = \sum_i p(s_i) \log \frac{1}{p(s_i)}$$

where $p(s)$ is the probability distribution for signal S and i is the signal state. Therefore, mutual information can be computed probabilistically by:

$$I(X;Y) = \sum_i \sum_j p(x_i y_j \log \frac{p(x_i y_j)}{p(x_i) p(y_j)}$$

where $p(x)$, $p(y)$ are the probability distributions for X and Y, and $p(x,y)$ is the joint probability distribution of X and Y across signal states i and j for X and Y, respectively.

While mutual information describes the relationship between the two signals (for our purpose: CSD and the extracortical signal, CSD and directed spatial attention, or the extracortical signal and directed spatial attention), it does not allow for the evaluation of two signals regarding a third (e.g., CSD and the extracortical signal regarding directed spatial attention). For analyses where we want to understand information regarding the allocation of directed attention from the synaptic currents in V4 to the extracortical signal we use a modified equation rooted in the same entropy/mutual information principles. In computing information transmission, we are interested in the information about X (directed spatial attention), transferred from Y (CSD in V4) to Z (extracortical signal) formalized as:

$$I_T(X;Y_{past}Z_{future}) = I_{min}(X;Z_{future},\{Z_{past},Y_{past}\}) - I_{min}(X;Z_{future},Z_{past})$$

where past and future describe the timepoints when the data is taken from. The information transmission (I_T) is taken as the difference between two minimum information calculations. The minimum information (I_{min}) is computed regarding the combination of the individual signals (S_1 and S_2) at the specified intervals as:

$$I_{min}(X;S_1,S_2) = \sum_x p(x) min\{I(X=x;S_1), I(X=x,S_2)\}$$

where $p(x)$ is the probability distribution for signal X and x are the possible states of X. By taking into account different timepoints for the signals we can interpret this computation as the information about X (directed spatial attention) shared by Y_{past} (e.g., earlier CSD in V4) and Z_{future} (e.g., later extracortical

signal) that was not already in Z_{past} (e.g., earlier extracortical signal).

Above information theory analyses were performed using the Neuroscience Information Theory Toolbox (Timme and Lapish, 2018). Pairwise mutual information and information transmission were computed at each timepoint across trials for each session using default parameters. Five uniform count bins were used for data binning. 10 ms was used for time lag for information transmission. Only correct trials were included. Information theory measures were computed for each millisecond for the entire interval displayed in each analyses' respective figure panel. CSD for each laminar compartment was computed by taking the average activity of 5 sites at the trial level included in each laminar compartment. For mutual information between target position and the extracortical signal, target position was binary where target was either contra- or ipsilaterally presented. For computations within V4, target position was binary where target was either in the RF or positioned opposite the RF. 5000 Monte Carlo simulations were used to generate a distribution of null model values which experimental values were compared to ($\alpha = 0.05$).

4.5.10 Feature Selectivity

For each recording site within a column, gamma power (30-150 Hz) (Maier et al., 2010) responses were computed when either a red distractor was presented to the RF of the column or when a green distractor was present to the RF. Responses were taken as the average activation 75–200 ms following array onset. An index was computed from these responses by subtracting the two and dividing by their sum (CSI). Values were therefore bounded between -1 and 1 where larger magnitude indicates greater selectivity for green (towards -1) or red (towards 1). Columnar color selectivity index (CCSI) was computed as the average of CSIs along the entire column. We performed Wilcoxon signed rank tests on the distribution of CSIs across the recording sites of a given cortical column to determine whether a column was significantly color selective (= 0.05). The selective columns were included in feature selectivity analyses where the preferred color and non-preferred color were defined as the color that elicited greater and lesser responses, respectively.

4.5.11 Estimating Field Potential from CSD

We calculated the event-related potential at arbitrary positions from the measured laminar CSD (ERP_{cal}) using a previously described model (Nicholson and Llinas, 1971; Kajikawa and Schroeder, 2011):

$$ERP_{cal}(d_i,t) = A\sum_j \frac{CSD(d_j,t)}{\sqrt{h^2+|d_j-d_i|^2}}$$

where ERP_{cal} at depth i (d_i) for each timepoint (t) is taken as the sum of CSD at depths j (d_j) for each timepoint divided by the Euclidean distance to account for the diminishing impact of local currents on more

distant field potentials. The factor A acts only as a scaling factor and we cannot accurately estimate the magnitude of the one-dimensional CSD-derived waveform, so we eliminate this parameter from the calculation. This omission is consistent with previous reports (Kajikawa and Schroeder, 2011) and limits our comparisons of observed ERP and ERP_{cal} to only shape. However, magnitude differences can be observed between conditions for ERP_{obs} and ERP_{cal}, independently. Also, for our purposes, we set h to 0 as we assume that our observed CSD and the calculated ERP are in the same vertical plane.

CHAPTER 5

Cortical Columnar Activation Recapitulates the Attention-indexing N2pc

*Herrera, B., *Westerberg, J. A., Schall, M. S., Maier, A., Woodman, G. F., Schall, J. D., and Riera, J. J. (2022). Resolving the mesoscopic missing link: Biophysical modeling of EEG from cortical columns in primates. *NeuroImage*, ??:??????????.

"Life is like a landscape. You live in the midst of it but can describe it only from the vantage point of distance."

- Charles Lindbergh

5.1 Summary

Event-related potentials (ERP) are among the most widely measured indices for studying human cognition. While their timing and magnitude provide valuable insights, their usefulness is limited by our understanding of their neural generators at the circuit level. Inverse source localization offers insights into such generators, but their solutions are not unique. To address this problem, scientists have assumed the source space generating such signals comprises a set of discrete equivalent current dipoles, representing the activity of small cortical regions. Based on this notion, theoretical studies have employed forward modeling of scalp potentials to understand how changes in circuit-level dynamics translate into macroscopic ERPs. However, experimental validation is lacking because it requires in vivo measurements of intracranial brain sources. Laminar local field potentials (LFP) offer a mechanism for estimating intracranial current sources. Yet, a theoretical link between LFPs and intracranial brain sources is missing. Here, we present a forward modeling approach for estimating mesoscopic intracranial brain sources from LFPs and predict their contribution to macroscopic ERPs. We evaluate the accuracy of this LFP-based representation of brain sources utilizing synthetic laminar neurophysiological measurements and then demonstrate the power of the approach in vivo to clarify the source of a representative cognitive ERP component. To that end, LFP was measured across the cortical layers of visual area V4 in macaque monkeys performing an attention demanding task. We show that area V4 generates dipoles through layer-specific transsynaptic currents that biophysically recapitulate the ERP component through the detailed forward modeling. The constraints imposed on EEG production by this method also revealed an important dissociation between computational and biophysical contributors. As such, this approach represents an important bridge between laminar microcircuitry, through the mesoscopic activity of cortical columns to the patterns of EEG we measure at the

scalp.

5.2 Introduction

Identifying the neural sources of EEG is a substantial challenge facing the human neuroscience community. Many basic and clinical research programs rely on EEG as a window into human sensation, perception, cognition, and action. However, some insights into the mechanisms of these neural operations are invisible through this method. While the macroscopic EEG contains information, some of it is lost relative to the microscopic activations it reflects. As such, researchers are developing methods to extract as much information regarding the neural sources of EEG to strengthen this staple of neuroscientific approaches. EEG inverse source localization methods have offered a tool to estimate plausible brain sources generating such signals and, hence, make inferences about the underlying cortical mechanisms (Grech et al., 2008; Michel et al., 2004). Unfortunately, the results are indefinite because a given cranial polarization pattern can arise from multiple current configurations, requiring additional assumptions (Grech et al., 2008; Nunez et al., 2006). Researchers constrain the number of possible brain source configurations by imposing biophysical models to address this problem. The most widely used models are based on the equivalent current dipole, with each dipole representing the activity of a small cortical region (Nunez et al., 2019). The equivalent dipole model has been implemented in different inverse solutions, from a few discrete dipoles (Scherg et al., 2019) to more distributed inverse solution algorithms (e.g., sLORETA, MNE, MxNE) (Gramfort et al., 2012; Grech et al., 2008; Nunez et al., 2019).

Our goal is to supplement the anatomical constraints on EEG inverse solutions with biophysical and physiological constraints. This bolsters EEG's interpretability regarding neural operations. We take a definite forward modeling approach. Detailed biophysical models of populations of neurons offer insights into the relationship between microscopic transmembrane currents and macroscopic cranial voltages through forward modeling (Cohen, 2017; Einevoll et al., 2019; Næss et al., 2021; Pesaran et al., 2018). Recent studies have linked summed transmembrane currents (STC) of pyramidal cells (PC) to equivalent dipoles and the dipoles to macroscopic EEG signals (Jones et al., 2009, 2007; Kohl et al., 2022; Næss et al., 2021). Information derived from local field potentials (LFP) sampled across all the layers of the cerebral cortex can validate these equivalent dipoles Murakami and Okada (2006); Riera et al. (2012). A previous study in rat somatosensory cortex measured the equivalent current dipole moments from the laminar current source density (CSD) – a derivative of LFP – and described their contribution to concurrently recorded EEG (Riera et al., 2012). As such, these considerations can generalize to model organisms more closely matching human cognition, such as the macaque monkey. Laminar recordings with CSD (Nicholson and Freeman, 1975; Pettersen et al., 2006) have already been used to elucidate the organization of multiple cortical areas

in macaques (Bastos et al., 2020; Buffalo et al., 2011; Engel et al., 2016; Ferro et al., 2021; Godlove et al., 2014; Hansen and Dragoi, 2011; Hembrook-Short et al., 2017; Kajikawa et al., 2017; Klein et al., 2016; Maier et al., 2011, 2010; Mehta et al., 2000a; Nandy et al., 2017; Ninomiya et al., 2015; Schroeder et al., 1998; Self et al., 2013; Tovar et al., 2020; Trautmann et al., 2019; van Kerkoerle et al., 2017; Westerberg et al., 2019, 2021) and their respective contributions to various EEG signals (Givre et al., 1994; Sajad et al., 2019; Westerberg et al., 2022b).

Despite this progress, the biophysical relationship between the mesoscopic laminar LFP/CSD and the microscopic cellular sources has not been evaluated. This gap of knowledge renders the validity of predicting spatial patterns of cranial EEG voltage from current sources derived from laminar LFP questionable. Hence, we describe a biophysically plausible forward modeling approach linking mesoscopic CSD derived from LFP to macroscopic ERPs.

Based on earlier demonstrations that macaque monkeys produce homologues of human cognitive ERP components (Cohen et al., 2009; Heitz et al., 2010; Purcell et al., 2013; Reinhart et al., 2012; Sajad et al., 2019; Westerberg et al., 2020b; Woodman et al., 2007), it is now possible to obtain data necessary to measure current dipoles in the cerebral cortex under conditions generating cognitive ERPs. Recently, Westerberg and colleagues (Westerberg et al., 2022b) reported current source density maps of the laminar distributions of transmembrane currents in extrastriate cortical area V4 associated with the cognitive ERP component known as the N2pc. We use these data to demonstrate the utility of our detailed forward modeling approach linking intracranial patterns of laminar activity to the overlying EEG. We show that V4 generates dipoles through layer-specific transsynaptic currents that biophysically contribute to ERP generation. Forward modeling this cortical activity renders EEG at the scalp consistent with that of previous reports of the representative ERP. Moreover, in evaluating the potential contributions of other cortical areas computationally involved in the ERP-indexed operation, this approach revealed that these computational contributors need not biophysically contribute to EEG production. In establishing a mesoscopic link between microscopic neural currents and macroscopic cranial voltages, this finding represents the first, definite forward model of a cognitive ERP from current dipoles derived from neural activity in primates.

5.3 Results

We introduce an approach for estimating the mesoscopic cortical columnar current dipoles from laminar in vivo field potential recordings to determine the contribution of distinct areas to a particular macroscopic EEG signal through forward modeling. The approach consists of the following steps: First, the current sources across depth were determined using CSD methods from laminar field potential recordings. Second, current dipole moments were calculated from the estimated CSD values. Third, the estimated current dipoles

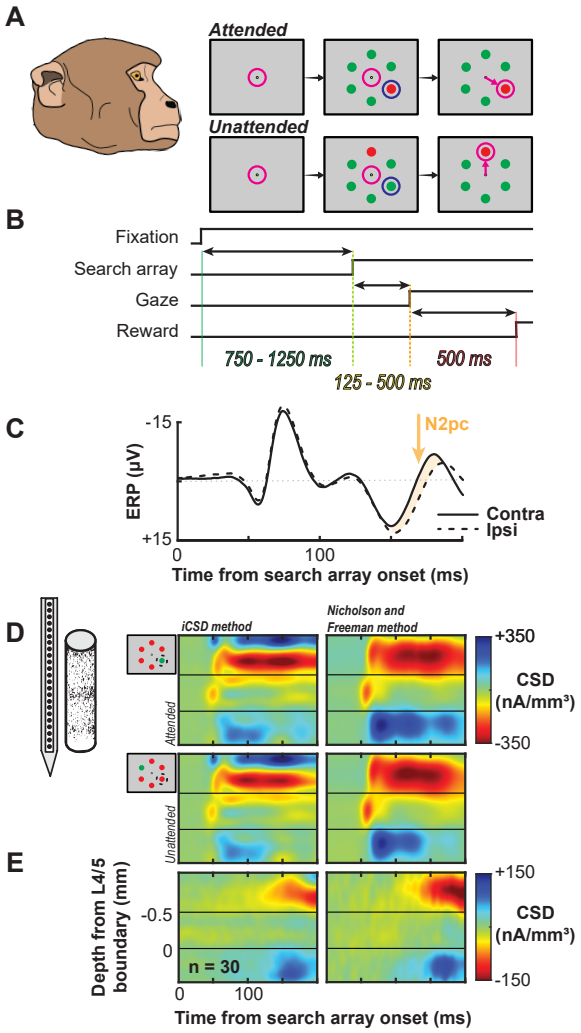

Figure 5.1: Experimental Design and Laminar Current Source Density
A. Monkeys viewed a fixation point and following a variable delay, a six-item visual search array appeared where one item was saliently different that the others (red among green or green among red). Monkeys shifted gaze to the oddball to receive a juice reward. Magenta circle indicates position of gaze. The oddball sometimes appeared in the receptive field (1/6 of trials) resulting in the attended condition. Blue circle indicates the position of the RF. All other trials were considered unattended. B. Timing of events in each trial. A dot appeared at the centered of the screen and once monkeys successfully made fixation, a 750-1250 ms delay ensued. The array appeared and monkeys made a saccade to the target as rapidly as possible (125 - 500 ms). Monkeys maintained fixation of the target for 500 ms to receive a juice reward. C. Proxy extracranial signal from an electrode placed outside the brain, above area V4. N2pc serves as our representative cognitive ERP indicating directed selective attention and can be observed 150-190 ms following search array onset and is highlighted in orange. D. Laminar current density computed across electrodes positioned along V4 layers averaged across sessions following alignment relative to the layer 4/5 boundary. Profiles shown for the attention condition (top) and unattended condition (bottom) and are plotted relative to the search array onset. E. Difference in current density profiles between attention conditions (attended – unattended) showing a difference in extragranular currents during the N2pc window.

were used as current sources of forward models, incorporating their location and orientation. We validated this approach by simulating synthetic field potential recordings generated from detailed biophysical models

of cortical pyramidal neurons. Spatial EEG patterns derived from the two approaches were compared to the spatial EEG pattern obtained from a compartment-based approach (Herrera et al., 2020). We will refer to this as the ground-truth EEG. The first approach derived a single dipole from the simulated CSD; we will refer to this as the CSD single-dipole. The second approach derived a single dipole from the transmembrane currents summed over all the simulated L3 and L5 pyramidal cells within a 3 mm diameter cylinder; we will refer to this as the summed transmembrane currents (STC) single-dipole. This methodological framework was then applied to elucidate the neuronal generators of the ERP component known as the N2pc.

5.3.1 Intracranial Current Sources Can Be Estimated Accurately From LFPs

To evaluate the validity of intracranial current sources derived from CSD in the identification of cortical areas contributing to a spatial EEG pattern, we applied the new forward modeling approach to synthetic local field potentials generated from biophysical models of pyramidal cell activity. We first simulated the activity evoked by a noisy current pulse with a mean amplitude of 1.90 nA and a standard deviation of 0.3 nA in 2,200 L3 and 1,000 L5 pyramidal cells randomly distributed within a 3 mm diameter cylindrical cortical column but unconnected from each other or any other neuron (Figure 5.2C-D). The current pulses elicited soma Na^{+} spikes in L3 and L5 pyramidal cells followed by Ca2+ spikes arising in the apical dendrites of L5 pyramidal cells (Figure 5.2D). As expected, the L3 and L5 pyramidal cell populations produced distinctly different laminar LFP and CSD patterns (Figure 5.2E). The current dipole moments based on the STC and on the CSD agree reasonably well for each pyramidal cell population separately (Figure 5.2F). The summation of the activity across the L3 and L5 pyramidal cells produced LFP and CSD patterns that resembled observed patterns (Figure 5.2G), and the current dipole moments calculated through STC or CSD exhibited excellent agreement when ($RDM = 0.69$; $MAG = 0.94$) (Figure 5.2H).

To simulate the lateralized N2pc component, we modeled two columns of independent, unconnected L3 and L5 pyramidal cells, one in each hemisphere placed on the lunate gyrus surface of extrastriate visual area V4 (Figure 5.2B). To simulate the asymmetry observed in the experimental recordings from V4 associated with the focus of attention directed to one hemifield, the mean amplitude of the input to neurons in the left hemisphere was 1.90 nA (representing the focus of attention in the right hemifield), while that to neurons in the right hemisphere was reduced to 1.85 nA. This decreased the probability of eliciting dendritic Ca^{2+}-spikes and reduced the amplitude of the late CSD sink/sources. With this more complete simulation, we calculated the spatial distribution of voltages at two time points based on the ground-truth, the STC, and the CSD approaches and observed virtually indistinguishable patterns (Figure 5.2I).

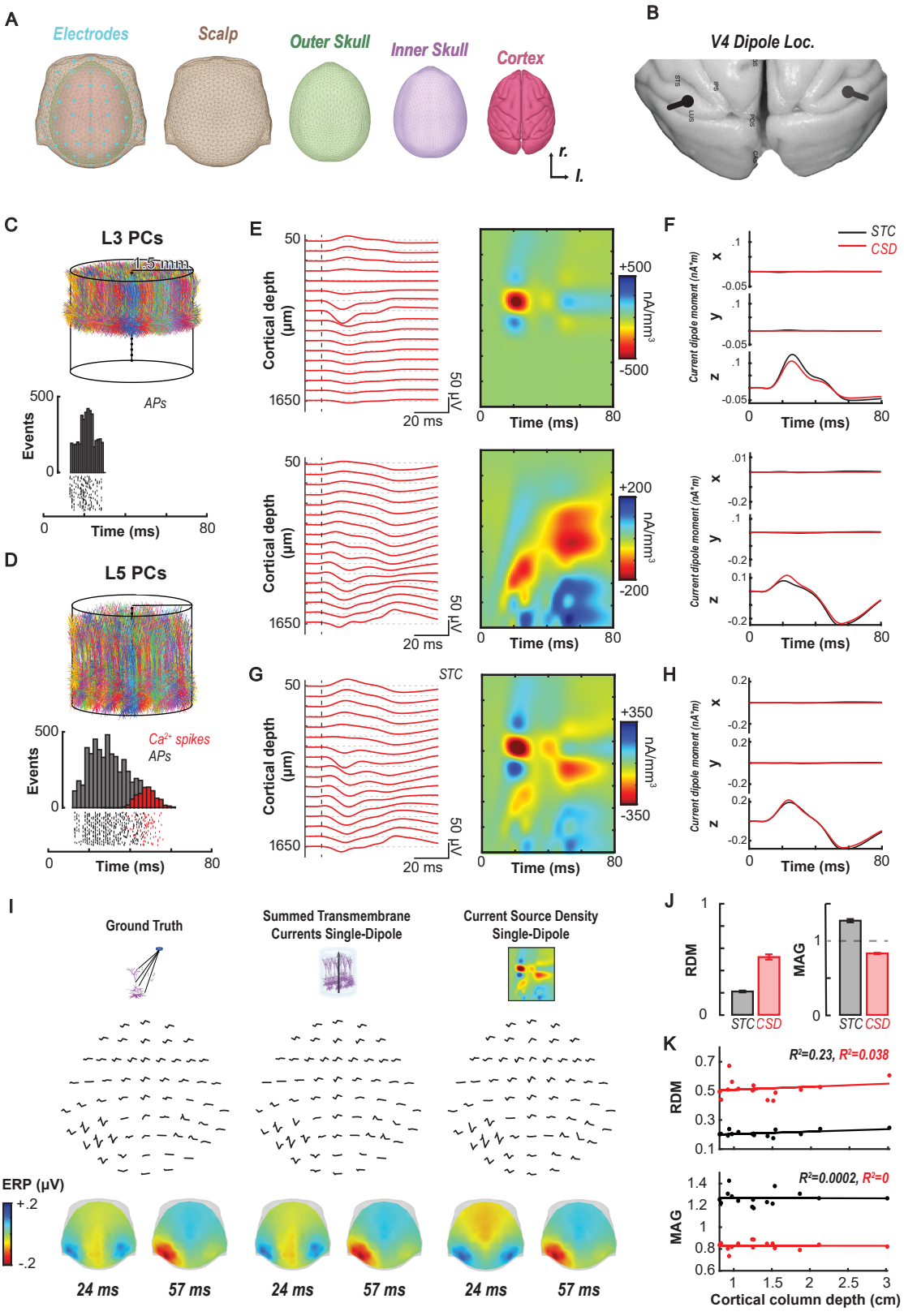

Figure 5.2: Biophysical forward modeling of synthetic data
(Continued on the following page.)

Figure 5.2: A. Boundary element model composite with electrode locations and color-coded surfaces obtained from the NIMH Macaque Template version 2.0 derived from 31 macaque brains. B. Illustration of simulated stronger (black) and weaker (gray) dipoles in area V4 between the superior temporal sulcus and lunate sulcus. C-D. Top, Simulated cortical column of 3 mm diameter comprised of 2,200 L3 (C) and 1,000 L5 pyramidal cells (D). The somas were randomly distributed in the cylinder at depths corresponding to the vertical extent of deep L3 and of L5 in area V4. Bottom, Raster plots and associated poststimulus time histograms of soma Na^+ action potentials (black) and dendritic Ca^{2+} spikes (red) produced by 100 randomly selected L3 pyramidal cells (C) and L5 pyramidal cells (D) in response to brief suprathreshold stimulation with a noisy current pulse (mean amplitude: 1.9 nA). Each neuron received stimulation with uniform probability between 10 and 20 ms after the launch of each simulated testing trial. E. LFP (left) and CSD (right) evoked by the suprathreshold stimulation of the collection of L3 (top) and L5 (bottom) pyramidal cells. Each neuron received stimulation with uniform probability between 10 and 20 ms after the beginning of each simulated testing trial. F. X, Y, and Z components of the current dipole moment calculated from the summed transmembrane currents of all neurons (STC, black) and from the CSD (red) for the L3 (top) and L5 (bottom) cells. G. LFPs (left) and CSD (right) evoked by combined suprathreshold stimulation of L3 and L5 pyramidal cells. H. X, Y, and Z components of the current dipole moment calculated from the summed transmembrane currents of all L3 and L5 pyramidal cells (black) and from the CSD (red) derived from L3 and L5 pyramidal neurons. I. Spatial EEG derived from populations of L3 and L5 pyramidal cells in V4 on the lunate gyrus of each cortical hemisphere with weaker current pulses in the right hemisphere. Results are compared between the ground-truth compartment-based calculation (left), the STC single-dipole (middle), and the CSD single-dipole (right). The spatial distributions of cranial voltages derived from each approach (bottom) are difficult to distinguish from one another. J. Comparison of the EEG estimated from the STC single-dipole (black) and the CSD single-dipole (red) to the ground-truth compartment based EEG at 15 random locations in the monkey's brain based on the relative difference (RDM) (top) and magnitude (MAG) (bottom) measures. K. RDM (top) and MAG (bottom) measures comparing ground-truth compartment-based EEG to that derived from STC (black) and CSD (red) as a function of the depth of the center of mass of cylinder of 2,200 L3 and 1,000 L5 simulated pyramidal cells relative to the scalp. Across 15 random cortical column locations in the macaque brain neither estimate derived from either method varied with depth.

To account for different depths and orientations of cortical columns in these estimates derived from combined L3-L5 activity, to the ground-truth EEG we compared the EEG derived from the STC single-dipole method and from the CSD single-dipole method placing the cylinders of simulated pyramidal cells at 15 randomly selected locations throughout the monkey brain. Relative to the ground-truth EEG, the EEG derived from the STC single-dipole corresponded better ($RDM = 0.21 \pm 0.01$; $MAG = 1.27 \pm 0.02$) than that derived from the CSD single-dipole ($RDM = 0.52 \pm 0.02$; $MAG = 0.83 \pm 0.01$) (Figure 5.2J). Given the relationship between electric field strength relative to dipole distance, we examined whether RDM or MAG values varied with cortical column depth relative to the scalp. A linear regression of these measures as a function of depth showed no variation for either the STC (R^2 for $RDM = 0.23$, for $MAG = 0.00$) or the CSD (R^2 for $RDM = 0.04$, for $MAG = 0.00$) (Figure 5.2K). Thus, we demonstrate that the synthetic application of this approach is sufficient to yield expected spatio-temporal EEG patterns. We now proceed to employing these methods through forward modeling of empirical data.

5.3.2 Experimental Design

Before forward modeling, three objectives must be accomplished. First, monkeys must be trained to perform the cognitive task to proficiency. The representative ERP component used do demonstrate the novel forward modeling approach was the N2pc. The N2pc manifests as a function of the deployment of selective visual attention (Eimer, 1996; Luck and Hillyard, 1994, 1990; Woodman and Luck, 1999) (Eimer, 1996; Luck and Hillyard, 1990, 1994; Woodman and Luck, 1999). To investigate the N2pc, we trained macaque monkeys to perform a visual search task (Figure 5.1A-B) requiring selective attention's rapid deployment. Previous work demonstrates this task elicits an N2pc in macaque monkeys (Purcell et al., 2013). Two macaque monkeys (designated Ca, He) performed visual search for an oddball color target (red or green), presented within an array of 5 uniform distractors (green or red) (N sessions: monkeys Ca, 21; He, 9). Each animal performed above chance [$chance = 0.166$] (behavioral accuracy: monkeys Ca, $M = 0.88$, $SEM = 0.021$; He, $M = 0.81$, $SEM = 0.024$) indicating they understood the task and were selectively deploying attention to accomplish it. Second, the ERP must be obtained to confirm it is being elicited. We sampled extracranial voltage fluctuations from an electrode placed outside the brain and above area V4. An N2pc was observed (Figure 5.1B) with this electrode. Third, suitable and replicable intracranial recordings must be obtained to measure local field potentials and calculate the current dipole during task performance. We obtained neural samples across the cortical layers with linear electrode arrays. After establishing that each penetration was orthogonal to the cortical surface and restricted to a cortical column, the synaptic activation was measured during task performance. The spatiotemporal profiles of synaptic currents are displayed in Figure 5.1C for both the attended condition (when the search target was present in the column receptive field) and the unattended condition (when the target was positioned outside the column receptive field). Recordings were restricted to area V4 on the prelunate gyrus, a hypothesized contributor to the N2pc (Westerberg et al., 2022b; Woodman et al., 2007) and location where laminar activity orthogonal to the cortical surface can be reliably measured (Nandy et al., 2017). Coincident with the N2pc, we observed differences in synaptic currents across the layers of V4 (Figure 5.1D).

5.3.3 Modeling Application to In Vivo Cortical Activity

We employed forward modeling to compute the voltage distribution on the cranial surface caused by the translaminar currents in V4 (Nunez et al., 2019; Riera et al., 2012). Acknowledging that the currents generated by one column within area V4 are probably too weak to produce observable cranial voltages, we treated the current measured in one column as representative for the broader cortical tissue within the 3 mm cylinder contributing to the EEG. Based on the average V4 current density (Figure 5.3A), we derived the dipole moment (Figure 5.3B) embedded in a boundary element model (BEM) of a macaque monkey head

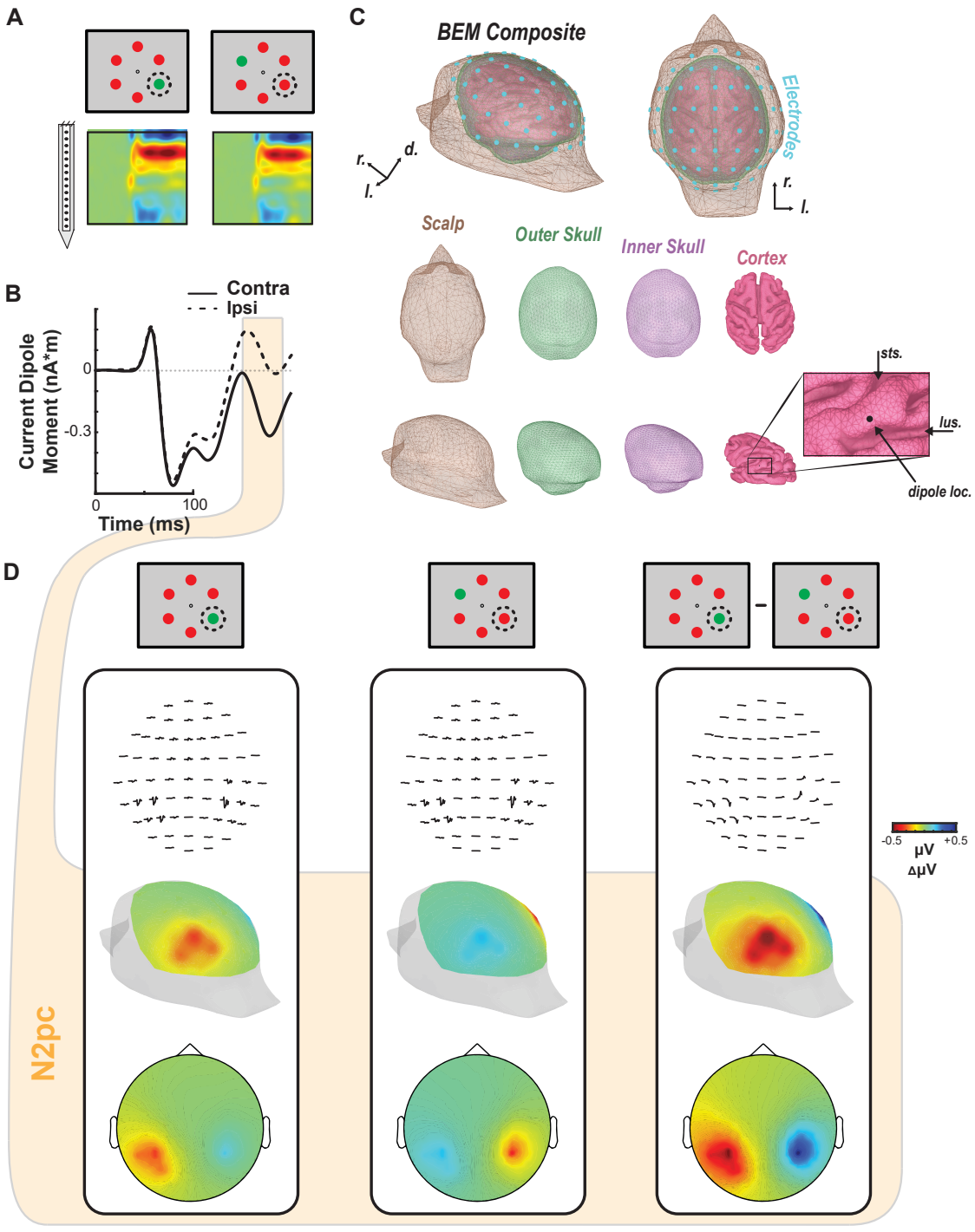

Figure 5.3: Biophysical forward modeling
(Continued on the following page.)

(Figure 5.3C). That dipole was strongest when the target was within the receptive field of the column. Lead fields were generated for a dipole on the convexity between the lunate and superior temporal sulci, where

Figure 5.3: A. Contrasting conditions (i.e., attended target in RF vs. attended target opposite RF) and corresponding CSD ($n = 30$ sessions) used for determining the current dipole moment used for the forward model. B. Dipole moment computed from the session averaged CSD ($n = 30$) across the time of array presentation for the target in RF (solid line, contra) and target opposite RF (dashed line, ipsi) conditions. N2pc epoch, defined as 150-190 ms after array onset, highlighted in orange. C. Boundary element model composite and color-coded surfaces, generated from MR scans from monkey Y, used by the forward model. Bottom right inset shows the position of the dipole used to generate the simulated EEG. Cyan discs ($n = 61$) represent the locations used to measure the simulated EEG. D. Simulated EEG distributions for a target inside the RF (left), target opposite RF (middle), and the difference between conditions (right). Voltage line plots across time for each simulated EEG electrode are shown at top. Voltage heatmaps for each condition are shown from a perspective over visual cortex (posterolateral view, center) and in 2D disc view (bottom). Heatmaps are plotted as average polarization during the time of N2pc (150-190 ms following array onset).

neurophysiological samples were taken (Figure 5.3C). Forward model solutions were calculated during the N2pc (150-190 ms following array presentation). The resulting spatial distribution of voltages was maximal posterolaterally with higher values contralateral to the target (Figure 5.3D). The spatial distribution of the difference in voltages when the target versus distractor was in the receptive field exhibited negativity contralateral to the target that was maximal posterolaterally. These results of the forward model were effectively indistinguishable from previous reports of the N2pc. Moreover, the forward model voltage distributions were robust to data thinning. That is, they were qualitatively similar when using the CSD from a single session (Figure 5.4A) as well as the CSD from each monkey individually (Figure 5.4B-C). Thus, currents measured from columns in V4 are sufficient to produce a voltage distribution over the scalp that emulates the observed N2pc.

To investigate the specificity of this relationship, we calculated forward models produced by dipoles placed at other locations in V4. First, placing the dipole at two different locations on the convexity of the prelunate gyrus resulted in cranial voltage distributions that were qualitatively similar to one another as well as to the original dipole location (Figure 5.5A-B). This result confirms the robustness of the relationship between current dipoles in V4 and the N2pc. Second, the dipole was placed within V4 in the anterior bank of the lunate sulcus (Gattass et al., 1988) (Figure 5.5C). The dipole in this location is not oriented perpendicular to the cranial surface. Although LFP samples have not been measured in this region, there is no a priori reason to assume that the laminar profile of sulcal CSD would be different from that on the gyrus within the same cortical region. The dipole in the sulcus, hereafter referred to as lusV4, resulted in a more posterolateral spatial voltage distribution and similar lateralization relative to target hemifield. However, the forward model voltages were weaker than those derived from dipoles on the gyrus. These findings show that the summation of currents from multiple parts of V4, both gyral and sulcal, contribute to the N2pc. The spatially extensive appearance of the observed ERP thus can be partly understood as arising from variation

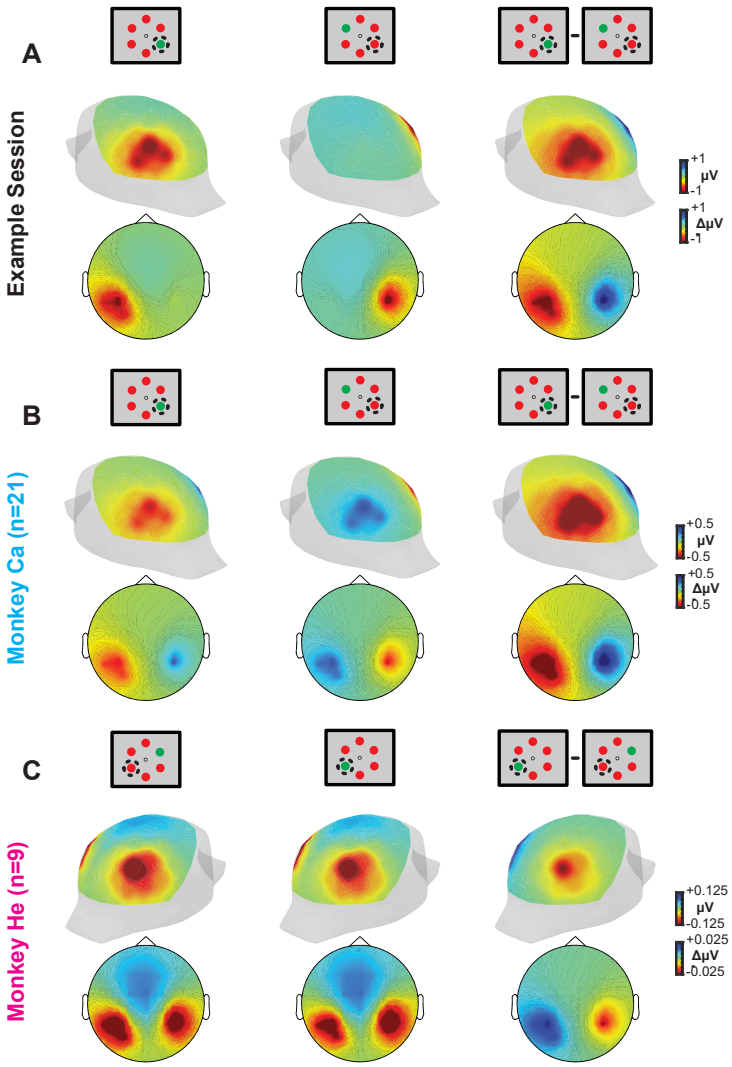

Figure 5.4: EEG forward models for example session CSD and individual monkey CSD. EEG voltage distribution over the scalp of the BEM simulated with a 61-channel electrode EEG array computed using CSD from an example session (A). and from CSD measured and averaged across sessions from monkey Ca (B) and monkey He (C). Both 3D posterolateral views and 2D disc views are shown for each subset of data. 3D head images are oriented such that the hemisphere in which the recordings were conducted are highlighted (left hemisphere, monkey Ca and example session; right hemisphere, monkey He). Note the difference plots are also computed such that the attention target ipsilateral to the recording chamber is subtracted from the contralateral presentations.

in the orientation of contributing dipoles.

It seems unlikely that an ERP would arise from just one cortical area. Certainly, other cortical areas contribute to target selection and attention allocation during visual search. Therefore, using this forward modeling tool, we explored the possible contributions of other cortical areas to the N2pc. Lacking a strong a priori rationale for variability off columnar currents between cortical areas, we adopted provisionally the most parsimonious assumption that the dipole measured in V4 is representative of that in other cortical areas.

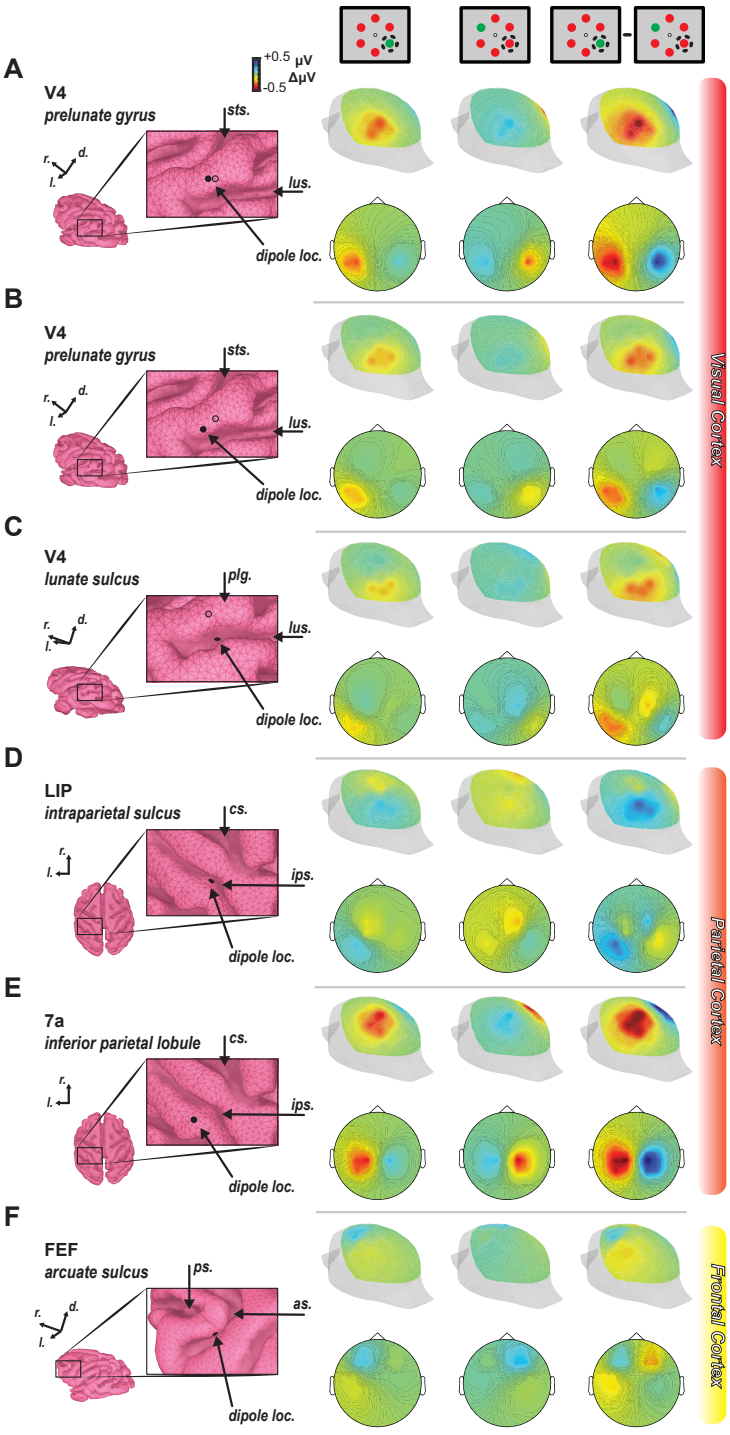

Figure 5.5: Forward models from different bilaterally symmetric dipole locations
(Continued on the following page.)

First, we modeled the possible contribution of two areas in parietal cortex (Figure 5.5D). The lateral intraparietal area (LIP), located on the lateral bank of the intraparietal sulcus, is known to contribute to

Figure 5.5: The dipole was calculated from the current source density measured 150-190 ms following array presentation. Positions are shown on the enlarged cortex boundary element model surface with filled circle. In visual cortex panels, an additional unfilled circle denotes the position of the dipole used in (Figure 5.2). Anatomical landmarks are indicated for reference in the inset images with the following abbreviations: sts – superior temporal sulcus, lus – lunate sulcus, plg – prelunate gyrus, cs – central sulcus, ips – intraparietal sulcus, ps – principal sulcus, as – arcuate sulcus. Cranial voltage heatmaps are displayed on posterolateral and 2D disc views for target in contralateral hemifield (left), target in ipsilateral hemifield (middle), and their difference (right). A-B. Dipoles placed at two other sites on the prelunate gyrus generate cranial voltages that were effectively indistinguishable from that observed with the first dipole location. C. Dipoles placed in part of V4 in the lunate sulcus generate a cranial voltage pattern with similar lateralization but different spatial distribution due to dipole orientation. D. The dipoles were also positioned in the lateral intraparietal area (LIP) on the lateral bank of the intraparietal sulcus, a previously hypothesized generator of the N2pc. E. Another location in parietal cortex (area 7a) was chosen as it also demonstrates robust attentional modulation and is located on a gyrus. F. Lastly, FEF was chosen as it has been related to the N2pc previously and also shows robust attentional modulation. It is important to note that the dipoles used throughout all panels were those measured in prelunate V4 and may or may not be a sufficient representation of the empirically measured currents in that area.

target selection during visual search and is a well-recognized node in the attention network Bisley et al. (2011); Goldberg et al. (2006); Ipata et al. (2006); Tanaka et al. (2015); Thomas and Paré (2007). Area 7a, occupying the inferior parietal gyrus, also shows robust attention-related modulation (Constantinidis and Steinmetz, 2001b,a; Rawley and Constantinidis, 2010; Steinmetz et al., 1994; Steinmetz and Constantinidis, 1995). Unlike LIP, area 7a is oriented to be more conducive to the biophysical generation of potentials measured at the scalp. The forward model of a dipole in LIP produced a voltage pattern with centromedial distribution and weak lateralization relative to target location. This indicates that neural processes in LIP contribute weakly if at all to the N2pc in macaques. Conversely, forward models of a dipole positioned in 7a produced robust potentials measurable at the scalp. However, these potentials were concentrated more centromedially than the posterolateral N2pc.

Next, we modeled the contribution of the frontal eye field (FEF) in the arcuate sulcus of the frontal lobe (Figure 5.5E). FEF plays a significant role in visual search and visual attention more generally (Schall, 2015), in part through direct influences on V4 (Moore and Armstrong, 2003; Moore and Zirnsak, 2017). Simultaneous recordings of spikes and LFP in FEF with occipital EEG have demonstrated correlations between LFP in FEF and N2pc polarization (Cohen et al., 2009; Purcell et al., 2013). Nevertheless, the forward model of the dipole in FEF produced a cranial voltage distribution different from the observed N2pc but sharing a modest degree of lateralization relative to target hemifield. The results of forward modeling dipoles in parietal and frontal areas demonstrate that cortical areas contributing little biophysically to an ERP can contribute neuro-computationally to the process indexed by that ERP.

A given cortical area is unlikely to be the only generator of an EEG signal. Thus, the locations and

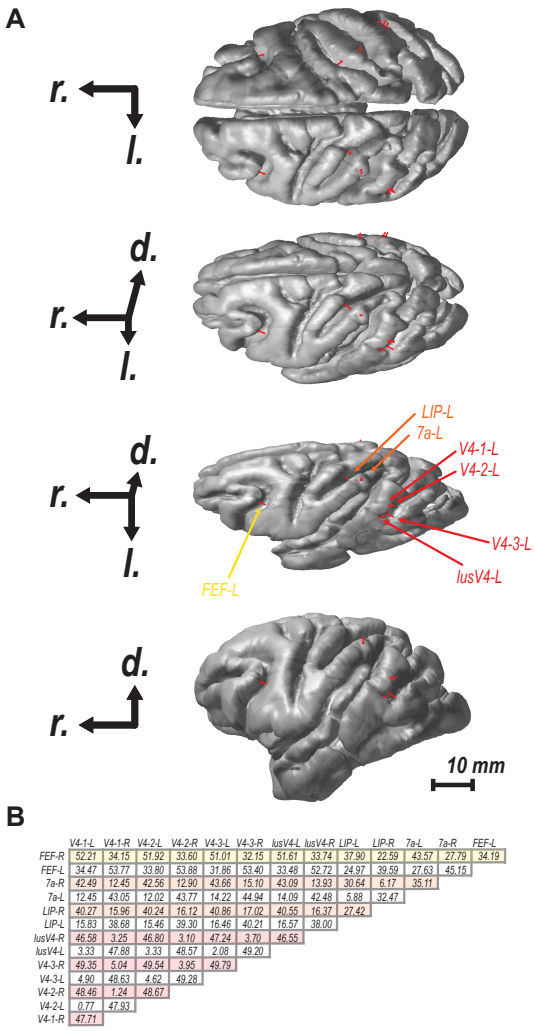

	V4-1-L	V4-1-R	V4-2-L	V4-2-R	V4-3-L	V4-3-R	lusV4-L	lusV4-R	LIP-L	LIP-R	7a-L	7a-R	FEF-L
FEF-R	52.21	34.15	51.92	33.60	51.01	32.15	51.61	33.74	37.90	22.59	43.57	27.79	34.19
FEF-L	34.47	53.77	33.80	53.88	31.86	53.40	33.48	52.72	24.97	39.59	27.63	45.15	
7a-R	42.49	12.45	42.56	12.90	43.66	15.10	43.09	13.93	30.64	6.17	35.11		
7a-L	12.45	43.05	12.02	43.77	14.22	44.94	14.09	42.48	5.88	32.47			
LIP-R	40.27	15.96	40.24	16.12	40.86	17.02	40.55	16.37	27.42				
LIP-L	15.83	38.68	15.46	39.30	16.46	40.21	16.57	38.00					
lusV4-R	46.58	3.25	46.80	3.10	47.24	3.70	46.55						
lusV4-L	3.33	47.88	3.33	48.57	2.08	49.20							
V4-3-R	49.35	5.04	49.54	3.95	49.79								
V4-3-L	4.90	48.63	4.62	49.28									
V4-2-R	48.46	1.24	48.67										
V4-2-L	0.77	47.93											
V4-1-R	47.71												

Figure 5.6: Spatial relationship between dipole sites
A. Four views of structural magnetic resonance rendering of the brain of monkey Y with dipole positions and orientations shown in red. Each plot shows a different 30° rotation around the rostral-caudal axis as indicated by the axes at left (r.: rostral, l.: lateral, d: dorsal). B. Euclidean distances between each of the 14 dipole locations across both hemispheres. V4-1 refers to the dipole used in Figure 5.3 and Figure 5.4. V4-2, The labels V4-3, lusV4, LIP, 7a, FEF are those used in (Figure 5.5). All distances are reported in millimeters (scale bar on lower right).

various dipole orientations of diverse sources could explain the spatial distribution of the EEG (Figure 5.6). Therefore, we modeled and quantitatively compared all combinations of plausible dipole sources to the N2pc measured from a monkey (identified as Z) performing the same visual search task across 18 recording sessions with an array of 15 EEG electrodes positioned across the cranium (Figure 5.7A). Crucially, this monkey did not have a craniotomy that would affect the spatial distribution of the EEG. Computing the forward solution for each of the 5 dipole locations and unique orientations, we linearly summed the solutions for each of the 31 combinations of dipoles across the areas. During the time period of the N2pc in

these data (150-190 ms after the visual search array based on data in monkeys Ca and He) we observe a significant N2pc at the posterior EEG recording sites P5 and P6 ($t(35) = 2.42$, $p = 0.02$) (Figure 5.7B).

For each of the 31 combinations of source locations, we measured the correlation between the empirical data and the modeled data at each of the matching 15 electrode positions. Note, a distinct forward model result was generated for each of the 30 laminar recording sessions meaning each correlation was between the empirical EEG voltage distribution and the 30 sessions of data for each of the 31 model configurations. A single example is shown in the inset of Figure 5.7C. Results of all correlations are summarized in Figure 5.7C with their corresponding configurations displayed below each bar. While many source configurations resulted in significant correlations with the empirical data, two stand out as superior to the others as indicated by their largest R-squared value – V4 + lusV4 and V4 + lusV4 + LIP. Note both of these models incorporate sources across both gyral and sulcal V4. Also, the better of the two also incorporates a parietal source. We found that the models have highest correlation with empirical values included gyral and sulcal V4 sources (Figure 5.7D). The most representative model exhibits the lateralized and posteriorly-distributed signature of the N2pc (Figure 5.7E).

5.4 Discussion

ERPs have been a powerful tool for investigating brain mechanisms of human cognition for decades. While further insights can be gained from EEG alone, its utility as a biomarker of disorder and index of mechanism is limited by uncertainty about its generation. In other words, knowing the composition of the neural circuitry generating specific cognitive signals in the EEG will improve understanding of what the cognitive signal represents and constrain models of the cortical circuitry enabling the cognitive process indexed by the EEG signal. A systematic search for EEG generators with invasive methods in humans is not possible. Fortunately, as a common animal model for human cognition, macaque monkeys exhibit EEG signals like the N2pc. Even so, key blocks in the bridge from neural activity within cortical columns to the macroscopic EEG signal are missing. Here we provided an approach by which measurement of neural activity across the cortical layers in macaque monkeys during cognitive tasks is forward modeled to infer its impact on the global EEG signal. To our knowledge, this is the first documentation of forward modeling synaptic currents across cortical layers to the EEG signal in awake, behaving primates. It is also the first experimental confirmation in primate cortical tissue of theoretical models developed with data from rodents.

In investigating the neural sources of the ERP component known as the N2pc as a demonstration for this approach, our results provide strong support for the hypothesis that it is generated from neural activity present in occipital and parietal areas. Early reports of the N2pc hypothesized that areas such as V4 contributed to its generation (Luck and Hillyard, 1994) with findings from an MEG study (Hopf et al., 2000)

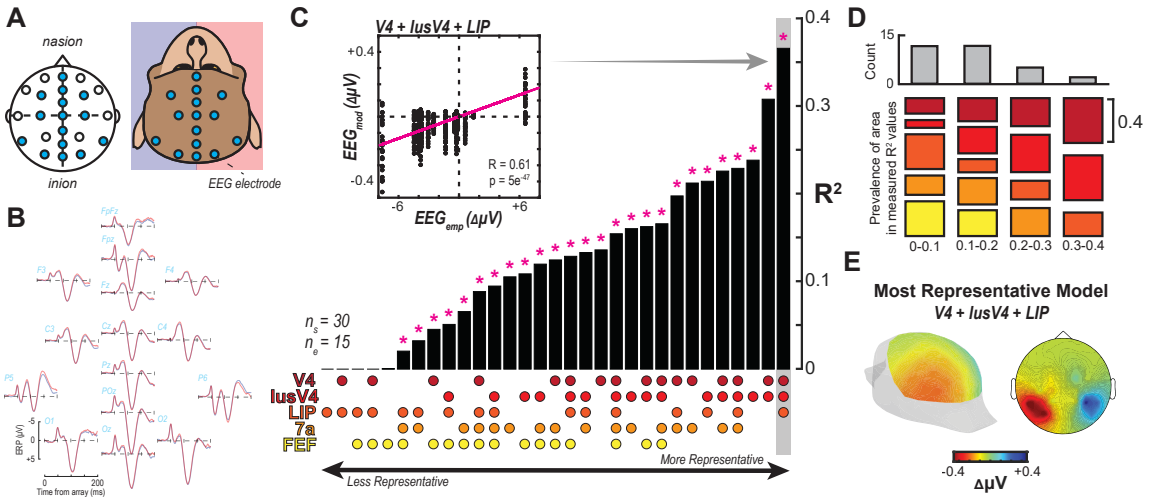

Figure 5.7: Comparison of N2pc voltage distribution over the scalp between empirical measurement and forward models

A. EEG was recorded in a subset of 10-10 configuration electrodes ($n = 15$) from a monkey with intact skull. B. Voltage potentials for contra- vs. ipsilateral presentations of an attentional target in the visual search task. Differences are observed primarily at posterior sites about 150-190 ms following array presentation. C. Pearson correlation between EEG signal measured empirically (EEGemp) and the forward modeled EEG signal (EEGmod) for the difference between a contra- and ipsilateral target presentation at each of the electrode sites present in the empirical recording ($n = 15$). Data was taken as the average difference between 150-190 ms following array presentation for both empirically measured and modeled data. EEG model was generated for each laminar recording session ($n = 30$). Correlation was performed for each possible combination of V4, lusV4, LIP, 7a, and FEF sources ($n = 31$). R-squared was computed and the bar plot reflects these values sorted from lowest to highest with significant correlation (following Bonferroni correction) indicated above with an asterisk. The combination of sources yielding each bar's value is indicated below by dots with the legend at left. Inset shows the correlation observed with data for a single bar (V4+lusV4+LIP). D. R-squared values were grouped into 0.1 bins. Histogram plotted at top for the frequency of R-squared values. For each of those bins, the prevalence of each source was evaluated where the size of each colored bar indicates the total number of times that source was present in a model resulting in a R-squared value in the respective bin. For example, only V4, lusV4, and LIP sources were present in R-squared value measurements in the 0.3-0.4 bin. E. EEG distribution from the modeled data at the 15 recording sites using the most representative model (V4+lusV4+LIP).

lending more direct support for occipital and parietal sources, specifically. Our comparison of various configurations of plausible neural sources with an empirically measured N2pc distribution suggests that the combination of sources in occipital area V4 and parietal area LIP best models the N2pc. This demonstration serves to highlight the importance of considering the biophysical geometry in EEG production. It is important to note that the dipole used for the modeling was measured in V4 and applied for all other areas in addition to V4. Therefore, neural recordings in LIP are necessary to determine whether a pattern of laminar activation sufficient to produce a dipole at the time of the N2pc is present. While that caveat for LIP remains, we can more confidently conclude that the laminar activation in V4 contributes to the N2pc as our measured activity comes specifically from that area.

While significant insight is gained from evaluating the biophysical plausibility of this variety of brain areas, the results highlight a potentially counterintuitive relationship. That is, FEF, LIP, and 7a—areas definitely contributing computationally to attentional control—do not contribute much biophysically to the N2pc indexing that attention. In particular, a source model of a single dipole in FEF is the least correlated with empirical data, and FEF is not present in the top 9 best-correlated models. This highlights an important consideration—locations of neural computation (e.g., target enhancement, distractor suppression, attention deployment) and locations of the biophysical sources of an ERP indexing those computations need not be the same. That is, while an area like FEF has activation paralleling the N2pc (Cohen et al., 2009; Purcell et al., 2013), its physical position is not sufficient to contribute to its manifestation. In contrast, V4, an area showing more modest attentional modulation than FEF, is oriented in such a way that it is conducive to the generation of electric fields which can be measured at the scalp. However, it is entirely possible that the modulation of activity yielding the difference in dipole present in V4 producing the N2pc originates from FEF (Westerberg and Schall, 2021). Previous work has established that a robust set of connections exist between V4 and FEF (Anderson et al., 2011; Pouget et al., 2009; Schall et al., 1995; Stanton et al., 1995; Ungerleider et al., 2008) and modulation of FEF activity impacts V4 (Moore and Armstrong, 2003; Noudoost et al., 2014). Work remains to better understand the configuration of neural circuitry generating cognitive EEG signals and importantly, the origins of these signals – not just the areas producing the signal measured at the scalp.

While this study represents an important step in mapping microscopic through mesoscopic to macroscopic signals, this research program is by no means complete. Recent work highlights the strength of investigating the neural mechanisms of EEG at an even finer scale. We can better understand the generation of these potentials by understanding the underlying neural processes at the level of individual synapses through simulations (Herrera et al., 2020; Næss et al., 2021). In our modeling, we compute a dipole from the CSD, which is then used to calculate the definite voltage distribution at the scalp. This process sacrifices laminar information about the functional architecture generating EEG. For example, it is difficult to discern whether an observed source/sink in supragranular layers reflects synaptic activation onto the apical dendrites of L5 pyramidal cells, L2/3 pyramidal cells, or some combination (Pesaran et al., 2018). Additionally, CSD methods obscure any variation of neuronal activity in the radial plane of the column (Pettersen et al., 2006), parallel to the cortical layers.

Several decomposition techniques have been proposed to distinguish the contribution of distinct populations of neurons across layers to the LFPs (Di et al., 1990; Einevoll et al., 2007; Głabska et al., 2014; Korovaichuk et al., 2010; Łeski et al., 2010; Makarov et al., 2010). Some methods are based on ICA and PCA decomposition methods that assume zero correlation or independence between the brain sources and

do not account for the biophysical properties of area-specific cortical circuits (Di et al., 1990; Korovaichuk et al., 2010; Łeski et al., 2010; Makarov et al., 2010). Other techniques, such as the laminar population analysis (Einevoll et al., 2007) and dynamic causal modeling (Pinotsis et al., 2017), fit generative models, constructed from knowledge about local circuit processing and architecture to LFP recordings to estimate distinct intracranial sources. Yet, a systematic translation of these different neuronal sources to individual current dipoles and from them to macroscopic EEG signals is still lacking. Riera et al. (Riera et al., 2012) proposed a biophysical modeling strategy to link these scales. Their approach consisted of estimating the characteristic dynamic equations of intracranial currents from phenomenological models of principal neurons, pyramidal cells, and employing them to develop a generalized inverse solver that accounted for distinct neuronal population dynamics. The estimated brain sources would then be used to reconstruct the dynamics of principal neuronal populations through their phenomenological models. Alternatively, recent studies have inferred the circuit-level dynamics underlying cognitive ERPs by fitting the exogenous drives of a predefined canonical cortical microcircuit model to replicate the event-related current dipoles estimated through inverse modeling (Jones et al., 2007, 2009; Law et al., 2022; Næss et al., 2021; Kohl et al., 2022). The canonical cortical microcircuit model was constructed based on anatomical and electrophysiological findings from sensory cortical areas (Jones et al., 2007, 2009). New data from the agranular frontal cortex indicates that this microcircuit model does not generalize (Godlove et al., 2014; Ninomiya et al., 2015).

Theoretical models have explained how patterns of activity across the layers of cortical columns can produce EEG. Previous testing of these models has focused on lissencephalic rodent brains. With the more complex macaque brain, we determined that the observed pattern of laminar activation in a cortical area yields spatial distributions of EEG indistinguishable from previously reported ERP components. In so doing, we demonstrated that the dipole derived from the mesoscopic CSD within a cortical column is a more than adequate representative of the transmembrane currents of pyramidal cells. This work resolves a missing link between microscopic neural signals and macroscopic EEG through mesoscopic columnar dipoles. Establishing this link reveals a cortical source for an important EEG component and offers tools to explore how other patterns of laminar activity contribute to different EEG signals.

5.5 Methods

5.5.1 Animal Care and Surgical Procedures

Procedures were in accordance with National Institutes of Health Guidelines, Association for Assessment and Accreditation of Laboratory Animal Care International Guide for the Care and Use of Laboratory Animals, and approved by the Vanderbilt Institutional Animal Care and Use Committee following United States Department of Agriculture and Public Health Services policies. In this study (Herrera et al., 2022),

two male macaque monkeys (Macaca radiata; monkey Ca, 7.5 kg; He, 7.3 kg) were implanted with MR compatible head posts and recording chambers with craniotomy over V4. One female macaque monkey (Macaca radiata; monkey Y, 7.3 kg) underwent an anesthetic event to perform anatomical imaging. Anesthetic induction was performed with ketamine (5–25 mg/kg). Monkeys were then catheterized and intubated. Surgeries were conducted aseptically with animals under isoflurane (1-5%) anesthesia. EKG, temperature, and respiration were monitored. Postoperative antibiotics and analgesics were administered. Further detail is documented elsewhere (Westerberg et al., 2020a,b).

5.5.2 Magnetic Resonance Imaging

Anesthetized animals were placed in a 3 Tesla Magnetic Resonance Imaging (MRI) scanner (Phillips) at the Vanderbilt University Institute of Imaging Science. T1-weighted 3D MPRAGE scans were acquired with a 32-channel head coil equipped for SENSE imaging. Images were acquired using 0.5 mm isotropic voxel resolution with parameters: repetition 5 s, echo 2.5 ms, flip angle 7°.

5.5.3 Cognitive Task - Visual Search

Monkeys performed a color pop-out search. Search arrays were presented on a CRT monitor at 60 Hz, at 57 cm distance. Stimulus generation and timing were done with TEMPO (Reflective Computing). Event times were assessed with a photodiode on the CRT. We used isoluminant red and green disks on a gray background. Target feature varied within a session. Trials were initiated by fixating within 0.5 degrees of visual angle (dva) of a fixation dot. The time between fixation and array onset was between 750 and 1250 ms. A nonaging foreperiod function was used to determine the fixation period on a trial-by-trial basis. Arrays comprised of 6 items. Array item size scaled with eccentricity at 0.3 dva per 1 dva eccentricity so that they were smaller than the average V4 receptive field (RF) (Freeman and Simoncelli, 2011). The angular position of items relative to fixation varied session to session so that 1 item was positioned at the center of the RF. Items were equally spaced relative to each other and located at the same eccentricity. In each trial, one array item was different from the others. Monkeys made a saccade to the oddball within 1 second and maintained fixation within 2–5 dva of the target for 500 ms. Juice reward was administered following the successful completion of the trial. The target item had an equal probability of being located at any of the 6 locations. Eye movements were monitored at 1 kHz using a corneal reflection system (SR Research Eyelink). If the monkey failed to saccade to the target, they experienced a timeout (1–5 s).

5.5.4 Laminar CSD Recording Procedure

Laminar V4 neurophysiology was acquired at 24 kHz using a PZ5 and RZ2 (Tucker-Davis). Signals were filtered between 0.1 Hz -12 kHz. V4 data was collected from 2 monkeys (monkey Ca: left hemisphere; He: right) across 30 sessions (monkey Ca: 21; monkey He: 9) using 32-channel linear electrode arrays with 0.1 mm interelectrode spacing (Plexon) introduced through the intact dura mater each session. Arrays spanned layers of V4 with a subset of electrode contacts deliberately left outside of cortex. We computed the CSD signal using the spline-iCSD method (Pettersen et al., 2006) as implemented in the CSDplotter toolbox with custom MATLAB (R2021b, The MathWorks) scripts. In Figure 1, we compare our estimated CSD maps with those reported by Westerberg and colleagues (Westerberg et al., 2022b) using the standard CSD method (Nicholson and Freeman, 1975). For the standard CSD method, CSD was computed from the raw signal by taking the second spatial derivative along electrodes (Schroeder et al., 1998; Mehta et al., 2000a; Westerberg et al., 2019; Nicholson and Freeman, 1975) and converting voltage to current (Logothetis et al., 2007). We computed the CSD by taking the second spatial derivative of the LFP:

$$CSD_{t,d} = -\sigma \left(\frac{x_{t,d-z} + x_{t,d+z} - 2x_{t,d}}{z^2} \right)$$

where x is the extracellular voltage at time t measured at an electrode contact at depth d, z is the inter-electrode distance, and σ is conductivity. CSD was baseline corrected at the trial level by subtracting the average activation during the 300 ms preceding array onset from the response at all timepoints. CSD was clipped 10 ms before saccade at the trial level to eliminate the influence of eye movements.

5.5.5 Laminar Alignment

Orthogonal array penetrations were confirmed online through a reverse-correlation RF mapping procedure (Cox et al., 2019b; Nandy et al., 2017; Westerberg et al., 2019). RFs were found to represent portions of visual space consistent with previous reports of V4 (Gattass et al., 1988). Positions of recording sites relative to V4 layers were determined using CSD (Nandy et al., 2017; Schroeder et al., 1998). Current sinks following visual stimulation first appear in the granular input layers of the cortex, then propagate to extragranular compartments. We computed CSD and identified the granular input sink session-wise. Sessions were aligned by this input sink. ‘L4’ refers to the granular input layer, ‘L2/3’ to the supragranular layers, and ‘L5/6’ to the infragranular layers.

5.5.6 Boundary Element Model

The monkey’s head was modeled as an isotropic and piecewise homogenous volume conductor comprised of the scalp, inner and outer skull, and the cortex surface. For the forward modeling of the experimental

data, we employed the surfaces of the cortex, and the scalp and skull compartments obtained from the segmentation of the T1-weighted MRI of monkey Y in SPM12 (Penny et al., 2011) and BrainSuite (Shattuck et al., 2001), respectively. In the detailed biophysical simulations, we utilized the symmetric surfaces provided in the NIMH Macaque Template version 2.0 (Jung et al., 2021) to construct the head model (Figure 5.2A). The position of the EEG electrodes for both models was defined employing the EEG 10-10 system and the monkey's scalp surface as described elsewhere (Giacometti et al., 2014). The scalp, skull, and brain conductivities were set as 0.43, 0.0063, and 0.33 S/m (Lee et al., 2015), respectively.

5.5.7 EEG Forward Model

The EEG scalp potential $V_e(\vec{r},t)$ at any position $\vec{r}_e$ evoked by a continuous field of microscopic electric currents $I(\vec{r},t)$ inside the brain R can be represented by the following inhomogeneous Fredholm integral equation of the second kind (Riera et al., 2012):

$$V_e(\vec{r}_e,t) = V_0(\vec{r}_e,t) + \frac{1}{4\pi\sigma_b}\sum_k \int_{\Omega_k} \vec{j}_k(I,\vec{r}) \cdot \nabla \left(\frac{1}{|\vec{r}_e - \vec{r}|}\right) d\vec{r}^3$$

$$V_0(\vec{r}_e,t) = \frac{1}{4\pi\sigma_b}\int_R \frac{I(\vec{r},t)}{|\vec{r}_e - \vec{r}|} d\vec{r}^3$$

$$\int_{\Omega_k} \vec{j}_k(I,\vec{r}) \cdot \nabla \left(\frac{1}{|\vec{r}_e - \vec{r}|}\right) d\vec{r}^3 \equiv (\sigma_{k+1} - \sigma_k) \int_{S_k} v_k(I,\vec{r}) \cdot \frac{\partial}{\partial \vec{n}_k} \left(\frac{1}{|\vec{r}_e - \vec{r}|}\right) d\vec{r}^2$$

with $\vec{j}_k(I,\vec{r}) = (\sigma_{k+1} - \sigma_k) v_k(I,\vec{r}) \vec{n}_k(\vec{r})/\Delta l$ representing the secondary currents defined for each elemental volumetric shell Ω_k (i.e., a surface S_k of thickness $\Delta l \to 0$). σ_k and $v_k(I,\vec{r})$ denote the conductivity and surface potential of the k-th compartment in the head model (i.e., brain (σ_b), skull, and scalp), and $\vec{n}_k(\vec{r})$ the normal vector to the surface ($\S_k$) of the k-th compartment at location $\vec{r}$.

We assume $I(\vec{r},t) = s(\vec{r},t)$ for $\vec{r} \in V$ and $I(\vec{r},t) = 0$ otherwise, where V is the volume of the brain region of interest, centered at $\vec{r}_m$. If the location of the EEG electrode ($\vec{r}_e$) is far enough from the center $\vec{r}_m$, then $V_0(\vec{r}_e,t)$ can be calculated as a function of the multipolar moments (Riera et al., 2012). Under the assumption of the dipolar model, the EEG forward model can be represented by the former and following equations for $V_0(\vec{r}_e,t)$:

$$V_0(\vec{r}_e,t) = \frac{1}{4\pi\sigma_b}\int_V \vec{d}(\vec{r},t) \cdot \nabla_{\vec{r}} \left(\frac{1}{|\vec{r}_e - \vec{r}|}\right) d\vec{r}^3$$

where $\vec{d}(\vec{r},t)$ denotes the current dipole moment. The theoretical framework and numerical stratgies used to compute the potentials ($v_k(I,\vec{r}), V_0(\vec{r}_e,t)$) to obtain the EEG scalp potential $V_e(\vec{r}_e,t)$ are detailed elsewhere

(Hämäläinen and Sarvas, 1989).

The current dipole moment $\vec{d}(\vec{r},t)$ is assumed to originate from postsynaptic currents caused mainly by the activation of pyramidal cells perpendicular to the cortical surface (Hämäläinen et al., 1993) and from nonlinear processes taking place in their dendrites (Herrera et al., 2020; Suzuki and Larkum, 2017). Therefore, we can write $\vec{d}(\vec{r},t)$ as $\vec{\mu}(\vec{r}) \cdot d(t)$, with $\vec{\mu}(\vec{r})$ and $d(t)$ representing its orientation and time-varying amplitude, respectively (Riera et al., 2012). The activation waveform $d(t)$ was estimated from the volumetric current sources (CSD) calculated from the laminar recordings, and the orientation of the dipoles from a weighted average of the normal to the cortical surface at the location of the dipole and the normal of its neighboring triangles. Considering the assumptions made to calculate the CSD, the amplitude $d(t)$ of the current dipole moment from the CSD in a volume of interest V is given by:

$$d_z(t) = \pi r_c^2 \int CSD(z,t)(z - z_m)dz$$

The z-axis is defined as the direction perpendicular to the cortex with positive and negative values toward the supragranular and infragranular layers, respectively. We modeled dipoles located in areas V4, lusV4, LIP, 7a, and FEF and assumed that the cortical columns in those areas were perfect cylinders of 3 mm radius (r_c). The integrals were calculated using the trapezoidal method, where each subinterval corresponds to a particular grid point in the corresponding CSD method.

5.5.8 Biophysical Simulations

We generated a synthetic data set using detailed biophysical models of neurons to evaluate the equivalent current dipole derived from the CSD. We simulated the responses to a current pulse of 30 ms duration with noisy random amplitude in two populations of independent (unconnected) L3 and L5 pyramidal cells described previously by (Eyal et al., 2018) (ModelDB, accession 238347, 2013_03_0603_789_H41_03, active model cell0603_08_model_602) and (Hay et al., 2011) (ModelDB, accession 139653, “cell 1”). The somas of the neurons were distributed uniformly in a 3 mm diameter cylinder with height corresponding to the vertical extent in area V4 of lower L3 (675-750 m below the pia matter) and of L5 (1250-1750 m) (Figure 2C). We determined the number of simulated neurons from each population, maintaining the ratio of neurons in L3 and L5 reported in the anatomical literature (Vanni et al., 2020) and finding the minimal number of neurons in a cortical column of 3 mm diameter under this stimulation paradigm necessary to reproduce the approximate amplitude of the CSD observed in the V4 experimental data (Figure 1D). We considered this approach since not all neurons are active at the same time during a task in a real cortical column composed of millions of neurons (e.g., see (Westerberg et al., 2022b)). We simulated 2,200 L3 and

1000 L5 pyramidal cells. The amplitude of the current pulse was sampled from a Gaussian distribution with a standard deviation of 0.3 nA. To simulate the asymmetry observed in the experimental recordings from V4, we used mean current amplitudes of 1.90 nA and 1.85 nA for neurons in the left and right hemispheres, respectively. Reducing the mean current amplitude for neurons in the right hemisphere decreased the probability of eliciting dendritic Ca^{2+}-spikes in L5 pyramidal cells, reducing the amplitude of the late sink/sources in the CSD map (Figure 5.2E) and creating a weaker dipole current source. The beginning of stimulation of each neuron was randomly sampled from a uniform distribution between 10 and 20 ms after the simulation was initiated. The somas of the neurons were distributed uniformly in a 3 mm diameter cylinder with height corresponding to the vertical extent in area V4 of lower L3 (675-750 μm below the pia matter) and of L5 (1250-1750 μm) (Figure 5.2C). All simulations were performed in Python using LFPy (Hagen et al., 2018), which builds on NEURON (Hines et al., 2009).

Simulating measurements with a linear microelectrode array, we calculated the LFP produced by the activity of the neurons at 17 equally spaced vertically aligned points located at the center of the cortical column. As in the experiments, the inter-electrode distance was 100 m. We employed the point-source approximation in LFPy to compute the extracellular potentials. The LFP was obtained by low-pass filtering at 100 Hz. The CSD patterns of the synthetic data sets were calculated using the spline-iCSD method (Pettersen et al., 2006) as implemented in the CSDplotter toolbox with custom MATLAB (R2021b, The MathWorks) scripts (Herrera et al., 2020).

We estimated the EEG produced by the simulated population of pyramidal neurons using three approaches: compartment-based, summed transmembrane currents single-dipole, and CSD single-dipole approaches. The compartment-based approach considers the transmembrane currents entering and escaping the extracellular medium as current sources/sinks. It calculates the EEG mapping the transmembrane currents of all neurons into the scalp potentials (Herrera et al., 2020; Næss et al., 2021). Thus, for the compartment-based approach, $V_0(\vec{r}_e,t)$ becomes (Herrera et al., 2020):

$$V_0(\vec{r}_e,t) = \frac{1}{4\pi\sigma_b}\sum_{p=1}^{N_n}\sum_{i=1}^{N_p}\sum_{c=1}^{N_c^i}\frac{I_{p,c}^i(t)}{|\vec{r}_e-\vec{r}_{p,c}^i|}$$

where N_n, N_p, and N_c^i denote the total number of neuron types, the number of neurons in the p-th population and the number of compartments, I, in the i-th neuron of the p-th population, respectively. The term $\vec{r}_{p,c}^i = x_{p,c}^i, y_{p,c}^i, z_{p,c}^i$ indicates the coordinates of the c-th compartment of the i-th neuron in the p-th population. The term $I_(p,c)^i(t)$ is the transmembrane current of the c-th compartment of the i-th neuron in the p-th population. In both the summed transmembrane currents single-dipole and CSD single-dipole approaches, the EEG is estimated using the EEG dipolar model which assumes the activity of a cortical

column can be accurately represented by an equivalent current dipole moment at the center of the column. The summed transmembrane currents single-dipole approach calculates the equivalent current dipole moment as the sum of all dipoles between the center of mass or center of the cortical column and every compartment of each neuron. Thus, the amplitude and orientation of the equivalent current dipole moment are given by the sum (Hagen et al., 2018; Næss et al., 2021),

$$\vec{d}(\vec{r},t) = \sum_{p=1}^{N_n} \sum_{i=1}^{N_p} \sum_{c=1}^{N_c^i} (\vec{r}_{p,c}^{\,i} - \vec{r}_m) I_{p,c}^i(t)$$

with $\vec{r}_m$ representing the center of mass of the cortical column, which is the coordinates of the dipole. In the CSD single-dipole approach, the orientation of the dipoles is fixed, corresponding to that of the cortical column, and the amplitude. For our simulations, $N_n = 2$, $N_{p=1,2}$ with $N_1 = N_{L3} = 2200$ and $N_1 = N_{L5} = 1000$. The estimated current dipole moments for each neuronal population and their combined activity were low-pass filtered at 100 Hz.

To validate the EEG estimated using the CSD single-dipole and the transmembrane currents single-dipole approaches, we compared them to the compartment-based EEG, considered as the "ground-truth" EEG. We quantified the mismatch between the transmembrane currents single-dipole and the CSD single-dipole estimations ($\hat{y}$) and the ground-truth EEG (y) by calculating the relative magnitude (*MAG*)) and the relative difference (*RDM*): (Meijs et al., 1989):

$$MAG = \frac{||\hat{y}||}{||y||} = \frac{\sqrt{\sum_t \hat{y}(t)^2}}{\sqrt{\sum_t y(t)^2}}$$

$$RDM \equiv \left|\left| \frac{y}{||y||} - \frac{\hat{y}}{||\hat{y}||} \right|\right| = \sqrt{\sum_t \left(\frac{y(t)}{\sqrt{\sum_t y(t)^2}} - \frac{\hat{y}(t)}{\sqrt{\sum_t \hat{y}(t)^2}} \right)^2}$$

where a relative difference (RDM) closer to 0 and magnitude (MAG) closer to 1 indicates a higher degree of similarity between a dipolar approach and the ground truth. To account for different depths and orientations of the cortical column, we calculated these measures at 15 randomly selected cortical columns throughout the monkey brain. Furthermore, given the relationship between electric field strength relative to dipole distance, we evaluated the dependence of these measures on the depth of the cortical column relative to the scalp. We defined the depth of the cortical column as the shortest distance between the center of mass of the cortical column and the scalp surface utilized in the EEG forward model. We calculated this distance using the Matlab point2trimesh function.

5.5.9 10-20 EEG Recordings

One monkey (monkey Z) was implanted with an array of electrodes approximating the human 10-20 system locations (FpFz, Fpz, F3, F4, Fz, Cz, C3, C4, Pz, P5, P6, Poz, O1, O2, Oz) (Jasper, 1958). Referencing was done through linked ears. The impedance of the individual electrodes was confirmed to be between 2–5 kOhm at 30 Hz, resembling electrodes used for human EEG. EEG was recorded using a Multichannel Acquisition Processor (Plexon) at 1 kHz and filtered between 0.7–170 Hz. The monkey performed a visual search task necessitating directed spatial attention. Data was aligned to array onset and baseline corrected by subtracting the average activity during the 50 ms preceding the array onset from all timepoints. Data was clipped 20 ms prior to saccade to eliminate eye movement artifacts.

5.5.10 Comparing 10-20 EEG Recordings and Forward Models

To understand the configuration of plausible neural sources contributing to the generation of the N2pc, the N2pc measured in the 10-20 recordings was compared to different compositions of neural sources. 31 different configurations were generated with all possible combinations of V4, lusV4, LIP, 7a, and FEF sources. A single source model was simply the EEG modeled from a single source localized to that dipole location. Combination of source locations were computed as the sum of voltages from each source location for each simulated electrode site. In these models, we only considered the 15 electrode sites present in the 10-20 recording dataset rather than the full 10-10 configuration modeled elsewhere. Comparisons we performed as a Pearson correlation between each of the 15 empirical recording sites and the 15 simulated sites for each of the 31 model configurations. Therefore, each correlation comprised 15x30 data points. Whether a model was significantly correlated with the empirical measurement was evaluated with a Bonferroni corrected p value.

CHAPTER 6

Discussion

"Left open for further thought and research."

- William Worrall Mayo, M.D.

6.1 Summary

We sought to better understand the neural circuitry contributing to attentional selection of useful stimuli and how that ultimately leads to the generation of an associated EEG signal. In this series of works, we primarily concerned ourselves with the role of sensory cortex, and sensory processing, in selective attentional processes. We employed a unique combination of neurophysiological recordings across the layers of visual cortical area V4 simultaneous with EEG. Macaque monkeys were trained to perform an attention-demanding task during recordings known to elicit the attention-associated component known as the N2pc. We found that the synaptic activity across the layers of V4 was sufficient to predict the N2pc. Moreover, biophysically plausible forward modeling of the empirical data demonstrated that the same synaptic currents were sufficient to recapitulate the canonical distribution of the N2pc. Further modeling demonstrated that other candidate brain areas for the generation of the N2pc were insufficient. Yet, cortical columns do not just serve to generate EEG, rather the EEG is a consequence of columnar activity. Columns also represent a canonical feature of neurobiology and seemingly play an important role as a fundamental unit of neural computation. In visual processing, the organization of columns across the cortical surface encodes information regarding the location and identity of objects. Accordingly, in our experiments these cortical structures showed robust selection signals for specific stimuli in time and space, and their functional architecture predicted relative contributions of individual cortical columns to the overlying N2pc-EEG signal. This suggests that nuances of cortical organization influence the relative contributions of individual cortical columns to the global EEG signal. While these findings represent substantive progress in our understanding of the contribution of cortical microcircuits to attentional selection, much remains to be considered.

6.2 Attention and Sensory Columnar Processing

From the outset, we sought to investigate whether attention altered sensory processing across cortical columns. Recent work has shown attention manifesting different magnitudes of effects across cortical layers in V4 (e.g., (Nandy et al., 2017)), but whether this occured in visual search tasks had not been investigated. Chapter two represents the bulk of findings in this pursuit and while we ultimately found several

layer-specific attentional modulations in V4, one of the most surprising discoveries made here was in how attention seemingly modulated sensory processing across cortical columns in a rhythmic fashion. We know from decades of prior work that sensory cortical columns are topographically organized to represent visual space and features (e.g., (Hubel and Wiesel, 1962, 1968; Mountcastle, 1997; Kaas, 2012)). Each cortical column shows selectivity for a specific aspect of a (or several) feature dimensions (e.g., the color [feature dimension] red [specific aspect]). And while other work has found that those selectivities can be tuned within the feature space with deployment of attention (Treue and Martínez Trujillo, 1999; Martinez-Trujillo and Treue, 2004; McAdams and Maunsell, 1999), and have been theorized to be critical for execution of visual search (Navalpakkam and Itti, 2007), we discovered a rather interesting, unforeseen dynamic. Specifically, we found that in selecting a pop-out feature, sensory cortical columns selective for that feature vacillated in their preference through time. A red-preferring color column in V4, when presented with a red pop-out item, became rhythmically more and less selective for red while that item was in the column's response field. However, while this is a noteworthy observation, in many ways this findings asks more questions than it answers. For one, is this a response characteristic generated by the columnar structure and its organization of connections? That is, does the sequence of processing happening along the layers of cortical columns result in this rhythmic selectivity? More likely it is driven through horizontal connections between columns of differing preferences given the topographic organization of feature space. If this is the case, it begs the question why do we observe the strongest rhythmic selectivity outside of the superficial cortical layers, where horizontal connections are perhaps most robust (Gilbert and Wiesel, 1979, 1983; Rockland and Lund, 1983; Martin and Whitteridge, 1984; McGuire et al., 1991; Anderson et al., 1993; Callaway, 1998)? Also, if this rhythmic selectivity generated by the topographic organization for features across columns, is the pop-out being of one feature and flanked by differing features in different parts of retinotopic space necessary for this rhythm to occur? If this is the case, this could be thought of more as a unique characteristic of sensory processing under pop-out conditions rather than it being predicated on attentional selection. On the other hand, this sort of peculiarity to sensory processing could be a factor resulting in the phenomenal observation giving 'pop-out' selection its name. Regardless, it remains to be investigated whether this rhythmic selectivity for feature exists when the pop-out feature is not to-be selected or present under differing attention demands. At the very least, these results demonstrate changes in columnar processing of sensory information as a function of attention during visual search tasks. Given the quality of cortical columns and their capacity to biophysically generate electric fields (Nunez et al., 2006), these findings establish that neural activity in sensory cortical columns show the dynamicity necessary to potentially be implicated in a variety of attention signals across measurement scales.

6.3 On the Form of Attentional Selection

In pursuit of identifying laminar contributions to attentional selection, we chose to use a pop-out visual search task. For one, it allowed for the most parsimonious experimental design to study the contributions of and consequences to sensory cortical feature maps with attention as discussed in the previous section. From a more practical perspective, it allowed for rapid training of and reliable performance in macaque monkeys. And crucially, this paradigm is often used to study attentional selection and has been shown to elicit the N2pc (e.g., (Eimer et al., 2010; Purcell et al., 2013)), the primary target for our more translational investigations in Chapters four and five. However, this approach is limited with respect to how it may or may not generalize to other, and in particular, less efficient forms of attentional selection. Less efficient search, in the simplest form, refers to search conditions where the attentional target does not pop-out from its surroundings. These searches are therefore more difficult and take longer to resolve (Treisman and Gelade, 1980). Thus, while color-based pop-out search afforded certain opportunities for scientific discovery as discussed in Chapter two, much remains in examining cortical microcircuitry for attentional selection in different visual search tasks.

Most notable of these visual search task distinctions is perhaps the difference between efficient or pop-out (e.g., red among green) and less efficient (e.g., T among L's) or multidimensional feature-based (e.g., red T among green T's and red and green L's) searches. For instance, previous work has repeatedly demonstrated that purely feedforward neural networks can reliably select salient stimuli (Itti and Koch, 2000, 2001). This salience-based mechanism for selection does not function as robustly for less efficient forms of search which do not rely on an obvious difference between the target of attention and distracting stimuli. As such, one could conceive that the selection process might unravel differently as a function of the form of visual search being performed just from the phenomenal description alone. In fact, the early component of attentional selection shown in Chapter three conforms to the purely feedforward, salience-based mechanisms. In relating back to the previous section, this purely feedforward selection could be intertwined with the rhythmic feature selectivity, thereby supporting the notion this might not be observed under different attention conditions.

Even so, while the sensory processing of an isolated feature among a homogeneous set of distractors could feasibly be resolved in sensory processing alone, the simplest multidimensional feature searches complicate this process. That is because the obvious feature gradient that makes up the salience difference in pop-out search is no longer present. As such, search for the target could not be resolved (with 100%, one-shot accuracy) without prior knowledge of the identity of the target. It remains to be investigated whether processing along visual cortical columns could be modulated in such a to promote feedforward

selection of a such a template or if early feedforward attentional selection does not exist and we only observe a later feedback-driven selection signal. In Chapter three, some evidence exists for promotion of certain features with knowledge of the attentional target. Speculatively, this might suggest that cortical columnar activity in sensory cortex might be able to be primed before the presentation of a search array which could in turn yield feedforward selection even without a salient feature gradient. However, that remains to be demonstrated. While not investigating the role of columnar circuits, other work demonstrated that the behavioral selection of the relevant multidimensional stimulus in V4 is secondary to feedback activation (Ogawa and Komatsu, 2004), seemingly from area FEF (Ogawa and Komatsu, 2006), and not present in the feedforward selection process. Perhaps the lack of laminar information skews this finding. Nonetheless, this highlights an important direction for attention research in cortical circuits: Can we disentangle feedforward vs. feedback contributions to attentional selection processes across different forms of search tasks.

The putative dissociation between early feedforward selection and that of a feedback modulation seems a next logical investigation for the application of laminar neurophysiology. Given models such as the canonical cortical microcircuit (Douglas et al., 1989; Douglas and Martin, 1991; Bastos et al., 2012), can we can perhaps infer something about the processing stages for visual search as a factor of the exact form of visual search? One hypothesis would be that pop-out visual search is resolved feedforward as observed through selective signals present in the granular input layers in Chapter three, but less efficient forms of search (e.g., T among L's) require selection outside of sensory cortex which then influence sensory processing through activation of the feedback recipient extragranular layers in sensory cortex. This secondary feedback modulation is likely still present in the pop-out case and is perhaps observed best in Chapter four with the extragranular currents demonstrating attentional selective signaling later in the search. In sum, a finer grain understanding of the laminar microcircuitry would likely shed further light on the attentional selection process. However, as one ultimate aim of this research program is to understand the neuronal circuits giving rise to EEG, these considerations highlight a couple of important questions. Which processing stage is being indexed by the N2pc and what does that mean for our interpretation of that signal if there are multiple stages to between dissociated between?

6.4 Biophysical vs. Computational Generators of EEG Signals

An important observation from this series of experiments is with respect to the interpretability of neural signals, especially at the level of their extracranial manifestations. With the increasing interest and prevalence in brain-machine interface and EEG for medical diagnosis (as will be discussed below), an understanding of the exact information content of individual EEG components is crucial. We confirmed from these experiments that visual cortical area V4 is sufficient to generate an attention-associated signal

measurable extracranially, namely the N2pc (Chapters four and five). However, we know that many other brain areas are involved in the selection of attentional targets. A well-documented example being the frontal eye fields (FEF) (Schall, 2015). However, FEF is one such area that was deemed unlikely capable of contributing to the biophysical generation of the N2pc in our simulations (Chapter five). Yet, we know from previous work that the attentional target selection process in FEF precedes and predicts the N2pc (Cohen et al., 2009) and FEF has causal power in influencing V4 activity (Moore and Armstrong, 2003; Armstrong et al., 2006; Armstrong and Moore, 2007). How then should we approach interpreting the N2pc from a neural circuits perspective?

The attentional modulation indexed by the N2pc may well be secondary. That is, given the timing of the modulation and known pathways for attention, another area like FEF could be instantiating the selection of a stimulus with modulations across a wider range of areas predicated on that initial stage. This would suggest that the N2pc-generating V4 activations are potentially one or more stages removed from the behavior-dictating selection circuitry. Why do we not see FEF contributing to the N2pc, then? As expanded on in Chapter five, the biophysical geometry of FEF (it being within the arcuate sulcus and parallel, rather than perpendicular, to the brain surface) makes it unlikely that FEF-generated electric fields would be measurable via surface EEG. Perhaps the 'best' extracortical N2pc exists within the intrasulcal space of the arcuate. Nonetheless, this model would indicate a notable distinction between the brain areas instantiating the cognitive or perceptual process indexed by an EEG component and those brain areas with the biophysical geometry conducive for the generation of an extracranially measurable signal.

6.5 A Mosaic for EEG

While the deeper appreciation we gained of computational vs. biophysical contributors to EEG from these studies, in particular from Chapter five, an equally intriguing aspect was observed in Chapter four. The same EEG event-related potential from one trial to the next can be generated by functionally distinct configurations of mesoscopic neural circuits. In other words, the N2pc on trial 1 can look qualitatively indistinct from the N2pc on trial 2, but depending on what exactly was attended to, the cortical columns primarily generating the N2pc on 1 can be entirely different than on 2. In Chapter four this was observed as differential contributions of red- vs. green-preferring sensory cortical columns to the N2pc when a red vs. green item was being attended to. As such, we come to a hypothesis regarding the macrostructure of EEG production, at least for the N2pc. The N2pc can be generated from functionally different combinations of cortical columns depending on the attention conditions. In this sense, you have a mosaic of cortical columns with varying contribution to the overlying EEG signal. As such, this puts forward considerations for interpreting the EEG. For instance, the variability in the EEG signal need not necessary stem from

variability in the process being studied. Such variability could stem from the exact configuration of cortical columns contributing on a trial-by-trial basis. Much is left to explore in how this discovery could, if at all, be practically applied for EEG research. At the very least it demonstrates that cortical functional organization impacts even global signals like the EEG.

6.6 Towards Practical Applications: Clinical Utility and Brain-machine Interface

Sophisticated brain-machine interface (BMI) is rapidly becoming a reality with modern advances in neural recording technologies. Major companies like Neuralink aim to implant humans with high-density intracranial recording devices within the next few years. However, to intelligently use BMI, it will be important to know where to place them to record and possibly affect areas in the brain that are of interest. An example of this might be a device to readout attentional state which may be useful in cases of cognitive disruption such as schizophrenia (Luck et al., 2006; Verleger et al., 2013; Fuggetta et al., 2015) or attention-deficit/hyperactivity disorder (Wang et al., 2016, 2017; Shushakova et al., 2018; Rodriguez-Martinez et al., 2021). For example, the electroencephalogram can be used to readout and, coupled with transcranial direct current stimulation, affect performance in cognitive tasks (Reinhart et al., 2015). While we know we can measure and manipulate these cognitive abilities, our understanding is in its infancy. Perhaps the reason the EEG has not had the same impact on neurology and psychiatry that the EKG has had on cardiology is due to our relatively poor understanding of the neuronal generators for EEG. Each polarization of the EKG has a well-defined physiological generator, something we are lacking for most EEG polarizations. This is moreover complicated by the relatively distributed processing the brain uses to perform perceptual and cognitive operations. If we consider again the computational vs. biophysical generators of EEG, it may not be most effective to causally affect areas generating the EEG if we know a precursor area is performing the computation of interest (e.g., affecting V4 vs. FEF for an attention-demanding task). These 'confusion' elements should be carefully considered when thinking to use EEG for practical purposes as affecting the generator would not necessarily affect the computational process. Beginning to understand in more detail where sources of these cognitive signals in the brain, not just the biophysical generators, are localized through invasive neurophysiologyical recordings will allow us to more effectively use EEG in the clinic and BMI in practice.

6.7 A Digression to Conscious Perception

And while the practical applications of this research could be quite broad, there are also broader considerations to basic science. For instance, how might we consider approaching consciousness research. In considering feedforward and feedback contributions to attentional selection and the idea of a speculative

sequence of selective processes presented in earlier sections, a question springs to mind. One could ask when does the recognition of an object as the 'target' arise? That is, when, where, and why is an object consciously perceived as the target. This is perhaps the putative selection stage that we are most interested in from a cognitive perspective, distinguishing it from purely sensory selective and motor selective processes. While V4 can perhaps identify the behavioral target in the feedforward sensory response as documented in Chapter three, are we already consciously aware at that earliest selection time that the target is present? On the other hand, it seems too late that we are consciously aware only once we are planning an eye movement to the item. It seems a timely question given the resurgence in consciousness research, when in visual search is the target consciously perceived and how does that relate to when certain brain areas are showing selective responses to that stimulus. Some recent work might suggest that conscious perception of a minimally-visible stimulus requires engagement of frontal cortex (van Vugt et al., 2018) with prior physiological studies suggesting such a role (Thompson and Schall, 1999, 2000; Libedinsky and Livingstone, 2011), but placing that within the framework of a visual search task remains to be performed. Ultimately, conscious perception during visual search is perhaps a difficult question to ask in the macaque monkey where these recordings are available, but one that has the potential to shed light on one of modern neuroscience's greatest questions: what are the neural substrates of conscious perception.

6.8 Conclusions

In sum, this dissertation sought to provide a better understanding of circuits performing attentional selection and their consequent signals through two aims. A combination of experimentation and computational modeling demonstrated that cortical columns in primates can generate EEG signals through an exploration of attentional selection and the N2pc, leading to a more comprehensive understanding of the meaning of attention-associated signals across spatial scales. Also, in evaluating the functional architecture of cortex we reveal new discoveries underpinning the organization of mesoscopic circuitry comprising EEG production and attentional modulation and selection, more generally. From these results, we made new discoveries in sensory coding during attentional selection and gained insight into the origins and interpretative value of EEG signals, shedding new light on findings past, present, and future.

References

Adams, D. L. and Zeki, S. (2001). Functional organization of macaque V3 for stereoscopic depth. *Journal of Neurophysiology*, 86(5):2195–2203.

Albrecht, D. G., Farrar, S. B., and Hamilton, D. B. (1984). Spatial contrast adaptation characteristics of neurones recorded in the cat's visual cortex. *The Journal of Physiology*, 347(1):713–739. _eprint: https://onlinelibrary.wiley.com/doi/pdf/10.1113/jphysiol.1984.sp015092.

Anderson, J. C., Kennedy, H., and Martin, K. A. C. (2011). Pathways of Attention: Synaptic Relationships of Frontal Eye Field to V4, Lateral Intraparietal Cortex, and Area 46 in Macaque Monkey. *Journal of Neuroscience*, 31(30):10872–10881. Publisher: Society for Neuroscience Section: Articles.

Anderson, J. C., Martin, K. A., and Whitteridge, D. (1993). Form, function, and intracortical projections of neurons in the striate cortex of the monkey Macacus nemestrinus. *Cerebral Cortex (New York, N.Y.: 1991)*, 3(5):412–420.

Armstrong, K. M., Fitzgerald, J. K., and Moore, T. (2006). Changes in visual receptive fields with microstimulation of frontal cortex. *Neuron*, 50(5):791–798.

Armstrong, K. M. and Moore, T. (2007). Rapid enhancement of visual cortical response discriminability by microstimulation of the frontal eye field. *Proceedings of the National Academy of Sciences of the United States of America*, 104(22):9499–9504.

Averbeck, B. B., Latham, P. E., and Pouget, A. (2006). Neural correlations, population coding and computation. *Nature Reviews Neuroscience*, 7(5):358–366. Number: 5 Publisher: Nature Publishing Group.

Bao, M., Yang, L., Rios, C., He, B., and Engel, S. A. (2010). Perceptual learning increases the strength of the earliest signals in visual cortex. *Journal of Neuroscience*, 30(45):15080–15084.

Bastos, A. M., Lundqvist, M., Waite, A. S., Kopell, N., and Miller, E. K. (2020). Layer and rhythm specificity for predictive routing. *Proceedings of the National Academy of Sciences*, 117(49):31459–31469. Publisher: National Academy of Sciences Section: Biological Sciences.

Bastos, A. M., Usrey, W. M., Adams, R. A., Mangun, G. R., Fries, P., and Friston, K. J. (2012). Canonical Microcircuits for Predictive Coding. *Neuron*, 76(4):695–711.

Beer, R. D. and Williams, P. L. (2015). Information processing and dynamics in minimally cognitive agents. *Cognitive Science*, 39(1):1–38.

Bekisz, M. and Wróbel, A. (2003). Attention-dependent coupling between beta activities recorded in the cat's thalamic and cortical representations of the central visual field. *European Journal of Neuroscience*, 17(2):421–426.

Bengio, Y. and Grandvalet, Y. (2004). No unbiased estimator of the variance of K-fold cross-validation. *Journal of Machine Learning Research*, 5:1089–1105. Place: Brookline Publisher: Microtome Publishing WOS:000236328100001.

Berens, P., Keliris, G. A., Ecker, A. S., Logothetis, N. K., and Tolias, A. S. (2008). Feature selectivity of the gamma-band of the local field potential in primate primary visual cortex. *Frontiers in Neuroscience*, 2(1):199–207. Place: Lausanne Publisher: Frontiers Media Sa WOS:000446090600037.

Berger, H. (1929). Über das Elektrenkephalogramm des Menschen. *Archiv für Psychiatrie und Nervenkrankheiten*, 87(1):527–570.

Bichot, N. P., Heard, M. T., DeGennaro, E. M., and Desimone, R. (2015). A Source for Feature-Based Attention in the Prefrontal Cortex. *Neuron*, 88(4):832–844.

Bichot, N. P., Rossi, A. F., and Desimone, R. (2005). Parallel and serial neural mechanisms for visual search in macaque area V4. *Science*, 308(5721):529–534.

Bichot, N. P. and Schall, J. D. (2002). Priming in Macaque Frontal Cortex during Popout Visual Search: Feature-Based Facilitation and Location-Based Inhibition of Return. *Journal of Neuroscience*, 22(11):4675–4685. Publisher: Society for Neuroscience Section: ARTICLE.

Bichot, N. P., Thompson, K. G., Rao, S. C., and Schall, J. D. (2001). Reliability of Macaque Frontal Eye Field Neurons Signaling Saccade Targets during Visual Search. *Journal of Neuroscience*, 21(2):713–725. Publisher: Society for Neuroscience Section: ARTICLE.

Bichot, N. P., Xu, R., Ghadooshahy, A., Williams, M. L., and Desimone, R. (2019). The role of prefrontal cortex in the control of feature attention in area V4. *Nature Communications*, 10(1):5727. Number: 1 Publisher: Nature Publishing Group.

Bisley, J. W. and Mirpour, K. (2019). The neural instantiation of a priority map. *Current Opinion in Psychology*, 29:108–112.

Bisley, J. W., Mirpour, K., Arcizet, F., and Ong, W. S. (2011). The role of the lateral intraparietal area in orienting attention and its implications for visual search. *European Journal of Neuroscience*, 33(11):1982–1990. _eprint: https://onlinelibrary.wiley.com/doi/pdf/10.1111/j.1460-9568.2011.07700.x.

Bohon, K. S., Hermann, K. L., Hansen, T., and Conway, B. R. (2016). Representation of Perceptual Color Space in Macaque Posterior Inferior Temporal Cortex (the V4 Complex). *eNeuro*, 3(4):ENEURO.0039–16.2016.

Bollimunta, A., Chen, Y., Schroeder, C. E., and Ding, M. (2008). Neuronal Mechanisms of Cortical Alpha Oscillations in Awake-Behaving Macaques. *Journal of Neuroscience*, 28(40):9976–9988. Publisher: Society for Neuroscience Section: Articles.

Bosman, C. A., Schoffelen, J.-M., Brunet, N., Oostenveld, R., Bastos, A. M., Womelsdorf, T., Rubehn, B., Stieglitz, T., De Weerd, P., and Fries, P. (2012). Attentional stimulus selection through selective synchronization between monkey visual areas. *Neuron*, 75(5):875–888.

Brant, R. (1990). Assessing Proportionality in the Proportional Odds Model for Ordinal Logistic-Regression. *Biometrics*, 46(4):1171–1178. Place: Washington Publisher: International Biometric Soc WOS:A1990EV52100023.

Broadbent, D. E. (1958). *Perception and communication*. Perception and communication. Pergamon Press, Elmsford, NY, US. Pages: v, 340.

Brodmann, K. (1909). *Vergleichende Lokalisationslehre der Grosshirnrinde in ihren Prinzipien dargestellt auf Grund des Zellenbaues*. Barth.

Bruyns-Haylett, M., Luo, J., Kennerley, A. J., Harris, S., Boorman, L., Milne, E., Vautrelle, N., Hayashi, Y., Whalley, B. J., Jones, M., Berwick, J., Riera, J., and Zheng, Y. (2017). The neurogenesis of P1 and N1: A concurrent EEG/LFP study. *NeuroImage*, 146:575–588.

Buffalo, E. A., Fries, P., Landman, R., Buschman, T. J., and Desimone, R. (2011). Laminar differences in gamma and alpha coherence in the ventral stream. *Proceedings of the National Academy of Sciences*, 108(27):11262–11267. Publisher: National Academy of Sciences Section: Biological Sciences.

Buffalo, E. A., Fries, P., Landman, R., Liang, H., and Desimone, R. (2010). A backward progression of attentional effects in the ventral stream. *Proceedings of the National Academy of Sciences of the United States of America*, 107(1):361–365.

Burrows, B. E. and Moore, T. (2009). Influence and limitations of popout in the selection of salient visual stimuli by area V4 neurons. *Journal of Neuroscience*, 29(48):15169–15177.

Buschman, T. J. and Miller, E. K. (2007). Top-down versus bottom-up control of attention in the prefrontal and posterior parietal cortices. *Science*, 315(5820):1860–1862.

Bushnell, B. N. and Pasupathy, A. (2012). Shape encoding consistency across colors in primate V4. *Journal of Neurophysiology*, 108(5):1299–1308.

Callaway, E. M. (1998). Local circuits in primary visual cortex of the macaque monkey. *Annual Review of Neuroscience*, 21:47–74.

Carandini, M. (2000). Visual cortex: Fatigue and adaptation. *Current Biology*, 10(16):R605–R607.

Carpenter, A. (1948). The rate of blinking during prolonged visual search. *Journal of Experimental Psychology*, 38(5):587–591. Place: US Publisher: American Psychological Association.

Carrasco, M. (2011). Visual attention: The past 25 years. *Vision Research*, 51(13):1484–1525. Place: Oxford Publisher: Pergamon-Elsevier Science Ltd WOS:000293549100006.

Caton, R. (1875). Electrical Currents of the Brain. *The Journal of Nervous and Mental Disease*, 2(4):610.

Chen, X., Zirnsak, M., Vega, G. M., Govil, E., Lomber, S. G., and Moore, T. (2020). Parietal Cortex Regulates Visual Salience and Salience-Driven Behavior. *Neuron*, 106(1):177–187.e4.

Cherry, E. C. (1953). Some Experiments on the Recognition of Speech, with One and with Two Ears. *The Journal of the Acoustical Society of America*, 25(5):975–979. Publisher: Acoustical Society of America.

Chun, M. M., Golomb, J. D., and Turk-Browne, N. B. (2011). A taxonomy of external and internal attention. *Annual Review of Psychology*, 62:73–101.

Clifford, C. W. G., Webster, M. A., Stanley, G. B., Stocker, A. A., Kohn, A., Sharpee, T. O., and Schwartz, O. (2007). Visual adaptation: Neural, psychological and computational aspects. *Vision Research*, 47(25):3125–3131.

Cohen, J. Y., Heitz, R. P., Schall, J. D., and Woodman, G. F. (2009). On the Origin of Event-Related Potentials Indexing Covert Attentional Selection During Visual Search. *Journal of Neurophysiology*, 102(4):2375–2386. Publisher: American Physiological Society.

Cohen, M. R. and Maunsell, J. H. R. (2011). Using neuronal populations to study the mechanisms underlying spatial and feature attention. *Neuron*, 70(6):1192–1204.

Cohen, M. X. (2017). Where Does EEG Come From and What Does It Mean? *Trends in Neurosciences*, 40(4):208–218.

Colby, C. L. and Goldberg, M. E. (1999). Space and attention in parietal cortex. *Annual Review of Neuroscience*, 22:319–349. Place: Palo Alto Publisher: Annual Reviews Inc WOS:000079267400014.

Cole, G. R. and Hine, T. (1992). Computation of cone contrasts for color vision research. *Behavior Research Methods, Instruments & Computers*, 24(1):22–27. Place: US Publisher: Psychonomic Society.

Constantinidis, C. and Steinmetz, M. A. (2001a). Neuronal Responses in Area 7a to Multiple-stimulus Displays: I. Neurons Encode the Location of the Salient Stimulus. *Cerebral Cortex*, 11(7):581–591.

Constantinidis, C. and Steinmetz, M. A. (2001b). Neuronal Responses in Area 7a to Multiple Stimulus Displays: II. Responses Are Suppressed at the Cued Location. *Cerebral Cortex*, 11(7):592–597.

Conway, B. R., Moeller, S., and Tsao, D. Y. (2007). Specialized color modules in macaque extrastriate cortex. *Neuron*, 56(3):560–573. Place: Cambridge Publisher: Cell Press WOS:000250774600014.

Conway, B. R. and Tsao, D. Y. (2009). Color-tuned neurons are spatially clustered according to color preference within alert macaque posterior inferior temporal cortex. *Proceedings of the National Academy of Sciences*, 106(42):18034–18039. Publisher: National Academy of Sciences Section: Biological Sciences.

Cosman, J. D., Lowe, K. A., Zinke, W., Woodman, G. F., and Schall, J. D. (2018). Prefrontal Control of Visual Distraction. *Current Biology*, 28(3):414–420.e3.

Cover, T. M. and Thomas, J. A. (2012). *Elements of Information Theory*. John Wiley & Sons. Google-Books-ID: VWq5GG6ycxMC.

Cox, M. A., Dougherty, K., Adams, G. K., Reavis, E. A., Westerberg, J. A., Moore, B. S., Leopold, D. A., and Maier, A. (2019a). Spiking Suppression Precedes Cued Attentional Enhancement of Neural Responses in Primary Visual Cortex. *Cerebral Cortex*, 29(1):77–90.

Cox, M. A., Dougherty, K., Westerberg, J. A., Schall, M. S., and Maier, A. (2019b). Temporal dynamics of binocular integration in primary visual cortex. *Journal of Vision*, 19(12):13.

Cox, M. A., Schmid, M. C., Peters, A. J., Saunders, R. C., Leopold, D. A., and Maier, A. (2013). Receptive field focus of visual area V4 neurons determines responses to illusory surfaces. *Proceedings of the National Academy of Sciences*, 110(42):17095–17100.

DeAngelis, G. C. and Newsome, W. T. (1999). Organization of disparity-selective neurons in macaque area MT. *Journal of Neuroscience*, 19(4):1398–1415.

Desimone, R. and Duncan, J. (1995). Neural mechanisms of selective visual attention. *Annual Review of Neuroscience*, 18:193–222.

Deyoe, E., Felleman, D., Vanessen, D., and Mcclendon, E. (1994). Multiple Processing Streams in Occipitotemporal Visual-Cortex. *Nature*, 371(6493):151–154. Place: London Publisher: Macmillan Magazines Ltd WOS:A1994PF19100062.

Deyoe, E. and Vanessen, D. (1988). Concurrent Processing Streams in Monkey Visual-Cortex. *Trends in Neurosciences*, 11(5):219–226. Place: Oxford Publisher: Elsevier Sci Ltd WOS:A1988N173600015.

Di, S., Baumgartner, C., and Barth, D. S. (1990). Laminar analysis of extracellular field potentials in rat vibrissa/barrel cortex. *Journal of Neurophysiology*, 63(4):832–840. Publisher: American Physiological Society.

Dobkins, K. R., Thiele, A., and Albright, T. D. (2000). Comparison of red-green equiluminance points in humans and macaques: evidence for different L:M cone ratios between species. *Journal of the Optical Society of America. A, Optics, Image Science, and Vision*, 17(3):545–556.

Dougherty, K., Cox, M. A., Ninomiya, T., Leopold, D. A., and Maier, A. (2017). Ongoing Alpha Activity in V1 Regulates Visually Driven Spiking Responses. *Cerebral Cortex (New York, N.Y.: 1991)*, 27(2):1113–1124.

Dougherty, K., Cox, M. A., Westerberg, J. A., and Maier, A. (2019). Binocular Modulation of Monocular V1 Neurons. *Current Biology*, 29(3):381–391.e4.

Douglas, R. and Martin, K. (1991). A Functional Microcircuit for Cat Visual-Cortex. *Journal of Physiology-London*, 440:735–769. Place: New York Publisher: Cambridge Univ Press WOS:A1991GA34700042.

Douglas, R. J., Martin, K. A., and Whitteridge, D. (1989). A Canonical Microcircuit for Neocortex. *Neural Computation*, 1(4):480–488. Conference Name: Neural Computation.

Dragoi, V., Sharma, J., and Sur, M. (2000). Adaptation-Induced Plasticity of Orientation Tuning in Adult Visual Cortex. *Neuron*, 28(1):287–298.

Eimer, M. (1996). The N2pc component as an indicator of attentional selectivity. *Electroencephalography and Clinical Neurophysiology*, 99(3):225–234.

Eimer, M., Kiss, M., and Cheung, T. (2010). Priming of pop-out modulates attentional target selection in visual search: Behavioural and electrophysiological evidence. *Vision Research*, 50(14):1353–1361.

Einevoll, G. T., Destexhe, A., Diesmann, M., Grün, S., Jirsa, V., de Kamps, M., Migliore, M., Ness, T. V., Plesser, H. E., and Schürmann, F. (2019). The Scientific Case for Brain Simulations. *Neuron*, 102(4):735–744.

Einevoll, G. T., Pettersen, K. H., Devor, A., Ulbert, I., Halgren, E., and Dale, A. M. (2007). Laminar Population Analysis: Estimating Firing Rates and Evoked Synaptic Activity From Multielectrode Recordings in Rat Barrel Cortex. *Journal of Neurophysiology*, 97(3):2174–2190. Publisher: American Physiological Society.

Ekstrom, L. B., Roelfsema, P. R., Arsenault, J. T., Bonmassar, G., and Vanduffel, W. (2008). Bottom-up dependent gating of frontal signals in early visual cortex. *Science (New York, N.Y.)*, 321(5887):414–417.

Ellis, F. P. (1947). Effects of a tropical climate on men in warships. *British Medical Bulletin*, 5(1):13–19.

Engel, T. A., Steinmetz, N. A., Gieselmann, M. A., Thiele, A., Moore, T., and Boahen, K. (2016). Selective modulation of cortical state during spatial attention. *Science*, 354(6316):1140–1144. Publisher: American Association for the Advancement of Science.

Eriksen, C. W. (1952). Location of objects in a visual display as a function of the number of dimensions on which the objects differ. *Journal of Experimental Psychology*, 44(1):56–60.

Eyal, G., Verhoog, M. B., Testa-Silva, G., Deitcher, Y., Benavides-Piccione, R., DeFelipe, J., de Kock, C. P. J., Mansvelder, H. D., and Segev, I. (2018). Human Cortical Pyramidal Neurons: From Spines to Spikes via Models. *Frontiers in Cellular Neuroscience*, 12:181.

Fecteau, J. H. and Munoz, D. P. (2006). Salience, relevance, and firing: a priority map for target selection. *Trends in Cognitive Sciences*, 10(8):382–390.

Felleman, D. J. and Van Essen, D. C. (1991). Distributed hierarchical processing in the primate cerebral cortex. *Cerebral Cortex (New York, N.Y.: 1991)*, 1(1):1–47.

Felleman, D. J., Xiao, Y. P., and McClendon, E. (1997). Modular organization of occipito-temporal pathways: Cortical connections between visual area 4 and visual area 2 and posterior inferotemporal ventral area in macaque monkeys. *Journal of Neuroscience*, 17(9):3185–3200. Place: Washington Publisher: Soc Neuroscience WOS:A1997WU67500026.

Ferrier, D. and Burdon-Sanderson, J. S. (1875). Experiments on the brain of monkeys.—No. I. *Proceedings of the Royal Society of London*, 23(156-163):409–430. Publisher: Royal Society.

Ferro, D., Kempen, J. v., Boyd, M., Panzeri, S., and Thiele, A. (2021). Directed information exchange between cortical layers in macaque V1 and V4 and its modulation by selective attention. *Proceedings of the National Academy of Sciences*, 118(12). Publisher: National Academy of Sciences Section: Biological Sciences.

Fiebelkorn, I. C. and Kastner, S. (2021). Spike Timing in the Attention Network Predicts Behavioral Outcome Prior to Target Selection. *Neuron*, 109(1):177–188.e4.

Fiebelkorn, I. C., Pinsk, M. A., and Kastner, S. (2018). A Dynamic Interplay within the Frontoparietal Network Underlies Rhythmic Spatial Attention. *Neuron*, 99(4):842–+. Place: Cambridge Publisher: Cell Press WOS:000442351600019.

Fiebelkorn, I. C., Pinsk, M. A., and Kastner, S. (2019). The mediodorsal pulvinar coordinates the macaque fronto-parietal network during rhythmic spatial attention. *Nature Communications*, 10:215. Place: London Publisher: Nature Publishing Group WOS:000455596900002.

Fiebelkorn, I. C., Saalmann, Y. B., and Kastner, S. (2013). Rhythmic Sampling within and between Objects despite Sustained Attention at a Cued Location. *Current Biology*, 23(24):2553–2558. Place: Cambridge Publisher: Cell Press WOS:000328918900038.

Folk, C. L., Remington, R. W., and Johnston, J. C. (1992). Involuntary covert orienting is contingent on attentional control settings. *Journal of Experimental Psychology: Human Perception and Performance*, 18(4):1030–1044. Place: US Publisher: American Psychological Association.

Foster, J. J., Bsales, E. M., and Awh, E. (2020). Covert Spatial Attention Speeds Target Individuation. *The Journal of Neuroscience: The Official Journal of the Society for Neuroscience*, 40(13):2717–2726.

Freeman, J. and Simoncelli, E. P. (2011). Metamers of the ventral stream. *Nature Neuroscience*, 14(9):1195–1201. Number: 9 Publisher: Nature Publishing Group.

Fries, P., Reynolds, J. H., Rorie, A. E., and Desimone, R. (2001). Modulation of oscillatory neuronal synchronization by selective visual attention. *Science*, 291(5508):1560–1563.

Fries, P., Womelsdorf, T., Oostenveld, R., and Desimone, R. (2008). The effects of visual stimulation and selective visual attention on rhythmic neuronal synchronization in macaque area V4. *Journal of Neuroscience*, 28(18):4823–4835.

Fuggetta, G., Bennett, M. A., and Duke, P. A. (2015). An electrophysiological insight into visual attention mechanisms underlying schizotypy. *Biological Psychology*, 109:206–221.

Fujita, I., Tanaka, K., Ito, M., and Cheng, K. (1992). Columns for Visual Features of Objects in Monkey Inferotemporal Cortex. *Nature*, 360(6402):343–346. Place: London Publisher: Macmillan Magazines Ltd WOS:A1992JZ63000051.

Gagin, G., Bohon, K. S., Butensky, A., Gates, M. A., Hu, J.-Y., Lafer-Sousa, R., Pulumo, R. L., Qu, J., Stoughton, C. M., Swanbeck, S. N., and Conway, B. R. (2014). Color-detection thresholds in rhesus macaque monkeys and humans. *Journal of Vision*, 14(8):12.

Gattass, R., Sousa, A. P., and Gross, C. G. (1988). Visuotopic organization and extent of V3 and V4 of the macaque. *Journal of Neuroscience*, 8(6):1831–1845. Publisher: Society for Neuroscience Section: Articles.

Geisler, W. S., Albrecht, D. G., and Crane, A. M. (2007). Responses of neurons in primary visual cortex to transient changes in local contrast and luminance. *Journal of Neuroscience*, 27(19):5063–5067.

Giacometti, P., Perdue, K. L., and Diamond, S. G. (2014). Algorithm to find high density EEG scalp coordinates and analysis of their correspondence to structural and functional regions of the brain. *Journal of Neuroscience Methods*, 229:84–96.

Gilbert, C. D. and Wiesel, T. N. (1979). Morphology and intracortical projections of functionally characterised neurones in the cat visual cortex. *Nature*, 280(5718):120–125.

Gilbert, C. D. and Wiesel, T. N. (1983). Clustered intrinsic connections in cat visual cortex. *The Journal of Neuroscience: The Official Journal of the Society for Neuroscience*, 3(5):1116–1133.

Givre, S. J., Schroeder, C. E., and Arezzo, J. C. (1994). Contribution of extrastriate area V4 to the surface-recorded flash VEP in the awake macaque. *Vision Research*, 34(4):415–428.

Godlove, D. C., Maier, A., Woodman, G. F., and Schall, J. D. (2014). Microcircuitry of Agranular Frontal Cortex: Testing the Generality of the Canonical Cortical Microcircuit. *Journal of Neuroscience*, 34(15):5355–5369. Publisher: Society for Neuroscience Section: Articles.

Goldberg, M. E., Bisley, J. W., Powell, K. D., and Gottlieb, J. (2006). Saccades, salience and attention: the role of the lateral intraparietal area in visual behavior. *Progress in Brain Research*, 155:157–175.

Gramfort, A., Kowalski, M., and Hämäläinen, M. (2012). Mixed-norm estimates for the M/EEG inverse problem using accelerated gradient methods. *Physics in Medicine and Biology*, 57(7):1937–1961. Publisher: IOP Publishing.

Grech, R., Cassar, T., Muscat, J., Camilleri, K. P., Fabri, S. G., Zervakis, M., Xanthopoulos, P., Sakkalis, V., and Vanrumste, B. (2008). Review on solving the inverse problem in EEG source analysis. *Journal of NeuroEngineering and Rehabilitation*, 5(1):25.

Gregoriou, G. G., Gotts, S. J., and Desimone, R. (2012). Cell-Type-Specific Synchronization of Neural Activity in FEF with V4 during Attention. *Neuron*, 73(3):581–594.

Gregoriou, G. G., Gotts, S. J., Zhou, H., and Desimone, R. (2009). High-Frequency, Long-Range Coupling Between Prefrontal and Visual Cortex During Attention. *Science*, 324(5931):1207–1210. Publisher: American Association for the Advancement of Science.

Grothe, I., Neitzel, S. D., Mandon, S., and Kreiter, A. K. (2012). Switching neuronal inputs by differential modulations of gamma-band phase-coherence. *Journal of Neuroscience*, 32(46):16172–16180.

Głabska, H., Potworowski, J., Łeski, S., and Wójcik, D. K. (2014). Independent Components of Neural Activity Carry Information on Individual Populations. *PLOS ONE*, 9(8):e105071. Publisher: Public Library of Science.

Hagen, E., Næss, S., Ness, T. V., and Einevoll, G. T. (2018). Multimodal Modeling of Neural Network Activity: Computing LFP, ECoG, EEG, and MEG Signals With LFPy 2.0. *Frontiers in Neuroinformatics*, 12.

Hamker, F. H. (2005). The reentry hypothesis: the putative interaction of the frontal eye field, ventrolateral prefrontal cortex, and areas V4, IT for attention and eye movement. *Cerebral Cortex*, 15(4):431–447.

Hansen, B. J. and Dragoi, V. (2011). Adaptation-induced synchronization in laminar cortical circuits. *Proceedings of the National Academy of Sciences*, 108(26):10720–10725. ISBN: 9781102017103 Publisher: National Academy of Sciences Section: Biological Sciences.

Hay, E., Hill, S., Schürmann, F., Markram, H., and Segev, I. (2011). Models of Neocortical Layer 5b Pyramidal Cells Capturing a Wide Range of Dendritic and Perisomatic Active Properties. *PLOS Computational Biology*, 7(7):e1002107. Publisher: Public Library of Science.

Heitz, R. P., Cohen, J. Y., Woodman, G. F., and Schall, J. D. (2010). Neural Correlates of Correct and Errant Attentional Selection Revealed Through N2pc and Frontal Eye Field Activity. *Journal of Neurophysiology*, 104(5):2433–2441. Publisher: American Physiological Society.

Helfrich, R. F., Fiebelkorn, I. C., Szczepanski, S. M., Lin, J. J., Parvizi, J., Knight, R. T., and Kastner, S. (2018). Neural Mechanisms of Sustained Attention Are Rhythmic. *Neuron*, 99(4):854–865.e5.

Hembrook-Short, J. R., Mock, V. L., and Briggs, F. (2017). Attentional Modulation of Neuronal Activity Depends on Neuronal Feature Selectivity. *Current Biology*, 27(13):1878–1887.e5.

Herrera, B., Sajad, A., Woodman, G. F., Schall, J. D., and Riera, J. J. (2020). A Minimal Biophysical Model of Neocortical Pyramidal Cells: Implications for Frontal Cortex Microcircuitry and Field Potential Generation. *Journal of Neuroscience*, 40(44):8513–8529. Publisher: Society for Neuroscience Section: Research Articles.

Herrera, B., Westerberg, J. A., Schall, M. S., Maier, A., Woodman, G. F., Schall, J. D., and Riera, J. J. (2022). Resolving the mesoscopic missing link: Biophysical modeling of EEG from cortical columns in primates. *bioRxiv*, 2022.03.16.484595.

Hickey, C., Di Lollo, V., and McDonald, J. J. (2009). Electrophysiological indices of target and distractor processing in visual search. *Journal of Cognitive Neuroscience*, 21(4):760–775.

Hines, M., Davison, A., and Muller, E. (2009). NEURON and Python. *Frontiers in Neuroinformatics*, 3.

Hof, P. and Morrison, J. (1995). Neurofilament Protein Defines Regional Patterns of Cortical Organization in the Macaque Monkey Visual-System - a Quantitative Immunohistochemical Analysis. *Journal of Comparative Neurology*, 352(2):161–186. Place: Hoboken Publisher: Wiley WOS:A1995QL21000001.

Hopf, J.-M., Luck, S. J., Girelli, M., Hagner, T., Mangun, G. R., Scheich, H., and Heinze, H.-J. (2000). Neural Sources of Focused Attention in Visual Search. *Cerebral Cortex*, 10(12):1233–1241.

Hubel, D. H. and Wiesel, T. N. (1962). Receptive fields, binocular interaction and functional architecture in the cat's visual cortex. *The Journal of Physiology*, 160:106–154.

Hubel, D. H. and Wiesel, T. N. (1968). Receptive fields and functional architecture of monkey striate cortex. *The Journal of Physiology*, 195(1):215–243.

Hubel, D. H. and Wiesel, T. N. (1974). Sequence regularity and geometry of orientation columns in the monkey striate cortex. *Journal of Comparative Neurology*, 158(3):267–293.

Hubel, D. H., Wiesel, T. N., and Stryker, M. P. (1977). Orientation columns in macaque monkey visual cortex demonstrated by the 2-deoxyglucose autoradiographic technique. *Nature*, 269(5626):328–330.

Hämäläinen, M., Hari, R., Ilmoniemi, R. J., Knuutila, J., and Lounasmaa, O. V. (1993). Magnetoencephalography—theory, instrumentation, and applications to noninvasive studies of the working human brain. *Reviews of Modern Physics*, 65(2):413–497. Publisher: American Physical Society.

Hämäläinen, M. and Sarvas, J. (1989). Realistic conductivity geometry model of the human head for interpretation of neuromagnetic data. *IEEE Transactions on Biomedical Engineering*, 36(2):165–171. Conference Name: IEEE Transactions on Biomedical Engineering.

Ipata, A. E., Gee, A. L., Bisley, J. W., and Goldberg, M. E. (2009). Neurons in the lateral intraparietal area create a priority map by the combination of disparate signals. *Experimental Brain Research*, 192(3):479–488.

Ipata, A. E., Gee, A. L., Goldberg, M. E., and Bisley, J. W. (2006). Activity in the Lateral Intraparietal Area Predicts the Goal and Latency of Saccades in a Free-Viewing Visual Search Task. *Journal of Neuroscience*, 26(14):3656–3661. Publisher: Society for Neuroscience Section: Articles.

Itti, L. and Koch, C. (2000). A saliency-based search mechanism for overt and covert shifts of visual attention. *Vision Research*, 40(10-12):1489–1506.

Itti, L. and Koch, C. (2001). Computational modelling of visual attention. *Nature Reviews. Neuroscience*, 2(3):194–203.

Jasper, H. H. (1958). The ten-twenty electrode system of the international federation. *Electroencephalography and Clinical Neurophysiology*, 10:370–375.

Jellema, T., Brunia, C. H. M., and Wadman, W. J. (2004). Sequential activation of microcircuits underlying somatosensory-evoked potentials in rat neocortex. *Neuroscience*, 129(2):283–295.

Jones, S. R., Pritchett, D. L., Sikora, M. A., Stufflebeam, S. M., Hämäläinen, M., and Moore, C. I. (2009). Quantitative Analysis and Biophysically Realistic Neural Modeling of the MEG Mu Rhythm: Rhythmogenesis and Modulation of Sensory-Evoked Responses. *Journal of Neurophysiology*, 102(6):3554–3572. Publisher: American Physiological Society.

Jones, S. R., Pritchett, D. L., Stufflebeam, S. M., Hämäläinen, M., and Moore, C. I. (2007). Neural Correlates of Tactile Detection: A Combined Magnetoencephalography and Biophysically Based Computational Modeling Study. *Journal of Neuroscience*, 27(40):10751–10764. Publisher: Society for Neuroscience Section: Articles.

Jung, B., Taylor, P. A., Seidlitz, J., Sponheim, C., Perkins, P., Ungerleider, L. G., Glen, D., and Messinger, A. (2021). A comprehensive macaque fMRI pipeline and hierarchical atlas. *NeuroImage*, 235:117997.

Kaas, J. H. (1991). Plasticity of sensory and motor maps in adult mammals. *Annual Review of Neuroscience*, 14:137–167.

Kaas, J. H. (1997). Topographic maps are fundamental to sensory processing. *Brain Research Bulletin*, 44(2):107–112. Place: Oxford Publisher: Pergamon-Elsevier Science Ltd WOS:A1997XU59900002.

Kaas, J. H. (2012). Evolution of columns, modules, and domains in the neocortex of primates. *Proceedings of the National Academy of Sciences of the United States of America*, 109 Suppl 1:10655–10660.

Kajikawa, Y. and Schroeder, C. E. (2011). How Local Is the Local Field Potential? *Neuron*, 72(5):847–858. Place: Cambridge Publisher: Cell Press WOS:000297971100017.

Kajikawa, Y., Smiley, J. F., and Schroeder, C. E. (2017). Primary Generators of Visually Evoked Field Potentials Recorded in the Macaque Auditory Cortex. *Journal of Neuroscience*, 37(42):10139–10153. Publisher: Society for Neuroscience Section: Research Articles.

Kastner, S., Pinsk, M. A., De Weerd, P., Desimone, R., and Ungerleider, L. G. (1999). Increased activity in human visual cortex during directed attention in the absence of visual stimulation. *Neuron*, 22(4):751–761.

Kastner, S. and Ungerleider, L. G. (2000). Mechanisms of visual attention in the human cortex. *Annual Review of Neuroscience*, 23:315–341.

Kienitz, R., Schmiedt, J. T., Shapcott, K. A., Kouroupaki, K., Saunders, R. C., and Schmid, M. C. (2018). Theta Rhythmic Neuronal Activity and Reaction Times Arising from Cortical Receptive Field Interactions during Distributed Attention. *Current Biology*, 28(15):2377–+. Place: Cambridge Publisher: Cell Press WOS:000440787800017.

Kiss, M., Jolicoeur, P., Dell'acqua, R., and Eimer, M. (2008). Attentional capture by visual singletons is mediated by top-down task set: new evidence from the N2pc component. *Psychophysiology*, 45(6):1013–1024.

Klein, C., Evrard, H. C., Shapcott, K. A., Haverkamp, S., Logothetis, N. K., and Schmid, M. C. (2016). Cell-Targeted Optogenetics and Electrical Microstimulation Reveal the Primate Koniocellular Projection to Supra-granular Visual Cortex. *Neuron*, 90(1):143–151.

Kobatake, E. and Tanaka, K. (1994). Neuronal Selectivities to Complex Object Features in the Ventral Visual Pathway of the Macaque Cerebral-Cortex. *Journal of Neurophysiology*, 71(3):856–867. Place: Bethesda Publisher: Amer Physiological Soc WOS:A1994NA91600003.

Kohl, C., Parviainen, T., and Jones, S. R. (2022). Neural Mechanisms Underlying Human Auditory Evoked Responses Revealed By Human Neocortical Neurosolver. *Brain Topography*, 35(1):19–35.

Kohn, A. (2007). Visual Adaptation: Physiology, Mechanisms, and Functional Benefits. *Journal of Neurophysiology*, 97(5):3155–3164. Publisher: American Physiological Society.

Kohn, A. and Movshon, J. A. (2004). Adaptation changes the direction tuning of macaque MT neurons. *Nature Neuroscience*, 7(7):764–772. Number: 7 Publisher: Nature Publishing Group.

Korovaichuk, A., Makarova, J., Makarov, V. A., Benito, N., and Herreras, O. (2010). Minor Contribution of Principal Excitatory Pathways to Hippocampal LFPs in the Anesthetized Rat: A Combined Independent Component and Current Source Density Study. *Journal of Neurophysiology*, 104(1):484–497. Publisher: American Physiological Society.

Kotake, Y., Morimoto, H., Okazaki, Y., Fujita, I., and Tamura, H. (2009). Organization of Color-Selective Neurons in Macaque Visual Area V4. *Journal of Neurophysiology*, 102(1):15–27. Place: Bethesda Publisher: Amer Physiological Soc WOS:000267446000005.

Krauzlis, R. J., Lovejoy, L. P., and Zenon, A. (2013). Superior Colliculus and Visual Spatial Attention. In Hyman, S. E., editor, *Annual Review of Neuroscience, Vol 36*, volume 36, pages 165–182. Annual Reviews, Palo Alto. ISSN: 0147-006X Journal Abbreviation: Annu. Rev. Neurosci. WOS:000323892300008.

Lakatos, P., Karmos, G., Mehta, A. D., Ulbert, I., and Schroeder, C. E. (2008). Entrainment of neuronal oscillations as a mechanism of attentional selection. *Science*, 320(5872):110–113. Place: Washington Publisher: Amer Assoc Advancement Science WOS:000254633000043.

Landau, A. N. and Fries, P. (2012). Attention Samples Stimuli Rhythmically. *Current Biology*, 22(11):1000–1004. Place: Cambridge Publisher: Cell Press WOS:000305034900022.

Law, R. G., Pugliese, S., Shin, H., Sliva, D. D., Lee, S., Neymotin, S., Moore, C., and Jones, S. R. (2022). Thalamocortical Mechanisms Regulating the Relationship between Transient Beta Events and Human Tactile Perception. *Cerebral Cortex*, 32(4):668–688.

Lee, W. H., Lisanby, S. H., Laine, A. F., and Peterchev, A. V. (2015). Electric Field Model of Transcranial Electric Stimulation in Nonhuman Primates: Correspondence to Individual Motor Threshold. *IEEE Transactions on Biomedical Engineering*, 62(9):2095–2105. Place: Piscataway Publisher: Ieee-Inst Electrical Electronics Engineers Inc WOS:000360394900001.

Legatt, A. D., Arezzo, J., and Vaughan, H. G. (1980). Averaged multiple unit activity as an estimate of phasic changes in local neuronal activity: effects of volume-conducted potentials. *Journal of Neuroscience Methods*, 2(2):203–217.

LeVay, S., Hubel, D. H., and Wiesel, T. N. (1975). The pattern of ocular dominance columns in macaque visual cortex revealed by a reduced silver stain. *Journal of Comparative Neurology*, 159(4):559–576.

Libedinsky, C. and Livingstone, M. (2011). Role of prefrontal cortex in conscious visual perception. *The Journal of Neuroscience: The Official Journal of the Society for Neuroscience*, 31(1):64–69.

Liebe, S., Logothetis, N. K., and Rainer, G. (2011). Dissociable effects of natural image structure and color on LFP and spiking activity in the lateral prefrontal cortex and extrastriate visual area V4. *Journal of Neuroscience*, 31(28):10215–10227.

Liu, J. and Newsome, W. T. (2003). Functional organization of speed tuned neurons in visual area MT. *Journal of Neurophysiology*, 89(1):246–256.

Logothetis, N. K., Kayser, C., and Oeltermann, A. (2007). In Vivo Measurement of Cortical Impedance Spectrum in Monkeys: Implications for Signal Propagation. *Neuron*, 55(5):809–823.

Logothetis, N. K., Pauls, J., Augath, M., Trinath, T., and Oeltermann, A. (2001). Neurophysiological investigation of the basis of the fMRI signal. *Nature*, 412(6843):150–157. Number: 6843 Publisher: Nature Publishing Group.

Lopes da Silva, F. H., van Rotterdam, A., Storm van Leeuwen, W., and Tielen, A. M. (1970). Dynamic characteristics of visual evoked potentials in the dog. II. Beta frequency selectivity in evoked potentials and background activity. *Electroencephalography and Clinical Neurophysiology*, 29(3):260–268.

Lowe, K. A. and Schall, J. D. (2018). Functional Categories of Visuomotor Neurons in Macaque Frontal Eye Field. *eNeuro*, 5(5):ENEURO.0131–18.2018.

Lowet, E., Gomes, B., Srinivasan, K., Zhou, H., Schafer, R. J., and Desimone, R. (2018). Enhanced Neural Processing by Covert Attention only during Microsaccades Directed toward the Attended Stimulus. *Neuron*, 99(1):207–214.e3.

Luck, S. J., Chelazzi, L., Hillyard, S. A., and Desimone, R. (1997a). Neural Mechanisms of Spatial Selective Attention in Areas V1, V2, and V4 of Macaque Visual Cortex. *Journal of Neurophysiology*, 77(1):24–42. Publisher: American Physiological Society.

Luck, S. J., Fuller, R. L., Braun, E. L., Robinson, B., Summerfelt, A., and Gold, J. M. (2006). The speed of visual attention in schizophrenia: Electrophysiological and behavioral evidence. *Schizophrenia Research*, 85(1):174–195.

Luck, S. J., Gaspelin, N., Folk, C. L., Remington, R. W., and Theeuwes, J. (2021). Progress toward resolving the attentional capture debate. *Visual Cognition*, 29(1):1–21. Publisher: Routledge _eprint: https://doi.org/10.1080/13506285.2020.1848949.

Luck, S. J., Girelli, M., McDermott, M. T., and Ford, M. A. (1997b). Bridging the Gap between Monkey Neurophysiology and Human Perception: An Ambiguity Resolution Theory of Visual Selective Attention. *Cognitive Psychology*, 33(1):64–87.

Luck, S. J. and Hillyard, S. A. (1990). Electrophysiological evidence for parallel and serial processing during visual search. *Perception & Psychophysics*, 48(6):603–617.

Luck, S. J. and Hillyard, S. A. (1994). Electrophysiological correlates of feature analysis during visual search. *Psychophysiology*, 31(3):291–308. _eprint: https://onlinelibrary.wiley.com/doi/pdf/10.1111/j.1469-8986.1994.tb02218.x.

Mackworth, N. H. (1948). The Breakdown of Vigilance during Prolonged Visual Search. *Quarterly Journal of Experimental Psychology*, 1(1):6–21. Publisher: SAGE Publications.

Maier, A. (2013). Neuroscience: the cortical layering of visual processing. *Current biology: CB*, 23(21):R959–961.

Maier, A., Adams, G., Aura, C., and Leopold, D. (2010). Distinct Superficial and Deep Laminar Domains of Activity in the Visual Cortex during Rest and Stimulation. *Frontiers in Systems Neuroscience*, 4.

Maier, A., Aura, C. J., and Leopold, D. A. (2011). Infragranular Sources of Sustained Local Field Potential Responses in Macaque Primary Visual Cortex. *Journal of Neuroscience*, 31(6):1971–1980. Publisher: Society for Neuroscience Section: Articles.

Maier, A., Wilke, M., Aura, C., Zhu, C., Ye, F. Q., and Leopold, D. A. (2008). Divergence of fMRI and neural signals in V1 during perceptual suppression in the awake monkey. *Nature Neuroscience*, 11(10):1193–1200.

Makarov, V. A., Makarova, J., and Herreras, O. (2010). Disentanglement of local field potential sources by independent component analysis. *Journal of Computational Neuroscience*, 29(3):445–457.

Maljkovic, V. and Nakayama, K. (1994). Priming of pop-out: I. Role of features. *Memory & Cognition*, 22(6):657–672.

Marshall, T. R., Esterer, S., Herring, J. D., Bergmann, T. O., and Jensen, O. (2016). On the relationship between cortical excitability and visual oscillatory responses - A concurrent tDCS-MEG study. *NeuroImage*, 140:41–49.

Martin, K. A. and Whitteridge, D. (1984). The relationship of receptive field properties to the dendritic shape of neurones in the cat striate cortex. *The Journal of Physiology*, 356:291–302.

Martinez-Trujillo, J. C. and Treue, S. (2004). Feature-based attention increases the selectivity of population responses in primate visual cortex. *Current Biology*, 14(9):744–751. Place: Cambridge Publisher: Cell Press WOS:000221341500016.

Martinez-Trujillo, J. C. and Treue, S. (2005). CHAPTER 70 - Attentional Modulation of Apparent Stimulus Contrast. In Itti, L., Rees, G., and Tsotsos, J. K., editors, *Neurobiology of Attention*, pages 425–428. Academic Press, Burlington.

Martínez-Trujillo, J. and Treue, S. (2002). Attentional modulation strength in cortical area MT depends on stimulus contrast. *Neuron*, 35(2):365–370.

McAdams, C. J. and Maunsell, J. H. (1999). Effects of attention on orientation-tuning functions of single neurons in macaque cortical area V4. *Journal of Neuroscience*, 19(1):431–441.

McAdams, C. J. and Maunsell, J. H. (2000). Attention to both space and feature modulates neuronal responses in macaque area V4. *Journal of Neurophysiology*, 83(3):1751–1755.

Mccullagh, P. (1980). Regression-Models for Ordinal Data. *Journal of the Royal Statistical Society Series B-Methodological*, 42(2):109–142. Place: Oxford Publisher: Blackwell Publ Ltd WOS:A1980KE16200001.

McGraw, K. O. and Wong, S. P. (1996). Forming inferences about some intraclass correlation coefficients. *Psychological Methods*, 1(1):30–46. Place: Washington Publisher: Amer Psychological Assoc WOS:A1996VV65700004.

McGuire, B. A., Gilbert, C. D., Rivlin, P. K., and Wiesel, T. N. (1991). Targets of horizontal connections in macaque primary visual cortex. *The Journal of Comparative Neurology*, 305(3):370–392.

Mehta, A. D., Ulbert, I., and Schroeder, C. E. (2000a). Intermodal selective attention in monkeys. I: distribution and timing of effects across visual areas. *Cerebral Cortex*, 10(4):343–358.

Mehta, A. D., Ulbert, I., and Schroeder, C. E. (2000b). Intermodal Selective Attention in Monkeys. II: Physiological Mechanisms of Modulation. *Cerebral Cortex*, 10(4):359–370.

Meijs, J., Weier, O., Peters, M., and Van Oosterom, A. (1989). On the numerical accuracy of the boundary element method (EEG application). *IEEE Transactions on Biomedical Engineering*, 36(10):1038–1049. Conference Name: IEEE Transactions on Biomedical Engineering.

Michel, C. M., Murray, M. M., Lantz, G., Gonzalez, S., Spinelli, L., and Grave de Peralta, R. (2004). EEG source imaging. *Clinical Neurophysiology*, 115(10):2195–2222.

Mitzdorf, U. (1985). Current source-density method and application in cat cerebral cortex: investigation of evoked potentials and EEG phenomena. *Physiological Reviews*, 65(1):37–100. Publisher: American Physiological Society.

Moore, T. and Armstrong, K. M. (2003). Selective gating of visual signals by microstimulation of frontal cortex. *Nature*, 421(6921):370–373. Number: 6921 Publisher: Nature Publishing Group.

Moore, T. and Zirnsak, M. (2017). Neural Mechanisms of Selective Visual Attention. In Fiske, S. T., editor, *Annual Review of Psychology, Vol 68*, volume 68, pages 47–72. Annual Reviews, Palo Alto. ISSN: 0066-4308 Journal Abbreviation: Annu. Rev. Psychol WOS:000396040000004.

Moran, J. and Desimone, R. (1985). Selective attention gates visual processing in the extrastriate cortex. *Science*, 229(4715):782–784.

Motter, B. C. (1993). Focal attention produces spatially selective processing in visual cortical areas V1, V2, and V4 in the presence of competing stimuli. *Journal of Neurophysiology*, 70(3):909–919.

Mountcastle, V. B. (1997). The columnar organization of the neocortex. *Brain*, 120 (Pt 4):701–722.

Murakami, S. and Okada, Y. (2006). Contributions of principal neocortical neurons to magnetoencephalography and electroencephalography signals. *The Journal of Physiology*, 575(3):925–936. _eprint: https://onlinelibrary.wiley.com/doi/pdf/10.1113/jphysiol.2006.105379.

Musall, S., von Pföstl, V., Rauch, A., Logothetis, N. K., and Whittingstall, K. (2014). Effects of neural synchrony on surface EEG. *Cerebral Cortex (New York, N.Y.: 1991)*, 24(4):1045–1053.

Nandy, A., Nassi, J. J., Jadi, M. P., and Reynolds, J. (2019). Optogenetically induced low-frequency correlations impair perception. *eLife*, 8:e35123.

Nandy, A. S., Nassi, J. J., and Reynolds, J. H. (2017). Laminar Organization of Attentional Modulation in Macaque Visual Area V4. *Neuron*, 93(1):235–246.

Navalpakkam, V. and Itti, L. (2007). Search Goal Tunes Visual Features Optimally. *Neuron*, 53(4):605–617.

Ng, B. S. W., Logothetis, N. K., and Kayser, C. (2013). EEG phase patterns reflect the selectivity of neural firing. *Cerebral Cortex (New York, N.Y.: 1991)*, 23(2):389–398.

Ni, A. M. and Maunsell, J. H. R. (2017). Spatially tuned normalization explains attention modulation variance within neurons. *Journal of Neurophysiology*, 118(3):1903–1913.

Ni, A. M. and Maunsell, J. H. R. (2019). Neuronal Effects of Spatial and Feature Attention Differ Due to Normalization. *Journal of Neuroscience*, 39(28):5493–5505.

Nicholson, C. and Freeman, J. A. (1975). Theory of current source-density analysis and determination of conductivity tensor for anuran cerebellum. *Journal of Neurophysiology*, 38(2):356–368. Publisher: American Physiological Society.

Nicholson, C. and Llinas, R. (1971). Field Potentials in Alligator Cerebellum and Theory of Their Relationship to Purkinje Cell Dendritic Spikes. *Journal of Neurophysiology*, 34(4):509–+. Place: Bethesda Publisher: Amer Physiological Soc WOS:A1971J815400003.

Nickerson, R. S. and Burnham, D. W. (1969). Response times with nonaging foreperiods. *Journal of Experimental Psychology*, 79(3, Pt.1):452–457. Place: US Publisher: American Psychological Association.

Ninomiya, T., Dougherty, K., Godlove, D. C., Schall, J. D., and Maier, A. (2015). Microcircuitry of agranular frontal cortex: contrasting laminar connectivity between occipital and frontal areas. *Journal of Neurophysiology*, 113(9):3242–3255. Publisher: American Physiological Society.

Ninomiya, T., Sawamura, H., Inoue, K.-i., and Takada, M. (2012). Segregated Pathways Carrying Frontally Derived Top-Down Signals to Visual Areas MT and V4 in Macaques. *Journal of Neuroscience*, 32(20):6851–6858. Publisher: Society for Neuroscience Section: Articles.

Noudoost, B., Clark, K. L., and Moore, T. (2014). A Distinct Contribution of the Frontal Eye Field to the Visual Representation of Saccadic Targets. *Journal of Neuroscience*, 34(10):3687–3698. Publisher: Society for Neuroscience Section: Articles.

Nunez, P. L., Nunez, E. P. o. B. E. P. L., and Srinivasan, R. (2006). *Electric Fields of the Brain: The Neurophysics of EEG*. Oxford University Press. Google-Books-ID: fUv54as56_8C.

Nunez, P. L., Nunez, M. D., and Srinivasan, R. (2019). Multi-Scale Neural Sources of EEG: Genuine, Equivalent, and Representative. A Tutorial Review. *Brain Topography*, 32(2):193–214.

Nunn, B. J., Schnapf, J. L., and Baylor, D. A. (1984). Spectral sensitivity of single cones in the retina of Macaca fascicularis. *Nature*, 309(5965):264–266.

Näätänen, R. (1970). The diminishing time-uncertainty with the lapse of time after the warning signal in reaction-time experiments with varying fore-periods. *Acta Psychologica*, 34:399–419.

Näätänen, R. (1971). Non-aging fore-periods and simple reaction time. *Acta Psychologica*, 35(4):316–327.

Næss, S., Halnes, G., Hagen, E., Hagler, D. J., Dale, A. M., Einevoll, G. T., and Ness, T. V. (2021). Biophysically detailed forward modeling of the neural origin of EEG and MEG signals. *NeuroImage*, 225:117467.

Ogawa, T. and Komatsu, H. (2004). Target selection in area V4 during a multidimensional visual search task. *Journal of Neuroscience*, 24(28):6371–6382.

Ogawa, T. and Komatsu, H. (2006). Neuronal dynamics of bottom-up and top-down processes in area V4 of macaque monkeys performing a visual search. *Experimental Brain Research*, 173(1):1–13. Place: New York Publisher: Springer WOS:000239170600001.

Optican, L. M. and Richmond, B. J. (1987). Temporal encoding of two-dimensional patterns by single units in primate inferior temporal cortex. III. Information theoretic analysis. *Journal of Neurophysiology*, 57(1):162–178.

Otero-Millan, J., Castro, J. L. A., Macknik, S. L., and Martinez-Conde, S. (2014). Unsupervised clustering method to detect microsaccades. *Journal of Vision*, 14(2):18.

Pagano, S. and Mazza, V. (2012). Individuation of multiple targets during visual enumeration: new insights from electrophysiology. *Neuropsychologia*, 50(5):754–761.

Pascual-Marqui, R. D. (2002). Standardized low-resolution brain electromagnetic tomography (sLORETA): technical details. *Methods and Findings in Experimental and Clinical Pharmacology*, 24 Suppl D:5–12.

Pashler, H. E. (1998). *The psychology of attention*. The psychology of attention. The MIT Press, Cambridge, MA, US. Pages: xiv, 494.

Penny, W. D., Friston, K. J., Ashburner, J. T., Kiebel, S. J., and Nichols, T. E. (2011). *Statistical Parametric Mapping: The Analysis of Functional Brain Images*. Elsevier. Google-Books-ID: G_qdEsDlkp0C.

Pesaran, B., Vinck, M., Einevoll, G. T., Sirota, A., Fries, P., Siegel, M., Truccolo, W., Schroeder, C. E., and Srinivasan, R. (2018). Investigating large-scale brain dynamics using field potential recordings: analysis and interpretation. *Nature Neuroscience*, 21(7):903–919. Number: 7 Publisher: Nature Publishing Group.

Pettersen, K. H., Devor, A., Ulbert, I., Dale, A. M., and Einevoll, G. T. (2006). Current-source density estimation based on inversion of electrostatic forward solution: Effects of finite extent of neuronal activity and conductivity discontinuities. *Journal of Neuroscience Methods*, 154(1):116–133.

Pettine, W. W., Steinmetz, N. A., and Moore, T. (2019). Laminar segregation of sensory coding and behavioral readout in macaque V4. *Proceedings of the National Academy of Sciences*, 116(29):14749–14754. Publisher: National Academy of Sciences Section: Biological Sciences.

Pinotsis, D. A., Geerts, J. P., Pinto, L., FitzGerald, T. H. B., Litvak, V., Auksztulewicz, R., and Friston, K. J. (2017). Linking canonical microcircuits and neuronal activity: Dynamic causal modelling of laminar recordings. *NeuroImage*, 146:355–366.

Pooresmaeili, A., Poort, J., Thiele, A., and Roelfsema, P. R. (2010). Separable codes for attention and luminance contrast in the primary visual cortex. *Journal of Neuroscience*, 30(38):12701–12711.

Poort, J., Raudies, F., Wannig, A., Lamme, V. A. F., Neumann, H., and Roelfsema, P. R. (2012). The role of attention in figure-ground segregation in areas V1 and V4 of the visual cortex. *Neuron*, 75(1):143–156.

Popov, T., Kastner, S., and Jensen, O. (2017). FEF-Controlled Alpha Delay Activity Precedes Stimulus-Induced Gamma-Band Activity in Visual Cortex. *The Journal of Neuroscience: The Official Journal of the Society for Neuroscience*, 37(15):4117–4127.

Pouget, P., Stepniewska, I., Crowder, E., Leslie, M., Emeric, E., Nelson, M., and Schall, J. (2009). Visual and motor connectivity and the distribution of calcium-binding proteins in macaque frontal eye field: implications for saccade target selection. *Frontiers in Neuroanatomy*, 3.

Purcell, B. A., Schall, J. D., and Woodman, G. F. (2013). On the origin of event-related potentials indexing covert attentional selection during visual search: timing of selection by macaque frontal eye field and event-related potentials during pop-out search. *Journal of Neurophysiology*, 109(2):557–569. Publisher: American Physiological Society.

Purcell, B. A., Weigand, P. K., and Schall, J. D. (2012). Supplementary Eye Field during Visual Search: Salience, Cognitive Control, and Performance Monitoring. *Journal of Neuroscience*, 32(30):10273–10285. Place: Washington Publisher: Soc Neuroscience WOS:000307125300017.

Rawley, J. B. and Constantinidis, C. (2010). Effects of task and coordinate frame of attention in area 7a of the primate posterior parietal cortex. *Journal of Vision*, 10(1):12.

Ray, S. and Maunsell, J. H. R. (2010). Differences in Gamma Frequencies across Visual Cortex Restrict Their Possible Use in Computation. *Neuron*, 67(5):885–896. Place: Cambridge Publisher: Cell Press WOS:000281938900021.

Ray, S. and Maunsell, J. H. R. (2011). Different origins of gamma rhythm and high-gamma activity in macaque visual cortex. *PLoS biology*, 9(4):e1000610.

Recanzone, G. H. and Wurtz, R. H. (2000). Effects of attention on MT and MST neuronal activity during pursuit initiation. *Journal of Neurophysiology*, 83(2):777–790.

Reich, D. S., Mechler, F., and Victor, J. D. (2001). Independent and redundant information in nearby cortical neurons. *Science (New York, N.Y.)*, 294(5551):2566–2568.

Reinhart, R. M. G., Heitz, R. P., Purcell, B. A., Weigand, P. K., Schall, J. D., and Woodman, G. F. (2012). Homologous Mechanisms of Visuospatial Working Memory Maintenance in Macaque and Human: Properties and Sources. *Journal of Neuroscience*, 32(22):7711–7722. Publisher: Society for Neuroscience Section: Articles.

Reinhart, R. M. G., Zhu, J., Park, S., and Woodman, G. F. (2015). Synchronizing theta oscillations with direct-current stimulation strengthens adaptive control in the human brain. *Proceedings of the National Academy of Sciences of the United States of America*, 112(30):9448–9453. Place: Washington Publisher: Natl Acad Sciences WOS:000358656500081.

Reynolds, J. H. and Chelazzi, L. (2004). Attentional modulation of visual processing. *Annual Review of Neuroscience*, 27:611–647.

Reynolds, J. H., Chelazzi, L., and Desimone, R. (1999). Competitive mechanisms subserve attention in macaque areas V2 and V4. *Journal of Neuroscience*, 19(5):1736–1753.

Reynolds, J. H. and Desimone, R. (2003). Interacting roles of attention and visual salience in V4. *Neuron*, 37(5):853–863.

Reynolds, J. H. and Heeger, D. J. (2009). The normalization model of attention. *Neuron*, 61(2):168–185.

Reynolds, J. H., Pasternak, T., and Desimone, R. (2000). Attention increases sensitivity of V4 neurons. *Neuron*, 26(3):703–714.

Richter, C. G., Thompson, W. H., Bosman, C. A., and Fries, P. (2017). Top-Down Beta Enhances Bottom-Up Gamma. *Journal of Neuroscience*, 37(28):6698–6711.

Riera, J. J., Ogawa, T., Goto, T., Sumiyoshi, A., Nonaka, H., Evans, A., Miyakawa, H., and Kawashima, R. (2012). Pitfalls in the dipolar model for the neocortical EEG sources. *Journal of Neurophysiology*, 108(4):956–975. Publisher: American Physiological Society.

Rockland, K. S. and Lund, J. S. (1983). Intrinsic laminar lattice connections in primate visual cortex. *The Journal of Comparative Neurology*, 216(3):303–318.

Rodriguez-Martinez, E., Arjona Valladares, A., Gomez-Gonzalez, J., Diaz-Sanchez, J. A., and Gomez, C. M. (2021). Neurophysiological differences between ADHD and control children and adolescents during the recognition phase of a working memory task. *Neuroscience Research*, 164:46–54. Place: Clare Publisher: Elsevier Ireland Ltd WOS:000620783600005.

Roe, A. W., Chelazzi, L., Connor, C. E., Conway, B. R., Fujita, I., Gallant, J. L., Lu, H., and Vanduffel, W. (2012). Toward a Unified Theory of Visual Area V4. *Neuron*, 74(1):12–29.

Roelfsema, P. R., Lamme, V. A., and Spekreijse, H. (1998). Object-based attention in the primary visual cortex of the macaque monkey. *Nature*, 395(6700):376–381.

Roelfsema, P. R., Lamme, V. A. F., and Spekreijse, H. (2004). Synchrony and covariation of firing rates in the primary visual cortex during contour grouping. *Nature Neuroscience*, 7(9):982–991.

Roelfsema, P. R., Tolboom, M., and Khayat, P. S. (2007). Different processing phases for features, figures, and selective attention in the primary visual cortex. *Neuron*, 56(5):785–792.

Rotermund, D., Taylor, K., Ernst, U. A., Kreiter, A. K., and Pawelzik, K. R. (2009). Attention improves object representation in visual cortical field potentials. *Journal of Neuroscience*, 29(32):10120–10130.

Saalmann, Y. B. and Kastner, S. (2011). Cognitive and Perceptual Functions of the Visual Thalamus. *Neuron*, 71(2):209–223. Place: Cambridge Publisher: Cell Press WOS:000293433900006.

Saalmann, Y. B., Pinsk, M. A., Wang, L., Li, X., and Kastner, S. (2012). The Pulvinar Regulates Information Transmission Between Cortical Areas Based on Attention Demands. *Science*, 337(6095):753–756.

Sajad, A., Godlove, D. C., and Schall, J. D. (2019). Cortical microcircuitry of performance monitoring. *Nature Neuroscience*, 22(2):265–274. Number: 2 Publisher: Nature Publishing Group.

Salazar, R. F., Dotson, N. M., Bressler, S. L., and Gray, C. M. (2012). Content-specific fronto-parietal synchronization during visual working memory. *Science*, 338(6110):1097–1100.

Sandhaeger, F., von Nicolai, C., Miller, E. K., and Siegel, M. (2019). Monkey EEG links neuronal color and motion information across species and scales. *eLife*, 8:e45645.

Sani, I., Santandrea, E., Morrone, M. C., and Chelazzi, L. (2017). Temporally evolving gain mechanisms of attention in macaque area V4. *Journal of Neurophysiology*, 118(2):964–985.

Sato, T. (1988). Effects of attention and stimulus interaction on visual responses of inferior temporal neurons in macaque. *Journal of Neurophysiology*, 60(1):344–364.

Schall, J. D. (2004). On the role of frontal eye field in guiding attention and saccades. *Vision Research*, 44(12):1453–1467.

Schall, J. D. (2015). Visuomotor Functions in the Frontal Lobe. *Annual Review of Vision Science*, 1(1):469–498. _eprint: https://doi.org/10.1146/annurev-vision-082114-035317.

Schall, J. D., Morel, A., King, D. J., and Bullier, J. (1995). Topography of visual cortex connections with frontal eye field in macaque: convergence and segregation of processing streams. *Journal of Neuroscience*, 15(6):4464–4487. Publisher: Society for Neuroscience Section: Articles.

Schall, J. D., Stuphorn, V., and Brown, J. W. (2002). Monitoring and control of action by the frontal lobes. *Neuron*, 36(2):309–322. Place: Cambridge Publisher: Cell Press WOS:000178554700010.

Schein, S., Marrocco, R., and Demonasterio, F. (1982). Is There a High-Concentration of Color-Selective Cells in Area V4 of Monkey Visual-Cortex. *Journal of Neurophysiology*, 47(2):193–213. Place: Bethesda Publisher: Amer Physiological Soc WOS:A1982NC08800005.

Schein, S. J. and Desimone, R. (1990). Spectral properties of V4 neurons in the macaque. *Journal of Neuroscience*, 10(10):3369–3389.

Scherg, M., Berg, P., Nakasato, N., and Beniczky, S. (2019). Taking the EEG Back Into the Brain: The Power of Multiple Discrete Sources. *Frontiers in Neurology*, 10.

Schmid, M. C., Oeltermann, A., Juchem, C., Logothetis, N. K., and Smirnakis, S. M. (2006). Simultaneous EEG and fMRI in the macaque monkey at 4.7 Tesla. *Magnetic Resonance Imaging*, 24(4):335–342.

Schmiedt, J. T., Maier, A., Fries, P., Saunders, R. C., Leopold, D. A., and Schmid, M. C. (2014). Beta oscillation dynamics in extrastriate cortex after removal of primary visual cortex. *Journal of Neuroscience*, 34(35):11857–11864.

Schmolesky, M. T., Wang, Y., Hanes, D. P., Thompson, K. G., Leutgeb, S., Schall, J. D., and Leventhal, A. G. (1998). Signal timing across the macaque visual system. *Journal of Neurophysiology*, 79(6):3272–3278.

Schroeder, C. E., Mehta, A. D., and Givre, S. J. (1998). A spatiotemporal profile of visual system activation revealed by current source density analysis in the awake macaque. *Cerebral Cortex*, 8(7):575–592.

Schroeder, C. E., Tenke, C. E., and Givre, S. J. (1992). Subcortical contributions to the surface-recorded flash-VEP in the awake macaque. *Electroencephalography and Clinical Neurophysiology*, 84(3):219–231.

Self, M. W., van Kerkoerle, T., Supèr, H., and Roelfsema, P. R. (2013). Distinct Roles of the Cortical Layers of Area V1 in Figure-Ground Segregation. *Current Biology*, 23(21):2121–2129.

Shannon, C. (1948). A Mathematical Theory of Communication. *Bell System Technical Journal*, 27(3):379–423. Place: New York Publisher: Amer Telephone Telegraph Co WOS:A1948UH03900001.

Shapcott, K. A., Schmiedt, J. T., Saunders, R. C., Maier, A., Leopold, D. A., and Schmid, M. C. (2016). Correlated activity of cortical neurons survives extensive removal of feedforward sensory input. *Scientific Reports*, 6(1):34886. Number: 1 Publisher: Nature Publishing Group.

Shattuck, D. W., Sandor-Leahy, S. R., Schaper, K. A., Rottenberg, D. A., and Leahy, R. M. (2001). Magnetic Resonance Image Tissue Classification Using a Partial Volume Model. *NeuroImage*, 13(5):856–876.

Shepherd, G. M. G. (2009). Intracortical cartography in an agranular area. *Frontiers in Neuroscience*, 3(3):337–343. Place: Lausanne Publisher: Frontiers Media Sa WOS:000419790300004.

Shrout, P. E. and Fleiss, J. L. (1979). Intraclass correlations: uses in assessing rater reliability. *Psychological Bulletin*, 86(2):420–428.

Shushakova, A., Wiesner, C. D., Ohrmann, P., and Pedersen, A. (2018). Electrophysiological evidence of an attentional bias towards appetitive and aversive words in adults with attention-deficit/hyperactivity disorder. *Clinical Neurophysiology*, 129(9):1937–1946.

Snyder, A. C. and Smith, M. A. (2015). Stimulus-dependent spiking relationships with the EEG. *Journal of Neurophysiology*, 114(3):1468–1482.

Soltani, A. and Koch, C. (2010). Visual saliency computations: mechanisms, constraints, and the effect of feedback. *Journal of Neuroscience*, 30(38):12831–12843.

Stanton, G. B., Bruce, C. J., and Goldberg, M. E. (1995). Topography of projections to posterior cortical areas from the macaque frontal eye fields. *Journal of Comparative Neurology*, 353(2):291–305. _eprint: https://onlinelibrary.wiley.com/doi/pdf/10.1002/cne.903530210.

Steinmetz, M. A., Connor, C. E., Constantinidis, C., and McLaughlin, J. R. (1994). Covert attention suppresses neuronal responses in area 7a of the posterior parietal cortex. *Journal of Neurophysiology*, 72(2):1020–1023. Publisher: American Physiological Society.

Steinmetz, M. A. and Constantinidis, C. (1995). Neurophysiological Evidence for a Role of Posterior Parietal Cortex in Redirecting Visual Attention. *Cerebral Cortex*, 5(5):448–456.

Steinmetz, N. A. and Moore, T. (2014). Eye movement preparation modulates neuronal responses in area V4 when dissociated from attentional demands. *Neuron*, 83(2):496–506.

Stemmann, H. and Freiwald, W. A. (2019). Evidence for an attentional priority map in inferotemporal cortex. *Proceedings of the National Academy of Sciences*, 116(47):23797–23805. Publisher: National Academy of Sciences Section: PNAS Plus.

Stănişor, L., van der Togt, C., Pennartz, C. M. A., and Roelfsema, P. R. (2013). A unified selection signal for attention and reward in primary visual cortex. *Proceedings of the National Academy of Sciences*, 110(22):9136–9141.

Supèr, H. and Roelfsema, P. R. (2005). Chronic multiunit recordings in behaving animals: advantages and limitations. *Progress in Brain Research*, 147:263–282.

Supèr, H., van der Togt, C., Spekreijse, H., and Lamme, V. A. F. (2003). Internal state of monkey primary visual cortex (V1) predicts figure-ground perception. *The Journal of Neuroscience: The Official Journal of the Society for Neuroscience*, 23(8):3407–3414.

Sutterer, D. W., Coia, A. J., Sun, V., Shevell, S. K., and Awh, E. (2021). Decoding chromaticity and luminance from patterns of EEG activity. *Psychophysiology*, 58(4):e13779.

Suzuki, M. and Larkum, M. E. (2017). Dendritic calcium spikes are clearly detectable at the cortical surface. *Nature Communications*, 8(1):276. Number: 1 Publisher: Nature Publishing Group.

Tallon-Baudry, C., Bertrand, O., Hénaff, M.-A., Isnard, J., and Fischer, C. (2005). Attention modulates gamma-band oscillations differently in the human lateral occipital cortex and fusiform gyrus. *Cerebral Cortex*, 15(5):654–662.

Tanaka, K. (1996). Inferotemporal cortex and object vision. *Annual Review of Neuroscience*, 19:109–139. Place: Palo Alto Publisher: Annual Reviews Inc WOS:A1996TY51800005.

Tanaka, K. (2003). Columns for complex visual object features in the inferotemporal cortex: Clustering of cells with similar but slightly different stimulus selectivities. *Cerebral Cortex*, 13(1):90–99. Place: Cary Publisher: Oxford Univ Press Inc WOS:000179667500013.

Tanaka, T., Nishida, S., Aso, T., and Ogawa, T. (2013). Visual response of neurons in the lateral intraparietal area and saccadic reaction time during a visual detection task. *European Journal of Neuroscience*, 37(6):942–956.

Tanaka, T., Nishida, S., and Ogawa, T. (2015). Different target-discrimination times can be followed by the same saccade-initiation timing in different stimulus conditions during visual searches. *Journal of Neurophysiology*, 114(1):366–380. Publisher: American Physiological Society.

Tanigawa, H., Lu, H. D., and Roe, A. W. (2010). Functional organization for color and orientation in macaque V4. *Nature Neuroscience*, 13(12):1542–1548. Number: 12 Publisher: Nature Publishing Group.

Teeuwen, R. R. M., Wacongne, C., Schnabel, U. H., Self, M. W., and Roelfsema, P. R. (2021). A neuronal basis of iconic memory in macaque primary visual cortex. *Current Biology*, 31(24):5401–5414.e4.

Theeuwes, J. (1993). Visual selective attention: A theoretical analysis. *Acta Psychologica*, 83(2):93–154.

Thiele, A., Pooresmaeili, A., Delicato, L. S., Herrero, J. L., and Roelfsema, P. R. (2009). Additive effects of attention and stimulus contrast in primary visual cortex. *Cerebral Cortex*, 19(12):2970–2981.

Thomas, N. W. D. and Paré, M. (2007). Temporal Processing of Saccade Targets in Parietal Cortex Area LIP During Visual Search. *Journal of Neurophysiology*, 97(1):942–947. Publisher: American Physiological Society.

Thompson, K. G., Bichot, N. P., and Sato, T. R. (2005a). Frontal Eye Field Activity Before Visual Search Errors Reveals the Integration of Bottom-Up and Top-Down Salience. *Journal of Neurophysiology*, 93(1):337–351. Publisher: American Physiological Society.

Thompson, K. G., Biscoe, K. L., and Sato, T. R. (2005b). Neuronal basis of covert spatial attention in the frontal eye field. *The Journal of Neuroscience: The Official Journal of the Society for Neuroscience*, 25(41):9479–9487.

Thompson, K. G. and Schall, J. D. (1999). The detection of visual signals by macaque frontal eye field during masking. *Nature Neuroscience*, 2(3):283–288.

Thompson, K. G. and Schall, J. D. (2000). Antecedents and correlates of visual detection and awareness in macaque prefrontal cortex. *Vision Research*, 40(10-12):1523–1538.

Timme, N. M. and Lapish, C. (2018). A Tutorial for Information Theory in Neuroscience. *eNeuro*, 5(3):ENEURO.0052–18.2018.

Tootell, R. B. and Hamilton, S. L. (1989). Functional anatomy of the second visual area (V2) in the macaque. *Journal of Neuroscience*, 9(8):2620–2644.

Tootell, R. B. H. and Nasr, S. (2017). Columnar Segregation of Magnocellular and Parvocellular Streams in Human Extrastriate Cortex. *Journal of Neuroscience*, 37(33):8014–8032.

Tootell, R. B. H., Nelissen, K., Vanduffel, W., and Orban, G. A. (2004). Search for color 'center(s)' in macaque visual cortex. *Cerebral Cortex*, 14(4):353–363. Place: Cary Publisher: Oxford Univ Press Inc WOS:000220339600001.

Tovar, D. A., Westerberg, J. A., Cox, M. A., Dougherty, K., Carlson, T. A., Wallace, M. T., and Maier, A. (2020). Stimulus Feature-Specific Information Flow Along the Columnar Cortical Microcircuit Revealed by Multivariate Laminar Spiking Analysis. *Frontiers in Systems Neuroscience*, 14.

Trautmann, E. M., Stavisky, S. D., Lahiri, S., Ames, K. C., Kaufman, M. T., O'Shea, D. J., Vyas, S., Sun, X., Ryu, S. I., Ganguli, S., and Shenoy, K. V. (2019). Accurate Estimation of Neural Population Dynamics without Spike Sorting. *Neuron*, 103(2):292–308.e4.

Treisman, A. and Gelade, G. (1980). Feature-Integration Theory of Attention. *Cognitive Psychology*, 12(1):97–136. Place: San Diego Publisher: Academic Press Inc Elsevier Science WOS:A1980JA13200004.

Treue, S. and Martínez Trujillo, J. C. (1999). Feature-based attention influences motion processing gain in macaque visual cortex. *Nature*, 399(6736):575–579.

Ungerleider, L. G., Galkin, T. W., Desimone, R., and Gattass, R. (2008). Cortical Connections of Area V4 in the Macaque. *Cerebral Cortex*, 18(3):477–499.

van der Togt, C., Kalitzin, S., Spekreijse, H., Lamme, V. A. F., and Supèr, H. (2006). Synchrony dynamics in monkey V1 predict success in visual detection. *Cerebral Cortex (New York, N.Y.: 1991)*, 16(1):136–148.

van Kerkoerle, T., Self, M. W., Dagnino, B., Gariel-Mathis, M.-A., Poort, J., Togt, C. v. d., and Roelfsema, P. R. (2014). Alpha and gamma oscillations characterize feedback and feedforward processing in monkey visual cortex. *Proceedings of the National Academy of Sciences*, 111(40):14332–14341. Publisher: National Academy of Sciences Section: Feature Article.

van Kerkoerle, T., Self, M. W., and Roelfsema, P. R. (2017). Layer-specificity in the effects of attention and working memory on activity in primary visual cortex. *Nature Communications*, 8(1):13804. Number: 1 Publisher: Nature Publishing Group.

van Vugt, B., Dagnino, B., Vartak, D., Safaai, H., Panzeri, S., Dehaene, S., and Roelfsema, P. R. (2018). The threshold for conscious report: Signal loss and response bias in visual and frontal cortex. *Science*, 360(6388):537–542.

Vanduffel, W., Tootell, R. B. H., Schoups, A. A., and Orban, G. A. (2002). The organization of orientation selectivity throughout macaque visual cortex. *Cerebral Cortex*, 12(6):647–662.

Vanni, S., Hokkanen, H., Werner, F., and Angelucci, A. (2020). Anatomy and Physiology of Macaque Visual Cortical Areas V1, V2, and V5/MT: Bases for Biologically Realistic Models. *Cerebral Cortex*, 30(6):3483–3517.

VanRullen, R. and Thorpe, S. J. (2002). Surfing a spike wave down the ventral stream. *Vision Research*, 42(23):2593–2615.

Verleger, R., Talamo, S., Simmer, J., Śmigasiewicz, K., and Lencer, R. (2013). Neurophysiological sensitivity to attentional overload in patients with psychotic disorders. *Clinical Neurophysiology*, 124(5):881–892.

Vinck, M., Womelsdorf, T., Buffalo, E. A., Desimone, R., and Fries, P. (2013). Attentional modulation of cell-class-specific gamma-band synchronization in awake monkey area v4. *Neuron*, 80(4):1077–1089.

Wade, A., Augath, M., Logothetis, N., and Wandell, B. (2008). fMRI measurements of color in macaque and human. *Journal of Vision*, 8(10):6.1–19.

Wang, E., Sun, L., Sun, M., Huang, J., Tao, Y., Zhao, X., Wu, Z., Ding, Y., Newman, D. P., Bellgrove, M. A., Wang, Y., and Song, Y. (2016). Attentional Selection and Suppression in Children With Attention-Deficit/Hyperactivity Disorder. *Biological Psychiatry: Cognitive Neuroscience and Neuroimaging*, 1(4):372–380.

Wang, E., Sun, M., Tao, Y., Gao, X., Guo, J., Zhao, C., Li, H., Qian, Q., Wu, Z., Wang, Y., Sun, L., and Song, Y. (2017). Attentional selection predicts rapid automatized naming ability in Chinese-speaking children with ADHD. *Scientific Reports*, 7(1):939. Number: 1 Publisher: Nature Publishing Group.

Wegener, D., Freiwald, W. A., and Kreiter, A. K. (2004). The influence of sustained selective attention on stimulus selectivity in macaque visual area MT. *Journal of Neuroscience*, 24(27):6106–6114.

Westerberg, J. A., Cox, M. A., Dougherty, K., and Maier, A. (2019). V1 microcircuit dynamics: altered signal propagation suggests intracortical origins for adaptation in response to visual repetition. *Journal of Neurophysiology*, 121(5):1938–1952. Publisher: American Physiological Society.

Westerberg, J. A., Maier, A., and Schall, J. D. (2020a). Priming of Attentional Selection in Macaque Visual Cortex: Feature-Based Facilitation and Location-Based Inhibition of Return. *eNeuro*, 7(2). Publisher: Society for Neuroscience Section: Research Article: New Research.

Westerberg, J. A., Maier, A., Woodman, G. F., and Schall, J. D. (2020b). Performance Monitoring during Visual Priming. *Journal of Cognitive Neuroscience*, 32(3):515–526.

Westerberg, J. A. and Schall, J. D. (2021). Neural mechanism of priming in visual search. *Attention, Perception, & Psychophysics*, 83(2):587–602.

Westerberg, J. A., Schall, J. D., Woodman, G. F., and Maier, A. (2022a). Feedforward attentional selection in sensory cortex. *bioRxiv*, 022.06.06.495037.

Westerberg, J. A., Schall, M. S., Maier, A., Woodman, G. F., and Schall, J. D. (2022b). Laminar microcircuitry of visual cortex producing attention-associated electric fields. *eLife*, 11:e72139. Publisher: eLife Sciences Publications, Ltd.

Westerberg, J. A., Sigworth, E. A., Schall, J. D., and Maier, A. (2021). Pop-out search instigates beta-gated feature selectivity enhancement across V4 layers. *Proceedings of the National Academy of Sciences*, 118(50). Publisher: National Academy of Sciences Section: Biological Sciences.

Whittingstall, K. and Logothetis, N. K. (2009). Frequency-band coupling in surface EEG reflects spiking activity in monkey visual cortex. *Neuron*, 64(2):281–289.

Wilke, M., Logothetis, N. K., and Leopold, D. A. (2006). Local field potential reflects perceptual suppression in monkey visual cortex. *Proceedings of the National Academy of Sciences*, 103(46):17507–17512.

Williford, T. and Maunsell, J. H. R. (2006). Effects of spatial attention on contrast response functions in macaque area V4. *Journal of Neurophysiology*, 96(1):40–54.

Womelsdorf, T., Schoffelen, J.-M., Oostenveld, R., Singer, W., Desimone, R., Engel, A. K., and Fries, P. (2007). Modulation of neuronal interactions through neuronal synchronization. *Science*, 316(5831):1609–1612. Place: Washington Publisher: Amer Assoc Advancement Science WOS:000247239900039.

Woodman, G. F., Kang, M.-S., Rossi, A. F., and Schall, J. D. (2007). Nonhuman primate event-related potentials indexing covert shifts of attention. *Proceedings of the National Academy of Sciences*, 104(38):15111–15116. Publisher: National Academy of Sciences Section: Biological Sciences.

Woodman, G. F. and Luck, S. J. (1999). Electrophysiological measurement of rapid shifts of attention during visual search. *Nature*, 400(6747):867–869. Number: 6747 Publisher: Nature Publishing Group.

Xiao, Y. P., Zych, A., and Felleman, D. J. (1999). Segregation and convergence of functionally defined V2 thin stripe and interstripe compartment projections to area V4 of macaques. *Cerebral Cortex*, 9(8):792–804. Place: Cary Publisher: Oxford Univ Press Inc WOS:000084114400004.

Xing, D., Yeh, C.-I., Burns, S., and Shapley, R. M. (2012). Laminar analysis of visually evoked activity in the primary visual cortex. *Proceedings of the National Academy of Sciences of the United States of America*, 109(34):13871–13876.

Xing, D., Yeh, C.-I., and Shapley, R. M. (2009). Spatial spread of the local field potential and its laminar variation in visual cortex. *The Journal of Neuroscience: The Official Journal of the Society for Neuroscience*, 29(37):11540–11549.

Yoshioka, T., Dow, B. M., and Vautin, R. G. (1996). Neuronal mechanisms of color categorization in areas V1, V2 and V4 of macaque monkey visual cortex. *Behavioural Brain Research*, 76(1-2):51–70. Place: Amsterdam Publisher: Elsevier Science Bv WOS:A1996UK30900005.

Yoshioka, T., Levitt, J., and Lund, J. (1992). Intrinsic Lattice Connections of Macaque Monkey Visual Cortical Area-V4. *Journal of Neuroscience*, 12(7):2785–2802. Place: Washington Publisher: Soc Neuroscience WOS:A1992JC51200031.

Zalta, A., Petkoski, S., and Morillon, B. (2020). Natural rhythms of periodic temporal attention. *Nature Communications*, 11(1):1051. Place: London Publisher: Nature Publishing Group WOS:000564290500005.

Zeki, S. (1969). Representation of Central Visual Fields in Prestriate Cortex of Monkey. *Brain Research*, 14(2):271–&. Place: Amsterdam Publisher: Elsevier Science Bv WOS:A1969D730800003.

Zeki, S. (1973). Color Coding in Rhesus-Monkey Prestriate Cortex. *Brain Research*, 53(2):422–427. Place: Amsterdam Publisher: Elsevier Science Bv WOS:A1973P558900015.

Zeki, S. (1980). The Representation of Colors in the Cerebral-Cortex. *Nature*, 284(5755):412–418. Place: London Publisher: Macmillan Magazines Ltd WOS:A1980JL65400034.

Zhou, H. and Desimone, R. (2011). Feature-Based Attention in the Frontal Eye Field and Area V4 during Visual Search. *Neuron*, 70(6):1205–1217.

Łeski, S., Kublik, E., Świejkowski, D. A., Wróbel, A., and Wójcik, D. K. (2010). Extracting functional components of neural dynamics with Independent Component Analysis and inverse Current Source Density. *Journal of Computational Neuroscience*, 29(3):459–473.